Université Paul Cézanne

Faculté des Sciences et Techniques

Aix-Marseille III

Mémoire

Présenté pour l'obtention de

L'Habilitation à Diriger des Recherches

Par

Anicet BEAUVAIS

LATERITES ET MORPHOGENESE

Processus, bilans, évolutions

- 16 Décembre 2005 -

Centre Européen de Recherche et d'Enseignement de Géosciences de l'Environnement

Unité mixte de recherche 161

Université Paul Cézanne

Université Paul Cézanne

Faculté des Sciences et Techniques

Aix-Marseille III

Mémoire

Présenté pour l'obtention de

L'habilitation à Diriger des Recherches

Par

Anicet BEAUVAIS

LATERITES ET MORPHOGENESE

Processus, bilans, évolutions

- 16 Décembre 2005 -

Centre Européen de Recherche et d'Enseignement de Géosciences de l'Environnement

Unité mixte de recherche 161

Université Paul Cézanne

Anicet Beauvais, UMR 161 IRD-CEREGE, Centre IRD BP. A5, 98848 Nouméa Cedex, Nouvelle-Calédonie (Anicet.Beauvais@noumea.ird.nc; Tél : (687) 26 07 59 ; Fax : (687) 26 07 69)

SOMMAIRE

SYNTHESE SCIENTIFIQUE

FICHE RESUMEE DE L'ACTIVITE SCIENTIFIQUE

Géologue de la Surface, j'ai été formé entre 1981 et 1984 à l'étude des altérations latéritiques au laboratoire de Pétrologie et Géochimie de la Surface de l'Université de Poitiers dirigé par Daniel Nahon, et où j'ai obtenu un doctorat de 3è Cycle intitulé "*Concentrations manganésifères latéritiques. Étude pétrologique de deux gîtes sur roches sédimentaires précambriennes, gisements de Moanda (Gabon) et d'Azul (Brésil)*".

De 1985 à 1988, j'ai enseigné la pétrologie et la géochimie des altérations latéritiques au titre de la Coopération à l'Université de Bangui (RCA). Durant cette période, j'ai également mené des recherches sur les latérites du Sud-Est de la RCA dans le cadre d'un programme de recherche (CNRS-IRD) " Géochimie des latérites d'Afrique et reconstitutions paléoclimatiques" (PIRAT) dirigé par Yves Tardy.

En septembre 1988, j'ai été recruté par l'ORSTOM, ce qui m'a permis de poursuivre et achever mes études sur les latérites centrafricaines affecté au centre ORSTOM de Bangui (RCA) jusqu'en 1990.

De retour en France, j'ai été affecté de 1991 à 1992 au laboratoire de Géochimie de la Surface de l'Université de Poitiers dirigé alors par Alain Decarreaux. J'ai mis à profit cette affectation pour rédiger un mémoire de Doctorat d'Université intitulé "*Paléoclimats et dynamique d'un paysage cuirassé du Centrafrique. Morphologie, Pétrologie et Géochimie*" soutenu en Décembre 1991.

De 1993 à 1994, le Département des Sciences Géologiques de l'Université de Washington à Seattle m'a alors accueilli dans le laboratoire de géomorphologie quantitative dirigé par Thomas Dunne. Durant ces deux années, je me suis intéressé en collaboration avec David Montgomery à des problèmes de géomorphologie et de géométrie fractale des rivières et des réseaux de drainage, thème sur lequel je m'étais déjà engagé au cours de ma thèse de doctorat, motivé par ma rencontre avec Jacques Dubois de l'IPG.

À mon retour des USA en 1995, j'ai rejoint une équipe de recherche dirigée par JP. Muller au centre ORSTOM de Bondy. Je me suis alors impliqué dans l'étude géomorphologique des paysages latéritiques du Cameroun jusqu'en 1997, puis au Sénégal Oriental à partir de 1998 dans une équipe co-dirigée par G. Grandin et G. Hérail, avant de rejoindre le CEREGE en septembre 2001 et l'UR 37

"*Biogéodynamique supergène et géomorphologie tropicale*" dirigée par F. Colin. Je suis aujourd'hui affecté au centre IRD (ex. ORSTOM) de Nouméa. Outre la co-direction de l'UMR161 depuis septembre 2004, je mène des recherches sur l'évolution géomorphologique de la Grande-Terre en relation avec son soulèvement tectonique et les variations climatiques Néogène. J'étudie également les processus d'érosion (chimique et mécanique) responsables de la dénudation des massifs de roches ultrabasiques à l'échelle des bassins versants drainant ces massifs. Par ailleurs, je mène aussi des études sur l'évolution long terme des paysages latéritiques des cratons stables de la zone intertropicale à partir de datations absolues des produits de l'altération latéritique (oxyhydroxydes de manganèse et de fer).

Dans le tableau 1 est résumé mon parcours post-doctorat d'Université.

Période	Fonction et lieu d'exercice	Programme de recherche	Unité ou laboratoire de recherche IRD	Articles rang A
1991-1992	CR2 Laboratoire de géochimie de la surface (Université de Poitiers)	Étude cartographique, pétrologique et géochimique des cuirasses ferrugineuses du Sud-Est du Centrafrique *Doctorat d'Université*	Laboratoire de géochimie de la Surface (Université de Poitiers) Unité de Recherche (UR) IRD " Bio-géodynamique des formations latéritiques " (GEOLAT)	1 (1)
1993-1994	CR1 Département des sciences géologiques de l'Université de Washington à Seattle (USA)	Géomorphologie quantitative des réseaux de drainage (analyse fractale)	UR GEOLAT	2 (2)
1995-2001	CR1 Centre ORSTOM de Bondy (Géoscience de l'environnement tropical)	Géodynamique des bassins de drainage et géomorphologie des paysages latéritiques d'Afrique	UR" Bio-géoDynamique des sols Latéritiques " (DYLAT)	7 (5)
2001-2002	CR1 CEREGE (Aix-en-Provence)	Étude géomorphologique et géophysique des formations latéritiques du Sénégal	UR-037 " Bio-géodynamique supergène et géomorphologie tropicale "	2 (1)
2002-	CR1 IRD Nouméa (Nouvelle-Calédonie)	Étude géomorphologique et géophysique des formations latéritiques de Nouvelle-Calédonie	UMR 161 (IRD-CEREGE)	5 (2) **Total : 17 (11)**

Tableau. 1 - Résumé de carrière depuis mon doctorat d'université au service de l'ORSTOM puis de l'IRD ; les chiffres entre parenthèses dans la colonne Articles publiés indique le nombre d'articles en premier auteur)

Curriculum Vitae

ANICET BEAUVAIS

Géologue de la Surface (CR1)

Né le 07 Octobre 1956 à Tours (Indre et Loire)
Marié, 1 enfant

POSITION ACTUELLE

Unité mixte de Recherche IRD-CEREGE n° 161 "*Bio-géodynamique supergène et Géomorphologie Tropicale*"
Centre IRD de Nouméa
BP A5
98848 Nouméa Cedex - Nouvelle-Calédonie
Tél. : (687) 26 07 59/ Fax : (687) 26 07 69/ E-Mail : Anicet.Beauvais@noumea.ird.nc

DOMAINES SCIENTIFIQUES

Processus d'altération et d'érosion des roches en environnement tropical.
Propriétés géoélectriques des manteaux d'altération latéritique.
Morphométrie et propriétés d'échelles des réseaux hydrographiques
Qualification et quantification des processus d'érosion à l'échelle de bassins versants de taille moyenne.
Facteurs de la morphogenèse continentale en environnement tropical.
Signatures climatiques des matériaux d'altération latéritiques et des surfaces d'aplanissement associées.
Datations isotopiques des latérites.

FORMATION ET DIPLOMES

1991 : **Thèse de Doctorat** de l'Université de Poitiers (Spécialité : Géochimie de la Surface), mention très honorable et félicitations du jury, Faculté des Sciences Fondamentales et Appliquées de l'Université de Poitiers.

" *Paléoclimats et dynamique d'un paysage cuirassé du Centrafrique. Morphologie, Pétrologie et Géochimie .*" (Directeur de thèse : Yves Tardy; Jury : Jean-Jacques Trescases, Jacques Dubois, Adrien Herbillon, Yves Tardy, Alain Decarreau, Daniel Nahon).

1984 : **Thèse de 3è Cycle** Géologie Appliquée *" Sols et Altérations "*, mention très honorable et félicitations du jury, U.E.R. Sciences Fondamentales et Appliquées de l'Université de Poitiers.

"*Concentrations manganésifères latéritiques. Étude pétrologique de deux gîtes sur roches sédimentaires précambriennes, gisements de Moanda (Gabon) et d'Azul (Brésil)"* (Directeur de thèse : Daniel Nahon; Jury: Daniel Nahon, Jean-Jacques Trescases, Alain Meunier, Francis Weber, Adolfo Melfi, Alain Ruellan)·

1982 : **Diplôme d'Etude Approfondies** de Géologie Appliquée, mention AB, U.E.R. Sciences Fondamentales et Appliquées de l'Université de Poitiers.

1981 : **Maîtrise** des Sciences de la Terre, mention AB, U.E.R. Sciences Fondamentales et Appliquées de l'Université de Poitiers.

EXPERIENCE PROFESSIONNELLE ET AFFECTATIONS

2002- : CR1 affecté au centre IRD de Nouméa (UR161CEREGE-IRD).
2001-2001 : CR1 affecté au CEREGE (Aix-en-Provence), équipe de Pétrologie et Géochimie exogène.
1995-2001 : CR1 affecté au Laboratoire des formations superficielles du centre IRD de Bondy.
1993-1994 : CR1 affecté au Département de Sciences Géologiques de l'Université de Washington State à Seattle (Pr. Thomas Dunne et Dr. David R. Montgomery).
1992 : CR1 à l'ORSTOM (aujourd'hui IRD)
1991 : CR2 affecté au laboratoire de Pétrologie de la Surface (Université de Poitiers)
1988 : CR2 Recruté à l'ORSTOM le 08 Septembre 1988, affecté à Bangui (RCA) jusqu'en septembre 1990.
1985-88 : professeur assistant (équivalent maître de conférence) à l'Institut Polytechnique de l'Université de Bangui (République Centrafricaine, RCA).

PUBLICATIONS

19 articles dans des revues à comité de lecture de rang A (dont 12 en premier auteur) et 5 à comité de lecture de rang B (3 en premier auteur) ; 3 articles de rang A soumis ; 39 communications à des congrès, colloques et séminaires nationaux et internationaux. 1 fiche scientifique d'actualité IRD.

Publications principales

Beauvais A., Colin, F. Formation and transformation processes of iron duricrusts in tropical humid environment. *Chemical Geology*, (1993), **106**, 77-101.

Beauvais A., Roquin C. Petrological differentiation patterns and geomorphic distribution of ferricretes in Central Africa. *Geoderma*, (1996), **73**, 63-82.

Beauvais A. A., Montgomery D. R. Influence of valley type on the scaling properties of river planforms. *Water Resources Research*, (1996), **32** (5), 1441-1448.

Ruffet, G., Innocent C., Michard A., Féraud G., Beauvais A., Nahon D., Hamelin B. A geochronological $^{40}Ar/^{39}Ar$ and $^{87}Rb/^{87}Sr$ study of K-Mn oxides from the weathering sequence of Azul, Brazil. *Geochimica et Cosmochimica Acta*, (1996), **60** (12), 2219-2232.

Beauvais A., Montgomery D. R. Are channel networks statistically self-similar ?. *Geology*, (1997), **25** (12), 1063-1066.

Ritz M., Parisot J-C., Diouf S., Beauvais A., Diome F., Niang M. Electrical imaging of lateritic weathering mantles over granitic and metamorphic basement of eastern Senegal, West Africa. *Journal of Applied Geophysics*, (1999), **41**, 335-344.

Beauvais A., Ritz M., Parisot J-C., Dukhan, M., Bantsimba, C. Analysis of poorly stratified lateritic terrains overlying a granitic bedrock in West Africa, using 2D electrical resistivity tomography. *Earth and Planetary Science Letters*, (1999), **173**, 413–424.

Beauvais A. Geochemical balance of lateritization processes and climatic signatures in weathering profiles overlain by ferricretes in Central Africa. *Geochimica et Cosmochimica Acta*, (1999), **63**, 23/24, 3939 - 3957.

Beauvais A., Bertaux J. *In situ* characterization and differentiation of kaolinites in lateritic weathering profiles using infrared microspectrometry. *Clays and Clay Minerals*, (2002), **50**, 3, 314-330.

Beauvais A., Ritz M., Parisot J-C., Bantsimba, C. Testing etching hypothesis in shaping granite dome structures beneath lateritic weathering landsurfaces using ERT method. *Earth Surface Processes and Landforms*, (2003), **28** (10), 1071-1080.

Beauvais A., Ritz M., Parisot J-C., Bantsimba, C., Dukhan, M. Combined ERT and GPR methods for investigating two stepped lateritic weathering systems. *Geoderma*, (2004), **119**, 121-132.

Colin F., Beauvais A., Ruffet G., Hénocque O. First $^{40}Ar/^{39}Ar$ geochronology of lateritic manganiferous pisolites: implications for the Paleogene history of a West African landscape. *Earth and Planetary Science Letters*, (2005), **238**, 172-188.

ACTIVITES ET PROGRAMMES DE RECHERCHE

I. Activités post-doctorat (1992 - 1994)

Après la soutenance de ma thèse de Doctorat en 1991, un séjour de 20 mois entre mars 1993 et janvier 1995 au Département des Sciences Géologiques de l'Université de Washington à Seattle m'a permis de tester les méthodes d'analyse fractale aux rivières et réseaux de rivières du nord-ouest américain dans les chaînes montagneuses des Cascades et des Olympics. L'une de ces méthodes avait été appliquée au préalable sur les cours d'eau centrafricains (Beauvais, 1991 ; Beauvais et al., 1994). L'étude des rivières et réseaux américains a pu être réalisé grâce à la collaboration de David Montgomery et Harvey Greenberg. Ensemble, nous avons pu mettre à l'épreuve le modèle fractal admis à l'époque par de nombreux géomorphologues pour les réseaux hydrographiques. Les premiers résultats ont été présentés au Meeting international de l'AGU à San Francisco (Beauvais et al., 1994). Mon séjour au Etats-Unis a été aussi mis à profit pour rédiger des articles découlant des résultats obtenus sur les caractéristiques pétro-géochimiques des latérites du Sud-Est de la RCA dans le cadre de ma thèse de doctorat (Beauvais et Colin, 1993 ; Beauvais et Tardy, 1993).

II. Activités post-séjour aux USA (1995 - 1997)

De retour en France en 1995, mon affectation au centre ORSTOM de Bondy au Laboratoire des Formations Superficielles (LFS) dans l'Unité de Recherche (UR) (DYLAT) dirigée par JP. Muller sur le programme '*BiogéohydroDynamique des sols Latéritiques*'. J'y ai mené des études sur la géomorphologie et la dynamique des paysages latéritiques et réseaux de drainage du Sud du Cameroun, et j'ai participé au développement d'un volet géomorphologie et spatialisation des couvertures latéritiques dans la zone forestière du sud Cameroun, en utilisant des outils de télédétection et de spatialisation développés par Frédérique Seyler, chargé de recherche dans l'UR. Ce projet a été développé en partenariat avec des chercheurs camerounais de l'Université et de l'Institut Polytechnique de Yaoundé (Paul Bilong, Dieudonné Bitom, Alain Akono, P. Tonyé) et l'institut de Recherches Géologiques et Minières du Cameroun (G. Ekodek et Véronique Kamkang) ; en collaboration avec Jean-Paul Rudant (LGGST, Paris VI) et Pascal Sailhac (IPGP). En interne, l'Atelier Informatique (Annick Legeley-Padovani) et

le Laboratoire des Formations Superficielles-Unité Traitement Graphique des Données (Paul Faure et Boris Volkoff)) du Centre ORSTOM d'Ile de France de Bondy collaboraient à ce programme. Ce programme prenait en compte non seulement la nature des sols et les structures des couvertures d'altération, mais aussi la couverture végétale (nature et densité) et les formes et densités des réseaux hydrographiques des paysages de transition forêt savane à l'échelle de plusieurs bassins versants.

Un projet "*Utilisation d'images SAR pour la spatialisation de données de terrain acquises dans différents sites représentatifs du plateau forestier du sud Cameroun*" a permis d'obtenir des images SAR de l'Agence Européenne de recherche Spatiale (ESA). L'analyse de données de terrain et de données numériques radar (SAR-ERS1) a permis d'établir une cartographie de grands domaines morpho climatiques régis par une dynamique d'altération et d'érosion spécifique. Les résultats principaux ont été présentés au 3è symposium ERS organisé par l'ESA (European Space Agency) à Florence (Legeley-Padovani et al., 1997a, 1997b).

Durant les deux premières années à Bondy j'ai pu aussi finaliser deux publications découlant des travaux réalisés à Seattle sur l'analyse des propriétés d'échelle des rivières et réseaux hydrographiques du nord-ouest américain (Beauvais et Montgomery, 1996, 1997). J'ai pu aussi valoriser mes travaux de thèse de 3è Cycle et de Doctorat par deux articles (Ruffet et al., 1996 ; Beauvais et Roquin, 1996).

III. Activités de 1997 à 2002

En 1997, j'ai intégré l'UR dirigée par G. Grandin et G. Hérail et participé au programme '*Ressources Minérales, géodynamique et aide à l'exploration*' né de la réunion transitoire entre les géomorphologues et géologues-métallogénistes de la surface (unité dirigée par Georges Grandin) et les géologues structuralistes et tectoniciens (unité dirigée par Gérard Hérail). Concrètement, j'ai participé au projet '*Ressources minérales d'intérêt économique en Afrique*', et en particulier au volet Sénégal Oriental avec JC. Parisot et M. Ritz, en partenariat avec des chercheurs Sénégalais et Congolais (Diouf, F. Diome, P. Nyang, C. Bantsimba) de l'Université Cheikh Anta Diop de Dakar, UCAD, (Dr. Dina Paté Diallo). L'objectif principal du volet Sénégal Oriental était de mieux comprendre les modes de mise en place des matériaux latéritiques et l'évolution des paysages associés. L'apport de l'outil

géophysique tomographie de résistivité électrique (Michel Ritz, Christian Bantsimba) a été déterminant pour l'acquisition de cette compréhension. Le couplage des études géomorphologiques et pétrologiques avec les mesures de tomographie de résistivité électrique (TRE) a permis d'améliorer la connaissance des systèmes d'altération cuirassés de cette région, leur mode de mise en place et leur évolution (Ritz et al., 1999 ; Beauvais et al., 1999).

Les résultats obtenus au Sénégal Oriental ont ensuite permis de lancer le volet géophysique du programme de '*Biogéodynamique Supergène et Géomorphologie Tropicale*' (UR037) sur le chantier Nouvelle-Calédonie.

Durant les deux dernières années d'affectation à l'IRD de Bondy, J'ai pu également publier des résultats de ma thèse de Doctorat (Beauvais, 1999), et développer une collaboration avec Jacques Bertaux de l'UR 'Paléotropique', dirigée par Luc Ortlieb. Ensemble, nous avons étudié les matériaux argileux des profils d'altération du sud-est de la RCA par microscopie Infrarouge afin de caractériser différentes générations de kaolinites et d'utiliser la signature cristallochimique de l'une d'elles pour tracer la dégradation géochimique récente des cuirasses ferrugineuses de cette région. Les résultats de cette étude ont été publiés (Beauvais et Bertaux, 2002) lors de l'année passée au CEREGE (2001-2002) au sein de l'UR '*Bio-géodynamique Supergène et Géomorphologie Tropicale*' (UR037) dirigée par F. Colin. Durant cette année (2001-2002), j'ai aussi effectué une mission prospective en Nouvelle-Calédonie pour préparer ma future affectation à Nouméa.

IV. Activités depuis 2002

Depuis Septembre 2002, je suis affecté par l'IRD à Nouméa en Nouvelle-Calédonie au sein de l'UMR161 (ex. UR037 de l'IRD) et participe au programme de recherche pluridisciplinaire intitulé "Biogéodynamique Supergène et Géomorphologie Tropicale". Je mène des études géomorphologiques à l'échelle des bassins versants des massifs de roches ultrabasiques, afin de qualifier et quantifier les processus d'érosion chimique et physique. Je participe également à des études plus globales sur la morphogenèse de la Grande-Terre de Nouvelle-Calédonie et des paysages continentaux d'Afrique de l'Ouest, afin d'établir des relations entre la dénudation et la sédimentation en relation avec les paléoclimats et les grands évènements tectoniques

en Collaboration avec Dominique Chardon (CEREGE, Université Paul Cézanne d'Aix-en-Provence) et Violaine Chevillotte (Post-Doctorante ATER à l'Université de Nouvelle-Calédonie). Je participe aussi aux études géophysiques sur sites miniers en collaboration avec la société minière le Nickel (SLN) au sein d'une équipe composée de M. Ritz, J-C Parisot et B. Robineau. Depuis Septembre 2004, je suis co-responsable de l'équipe devenue UMR 161 (IRD-CEREGE), le directeur étant le Professeur Bruno Hamelin.

Je participe aussi à un programme de recherche du GDR Transmet intitulé '*Comportement bio-géochimique du chrome et des éléments métalliques associés dans les écosystèmes latéritiques de Nouvelle-Calédonie'*. L'objectif de ce programme est de suivre la dynamique du chrome et notamment celle du Cr VI au sein d'un bassin versant drainant un massif de roche ultrabasique, qui sera prochainement impacté par l'activité minière. Des collaborations ont été développées avec plusieurs équipes : CEREGE (Jérôme Rose) ; LGE-Paris VI (Marc Benedetti, M. Castrec) ; LMPMC-Paris VI (Thierry Allard, Etienne Balan, G. Morin) ; G2R-Vandoeuvre-les-Nancy (P. Faure, C. Peiffert, M. Cathelineau) ; CGS-EOST Strasbourg (F. Chabaux, N. Clauer) ; Orsay-Terre Paris XI (Cécile Quantin).

En 2004-2005, une demande a également été faite aux volets ECODYN et PNBC du programme national ACI-ECCO NFS pour élargir l'étude à d'autres métaux (Mn, Ni, Co et Fe) dans un projet intitulé " *Bio-géochimie d'éléments métalliques (Fe, Ni, Cr, Mn, Co,) dans le continuum sols - eaux - plantes des écosystèmes latéritiques de Nouvelle-Calédonie : activités anthropiques vs cycle naturel "*. Je participe à ce projet (0,30 etp), Jean-Paul Ambrosi géochimiste en accueil-détachement dans l'équipe depuis septembre 2003 en assumant la responsabilité. Ce projet vise à déterminer l'impact des activités anthropiques sur la dynamique des éléments métalliques dans les eaux (solutions du sol, rivières et zones humides), aux fronts redox et aux interfaces biologiques. Outre les collaborations avec le CEREGE, le LGE, le LMCP et Orsay-Terre, existant déjà dans le cadre du projet GDR Transmet, collaborent aussi à ce projet : le LBPVA de l'Université de Nouvelle-Calédonie (Hamid Amir), le laboratoire des symbioses tropicales et méditerranéennes (LSTM ; UMR 82) et le Laboratoire d'Ecologie Microbienne (UMR 5557 CNRS-Université Lyon 1). La demande exprimée

au préalable sous forme de lettre d'intention s'est concrétisée par un projet finalisé et financé en 2005 pour 3 ans.

Depuis mon affectation à Nouméa, j'ai également finalisé les études géomorphologiques et géophysiques de paysages latéritiques du Sénégal Oriental par deux publications (Beauvais et al., 2003 , 2004), et participé à la finalisation des études menées sur les processus d'altération-érosion et la datation (méthode $^{40}Ar/^{39}Ar$) des latérites manganésifères du Burkina Faso (Colin et al., 2005).

ACTIVITES DE FORMATION

I. Participations au co-encadrement de thèses (#3)

BANTSIMBA C. (2001) - Contribution à la caractérisation des couvertures latéritiques par les imageries électrique et radar, Sénégal Oriental. Thèse 3ème Cycle, Université Cheikh Anta Diop, Dakar, Sénégal, 109 p.

MOUELE F. (2004) - Evolution des latértites manganésifères de Derra do Navio (Brésil). Pétrologie et datation $^{40}Ar/^{39}Ar$ des cryptomélanes. Thèse de Doctorat, CEREGE, Université d'Aix-Marseille III, 283 p.

TRAORE D. (2005) - Altération supergène et évolution des platinoïdes en milieu tropical : étude de la minéralisation platinifère de la rivière des Pirogues (Nouvelle-Calédonie). Soutenance prévue février 2005 à l'Université de Nouvelle-Calédonie.

II. Participations au co-encadrement de Masters et DEA (#3)

BEZIS M. (2003) - Détermination et évolution de la résistivité electrique en fonction de la teneur en eau. DEA co-encadré à Nouméa, soutenu en 2003 au CEREGE (Université Paul Cézanne d'Aix-en-Provence)

MATHE D. (2003) - Etude des paramètres physico-chimiques contrôlant la résistivité électrique des produits d'altération des roches ultrabasiques de Tiébaghi. DEA co-encadré à Nouméa, soutenu en 2003 au CEREGE (Université Paul Cézanne d'Aix-en-Provence)

LARDIN P-E. (2004) - Modélisation de mesures de potentiel électrique spontané proche d'une mine de nickel pour conduire à une tomographie des flux hydriques. Rapport IIe année de Maîtrise Sciences et Techniques (MST) E.P.G., ULP-EOST Strasbourg (Stage effectué en France, co-encadré par P. Sailhac et A. Beauvais).

III. Participations au co-encadrement des partenaires IRD

AKONO A. (1996)- Séjour scientifique Haut-niveau courte durée (1/05-30/08/96), Laboratoire des Formations Superficielles et Atelier Informatique, Centre ORSTOM d'Ile de France, "Traitement des images SAR ERS1 pour l'analyse géomorphologique des paysages du plateau forestier sud-camerounais". Responsable : A. Beauvais (collaboration A. Legeley-Padovani, Bondy; J.P. Rudant et Fabrice Desré, LGGST, Paris VI).

BITOM D. (1996) - Séjour scientifique Haut-niveau courte durée (1/05-30/08/96), Laboratoire des Formations Superficielles et Traitement Graphique des Données, Centre ORSTOM d'Ile de France, "Etude des processus d'altération et spatialisation des sols dans le Haut-Nyong au Sud Cameroun". Responsable : B. Volkoff (collaboration A. Beauvais, et F. Seyler).

IV. Enseignements dispensés

2001-2002 : 2 encadrements de Travaux personnels assistés (TPA) + 3 H de cours-séminaire sur l'altération supergène des roches et les latérites dans le cadre du DEA du CEREGE.

IV. Rattachement à une école doctorale

2001 : École doctorale du CEREGE (Université Paul Cézanne d'Aix-en-Provence)
2002 : Rapporteur d'un DEA pour l'école doctorale du CEREGE . Un sujet de DEA proposé.
2005 : Cinq sujets de doctorats et deux sujets de stage Master 2 proposés.

AUDIENCE NATIONALE ET INTERNATIONALE

I. Workshops et sessions dans les congrès

2006 : Goldschmidt Conference, 27 Août 01 Septembre à Melbourne (Australie), Theme 10 ‘Surface processes, low temperature systems and landscape evolution’ convenor associé de la session S10-04 ‘Biogeochemical cycling of elements in the surficial environment’

2004 : membre du Risk working group, à la 21e Star Session de la 33e SOPAC Session, 17-27/09/2004, Warwick, Fidji.

1996 : réunion DBT Université de Marseille Luminy

II. Révisions d’articles et de projets scientifiques

1992 : 1 article pour *Comptes Rendus de l’Académie des Sciences*
1997 : 1 article pour *Water Resource Research*
1998 : 1 article pour *Nature*
2001-2002 : 3 articles pour *Catena*
2003-2005 : *1 article pour Earth & Planetary Science Letters*, 1 article pour *Geoderma* 3 articles pour *Comptes Rendus Géosciences* dont 2 pour le Numéro Thématique “ Transferts de matière à la surface de la Terre ”, D. Nahon et F. Colin (Eds).

2000 : Évaluation d’un projet " *Les basaltes du Maroc, de la Réunion et de la Nouvelle-Calédonie : quantification et cinétique des processus de développement des sols* " pour la création d’une Unité de formation et de recherche " *Géologie de surface et environnement* " au département de Géologie de l'Université Moulay Ismail de Meknès au Maroc.

III. Rapporteur de mémoires (thèses, master et DEA,..)

1998 : Rapporteur d'un Ph. D pour l'Université Nationale Australienne de Canberra (04-05/98)

2002 : Rapporteur d'un DEA pour l'école doctorale du CEREGE (Université Paul Cézanne d'Aix-en-Provence).

IV. Professeur-chercheur visitant

03/1993-01/1995 : Chercheur-visitant au Geological Sciences Department, University of Washington State (Seattle, USA). J'y ai mené des études géomorphologiques sur les modèles d'analyse fractale appliqués aux tracés des cours d'eau et des réseaux hydrographiques en collaboration avec David Montgomery et Harvey Greenberg.

ANIMATION DE LA RECHERCHE

2004 : responsable de l'Unité Mixte de Recherche, UMR 161, CEREGE-IRD à Nouméa (Nouvelle-Calédonie).

2005 : Rédaction, gestion et soumission de deux dossiers BESCD et d'un BSTD au Département Soutien et Formation (DSF) de l'IRD.

2005 : Rapport d'activité et demande budgétaire 2005-2006 de l'UMR161 IRD-CEREGE

2005 : Rédaction des perspectives de recherche et de développement pour notre équipe à la demande du haut-commissariat de la République (MAE) suite aux assises de la recherche dans le Pacifique (Août 2004).

2004 : Rédaction d'une lettre d'intention à l'ACI-ECCO "ECODYN" et "PNBC".
Rédaction d'un projet intitulé " *Quantification et spéciation de l'arsenic dans les rivières des îles Fidji* " pour demande de financement auprès de l'ambassade de France à Fidji (MAE).

2004 : Rédaction de la page Web pour l'équipe " Biogéodynamique Supergène et Géomorphologie Tropicale " (UMR 161) sur le site www.ird.nc.

2004 : Rapport d'activité et demande budgétaire 2004-2005 de l'UMR161 IRD-CEREGE

1995-1997 : Responsable et animateur d'équipe au Centre ORSTOM de Bondy au sein de l'UR DYLAT " *Biogéohydrodynamique des sols Latéritiques* " (JP. Muller directeur de l'unité de recherche).

THEMES DE RECHERCHE

À la suite de mon doctorat, j'ai poursuivi mes études sur les latérites en utilisant divers outils et approches, et j'ai employé des méthodes d'analyse morphométrique pour tester les propriétés fractales (alors admises par une large communauté) de la géométrie des tracés et arborescences des rivières et réseaux hydrographiques.

I. Processus géochimiques de l'altération latéritique et évolution des cuirasses ferrugineuses

L'étude des processus d'altération latéritique des roches de la zone intertropicale, de la mise en place et de l'évolution des cuirasses ferrugineuses en particulier, a constitué l'un des thème principal de mon activité de recherche à l'IRD.

En RCA, cette thématique a porté sur les paysages cuirassés et les manteaux d'altération latéritique associés de la région du Haut-Mbomou dans le sud-est du pays. Les observations et descriptions pétrographiques de profils (puits d'homme), couplées à des analyses géochimiques et minéralogiques d'échantillons prélevés in situ sur les parois des profils décrits ont permis de distinguer 3 systèmes d'altération cuirassés, et d'en déterminer leur chronologie relative. Différents processus d'altération et de ferruginisation ont été caractérisés, et des bilans de masse ont été calculés (Beauvais et Colin, 1993). L'évolution des vieux systèmes d'altération cuirassés et les transformations minéralogiques ont été étudiées vers l'humide à la transition entre la forêt équatoriale primaire et les savanes tropicales en relation avec le climat et les changements de climat (Beauvais et Tardy 1991). Plus tard, une étude géochimique et minéralogique plus détaillée des systèmes d'altération (Chapître 3 de ma thèse de doctorat) a montré que le phénomène de ferruginisation n'était pas continu dans le temps mais pouvait s'opérer en plusieurs étapes d'altération et d'érosion au gré des changements climatiques (Beauvais, 1999).

II. Propriétés cristallochimiques de la kaolinite

Une approche cristallochimique des matériaux argileux (kaolinite) contenus dans les profils d'altération du Haut-Mbomou en RCA a permis également de caractériser très précisément les types de kaolinites constituant ces matériaux et de tracer l'évolution récente des manteaux d'altération latéritique (Beauvais et Bertaux, 2002). Les

différentes générations de kaolinites ont été caractérisées et différenciées in situ sur lames minces pour la première fois au moyen de la micro spectroscopie Infrarouge. La même méthode a été aussi appliquée sur des kaolinites standard dont certaines sont régulièrement utilisées pour calibrer et tester les méthodes les plus avancées de la minéralogie et de la cristallochimie des argiles. Cette approche a permis de définir un index très pertinent pour caractériser l'ordre cristallin des kaolinites étudiées en fonction de leur taille. Les kaolinites les mieux cristallisées sont les plus grandes et les plus ferrugineuses. Ce sont aussi de bons traceurs minéralogiques de l'évolution récente des vieux profils d'altération latéritique d'Afrique Centrale.

III. Caractérisation pétro-géochimique, et différenciation géomorphologique des cuirasses ferrugineuses

En RCA, la cartographie des différents faciès de cuirasses, couplée à l'analyse statistique minéralogique et géochimique systématique, a permis aussi de mieux comprendre les propriétés géomorphologiques et les caractères évolutifs des systèmes de cuirasses ferrugineuses emboîtés dans l'espace et le temps (Beauvais et Roquin, 1996). Les relations entre les éléments chimiques en trace et les minéraux secondaires, kaolinite, hématite, goethite et gibbsite, ont été analysées pour et entre chaque système. La notion de richesse en minéraux peu hydratés (hématite, kaolinite) et-ou hydratés (goethite, gibbsite) de chaque système a permis de proposer un modèle d'évolution des systèmes cuirassés en fonction des modifications géomorphologiques (évolution du paysage) et des variations hydroclimatiques pouvant induire des transformations géochimiques et minéralogiques dans les différentes générations de cuirasses.

Au Cameroun, les études concernant cette thématique visaient à spatialiser les caractères pétrographiques et géomorphologiques des couvertures d'altération latéritiques de la méso échelle à l'échelle régionale afin d'obtenir une vision d'ensemble de leur distribution, de leur structure et de leurs relations avec les autres paramètres physiographiques du paysage comme la végétation, et le réseau hydrographique. L'étude menée dès 1997 dans la région d'Abong-Mbang sur le bassin amont du Nyong au Cameroun par Dieudonné Bitom en collaboration avec l'ORSTOM puis l'IRD a montré l'influence des héritages de cuirasses latéritques à l'aval des versants sur les processus d'érosion et sur la différenciation des couvertures d'altération latéritique et leur incidence sur l'évolution du modelé (Bitom et al., 2004).

Outre les surfaces portantes des cuirasses, les caractères géomorphologiques des rivières et réseaux de rivières peuvent refléter des variations de roches-mères et de structure. Si tel est le cas, l'analyse des proriétés fractales des tracés des rivières et de la géométrie des réseaux hydrographiques, peut contribuer à la caractérisation morphométrique de ces objets en relation avec les variations lithologiques et structurales (Beauvais et al., 1994), ce que les études pétrogéochimiques des manteaux d'altération cuirassés n'ont pas permis à l'échelle régionale (Beauvais et Roquin, 1996).

IV. Morphométrie des rivières et réseaux hydrographiques

Les propriétés d'échelle des rivières et des réseaux de rivières drainant des paysages latéritiques et non-latéritiques ont été définis en testant des méthodes d'analyse fractale. Les géométries 2-D des tracés hydrographiques ont été différenciées et hiérarchisées, par des mesures morphométriques et plus particulièrement par des analyses fractales de leur tracé et leur arborescence. Des variations de dimension fractale peuvent traduire, outre des différences morphologiques, des processus hydrauliques et géomorphologiques différenciés.

En RCA, l'analyse fractale des tracés hydrographiques a permis de les caractériser et de les différencier quantitativement selon les variations lithologiques et structurales sous-jacentes (Beauvais et al., 1994), ce que les méthodes d'étude pétrographique et géochimique sur les profils d'altération de ces roches n'avaient pas permis.

Dans le nord-ouest des Etats-Unis (Châines montagneuses des Cascades et Olympics), l'application de la méthode d'analyse fractale utilisée sur les rivières centrafricaines a permis de différencier 3 types de cours d'eau en fonction de la lithologie et de la morphométrie de leur vallée (Beauvais et Montgomery, 1996). L'hypothèse jamais démontrée selon laquelle les structures ramifiées des réseaux hydrographiques étaient partout fractales a été testée. Des résultats nouveaux ont montré que les réseaux de drainage n'étaient pas des fractales au sens de Mandelbrot (Beauvais et Montgomery, 1997), mais seulement auto affines dans des domaines d'échelles restreints, limités par des paramètres morphométriques mesurables sur le terrain et-ou sur modèle numérique de terrain (MNT), et ayant un sens physique en termes de processus d'érosion.

V. Structure géoélectrique des altérations latéritiques et morphogenèse

Les méthodes classiques d'analyse (pétrologie, géochimie et cristallochimie) des processus d'altération latéritique reposent sur l'implantation de forages (puits d'homme) d'au plus une vingtaine de mètres d'épaisseur enchaînés le long de topo séquences, ce qui ne fournit qu'une vision fragmentaire des manteaux d'altération latéritique depuis la roche-mère jusqu'à la surface avec de nombreuses imprécisions latérales. La tomographie de résistivité électrique permet d'obtenir des images 2-D très précises de la structure de ces manteaux d'altération (Ritz et al., 1999). L'intérêt de telles images est de mieux appréhender les processus d'altération et d'érosion en jeu dans la différentiation des manteaux d'altération latéritique. Les relations spatiales entre la surface topographique d'érosion et celle du bedrock au front d'altération sont riches d'enseignement en termes de processus d'altération érosion autochtones *vs.* allochtones (Beauvais et al., 1999, 2003). Le couplage de cette méthode au géoradar (GPR) a permis également de préciser les relations spatiales entre deux systèmes cuirassés étagés et d'avancer des interprétations cohérentes en termes de processus de ferruginisation, de degré d'évolution des profils d'altération sous-jacents aux cuirasses ferrugineuses, et d'évolution géomorphologique du paysage (Beauvais et al., 2004).

VI. Géochronologie et évolution morphoclimatique des latérites

Au Brésil, les matériaux d'altération riches en oxhydroxyde de manganèse potassique (cryptomélane) d'un gisement manganésifère supergène ont été datés par la méthode $^{40}Ar/^{39}Ar$ (Ruffet et al., 1996). Les résultats obtenus montrent que l'altération climatique était active à la transition entre le crétacé supérieur et le paléocène ainsi qu'à l'éocène moyen.

Au Burkina Faso, la même méthode a été appliquée à une formation manganésifère pisolitique. Trois groupes d'ages, 56-59, 44-47, et 24-27 Ma ont été obtenus respectivement au coeur, dans les cortex et dans les matrices emballant les pisolites (Colin et al., 2005). Outre la caractérisation temporelle de l'altération manganésifère, l'intervalle entre les deux groupes d'âges les plus anciens (56-47 Ma) contraint la période à effet de serre Tertiaire favorable au lessivage du potassium et du manganèse et à l'accumulation de l'aluminium et dans une moindre mesure du fer au sein de profils bauxitiques globalement répandus à l'éocène et aujourd'hui dénudés.

LISTE DES TRAVAUX ET PUBLICATIONS

LISTE DES TRAVAUX ET PUBLICATIONS

I. Articles dans des revues à comité de lecture de rang A

* articles retenus pour la rédaction du mémoire de travaux

83-1 Nahon D., Beauvais A., Boeglin J.L., Ducloux J., Nziengui-Mapangou P. Manganite formation in the first stage of the lateritic manganese ores in Africa. *Chemical Geology*, (1983), **40**, 25-42.

84-1 Nahon D., Beauvais A., Nziengui-Mapangou P., Ducloux J. Chemical weathering of Mn-garnets under lateritic conditions in northwest Ivory-Coast (West Africa). *Chemical Geology*, (1984), **45**, 53-71.

87-1 Beauvais A., Melfi A., Nahon D., Trescases J.J. Pétrologie du gisement latéritique manganésifère d'Azul (Brésil). *Mineralium Deposita*, (1987), **22**, 124-134.

89-1 Nahon D.B., Herbillon A.J., Beauvais A. The epigenetic replacement of kaolinite by lithiophorite in a Manganese Lateritic Profile (Brazil). *Geoderma*, (1989), **44**, 247-259

91-1 Beauvais A., Tardy Y. Formation et dégradation des cuirasses ferrugineuses sous climat tropical humide à la lisière de la forêt équatoriale. *Comptes Rendus de l'Académie des Sciences*, (1991), **313**, sér. II, 1539-1545.

93-1 Beauvais A., Colin F. Formation and transformation processes of iron duricrusts in tropical humid environment. *Chemical Geology*, (1993), **106**, 77-101.

94-1 Beauvais A., Dubois J., Badri A. Application d'une analyse fractale à l'étude morphométrique du tracé des cours d'eau : méthode de Richardson. *Comptes Rendus de l'Académie des Sciences*, (1994), **318**, série II, 219-225.

96-1 Beauvais A. A., Montgomery D. R. Influence of valley type on the scaling properties of river planforms. *Water Resources Research*, (1996), **32** (5), 1441-1448.

96-2* Beauvais A., Roquin C. Petrological differentiation patterns and geomorphic distribution of ferricretes in Central Africa. *Geoderma*, (1996), **73**, 63-82.

96-3* Ruffet, G., Innocent C., Michard A., Féraud G., Beauvais A., Nahon D., Hamelin B. A geochronological $^{40}Ar/^{39}Ar$ and $^{87}Rb/^{87}Sr$ study of K-Mn oxides from the weathering sequence of Azul, Brazil. *Geochimica et Cosmochimica Acta*, (1996), **60** (12), 2219-2232.

97-1 Beauvais A., Montgomery D. R. Are channel networks statistically self-similar ?. *Geology*, (1997), **25** (12), 1063-1066. (Journal cover ; *Stream networks not as Mandelbrot wrote*).

99-1* Ritz M., Parisot J-C., Diouf S., Beauvais A., Diome F., Niang M. Electrical imaging of lateritic weathering mantles over granitic and metamorphic basement of eastern Senegal, West Africa. *Journal of Applied Geophysics*, (1999), **41**, 335-344.

99-2* Beauvais A., Ritz M., Parisot J-C., Dukhan, M., Bantsimba, C. Analysis of poorly stratified lateritic terrains overlying a granitic bedrock in West Africa, using 2D electrical resistivity tomography. *Earth and Planetary Science Letters*, (1999), **173**, 413–424.

99-3* Beauvais A. Geochemical balance of lateritization processes and climatic signatures in weathering profiles overlain by ferricretes in Central Africa. *Geochimica et Cosmochimica Acta*, (1999), **63**, 23/24, 3939 - 3957.

02-1* Beauvais A., Bertaux J. *In situ* characterization and differentiation of kaolinites in lateritic weathering profiles using infrared microspectrometry. *Clays and Clay Minerals*, (2002), **50**, 3, 314-330.

03-1* Beauvais A., Ritz M., Parisot J-C., Bantsimba, C. Testing etching hypothesis in shaping granite dome structures beneath lateritic weathering landsurfaces using ERT method. *Earth Surface Processes and Landforms*, (2003), **28** (10), 1071-1080.

04-1* Beauvais A., Ritz M., Parisot J-C., Bantsimba, C., Dukhan, M. Combined ERT and GPR methods for investigating two stepped lateritic weathering systems. *Geoderma*, (2004), **119**, 121-132.

04-2 Bitom D., Volkoff B., Beauvais A., Seyler F., Ndjigui P-D. Rôle des hétitages latéritiques et niveau des nappes dans l'évolution des modelés et des sols en zone intertropicale forestière humide. *Comptes Rendus Geosciences*, (2004), **336**, 1161-1170.

05-1* Colin F., Beauvais A., Ruffet G., Hénocque O. First $^{40}Ar/^{39}Ar$ geochronology of lateritic manganiferous pisolites: implications for the Paleogene history of a West African landscape. *Earth and Planetary Science Letters*, (2005), **238**, 172-188.

06-1 Chardon D., Chevillotte V., Beauvais A., Grandin G., Boulangé B. Planation, bauxites and epeirogeny : one or two surfaces on the West African margin ?. *Geomorphology* (Soumis le 20/05/05).

06-2 Beauvais A., Parisot J-C., Savin C. Slope processes controlled by ultramafic rock weathering in a tropical environment of South West Pacific. *Geomorphology* (Soumis le 25/10/05).

06-3 Chevillotte V., Chardon D., Beauvais A., Maurizot P., Colin F. Long-term evolution of New Caledonia (Pacific SW) : time to abandon the Davisian peneplain. *Geomorphology* (Soumis le 31/10/05).

II. Articles dans des revues à comité de lecture de rang B

85-1 Beauvais A., Nahon D. Nodules et pisolites de dégradation de profils d'altération manganésifères sous conditions latéritiques. *Sciences Géologiques Bulletin Strasbourg*, (1985), **38**, 4, 359-381.

85-2 Nahon D., Beauvais A., Trescases J.J. Manganese concentration trough chemical weathering of metamorphic rocks under lateritic conditions. In *The Chemistry of weathering* J.I. Drever (ed.), (1985), Nato Publications, 277-291.

88-1 Beauvais A., Mazaltarim D. Etude des cuirasses latéritiques dans le région de Dembia-Zémio en Centrafrique. Pétrographie, minéralogie et géochimie. *Sciences Géologiques Bulletin Strasbourg*, (1988), **41**, 1, 47-69.

89-1 Beauvais A. Etude pétrographique et géochimique de profils d'altération des cuirasses latéritiques dans le Sud-Est de la République Centrafricaine. *Géodynamique* Orstom Paris, (1989), **4** (2), 71-91.

02-1 Bamba O., Parisot J-C., Grandin G., Beauvais A. Lateritic weathering and supergene gold behaviour tracing the ferricrete genesis in Burkina Faso, West Africa. *Geochemistry : Exploration, Environement, Analysis* (GEEA), (2002), **2** (1), 3-13.

III. Travaux universitaires

82-1 Beauvais A. Etude des altérations supergènes de protores silicatés et carbonatés manganésifères en milieu latéritique. *Mémoire de DEA de l'Université de Poitiers*, (1982), 56 p.

84-1 Beauvais A. Concentrations manganésifères latéritiques. Étude pétrologique de deux gîtes sur roches sédimentaires précambriennes, gisements de Moanda (Gabon) et d'Azul (Brésil). *Thèse de 3e Cycle de l'Université de Poitiers*, (1984), 156 p.

91-1 Beauvais A. Paléoclimats et dynamique d'un paysage cuirassé du Centrafrique. Morphologie, Pétrologie et Géochimie. *Thèse de Doctorat de l'Université de Poitiers*, (1991), 315 p.

IV. Communications à des congrès internationaux

* résumés publiés dans une revue de rang A (#4)

83-1 Beauvais A. et Nahon D. Weathering of Mn-garnets under lateritic conditions. Colloque International du CNRS, Paris : " Pétrologie des altérations et des sols ", (1983), Résumé-Poster.

89-1 Beauvais A. Les cuirasses latéritiques de la région de Dembia-Zémio, dans le Sud-Est de la République Centrafricaine. "African Earth Sciences", 28th

International geological Congress, Washington D. C., Forum CIFEG/UNESCO, "The Geology of Africa", *Pangea*, (1989), **15/16**, 145-146.

90-1* Beauvais A., Boeglin J.L., Colin F., Mazaltarim D. et Muller J.C. Geochemical evolution and degeneration of ferricretes under a humid tropical climate in the East of the Central African Republic. 2nd Int. Symp. "Geochemistry of the Earth's Surface and of Mineral Formation", 2-8/07/90, Aix en Provence, *Chemical Geology*, (1990), Y. Noack and D. Nahon (eds.), Special Issue **84** (1/4), 25-26.

91-1 Beauvais A. Formation and transformation processes of iron duricrust systems under tropical humid environment. EUROLAT'91, "Supergene Ore Deposits and Minerals Formation", 5th International Meeting, Berlin, (1991), 34-39.

93-1* Beauvais A. et Tardy Y. Degradation and dismantling of iron crusts under climatic changes in Central Africa.3rd Int. Symp. "Geochemistry of The Earth Surface", 1-6/08/93, University Park, *Chemical Geology*, (1993), L. Kump (ed.), Special Issue, **107**, 277-280.

94-1 Beauvais A., Montgomery D. R. et Dubois J. Planform scaling properties of rivers and channel networks. AGU Fall Meeting San Francisco, *EOS supplement*, (1994), **75**, 44, 303.

95-1 Beauvais A. et Dubois J. Attractor properties of a discharge river dynamical system. AGU Fall Meeting San Francisco, *EOS supplement*, (1995), **76**, 46, 234.

96-1 Beauvais A., Aubert D. et Dubois J. Application of the dynamic system theory to long time series of river discharge. XXI General Assembly EGS, The Hague, the Netherlands, *Annales Geophysicae*, Hydrology, Oceans, Atmosphere & Nonlinear Geophysics, supplement II, (1996), **14**, 625.

97-1 Legeley-Padovani A., Beauvais A., Seyler F., Volkoff B., Sailhac P., Akono A. et Rudant J. P. Texture analysis of SAR-ERS1 images from South Cameroon. Poster, 3rd ERS Symp. on Space at the service of our environment, Florence, 17-21/03/ 97 (ESA SP-414, 3 vols), (1997), 457-460.

97-2 Legeley-Padovani A., Beauvais A., Akono A., Tonye E. et Rudant J. P. Classification d'une image radar : application à la cartographie automatique de la mangrove autour de la région de Douala (Cameroun). Poster, 3rd ERS Symp. on Space at the service of our environment, Florence, 17-21/03/ 97 (ESA SP-414, 3 vols), (1997), 301-304.

98-1 Aubert D., Beauvais A., Dubois J., et Orange D. Non linear effects on the temporal evolution of fluvial discharge : case of the Oubangui river. EGS, *Annales Geophysicae,* Part IV, Society Symposia, Nonlinear Geophysics & Natural Hazards, supplement IV to volume **16**, (1998), C1071.

99-1 Aubert D., Beauvais A. et Dubois J. Application of the Correlation Integral Function tool to natural time series. Résumé accepté pour poster à XXIV EGS

General Assembly, Den Hague, 20-24/04/99. *Abst. Suppl., Annales Geophysicae*, (1999).

01-1 Beauvais A., et Bertaux J. Characterization of kaolinite polymorph mixtures in lateritic weathering profiles using *in situ* infrared microspectroscopy on polished thin sections. Résumé-Poster In Physics and Chemistry of Earth Material, Journal of Conference abstracts, Cambridge Pub., (2001), Vol. 6, EUG XI, Strasbourg, France, 04/8-12/2001, p. 649.

03-1 Savin. C., Robineau B., Monteil G., Beauvais A., Parisot J.C., et Ritz M. Electrical imaging of peridotite weathering mantles as a complementary tool for nickel ore exploration in New Caledonia. ASEG 16th Geophysical Conference and Exhibition, February 2003, Adelaide, Australia, (2003) p. 4.

03-2 Chevillotte V., Chardon D., Beauvais A., Lagabrielle Y., Maurizot P., et Colin F. Uplift, erosion and the distribution of planation surfaces in New-Caledonia : controls on the enrichment of lateritic Ni ore deposits. Résumé *EGS-AGU-EUG joint assembly*, Nice, 7 -11 Avril 2003. Geophysical research Abstracts, (2003), Vol. 5, 09903.

03-3 Parisot J-C., Mathe D., Bézis S., Combier V., Paugam A., Ritz M., Savin C., Robineau B., Beauvais A. Appraisal of physical and chemical parameters controlling the electrical resistivity of weathering materials of ultramafic rocks at Tiebaghi, New Caledonia. Poster Colloque international "Préservation et restauration écologique en environnement minier", 15-20/07/2003, IRD Nouméa, Nouvelle-Calédonie, (2003). Abstract.

03-4 Cathelineau M., Peiffert C., Traore D., Chabaux F., Clauer N., Larque P., Granet M., Beauvais A., et Colin F. Ni-CO transport and speciation in river waters : the effect of erosion on lateritic alteration products developed on ultrabasic formations and related metal concentrations (case study of the Rivière des Pirogues, New Caledonia). Poster Colloque international "Préservation et restauration écologique en environnement minier", 15-20/07/2003, IRD Nouméa, Nouvelle-Calédonie, (2003), Abstract.

04-1* Colin F., Mouélé F., Ferraud G., Beauvais A., Grandin G., Flicoteaux R. Ages and lateritic weathering rate in northern Brazil deduced from cryptomelane 40Ar/39Ar geochronology. Goldschmidt Conference, Copenhague, Juin, Danemark, résumé, *Geochimica et Cosmochimica Acta* 68 (11), (2004), A439.

04-2 Chevillotte V., Chardon D., Beauvais A., Lagabrielle Y., Maurizot P., et Colin F. Uplift, erosion and the distribution of planation surfaces in southern New-Caledonia. 21 th Star Session, 33rd SOPAC Session, 17-27/09/2004, Warwick, Fidji, (2004), 16-17.

04-3 Parisot J-C., Paugam A., Beauvais A., Savin C., Robineau B. Physical and chemical parameters controlling the electrical resistivity of ultramafic rock weathering materials of New Caledonia. 21 th Star Session, 33rd SOPAC Session, 17-27/09/2004, Warwick, Fidji, (2004), p. 52.

05-1* D. Traoré, A. Beauvais, T. Augé, F. Chabaux, J-C. Parisot, M. Cathelineau, C. Peiffert, F. Colin. Platinum and palladium mobility in supergene environement : The residual origin of the Pirogues River mineralization, New Caledonia. 7th symposium Geochemistry of the Earth Surface, GES7, 24-27/08/2005, Aix-en-Provence, (2005), *Journal of Geochemical Exploration* (Sous presse).

V. Colloques nationaux et régionaux (résumés)

91-1 Beauvais A. Processus de formation et de transformation de systèmes de cuirasses ferrugineuses sous un climat tropical humide. Journée Scientifique du Programme PIRAT, Strasbourg, 3p. (1 abstract + 1 poster + 1 oral communication), (1991).

93-1 Beauvais A. Weathering processes in Central African Republic. Communication orale. Hydrology Symposium, University of Washington - University of British Columbia, Vancouver, Canada, 29 Octobre, 1993.

93-2 Muller J.P., Malengreau N., Lauquet G., Allard T. et Beauvais A. Cristallochimie des matières minérales transportées dans la géosphère tropicale : résultats préliminaires et perspectives. Colloque PEGI: Grands Bassins Fluviaux Périatlantiques, Paris, 22-24/11/93, (1993).

94-1 Ruffet G., Innocent C., Michard A., Féraud G., Beauvais A., Nahon D. et Hamelin B. Datations par les méthodes ^{40}Ar-^{39}Ar et $^{87}Rb/^{87}Sr$ d'oxydes de Manganèse (Cryptomélane) d'une séquence latéritique (Série d'Azul, Brésil): résultats préliminaires et perpsectives. Colloque Programme Environnement Géosphère Intertropicale (PEGI): Erosion, Altération, Pédogenèse- Traceurs physiques, chimiques et biologiques, Paris, 12-13/12/94, (1994).

96-1 Ruffet G., Innocent C., Michard A., Féraud G., Beauvais A., Nahon D. et Hamelin B. Datations ^{40}Ar-^{39}Ar de surfaces latéritiques manganésifères. Colloque Programme Environnement Géosphère Intertropicale (PEGI): Grands Bassins Fluviaux, Bilans Hydriques et chimiques, Sols Intertropicaux, Paris, 17-18/01/96, (1996).

96-2 Beauvais A. Analyse fractale des réseaux. Communication orale, Ecole Thématique d'Eté DBT INSU/CNRS, Luminy, France, 15-19/07/96, "Géomorphologie : Processus et Modélisation", Ph. Davy, F. Guillocheau et B. Hamelin (coord.), Geosciences Rennes, (1996), 44-45.

03-2 Colin F., Perrier N., Beauvais A., Parisot J-C., Traore D. Les formations latéritiques de Nouvelle-Calédonie : bassins amont de zones potentielles de fermes aquacoles. Résumé Colloque Styli 2003, Nouméa-Koné (Nouvelle-Calédonie), (2003).

04-1 Parisot J-C., Mathe D., Bezis S., Combier V., Paugam A., Ritz M., Savin C., Robineau B., Beauvais A. Evolution des paramètres physico-chimiques contrôlant la résistivité électrique des manteaux d'altération latéritique du

massif péridotitique de Tiébaghi, Nouvelle-Calédonie. Assises de la recherche Française dans le Pacifique, 24-27/08/2004, Nouméa, (2004), p. 182.

04-2 Colin F., Beauvais A., Ambrosi JP., Nahon D. Les latérites en environnement tropical, sources de métaux économiques. Assises de la recherche Française dans le Pacifique, 24-27/08/2004, (2004), Nouméa, numéro spécial du Ministère des Affaires Etrangères (MAE), 103-107.

VI. Conférences : vulgarisation, fiches, séminaires

89-1 Beauvais A. Le cuirassement latéritique en République Centrafricaine. Séminaire sur les biogéodynamiques forestières, Yaoundé, (1989). Communication orale et résumé, 1page.

89-2 Beauvais A. Les cuirasses latéritiques de la région de Dembia-Zémio. University of Bangui, ORSTOM, Bangui, CAR, (1989), 8 pages.

94-1 Beauvais A. Laterisation processes in Central Africa ; Evolution pattern in a tropical humid environment. Geological Sciences Brown Bag Seminar series (Department of Geological Sciences and Quaternary Research Center, Univ. Washington, U.S.A, (1994).

94-2 Beauvais A. Fractal patterns of rivers and channel networks planform. Quaternary Research Center, Special Seminar (Department of Geological Sciences and Quaternary Research Center, Univ. Washington, U.S.A., (1994).

02-1 Beauvais A. Tomographie de résistivité électrique et structure des vieux manteaux d'altération latéritique. Exemple du Sénégal Oriental. Conférence au Centre IRD de Nouméa (Nouvelle-Calédonie), (2002).

03-1 Beauvais A. $^{40}Ar/^{39}Ar$ dating of West African lateritic cryptomelanes. Conférence au Centre de Recherche De Beers (Pretoria, Afrique du Sud), (2003).

03-2 Beauvais A. L'imagerie électrique pour décrire les couches latéritiques du sol. Actualités, Fiches Scientifiques, Sciences au Sud, IRD Paris, (2003), 174, p. 2.

04-1 Colin F., Beauvais A., Ambrosi JP., Nahon D. Les latérites en environnement tropical, sources de métaux économiques. Assises de la recherche Française dans le Pacifique (ARFP), 24-27/08/2004, (2004), Nouméa.

04-2 Ambrosi JP., Beauvais A., Colin F. Apports de la pétrologie à la compréhension des systèmes d'altération latéritiques. Célébration scientifique et amicale de la carrière du professeur Daniel Nahon, 15-16/09/2004, (2004), Aix-en-Provence.

05-1 Colin F., Beauvais A., Ambrosi JP., Nahon D. Les latérites en environnement tropical, sources de métaux économiques. Numéro spécial ARFP édité par le Ministère des Affaires Etrangères, 103-107.

DOSSIER DE TRAVAUX

LATERITES ET MORPHOGENÈSE

Processus, bilans, évolutions

Dans la continuité de mon doctorat intitulé “*Paléoclimats et dynamique d’un paysage cuirassé du Centrafrique. Morphologie, Pétrologie et Géochimie*” (Beauvais, 1991), je n’ai cessé de mener des études sur les latérites à différentes échelles, et en utilisant divers outils et approches. Après une introduction générale sur les latérites et les cuirasses ferrugineuses incluant une brève synthèse bibliographique, sont présentés les problématiques scientifiques puis les trois volets de mon mémoire, construit à partir d’articles scientifiques. L’ensemble m’amène ensuite à présenter mon projet de recherche en perspectives.

INTRODUCTION

Les latérites sont des traits morphologiques majeurs des régions intertropicales, certaines étant âgées de plusieurs millions d'années. À l'échelle du Globe terrestre, les latérites couvrent un tiers des surfaces émergées, la majorité se trouvant dans le domaine intertropical qui couvre pour sa part prés de 40 % des terres émergées (Fig. 1).

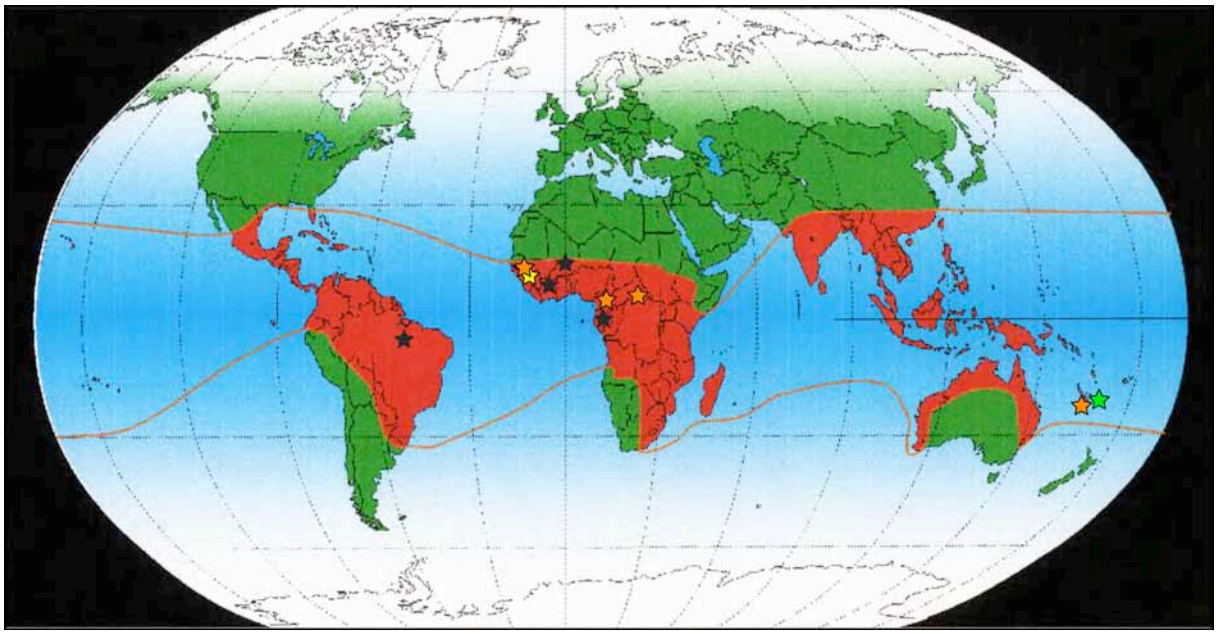

Figure 1. Distribution mondiale des latérites (Modifiée à partir de Pedro, 1968), et les sites d'études localisés par des étoiles (noir = gisements latéritiques de manganèse du Gabon, de Côte d'Ivoire, du Burkina Faso et du Brésil ; orange = cuirasses ferrugineuses de RCA, du Cameroun, du Sénégal et de Nouvelle-Caalédonie ; jaune = bauxites de Guinée ; vert = gisements latéritiques de Nickel de Nouvelle-Calédonie).

Les latérites résultent des interactions entre la lithosphère, l'hydrosphère, la biosphère et l'atmosphère, et présentent par conséquent des intérêts scientifiques multiples.

1. DEFINITION ET ATTRAITS SCIENTIFIQUES DES LATERITES

Le terme latérite, défini par Buchanan (1807), désigne un matériau d'Inde présentant après séchage à l'air les propriétés physiques de la brique. Les briques de latérite étaient utilisées pour la construction des maisons du Sud de l'Inde.

Pour Alexander et Cady (1962), les latérites sont des matériaux d'altération supergènes constitués pour l'essentiel d'oxydes et oxyhydroxydes de fer ou aluminium plus ou moins hydratés, ou d'autres éléments de transition (Mn, Ni, Cu, Co, Zn,…). Elles sont très

appauvries en alcalins et alcalino-terreux, dépourvues de minéraux silicatés primaires, mais peuvent contenir des quantités non négligeables de quartz selon la nature des roches mères dont elles dérivent et selon leur âge ou degré d'évolution. Les latérites sont meubles ou indurées. L'induration est un phénomène secondaire qui se manifeste au cours de processus d'humectation et dessiccation réitérés sous climat tropical contrasté à alternance de saisons humides et sèches. Ce phénomène s'accélère lors d'un changement climatique de l'humide vers le sec qui se traduit par l'érosion des sols meubles suite à la disparition du couvert végétal amenant ainsi les accumulations ferrugineuses à l'affleurement.

Les latérites matériaux supergènes, résiduels de la dénudation chimique et physique sélective des roches, recyclent les éléments les moins mobiles sous des formes minéralogiques en équilibre avec les conditions supergènes, comme les oxyhydroxydes métalliques et les argiles. Bien que masquant et diluant les signatures structurales et géochimiques des roches-mères plus ou moins minéralisées, les latérites constituent des métallotectes recélant des concentrations minérales (Fe, Mn, Ni, Cu, Co, Cr, Ti, mais aussi, Au, Ag, Pt), dont certaines sont d'intérêt économique pour les pays de la zone intertropicale. L'aluminium est ainsi concentré dans les bauxites, le fer et le manganèse dans les cuirasses, le nickel et le cuivre dans les saprolites, ainsi que nombre d'éléments peu mobiles (Au, Ag, Pd, Pt) dispersé dans les roches, qui peuvent être concentré dans les manteaux d'altération latéritique (Nahon, 1991 ; Tardy, 1993).

Bien que dépourvues d'éléments nutritifs, les latérites sont le substrat indispensable des écosystèmes des grands domaines phytogéographiques intertropicaux (savanes, forêts) comme ceux d'Afrique, d'Amérique du Sud ou d'Indonésie, abritant des niches de biodiversité, certaines étant des hot Spots mondiaux. On mentionnera ainsi les écosystèmes de Nouvelle-Calédonie qui se développent et évoluent sur des sols riches en nickel et métaux associés, et qui sont néanmoins riches en espèces végétales endémiques.

Les manteaux d'altération latéritique constituent des aquifères, importantes sources d'eau pour l'aménagement et le développement agricoles du monde rural intertropical.

Environ la moitié de l'écoulement continental global transite à travers les couvertures latéritiques avant de rejoindre les mers et les océans (Tardy et Roquin, 1998). L'érosion chimique et mécanique induite par le développement des formations latéritiques des bassins versants d'échelle continentale régule la moitié des flux globaux du CO_2 et de carbone

dissous ou particulaire à l'échelle globale (Berner et al., 1983 ; Tardy, 1986 ; Berner, 1994 ; Tardy et Roquin, 1998 et références citées).

1. SYNTHESE BIBLIOGRAPHIQUE

Les premières études sur les latérites et les paysages latéritiques ont été géographiques et géomorphologiques (King, 1962 ; Büdel, 1982 ; Thomas, 1994). Excepté la carte des latérites africaines de Petit (1982), diverses cartographies de formations latéritiques ont été réalisées aux échelles locales et régionales (Michel, 1973 ; Grandin, 1976 ; Boulet, 1974 ; Chauvel, 1977). À l'échelle régionale, ces cartographies ont été conduites dans un soucis de corrélations des surfaces géomorphologiques sur lesquelles différents matériaux, (bauxites, cuirasses ferrugineuses et manganésifères, pédiments), se sont développés et conservés (King, 1962 ; Michel, 1973 ; Grandin, 1976). La séquence géomorphologique étagée type consiste ainsi en trois surfaces bauxitiques anciennes (jurassique, crétacé et éocène), un niveau dit intermédiaire à cuirasse ferrugineuse et de trois glacis quaternaires à cuirassement ferrugineux (Michel, 1973). Ces différentes surfaces correspondent aux surfaces Gondwana, post-Gondwana, Africaine, post-africaine I, II et III des géomorphologues anglo-saxons (King, 1962 ; Partridge et Maud, 1987 ; Thomas, 1994).

À la fin des années soixante et surtout au cours des années soixante-dix des collaborations entre pédologues, géologues et géochimistes de la surface ont permis, sous l'impulsion de Georges Millot (1970, 1977), de mener des études pétrologiques et géochimiques sur des échantillons prélevés dans des puits d'homme et des forages miniers fonçés à travers les manteaux d'altération depuis la surface jusqu'à la roche mère. Les processus fondamentaux de l'altération des roches et de la formation et l'évolution des horizons ferrugineux et cuirassés ont été définis dans différents milieux morphoclimatiques depuis les zones sahéliennes jusqu'aux régions équatoriales (Nahon, 1976, 1986, 1991 ; Tardy, 1993). Des vitesses d'altération et d'érosion ont été calculées à partir d'analyses géochimiques des solutions percolant à travers les profils d'altération (Tardy, 1969). Des études thermodyamiques des équilibres minéraux-solutions (Garrels et Christ, 1965 ; Fritz, 1975 ; Fritz et Tardy, 1976 ; Didier et al., 1985 ; Trolard et Tardy, 1987) ont également permis une meilleure compréhension des processus géochimiques de l'altération latéritique.

Des études hydrogéochimiques des eaux superficielles drainant des bassins versants latéritiques d'échelle continentale ont permis d'estimer les vitesses de dénudation des roches

(Meybeck, 1987 ; Tardy et al., 1989 ; Probst, 1992 ; Probst et al., 1994 ; Stallard, 1995 ; Edmond et al., 1995 ; Gaillardet et al., 1997 ; Boeglin et Probst, 1998 ; Gibbs et al., 1999 ; Dupré et al., 2003).

Le bilan géochimique de l'altération incluant l'enrichissement relatif et absolu des métaux, Al, Fe et Mn, a été établi par des calculs de transfert de masses. Soit à volume constant (Millot et Bonifas, 1955 ; Ambrosi et Nahon, 1986a ; Beauvais, 1999), soit à partir d'éléments chimiques considérés comme mobiles, Ti, Zr, Th (Trescases, 1973 ; Brimhall et al., 1987 ; Colin et Vieillard, 1991 ; Beauvais et Colin, 1993 ; Braun et al., 1993). Ces bilans géochimiques n'ont cependant de signification qu'à l'échelle de profils verticaux ou tout au plus d'un demi-interfluve.

Les faciès minéralogiques et géochimiques des cuirasses bauxitiques et ferrugineuses ont été considérés comme de bons indicateurs des conditions climatiques et paléoclimatiques ayant présidé à leur formation (Tardy et al., 1988b; 1991). La base du raisonnement repose sur les minéraux constitutifs, déshydratés ou peu hydratés (hématite et kaolinite) et hydratés (goethite et gibbsite) dont la formation ou la transformation au sein des profils d'altération dépend des conditions hydriques (activité de l'eau), géochimique (pH-Eh, [Si], [Al], [Fe]) et thermodynamique (T°C, PO_2 et de PCO_2). L'interprétation paléoclimatique des kaolinites des dépots marins a permis de caractériser leur origine continentale et de discuter les relations entre les processus d'altération, d'érosion et de sédimentation (Thiry, 2000).

Récemment, les avancées de la géochimie cosmogénique ont permis d'obtenir des vitesses d'érosion et de déplacement des matériaux à la surface des versants de l'échelle du millénaire au million d'années (Brown et al., 1994, 2003 ; Braucher et al., 1998a, 1998b). Sur le plus long terme des ages de formation des cuirasses manganésifères et ferrugineuses ont été aussi obtenus (Vasconcelos et al., 1992, 1994, 1999 ; Ruffet et al., 1996 ; Hénocque et al., 1998 ; Girard et al., 2000, 2003). Des études paleomagnétiques ont aussi fourni des résultats convaincants acquis sur les latérites de Guyanne et du Suriname (Théveniaut et Freyssinet, 2002). Couplées à une bonne compréhension des processus géomorphologiques responsables du façonnement des surfaces, ces données permettent de préciser les relations spatio-temporelles entre différents systèmes latéritiques, comme entre surface bauxitique, et surfaces portant des cuirasses ferrugineuses et manganésifères (Colin et al., 2005).

Les latérites sont des systèmes naturels animés, réactifs et donc évolutifs. Si elles se forment sous des conditions morpho climatiques spécifiques, une fois formées elles ne réagissent pas moins aux changements climatiques et-ou aux mouvements épirogéniques. Les latérites évoluent sans cesse à composition géochimique quasi constante pour s'adapter aux nouvelles conditions de leur milieu en modifiant les proportions relatives de leurs minéraux constitutifs. Il en va ainsi des cuirasses ferrugineuses qui se forment, se transforment, se démantèlent et se reforment à des échelles de plusieurs millions d'années.

2. Les cuirasses ferrugineuses

Parmi les latérites, les cuirasses ferrugineuses tiennent une place toute particulière. Ce sont des matériaux latéritiques qui se sont formés sous des climats tropicaux contrastés. Ils sont essentiellement constitués de fer oxydé, d'alumine et de silice résiduelle auxquels s'ajoutent des traces en éléments de transition et terres rares selon la nature des roches mères. L'hématite et la goethite, la kaolinite et la gibbsite sont les minéraux principaux, auxquels s'ajoute du quartz et des minéraux lourds résiduels dont les quantités varient selon la nature des roches mères.

Les surfaces portant les cuirasses ferrugineuses sont des traits géomorphologiques remarquables des régions inter tropicales. Sur le continent africain, les cuirasses ferrugineuses sont des formations affleurantes ou sub-affleurantes sur des surfaces d'aplanissement et-ou des glacis étagés dans le paysage. Elles ont été (et sont encore !) considérées comme autochtones par les géochimistes lorsque formées par altération *in situ* des roches sous-jacentes (Ambrosi et Nahon, 1986a ; Nahon, 1986, 1991 ; Leprun, 1979 ; Tardy et Nahon, 1985). Un profil d'altération cuirassé type est généralement formé des roches-mères saines à la surface du sol : d'un horizon de saprolite, d'argiles tachétées, d'un horizon nodulaire ferrugineux ou d'une carapace et d'une cuirasse ferrugineuse (Tardy et Nahon, 1985). Les géomorphologues considèrent souvent les cuirasses comme allochtones lorsqu'elles remanient au sein des pédiments des éléments latéritiques d'origine diverse en transit à la surface des versants et glacis (Michel, 1973 ; Grandin, 1976 ; Thomas, 1994).

Le problème du cuirassement ferrugineux autochtone ou allochtone est un problème récurrent dès que l'on s'intéresse à la géomorphologie des régions tropicales. Qu'elles soient autochtones ou allochtones elles sont spécifiques de conditions géomorphologiques et climatiques qui leur sont propres.

Pour comprendre la dynamique des systèmes cuirassés ferrugineux il est devenu nécessaire de prendre en compte à la fois les processus d'altération géochimique et les processus d'érosion mécanique responsables de leur mise en place, leur développement, et leur évolution.

Les périodes où les climats tropicaux humides à saisons contrastées dominent sont généralement considérées propice à la formation et au développement des cuirasses ferrugineuses par altération géochimique *in situ* des roches (Tardy et Nahon, 1985 ; Nahon, 1986, 1991). Durant les périodes où les climats sont plus secs avec une saison sèche bien marquée, elles sont mécaniquement démantelées, et dispersées sur les versants, les processus d'érosion de surface façonnant les versants en glacis (Grandin, 1973). Les périodes à climats très humides avec une saison humide relativement plus longue que la saison sèche entraînent leur ameublissement, et leur transformation physico-chimique (Nahon et al., 1989 ; Beauvais, 1991 ; Beauvais et Tardy, 1991).

Les cuirasses ferrugineuses résultent de mécanismes et processus d'altération et d'érosions différenciées mais complémentaires, qui se succèdent et s'enchaînent dans l'espace et le temps. De tels processus peuvent mobiliser, après démantèlement, des éléments de cuirasses sur des distances plus ou moins longues et les accumuler plus à l'aval sur des glacis d'accumulation, où pourront, après retour de conditions climatiques plus humides mais contrastées, se former sur place de nouvelles cuirasses ferrugineuses autochtones à partir de matériaux ferrugineux allochtones plus anciens (Beauvais et al., 1999). Il résulte de tels processus le développement de cuirasses ferrugineuses polygéniques constituées d'éléments (minéraux) d'origine et d'âge différent sur des glacis.

PROBLEMATIQUES SCIENTIFIQUES

Mes études ont porté sur les latérites ferrugineuses d'Afrique (RCA et Sénégal), et sur les accumulations manganésifères supergènes du Brésil et du Burkina Faso. Les résultats obtenus selon diverses approches et présentés ici selon trois volets contribuent à donner des éléments de réponse à quelques questions fondamentales parmi lesquelles:

Quels sont les mécanismes et processus de formation et d'évolution des altérations latéritiques cuirassées ?

Ces altérations sont-elles en équilibre ou en déséquilibre avec les conditions morphoclimatiques actuelles ?

Les cuirasses ferrugineuses sont-elles d'origine autochtone ou renferment-elles des matériaux latéritiques d'origine allochtone ?

La diversité pétrographique, minéralogique et géochimique, de ces cuirasses reflète t-elle les variations morphoclimatiques passées?

1. ALTERATIONS LATERITIQUES, CUIRASSEMENT FERRUGINEUX ET EVOLUTION MORPHOCLIMATIQUE

Les cuirasses ferrugineuses du Sud-est la République Centre Africaine (RCA), les surfaces qui les portent et les altérations latéritiques sous-jacentes ont été étudiées depuis l'échelle des assemblages minéraux jusqu'aux échelles des interfluves et du paysage tout entier afin d'en déterminer les mécanismes et processus de formation et évolution (Beauvais, 1999 ; Beauvais et Bertaux, 2002 ; Beauvais et Roquin, 1996).

La RCA est l'un des pays les plus cuirassés du monde. On y trouve des cuirasses ferrugineuses évoluées à très évoluées, des carapaces ferrugineuses et des sols ferrugineux à gravillons et nodules ferrugineux dont certains sont issus du démantèlement des cuirasses (Beauvais et Tardy, 1991). La surface centrafricaine est couverte à 75 % de latérites dont la plupart sont ferrugineuses et indurées (Fig. 2). Les cuirasses les plus indurées et les plus épaisses se sont dévéloppées sur roches-mères basiques aux limites orientales et septentrionales de la surface Centrafricaine. Au Sud et au Nord de la surface centrafricaine, les manteaux d'altération cuirassés se trouvent en déséquilibre morphoclimatique. Au sud, les

cuirasses ont subi une dégradation géochimique dans le domaine équatorial, ce qui a conduit à la formation de sols rouges ferrallitiques à nodules ferrugineux. Au nord, elles sont démantelées et érodées dans le domaine tropical sec, ce qui a entrainé le développment de pédiments et-ou glacis.

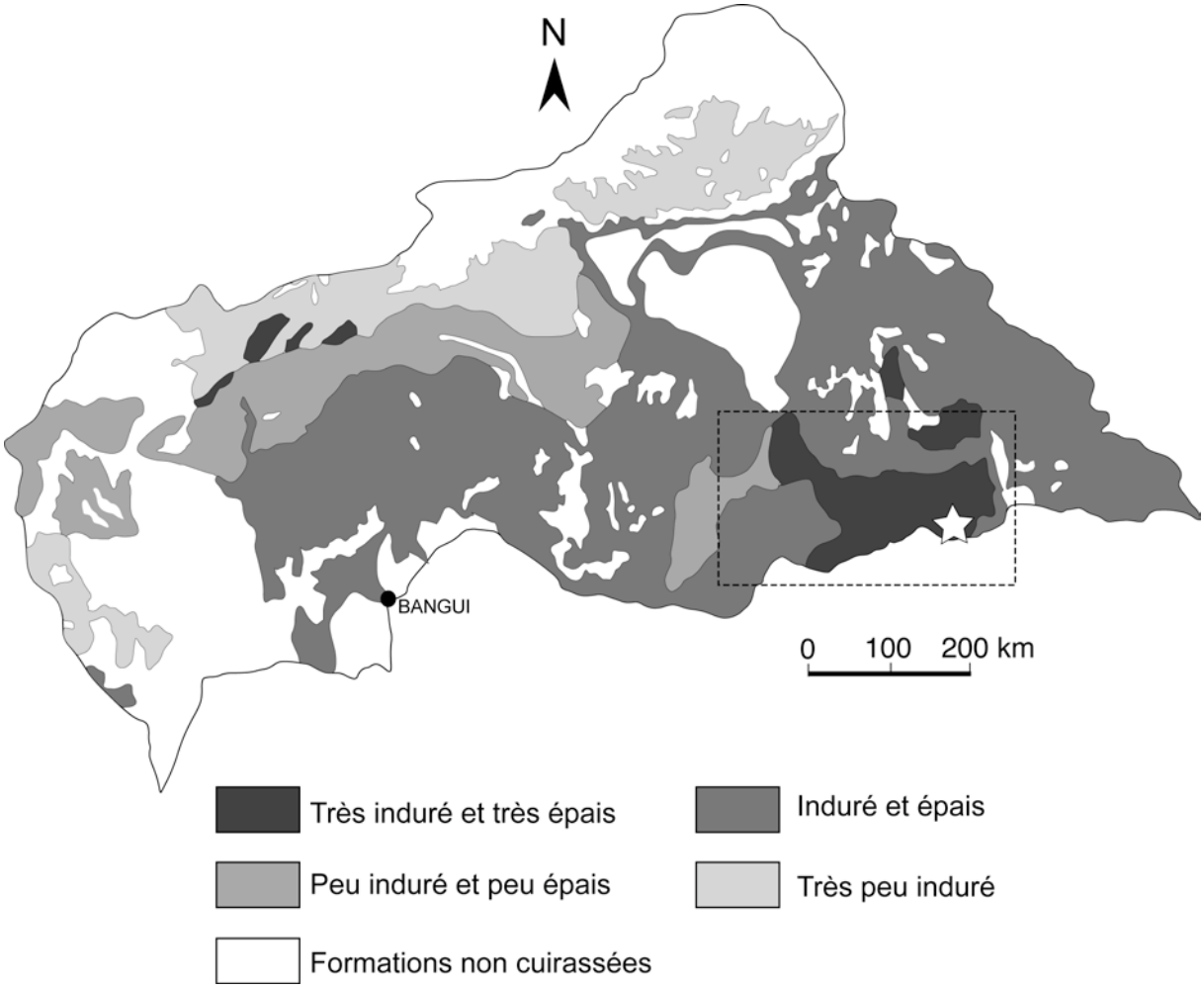

Figure 2. Carte du cuirassement latéritique ferrugineux et des formations non cuirassées en RCA (Modifié de Beauvais, 1991 ; cadre pointillé = figure 3 ; l'étoile Blanche localise la zone d'étude dans le Haut-Mbomou, figure 4)

La région sud-est dans le Haut-Mbomou est couverte à 90 % de latérites avec un gradient de cuirassement (induration ferrugineuse) d'ouest en est (Fig. 3), qui semble lié à la nature pétrologique des roches mères.

La situation de cette région, à la transition entre deux grans domaines climatiques, équatorial au Sud et tropical contrasté au Nord a permis le développement de cuirasses ferrugineuses à faciès pétrographiques différenciés, se distribuant sur différents niveaux géomorphologiques

(Fig. 4 ; Beauvais et Roquin, 1996). Des profils d'altération différenciés et d'épaisseur variable se sont développés sous ces cuirasses.

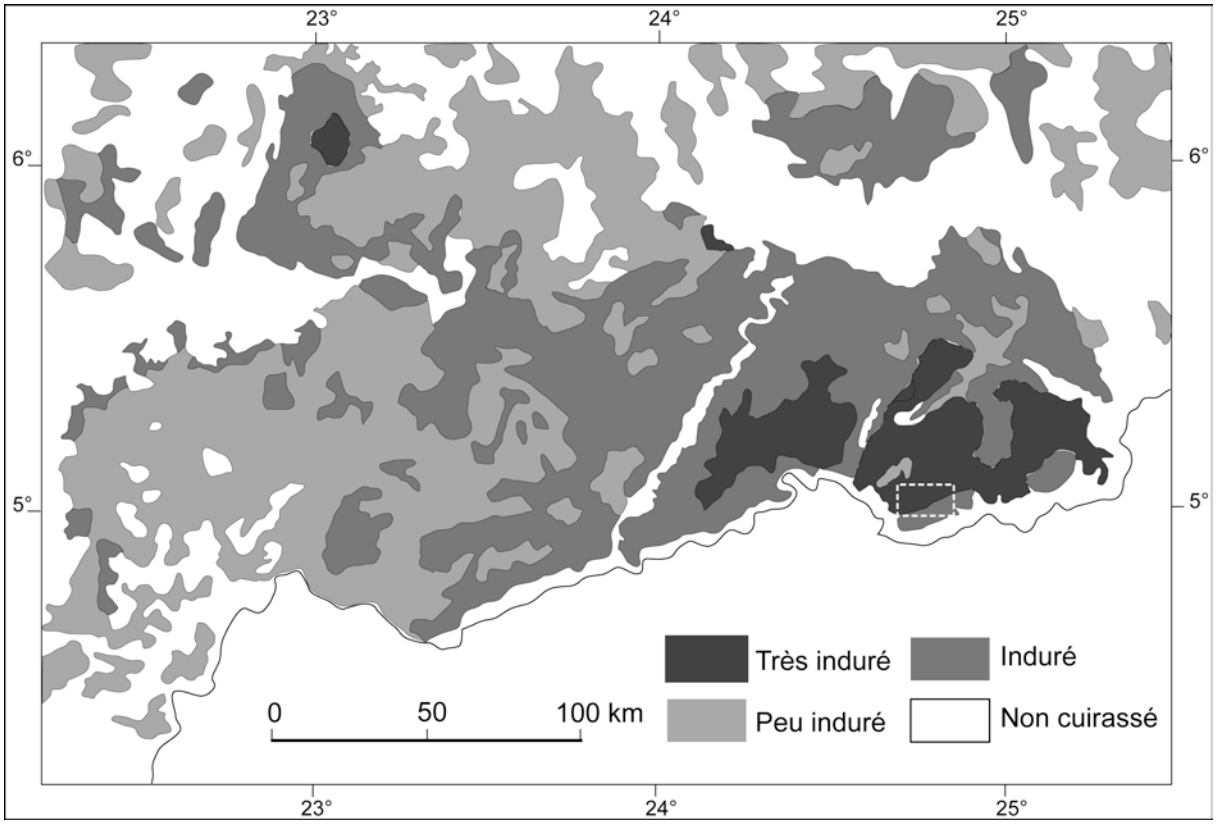

Figure 3. Intensité du cuirassement latéritique ferrugineux dans le Haut-Mbomou en RCA (Le triangle pointillé blanc délimite la figure 4).

Une approche pétrologique (pétrographique minéralogique et géochimique) a permis de comprendre les principaux processus supergènes responsables de la formation et de l'évolution de ces profils d'altération cuirassés (Beauvais, 1999). Les profils cuirassés situés sur les surfaces hautes sont en déséquilibre tandis que ceux qui se sont développés sur les surfaces basses sont plutôt en équilibre avec les conditions climatiques actuelles.

Une approche cristallochimique des matériaux argileux (kaolinite) contenus dans ces profils d'altération cuirassés a permis également de caractériser très précisément les différents types de kaolinites par leur taille et leur cristallinité, et de tracer l'évolution récente de ces profils cuirassés (Beauvais et Bertaux, 2002).

L'échelle limitée de ces études ne permet cependant pas d'avoir une compréhension globale des systèmes d'altération cuirassés.

Une approche cartographie des différents faciès pétrographiques de cuirasses (Fig. 4), couplée à une analyse statistique des données minéralogiques et géochimiques, a permis ainsi de mieux comprendre les propriétés pétrogéochimiques et les caractères géomorphologiques évolutifs des systèmes de cuirasses ferrugineuses emboîtés dans l'espace et le temps (Beauvais et Roquin, 1996).

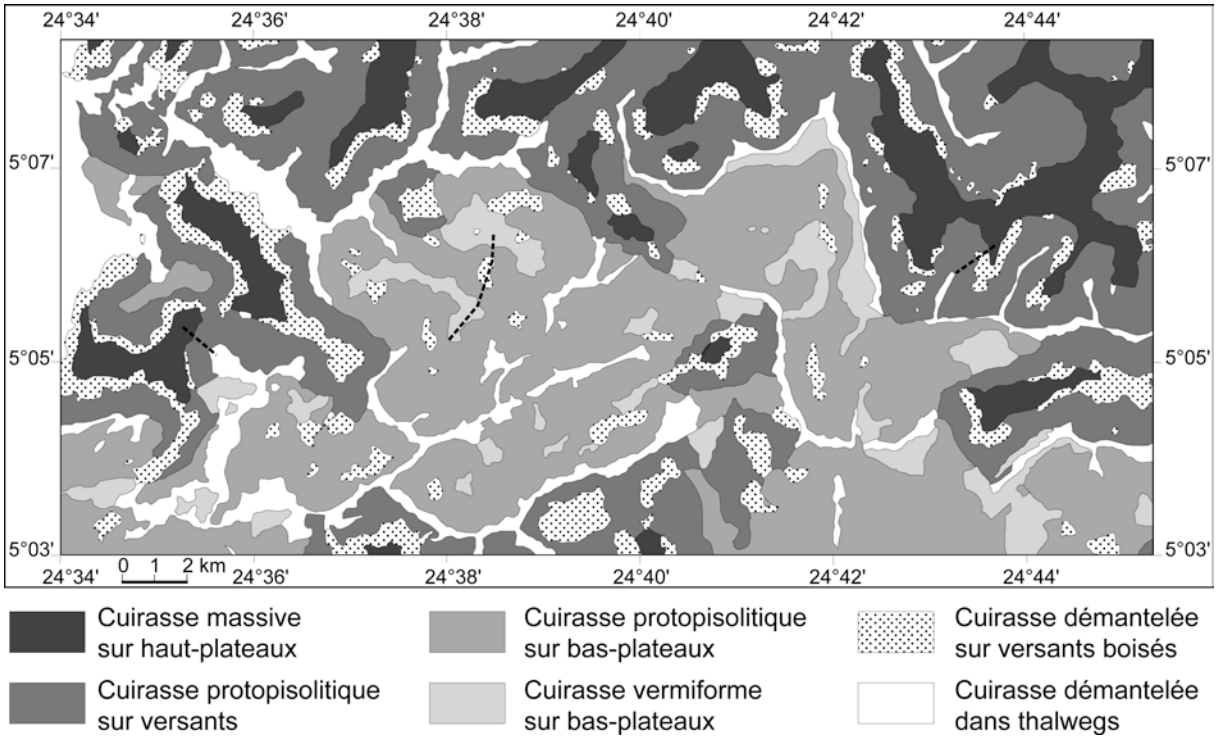

Figure 4. Distribution géomorphologique des différents faciès pétrographiques de cuirasse ferrugineuse dans le Haut-Mbomou en RCA (pointillés = toposéquences de puits étudiées dans Beauvais, 1991 et 1999).

Les méthodes classiques (pétrologie et cristallochimie) d'analyse des processus d'altération latéritique reposent sur l'implantation de forages (puits d'homme) d'au plus une vingtaine de mètres d'épaisseur enchaînés le long de topo séquences, ce qui ne fournit qu'une vision fragmentaire des manteaux d'altération latéritique depuis la roche-mère jusqu'à la surface avec de nombreuses imprécisions latérales. La capacité des méthodes géophysiques de surface d'imager en 2D la structures des altérations latéritiques a permis de lever ces imprécisions.

2. STRUCTURE GEOELECTRIQUE DES ALTERATIONS LATERITIQUES ET MORPHOGENESE

La structure interne des manteaux d'altération couverts de cuirasses ferrugineuses a été imagée en continu au Sénégal Oriental, en employant la tomographie de résistivité électrique et le géoradar (Ritz et al., 1999 ; Beauvais et al., 1999, 2003, 2004). Ces données nouvelles ont permis de rediscuter les relations entre les processus d'altération et d'érosion et de proposer un modèle d'évolution morphogénétique pour le Sénégal Oriental.

L'intérêt des images géoélectriques est, en particulier, de mieux comprendre les relations spatiales entre la surface topographique d'érosion et celle du bedrock au front d'altération, en termes de processus d'altération érosion, autochtones *versus* allochtones (Beauvais et al., 1999). L'altération différentielle des roches granitiques et son rôle dans la formation des inselbergs granitiques au sein des manteaux d'altération avant leur éventuelle exhumation, et dans le façonnement géomorphologique ("etching surface") a également été discutée (Beauvais et al., 2003). Les relations spatiales entre deux systèmes cuirassés étagés ont également été précisées en combinant la méthode ERT au géoradar (GPR) (Beauvais et al., 2004). Des interprétations cohérentes ont pu être avancées en termes de processus de ferruginisation, de degré d'évolution des profils d'altération sous-jacents aux cuirasses ferrugineuses, et d'évolution géomorphologique du paysage.

3. GEOCHRONOLOGIE DES ALTERATIONS LATERITIQUES

Les cuirasses manganésifères du Brésil et du Burkina Faso et les matériaux d'altération sous-jacents ont fait l'objet d'études pétrologiques, géohimiques et géochronologiques détaillées, ce qui a conduit à proposer un modèle d'évolution des paysages latéritiques en fonction des changements climatiques et géomorphologiques (Ruffet et al., 1996 ; Colin et al., 2005).

Des âges $^{40}Ar/^{39}Ar$ ont été obtenus sur la formation des oxydes et oxyhydroxydes de manganèse potassique (cryptomélanes) des cuirasses manganésifères emboîtées dans les systèmes latéritiques ferrugineux et alumineux. Des âges $^{40}Ar/^{39}Ar$ significatifs (Vasconcelos, 1999 ; Ruffet et al., 1996 ; Hénocque et al., 1998) permettent d'estimer des vitesses d'altération mais aussi d'érosion (Mouele, 2004) lorsque les objets datés (cuirasses manganésifères) sont intégrés à une séquence géomorphologique étagée dont la chronologie relative est au préalable bien établie (Colin et al., 2005).

VOLET I

VOLET I. ALTERATIONS LATERITIQUES, CUIRASSEMENT FERRUGINEUX ET EVOLUTION MORPHOCLIMATIQUE

1. BILAN GEOCHIMIQUE DES PROCESSUS D'ALTERATION LATERITIQUE

Les caractères minéralogiques et géochimiques des manteaux d'altération latéritique de la région du Haut-Mbomou en RCA ont été définis, et le bilan géochimique des processus de latéritisation (saprolitisation + ferruginisation) a été estimé de l'échelle des assemblages minéraux à celle des profils d'altération (Beauvais, 1999). Il a été montré qu'au cours du développement des profils d'altération cuirassés, la cuirasse ferrugineuse des sommets de profils n'était pas un faciès d'évolution de l'horizon nodulaire meuble sous-jacent, mais provenait de la ferruginisation de saprolite par accumulation absolue du fer. En fait, l'horizon nodulaire résulte pour partie de la dégradation géochimique et mécanique de la cuirasse, et pour partie de l'évolution des argiles tachetées sous-jacentes. Les manteaux d'altération cuirassés dérivent principalement d'une succession d'étapes d'altération et d'érosion contrôlées par les variations de conditions morpho climatiques qui déterminent les processus de formation (aggradation) et de transformation (dégradation) des cuirasses.

L'aggradation ferrugineuse au sein des matrices argileuses riches en kaolinite conduit à la formation d'hématite peu substituée en aluminium sous des conditions déshydratantes, oxydantes et de faible pH, ou à la néoformation de goethite plus fortement substituée en aluminium, pour laquelle l'activité de l'eau d'une part et de l'aluminium d'autre part est relativement plus élevée sous potentiel d'oxydoréduction plus faible. Les processus de dégradation des cuirasses favorisent la formation de la goethite aux dépens de l'hématite, la goethite étant alors caractérisée par des substitutions alumineuses relativement plus élevées. La kaolinite peut soit se dissoudre de manière incongruente et se transformer en gibbsite, soit se dissoudre de manière congruente, le silicium et l'aluminium libérés, pouvant reformer des kaolinites de grande taille dans les vides générés lors de la dégradation de la cuirasse.

2. PROPRIETES CRISTALLOCHIMIQUES DES KAOLINITES

Les études pétrologiques des altérations latéritiques du Haut-Mbomou en RCA ont mis en évidence différentes kaolinites selon des tailles et habitus variés. Dans les profils d'altération et les cuirasses étudiées, elles sont associées soit à la goethite, soit à l'hématite indépendamment de leur taille. Les propriétés cristallochimiques de la kaolinite et des

oxyhydroxydes de fer des sols latéritiques reflètent les propriétés géochimiques et physiques du milieu dans lequel ils se sont formés (Fitzpatrick et Schwertmann, 1982 ; Fitzpatrick, 1983 ; Schwertmann et Kämpf, 1985 ; Schwertmann et Carlson, 1994 ; Muller et al., 1995).

La micro spectroscopie Infra rouge (MIR) a été expérimentée sur des kaolinites de référence provenant de sols tropicaux et de sédiments, et employée pour caractériser et différencier les kaolinites de profils d'altération latéritique du Haut-Mbomou (Beauvais et Bertaux, 2002). L'application de cette technique à des matériaux altérés sur section polies généralement utilisées pour les observations et études pétrographiques en microscopie optique est novatrice. Elle permet, en effet, (1) l'analyse *in situ* des minéraux argileux sur des échantillons orientés non-perturbés et (2) la différenciation de kaolinites à structure ordonnée et désordonnée présentant des tailles et des textures différentes.

En spectrométrie Infra rouge classique basée sur l'analyse de pastilles de poudre de kaolinite mélangée à du KBr, la kaolinite est caractérisée par quatre bandes de vibrations des oxyhydroxyles OH à 3695, 3668, 3650 et 3620 cm^{-1}, notés respectivement, ν_1, ν_2, ν_3, et ν_4 ; plus une bande à 3595 cm^{-1} attribuée à la substitution octaédrique d'Al^{3+} par Fe^{3+}. Par rapport à la méthode classique, la technique MIR permet d'obtenir des informations de grande qualité uniquement entre 3700 et 3550 cm^{-1} ce qui suffit à bien distinguer les différents types de kaolinite.

Les spectres MIR des grandes kaolinites bien cristallisées ressemblent à ceux qui sont obtenus par réflectance diffuse car comparés aux spectres de pastilles de poudre KBr, les bandes à 3668 et 3650 cm^{-1} sont amplifiées, la forte bande d'absorption à 3695 cm^{-1} étant remplacée par une large bande plus faible autour de 3700-3680 cm^{-1}.

Les spectres MIR des petites kaolinites mal cristallisées montrent une bande amplifiée à 3650 cm^{-1} par rapport aux spectres de grandes kaolinites bien cristallisées, ce qui suggère un désordre structural en partie dû à des empilements de structures dickite ou nacrite dans la structure de ces petites kaolinites. La bande du fer à 3595 cm^{-1} est aussi beaucoup plus faible que pour les grandes kaolinites.

La diversité des spectres MIR obtenus sur les kaolinites latéritiques reflète l'inter croissance de polymorphes kaolinite-dickite, ou tout du moins des mélanges de kaolinites avec des quantités de défauts cristallins très variables, plutôt que des kaolinites pures, ce qui est le cas dans la plupart des sols et profils d'altération latéritique.

Les données MIR obtenues pour les kaolinites de référence de sols tropicaux et sédiments montrent que le rapport des aires de bandes $A\nu_2$ / $A\nu_3$ reste un indice d'ordre structural tout à

fait pertinent. Plus grand est cet indice, plus grande est la surface de la bande du fer à 3595 cm^{-1} et plus grande et mieux ordonnée est la kaolinite.
Les kaolinites les plus grandes néoformées dans les vides de dissolution des cuirasses sont les mieux cristallisées et les plus ferrugineuses, et sont de bons traceurs de l'évolution récente des vieux profils d'altération latéritique cuirassés du Haut-Mbomou en RCA.

L'approche pétrologique et cristallographique des produits et minéraux d'altération des profils verticaux ne contribuent cependant qu'à une compréhension parcellaire des manteaux d'altération, justifiant une approche cartographique des caractères pétro-géochimiques des cuirasses ferrugineuses en relation avec leur contexte géomorphologique.

3. CARTOGRAPHIE PETRO GEOCHIMIQUE DES CUIRASSES FERRUGINEUSES

Bien que les propriétés géochimiques des saprolites et des argiles tachetées des profils d'altération soient souvent liées à celles des roches mères sous-jacentes (Ambrosi et Nahon, 1986b ; Nahon, 1991 ; Tardy, 1993), cet héritage géochimique peut être fortement dilué, jusqu'à disparaître dans les cuirasses ferrugineuses, sous l'influence des facteurs environnementaux gouvernant l'évolution long terme des paysages latéritiques (Boeglin et Mazaltarim, 1989 ; Tardy et al., 1988a). Le substratum géologique du Haut-Mbomou en RCA étant composé de roches basiques métamorphiques indifférenciées (Mestraud, 1982 ; Beauvais, 1991), l'étude a porté sur les relations entre les faciès pétro géochimiques des cuirasses et leur distribution géomorphologique (Beauvais et Roquin, 1996).
Quatre faciès de cuirasses ont été définis et cartographiés sur des hauts plateaux, des versants et des bas plateaux (Fig. 4) entre 650-670 et 600-610 m d'altitude. Les cuirasses des hauts plateaux à faciès massif sont essentiellement constituées de minéraux supergènes peu ou pas hydratés comme la kaolinite, généralement de grande taille et bien cristallisée (Beauvais et Bertaux, 2002) et l'hématite. Les cuirasses des versants et des bas plateaux à faciès protopisolitique contiennent aussi de l'hématite et de la kaolinite mais sont aussi enrichies en minéraux supergènes hydratés comme la goethite et la gibbsite ; les cuirasses de bas plateaux à faciès vermiforme, aussi développées à la base des profils de bas versants (Beauvais, 1999), sont essentiellement constituées de kaolinite illuviée de petite taille, mal cristallisée (Beauvais et Bertaux, 2002), et de goethite.
Une analyse statistique en composante principale a été appliquée aux données géochimiques et minéralogique obtenues sur chacune des quatre populations de cuirasses ce qui a permis de

caractériser les principaux paramètres de différenciation de ces cuirasses en relation avec leur faciès pétro géochimique et leur situation géomorphologique. La distribution des minéraux secondaires et leur relation avec les éléments en trace reflète des différences de processus d'altération et d'érosion plutôt que des différences lithologiques.

Les cuirasses des hauts plateaux sont les plus anciennes et préservent encore la signature géochimique des roches amphibolo-schistes. Les cuirasses de versants et bas plateaux sont plus jeunes, puisqu'elles renferment des reliques de cuirasses plus anciennes. Elles dérivent d'une longue évolution du paysage sous les effets combinés des changements hydro climatiques et géomorphologiques qui ont contribué à brouiller progressivement la signature géochimique des roches.

4. PRINCIPAUX ENSEIGNEMENTS DU VOLET I

Les cuirasses massives des hauts plateaux, les plus anciennes, apparaissent comme les témoins d'un climat tropical plus contrasté que l'actuel et résultent de la ferruginisation (aggradation) *in situ* des saprolites riche en kaolinite de grande taille, en partie préservée au sein des matrices hématitiques (Beauvais, 1999). Le taux de substitution en aluminium relativement bas de l'hématite (<4%) s'accorde difficilement avec un remplacement par épigénie de la kaolinite par l'hématite (Ambrosi et al., 1986). Lorsque la cuirasse se dégrade, la kaolinite subit une dissolution incongruente avec formation de gibbsite qui se développe également dans les vides créés lors de la transformation de la cuirasse par dissolution de l'hématite et la kaolinite. Ce type de transformation minéralogique a déjà été prédit et observé dans des bauxites du Vénézuela (Soler et Lasaga, 1996). Cependant, les mobilisations de silice, alumine et fer résultant de la dégradation géochimique des cuirasses peuvent aussi conduire à la néoformation de grandes kaolinites ferrifères bien cristallisées dans les vides de dissolution de la cuirasse (Beauvais et Bertaux, 2002). La néoformation de gibbsite ou de kaolinite est contrôlée par l'activité de l'eau et de la silice au sein des profils (Fritz et Tardy, 1973 ; Tardy et Novikoff, 1988c ; Tardy , 1993).

Les cuirasses de versants plus riches en goethite et gibbsite dérivent en partie de la dégradation géochimique, de l'érosion et du remaniement des cuirasses massives à hématite et kaolinite au cours de l'enfoncement du réseau hydrographique dans le paysage sous l'effet des variations climatiques passées, depuis des climats contrastés vers des climats plus humides (Beauvais et Roquin, 1996).

5. ARTICLES SCIENTIFIQUES DU VOLET I

3 articles (RCA) : pétrogéochimie des manteaux d'altération cuirassés ; mécanismes, processus et évolution ; 3 échelles d'observation et de mesures.

Geoderma (Beauvais & Roquin, 1996) : pétrogéochimie, géomorphologie, spatialisation et différentiation des cuirasses ferrugineuses, évolution morphoclimatique.

Geochimica et Cosmochimica Acta (Beauvais, 1999) : bilan de masse minéralogique et géochimique à l'échelle de profils verticaux le long d'une toposéquence ; discussion sur les signatures climatiques possibles des faciès d'altération latéritique.

Clays and Clay Minerals (Beauvais & Bertaux, 2002) : propriétés cristallochimiques des kaolinites par microscopie Infra rouge ; traceurs de l'évolution des profils d'altération latéritique cuirassés.

ARTICLE 1

ELSEVIER

Geoderma 73 (1996) 63–82

GEODERMA

Petrological differentiation patterns and geomorphic distribution of ferricretes in Central Africa

Anicet Beauvais [a,*], Claude Roquin [b]

[a] *Institut Français de Recherche Scientifique pour le Développement en Coopération (ORSTOM), UR12-TOA, 32 Avenue Henri Varagnat, 93143 Bondy Cedex, France*

[b] *Centre de Géochimie de la Surface, UPR 6251 C.N.R.S, Institut de Géologie, 1, rue Blessig, 67084 Strasbourg Cedex, France*

Received 24 May 1995; accepted 24 April 1996

Abstract

Geomorphic distribution and petrological differentiation patterns of ferricretes widespread on landsurfaces were studied in the Dembia–Zemio area, southeastern Central African Republic. Four types of ferricretes are distributed on high plateaux, hillslopes and low plateaux. The main contrast corresponds to the differentiation between ferricretes of high plateaux rich in poorly hydrated minerals, hematite and kaolinite, and those covering hillslopes and low plateaux richer in hydrated minerals, goethite and gibbsite. A Principal Component Analysis of geochemical and mineralogical data was used to characterize the main differentiation patterns of ferricretes in relation with their petrographic facies and the geomorphic features of the landscape. The distribution of secondary minerals and their relationships to trace elements within and between the ferricrete types reflects differences in weathering and erosion processes. Our results document that the petrological patterns and the distribution of ferricretes are related to geomorphic features depending on hydroclimatic variations that govern the landscape evolution of many tropical shields.

Keywords: ferricrete; Central Africa ; petrology; geochemistry; geomorphology

1. Introduction

In southeastern Central African Republic, the bedrock is deeply weathered and uniformly covered by thick ferricretes. The weathering profiles developing from different parent rocks always exhibit the following upward succession of layers: saprolite, mottled clay and ferricrete (Tardy and Nahon, 1985; Nahon, 1986). The geochemical

* Corresponding author. E-mail: beauvais@bondy.orstom.fr

PII S0016-7061(96)00041-9

processes involved in the weathering profile development imply complete leaching of alkalis and earth-alkalis, partial desilication from the parent-rock minerals, and thus, relative accumulations of iron and aluminium (Delvigne, 1965; Tardy, 1969; Millot, 1970; Nahon, 1991). In contrast, the minor transition elements are generally trapped in the secondary Al- and Fe-oxihydroxides and clay minerals (Trescases, 1975; Schwertmann and Taylor, 1977; Mosser, 1980), which are, in turn, the main components of ferricretes (Nahon, 1976; Leprun, 1979; Tardy and Nahon, 1985; Tardy et al., 1988a). Under tropical climates with a pronounced dry season, bio-physical processes are often involved in the reworking of weathering profiles, implying either the dispersion of the heavy minerals and relict quartz onto the landsurface, or the vertical translocation through the macropores of weathering profiles (Brimhall and Dietrich, 1987; Butt and Zeegers, 1989; Freyssinet et al., 1989; Freyssinet, 1990; Lecomte and Colin, 1989; Colin and Vieillard, 1991; Colin et al., 1992). Geochemical and mineral prospecting in lateritic environments requires knowledge of the nature, the distribution and the geochemical patterns of lateritic formations concealing the parent rocks (Nalovic, 1977; Davies and Bloxham, 1979; Zeegers and Leprun, 1979; Matheis, 1981; Matheis and Pearson, 1982; Butt, 1987; Butt and Zeegers, 1989; Roquin et al., 1989; Boski and Herbosch, 1990).

Many studies have addressed the influence of parent rocks on the petrological differentiation patterns of vertical weathering profiles capped with old pedogenic ferricretes (Leprun, 1979; Zeegers and Leprun, 1979; Matheis, 1981; Ambrosi and Nahon, 1986; Nahon, 1991), but the processes governing the spatial distribution of ferricretes onto landsurfaces were rarely investigated (Butt and Zeegers, 1989; Roquin et al., 1989). However, more attention has been paid recently to the regional distribution of ferricretes tempering their effective relationships to parent rock variations and inferring that their mineralogical variation patterns over the world might be considered as reflecting climatic changes driven by continental plate drift (Tardy et al., 1988b,1991). Although the saprolite and the mottled clay layers of weathering profiles often relate to the parent-rock geochemistry (Ambrosi and Nahon, 1986; Nahon, 1991; Tardy, 1993), the ferricretes can lose this geochemical inheritance under the influence of environmental factors governing landscape evolution (Boeglin and Mazaltarim, 1989; Tardy et al., 1988a). Considering that the bedrock of our study area is composed of undifferentiated basic metamorphic rocks (Mestraud, 1982; Beauvais, 1991), we explore the relations between the ferricrete petrological differentiation patterns and their geomorphic distribution in the landscape.

2. Geographic features of the study area

The study area of 260 km^2 around the village of Guénékoumba between Dembia and Zemio (Figs. 1 and 2) forms part of the African shield, thought to have been tectonically stable for 70 My (Boulvert, 1996). This area is included in a wider geomorphic region of 3000 km^2 known as "Haut-Mbomou plateau" which was investigated for geological mapping and base metal prospection (Mestraud, 1982). The Haut-Mbomou plateau is extensively covered by ferricretes and the geological substratum corresponds to a large complex of basic rocks, named Complex of Mbomou and composed of metamorphic

volcano-sedimentary formations corresponding to amphibolite and green-schist facies crossed by elongated granitic intrusions and dykes of dolerites in the southwestern area of the Haut-Mbomou plateau (Mestraud, 1982). Although the extensive lateritic cover masks the parent rocks in our field area, some fresh rocks collected at the surface of plateaux and hillslopes are amphibole schists. Similar rocks were also identified in some deeply incised thalwegs. Hence, we consider these amphibole schists as the parent rocks in our study area.

This region has a tropical humid climate characterized by (1) a short dry season from December to February, a long wet season from May to October, and 3 months of interseason, in November, March and April; (2) a mean annual rainfall of 1600 mm; (3) a mean annual temperature of 25°C; and (4) a mean annual relative humidity of 80% ranging from 50% to 95% (Boulvert, 1986; Franquin et al., 1988; Beauvais, 1991). The vegetation cover consists of a semi-humid forested savanna. Large stretches of grass and bare lands alternate on the plateaux and hillslopes, while a dense humid forest occupies the valleys and the high plateau edges (Fig. 2).

Three main landform units were distinguished in the study area: high plateaux, hillslopes and low plateaux (Fig. 2). All three are armoured by 3 to 5 metres of ferricretes capping lateritic weathering profiles exhibiting thicknesses of several tens of metres (Beauvais, 1991). These geomorphic units are representative of the Haut-Mbomou plateau extending on several square kilometres. There is no evidence in the field to relate the geomorphic patterns to differentiation of the geological basement. The high plateaux as a whole form a regional warped erosion surface with many points culminating at 650 m above sea level (a.s.l.). This landsurface envelope gently slopes down (0.1 to 0.2%) towards the main hydrographic channels, the Ouara river to the West and the Mbomou river to the South. Individual high plateaux are limited by an erosion scarp of one metre height, and surrounded with a ring of dense semi-humid forest. Further downslope, another metric scarp separates the forested hillslope from the bare hillslope. The high plateau landsurface is globally planconvex with some concave area, while the

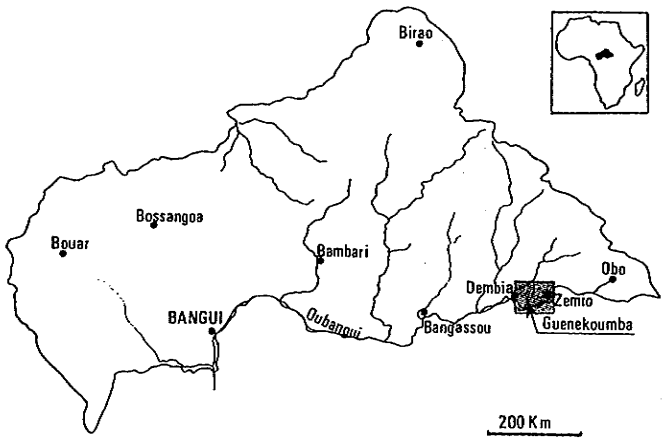

Fig. 1. Location of the study area in Central African Republic.

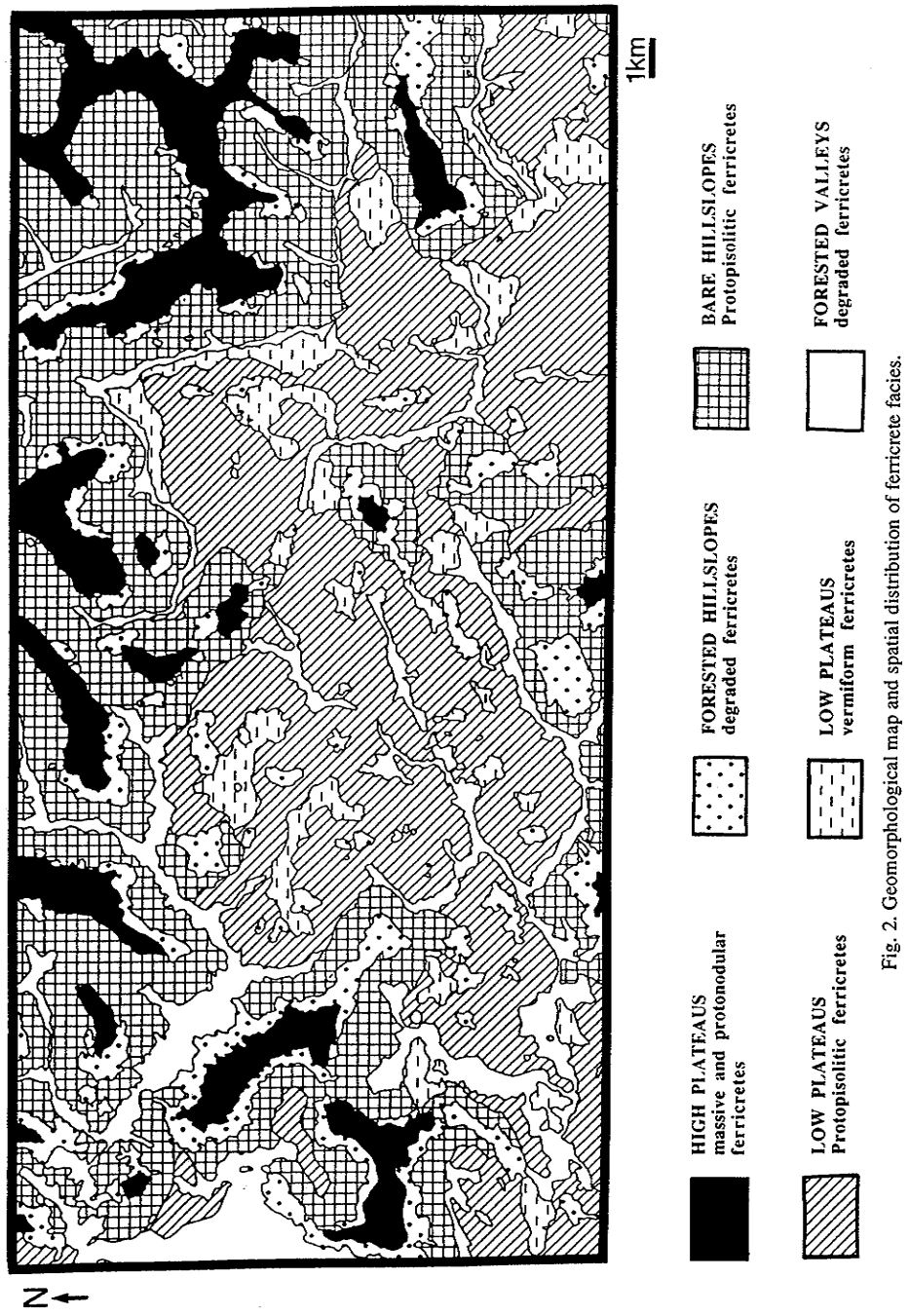

Fig. 2. Geomorphological map and spatial distribution of ferricrete facies.

hillslopes present straight and concave profiles with gradients ranging from 5% on the bare hillslope to 10% on the forested hillslope. In contrast, the low plateaux are planconcave and they are always separated from high plateaux by a thalweg or a hillslope (Fig. 2). Hillslope and low plateau landsurfaces are densely covered by termitaria (i.e., 1 per square metre, on average), whose the soft clayey–silty material is dispersed downslope by overland flow. During the rainy season, "swampy" area take place on concave surfaces by subsurface saturation flow.

3. Methods

The mapping of geomorphic units and associated lateritic formations was first realized at a 1:50000 scale from field and aerial photograph observations (Boulvert, 1976; Beauvais, 1991). The lateritic landsurface was then investigated and ferricretes were sampled to characterize their petrological differentiation patterns. Petrographic facies, mineralogical and chemical compositions were analysed for 204 samples and compared to the geomorphic, hydrologic and phytogeographic characteristics recorded at each sampling site. Ferricrete blocks of at least 1000 cm^3 were regularly collected on each landform unit at a depth ranging from 10 cm to 50 cm. Petrographic facies were described from macroscopic and microscopic observations. Each sample was then crushed to 5 mm and sorted to produce 100 g of powder with a sieve size ranging from 64 to 120 μm for chemical and mineralogical analysis.

Major element contents analysed by spark emission spectrometry (SiO_2, Al_2O_3, Fe_2O_3, MgO, CaO, P_2O_5, TiO_2) and by flame emission spectrometry (Na_2O, K_2O) are given in oxide percent. Trace elements analysed by plasma emission spectrometry ICP (Sr, Ba, V, Ni, Co, Cr, Cu, Zn, Sc, Y, Zr, Mn, La, Yb, and Nb) are given in ppm. Samples were dried prior to the analysis and weight loss on ignition (LOI) was measured after a 1000°C calcination. Elements with concentrations systematically below detection limits (d.l.) were neglected. Those are MgO (d.l. = 0.02%), CaO (d.l. = 0.20%), Na_2O and K_2O (d.l. = 0.01%), Eu (d.l. = 10 ppm) and Lu (d.l. = 1 ppm).

The mineralogical analyses were obtained from X-ray diffraction (XRD) of unoriented powder preparations. Mineral contents were estimated measuring characteristic intensity of X-ray peak weighted by a calibration coefficient defined for each mineral, employing normative calculations (Mazaltarim, 1989). The error in estimation ranges from 1 to 3%. Therefore, each sample was defined by seven mineralogical variables, corresponding to the estimated contents of kaolinite (Kaol), quartz (Quar), gibbsite (Gib), goethite (Goet), hematite (Hema), and the ratios, RHG equal to 100 * hematite/(goethite + hematite), and RKGi equal to 100 * kaolinite/(gibbsite + kaolinite).

The differentiation patterns for the whole set of ferricrete samples were defined applying a Principal Component Analysis (PCA) to geochemical and mineralogical data (SAS, 1985). This statistical procedure is based on the determination of eigenvectors with their associated eigenvalues from the correlation matrix, followed here by an application of the varimax rotation procedure (Lebart et al., 1979). The main differentiation trends in the data set are expressed by the first factors (i.e., the principal

components) which are new independent synthetic variables characterized by their association with some elements and/or minerals, as it was successfully applied to soils and weathering system studies (Litaor et al., 1989; Boski and Herbosch, 1990; Roquin et al., 1990; Donkin and Fey, 1991). Within each factor, for each element and mineral, the correlation loadings ranging from −0.4 to 0.4 were considered as non-significant. A representation of samples on factor score diagrams illustrates the ferricretes differentiation patterns within and between morpho-petrological categories identified in the field.

4. Field characteristics of ferricretes

4.1. Description of ferricretes

Four ferricrete facies were identified based on both macroscopic descriptions (Fig. 3), according to the typologic nomenclature recently proposed by Tardy (1993), and on previous microscopic observations (Beauvais, 1991; Beauvais and Colin, 1993).

(a) The massive ferricretes exhibit an indurated compact hematitic matrix purple-reddish coloured, with a fine porosity but without nodules or obviously defined geometric elements (Fig. 3a).

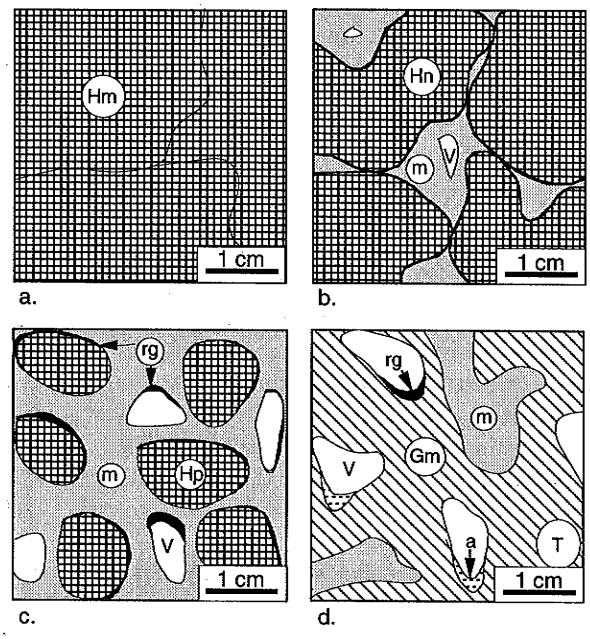

Fig. 3. Petrographical sketches of the four ferricrete facies sampled on the landsurface. (a) massive; (b) protonodular; (c) protopisolitic; (d) vermiform. (Hm = Hematitic matrix; Hn = hematitic nodular domain; m = clayey ferruginous matrix; V = vacuole; Hp = Hematitic protopisolite; rg = goethitic rim; Gm = goethitic matrix; a = argilan; T = tubule.)

(b) The protonodular ferricretes show large coalescent purple-reddish hematitic nodular domains (> 1 cm), coexisting with a slightly indurated clayey–ferruginous matrix crossed by small vacuoles (< 1 cm) (Fig. 3b). This facies may also exhibit small goethitic rims around the hematitic domains, and also some gibbsite scattered within the matrix. In both (a) and (b) facies, the ferruginous matrix is rich in hematite and kaolinite booklets of 100–200 μm in length, deriving from pseudomorphic weathering of micas, felspars and amphiboles.

(c) The protopisolitic ferricretes generally present purple-reddish hematitic protopisolites outlined by peripheral goethitic rims and cortex. The protopisolites have sizes approximating 1 cm and they are enclosed within a red-yellowish clayey–ferruginous matrix crossed by cm-sized vacuoles (Fig. 3c). Microscopic observations revealed the development of secondary gibbsite through the matrix and within the vacuoles. Also, we have observed some relics of ilmenite showing partial dissolution features.

(d) The vermiform ferricrete is essentially characterized by a yellow–brown matrix composed of microcrystalline mixture of kaolinite and goethite, with a few centimetre-length diffuse hematitic domains and some relics of quartz. The ferruginous matrix is intersected by a dense network of centimetric vacuoles and tubules, which are often filled with a white fine clayey matrix, and outlined by argillans and brown goethitic rims (Fig. 3d). To a lesser extent, manganesiferous concretions mainly composed of lithiophorite were also identified in facies (c) and (d), and some relics of micas or feldspars were observed under the microscope in facies (b), (c) and (d), although these minerals were never detected from XRD analyses.

4.2. Regional distribution of ferricretes

The regional distribution of ferricretes is shown on the morphopetrographic map (Fig. 2). About 80% of the total field mapped landsurface (TFML) is covered by ferricretes, while the remaining 20% correspond to forested areas wherein the ferricretes are degraded (Beauvais and Tardy, 1993). Four ferricrete facies, massive, protonodular, protopisolitic and vermiform were differentiated by their petrographic features, and by their location in the landscape. 31 samples of massive and 29 samples of protonodular ferricretes were collected on high plateaux representing 10.5% of TFML; 52 samples of protopisolitic ferricretes were collected on the hillslopes occupying 32% of TFML; 64 samples of protopisolitic ferricretes were sampled on the low plateaux representing 31% of TFML; 28 samples of vermiform ferricretes outcrop on the low plateaux occupying 6.5% of TFML. The protopisolitic ferricretes are widespread on the hillslopes and on the low plateaux, representing 61% of the sampling set. The massive and the protonodular ferricretes are the only two facies covering the surface of the high plateaux and they represent 26% of the sampling. The protopisolitic ferricrete layer of hillslopes may comprise blocks of massive ferricrete with decimetric sizes that exhibit a peripheral brown cortex of goethite. The vermiform ferricretes only outcrop on the low plateaux, and represent 13% of the sampling. This facies is also well developed within the weathering profiles of the hillslopes and low plateaux capped by a protopisolitic ferricrete (Beauvais, 1991; Beauvais and Colin, 1993).

5. Analytical results

5.1. Petrological patterns of ferricretes

The mean and standard deviation values of elements and minerals for the four main petrographic facies distributed on the three geomorphic units are presented in Table 1. At first glance, the mean geochemical compositions indicate that the contents of transition elements versus earth alkalis and rare earth elements do not permit to

Table 1
Comparison of mean chemical and mineralogical compositions of ferricretes according to their petrographic facies and geomorphic location (n = number of samples; M = massive; PN = protonodular; PP = protopisolitic; V = vermiform; m = mean; s = standard deviation; LOI = lost on ignition (1000°C); RHG = 100 * hematite/hematite + goethite; RKGi = 100 * kaolinite/kaolinite + gibbsite)

Location:	High plateaux				Hillslopes		Low plateaux			
facies:	M		PN		PP		PP		V	
n:	31		29		52		64		28	
	m	s	m	s	m	s	m	s	m	s
SiO_2 (%)	15.2	3.4	11.7	2.9	10.9	2.6	10.6	3.3	15.3	3.5
Al_2O_3	16.3	2.8	15.8	2.0	16.6	2.9	17.2	2.4	17.6	3.1
Fe_2O_3	57.2	6.3	61.2	4.9	59.7	4.5	58.4	4.9	52.6	6.9
TiO_2	1.7	0.3	1.6	0.3	1.4	0.3	1.3	0.3	1.4	0.4
P_2O_5	0.39	0.14	0.4	0.1	0.5	0.2	0.4	0.1	0.37	0.16
LOI	8.8	1.5	9.0	1.1	10.6	1.8	11.4	1.6	12.4	0.7
Sr (ppm)	54	49	30	25	24	26	13	16	12	8
Ba	47	36	28	19	93	239	54	138	39	57
V	1372	423	1469	286	1412	363	1325	306	1201	330
Mn	211	163	222	106	683	1169	612	1132	376	521
Ni	40	7	43	9	59	30	58	29	61	37
Co	15	5	14	4	27	17	18	10	19	17
Cr	330	212	555	187	467	243	609	214	372	159
Zn	52	21	59	20	74	49	82	41	101	51
Cu	100	44	95	33	193	173	274	178	528	264
Sc	46	12	47	12	50	18	62	18	73	18
Y	9	3	8	2	11	5	12	4	13	4
Zr	309	70	299	68	278	80	282	67	271	121
La	52	32	30	17	27	30	20	18	20	10
Ce	72	45	53	35	101	161	127	171	87	119
Yb	1.6	0.5	1.4	0.4	1.8	0.7	1.4	1	2.1	1
Nb	16	4	18	4	16	5	17	5	15	5
Quartz (%)	1	1	1	1	3	4	3	3	3	2
Kaolinite	35	9	28	9	23	10	20	7	26	8
Hematite	48	10	51	10	34	14	28	12	10	7
Goethite	12	8	13	5	30	18	36	13	58	13
Gibbsite	5	5	7	5	10	8	12	7	3	5
RHG	81	11	80	8	54	22	44	19	15	12
RKGi	90	10	81	12	71	22	63	19	91	12

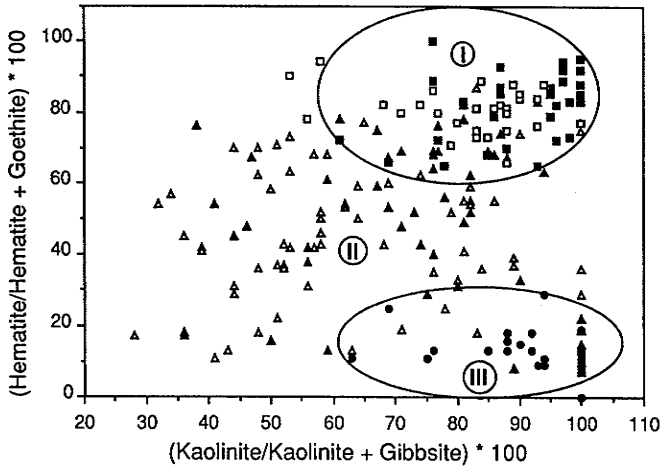

Fig. 4. Mineralogical variation pattern of ferricrete facies according to their geomorphological location (■ massive and □ protonodular of high plateaux; protopisolitic of ▲ hillslopes and △ low plateaux; ● vermiform of low plateaux).

distinguish different parent rocks for the different ferricrete facies. From the high plateaux to the low plateaux, the kaolinite and hematite contents progressively decrease while the goethite content increases with the highest value in the vermiform facies. The protopisolitic ferricretes exhibit the highest gibbsite content. The variations of ferricrete mineralogical composition are represented in a rectangular diagram, RHG versus RKGi (Fig. 4). The vermiform facies of low plateaux is relatively rich in goethite and poor in hematite and clearly separated from the massive and protonodular facies of high plateaux, which are defined by higher contents of hematite. Both are relatively high in kaolinite. Samples of protopisolitic facies of hillslopes and low plateaux present a wide range of composition between the ferricretes of high plateaux and the vermiform facies of low plateaux.

The mineralogical variations were also analysed by examining the moving average of each mineral abundance for classes of 5% Fe_2O_3 and Al_2O_3 with a re-covering step of 2.5%, i.e. for Fe_2O_3 amounts ranging from 40% to 45%, then from 42.5% to 47.5% and so forth... (Figs. 5 and 6). Three main trends are evidenced on these diagrams, justifying the distinction of three ferricrete categories, that is consistent with the differentiation patterns yielded by the Fig. 4.

The first category (I) corresponds to the massive and protonodular ferricretes of high plateaux which are, on the average, the richest in hematite and kaolinite, and the poorest in goethite (Table 1 and Fig. 4). When the iron content increases and the alumina decreases, the hematite content increases, the kaolinite and gibbsite contents decrease while quartz and goethite remain roughly constant (Figs. 5 and 6). For the two facies of high plateaux, the evolution curves of gibbsite and kaolinite versus Al_2O_3 are not parallel, an increase in Al_2O_3 for the massive ferricretes corresponding to an increase in gibbsite rather than in kaolinite (Fig. 6).

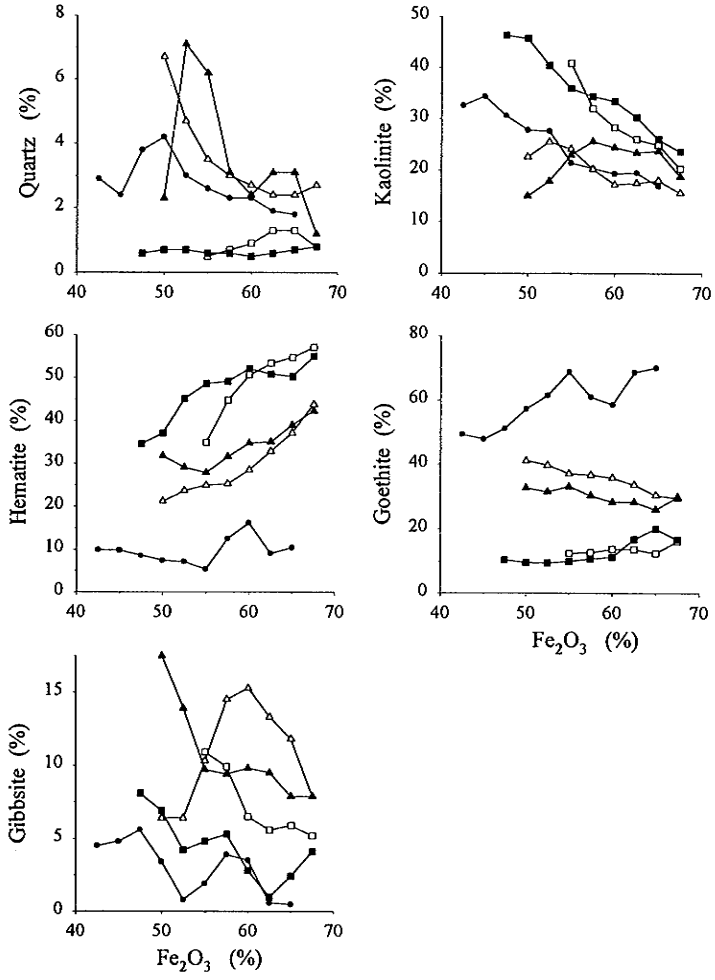

Fig. 5. Variation of mineral contents as a function of iron moving average calculated for classes of 5% Fe_2O_3. For symbols see Fig. 4.

The second category (II) is composed of protopisolitic ferricretes of hillslopes and low plateaux that are less hematitic but more goethitic. This facies presents the highest gibbsite contents, and also some quartz (Table 1 and Figs. 5 and 6). For these ferricretes, an increase in iron content is related to hematite rather than to goethite (Fig. 5), while an increase in aluminium content reflects an enrichment in gibbsite rather than in kaolinite (Fig. 6). Although the mineralogical evolution curves of the protopisolitic facies of hillslopes and low plateaux are very similar, the ferricretes of low plateaux are slightly richer in goethite and gibbsite and poorer in hematite and kaolinite than those of hillslopes (Table 1 and Fig. 6).

The third category (III), corresponds to the vermiform ferricretes of low plateaux that are the richest in goethite, the poorest in hematite and the less ferruginous (Table 1). In

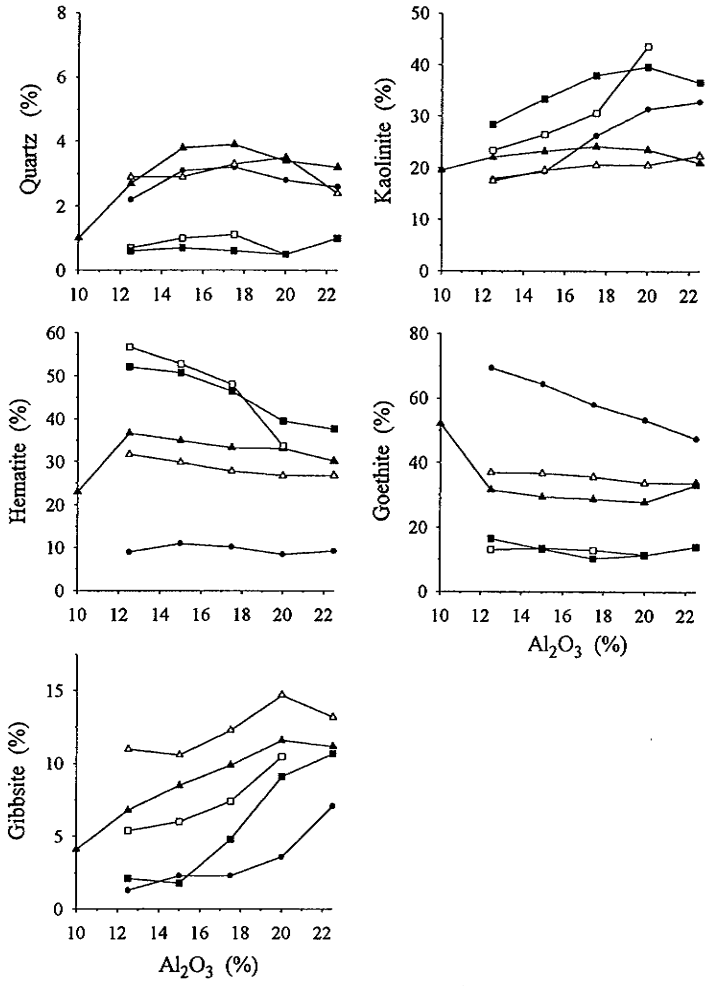

Fig. 6. Variation of mineral contents as a function of aluminium moving average calculated for classes of 5% Al_2O_3. For symbols see Fig. 4.

contrast with the protopisolitic facies, an increase in iron content and a decrease in alumina are related to an increase in goethite and a loss of kaolinite (Figs. 5 and 6). This ferricrete facies contains small amounts of quartz and gibbsite related to iron and aluminium contents respectively (Figs. 5 and 6).

For the massive and protonodular ferricretes of the high plateaux, iron is mainly related to the hematite content, while for the vermiform facies of low plateaux it is related to the goethite content (Fig. 5). For the protopisolitic ferricrete of hillslopes and low plateaux, the iron content decreases with the transformation of hematite to goethite. In contrast with the other facies, the decrease in iron content for the protopisolitic facies of hillslopes is also related to a loss of kaolinite and a strong increase in gibbsite (Fig. 5).

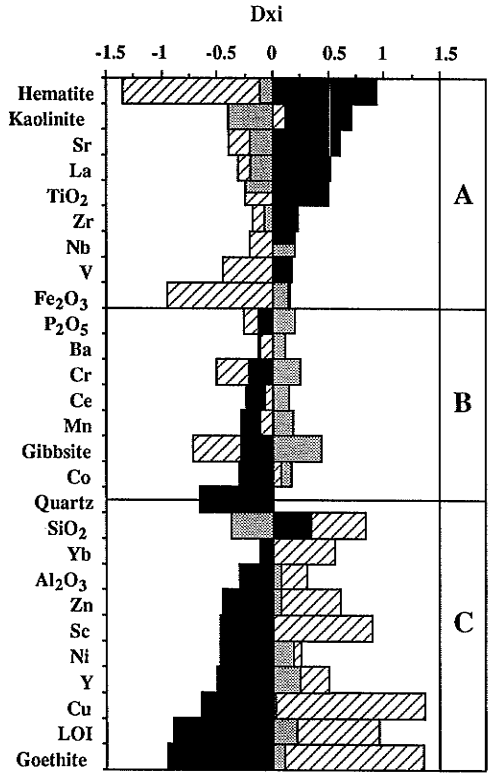

Fig. 7. Mineralogical and geochemical contrast of ferricrete categories according to the background differentiation index (Dx_i) of elements for the three ferricrete categories (LOI = loss on ignition; black: massive + protonodular facies of high plateaux; shaded: protopisolitic facies of hillslopes and low plateaux; hatched: vermiform facies of low plateaux; A, B and C represent the three groups of elements whose Dx_i is maximum in one of the three categories).

5.2. Geochemical differentiation contrasts between the ferricretes

A more synthetic analysis of petrological differentiation contrasts is given in Fig. 7 for the three categories of ferricretes described above: (I) massive and protonodular ferricretes of high plateaux; (II) protopisolitic ferricretes of hillslopes and low plateaux; and (III) vermiform ferricretes of low plateaux. A differentiation contrast index Dx_i for each chemical and mineral element x was calculated as the standardized deviation of within-group mean for each ferricrete sample category i such that:

$$Dx_i = (\text{mean}(x)_i - m(x))/s(x) \quad (1)$$

where $m(x)$ and $s(x)$ respectively represent the overall mean and standard deviation of element x for the whole sample set. A negative or positive value of Dx_i indicates the depletion or the enrichment contrast of element x relative to the overall mean of this element within a sample category i expressed in unit of standard deviation. The

elements were first ranked according to the decreasing contrast value Dx_i for the high plateau ferricrete samples, and then allocated to one of the three ferricrete categories according to their higher Dx_i in each category (Fig. 7). The first group of elements (A) is composed of Sr, TiO_2, La, V, and also Zr and Nb, associated to hematite and kaolinite, which exhibit higher positive Dx_i in the ferricretes of high plateaux. In contrast, these elements have negative Dx_i in the vermiform ferricretes of low plateaux, except for kaolinite. They also tend to be more depleted in the protopisolitic facies. The second group of elements (B) is characterized by higher contents of gibbsite in the protopisolitic facies contrasting with lower content of kaolinite (Fig. 7). The development of Mn- oxy-hydroxides in this facies is reflected by highest positive Dx_i for Mn and associated elements, Ba, Ce, and Co. A relative enrichment of P_2O_5 and Cr can also be noticed. The third group of elements (C) corresponds to higher contents of SiO_2, Al_2O_3, LOI, and also Cu, Y, Sc, Ni, Zn, Yb associated to goethite enrichment characterizing the vermiform ferricretes of the low plateaux. The ferricretes of high plateaux are the richest in poorly hydrated minerals, kaolinite and hematite, as well as in chemical elements with low mobility, except Sr. In contrast, the protopisolitic and vermiform ferricretes of hillslopes and low plateaux are the richest in hydrated minerals, gibbsite and goethite respectively, and they are also the richest in chemical elements which generally present a higher mobility in the lateritic environments (Tardy, 1969; Nalovic, 1977; Davies and Bloxham, 1979; Matheis, 1981; Roquin et al., 1989).

5.3. Principal component analysis

The principal component analysis (PCA) applied to the whole data set yields six independent factors explaining 70.1% of the total variance (Table 2). Comparison of results of the Table 2 and Fig. 7 allows to interpret each factor. The first factor contributing to 29.5% of the explained variance is positively loaded with the goethite correlated to LOI and trace elements Cu, Sc, Zn, Ni, Y and Yb and negatively loaded

Table 2
Correlation of chemical elements and minerals with each factorial axis defined by the Principal Component Analysis (LOI = loss on ignition; loading values are given in parentheses)

Factorial axis	% explained variance	Positive loadings	Negative loadings
F1	29.5	LOI (0.76), Ni (0.56), Zn (0.68), Cu (0.88), Y (0.74), Sc (0.74), Yb (0.5), Goethite (0.86)	Hematite (0.82)
F2	17.5	SiO_2 (0.69), Al_2O_3 (0.81), Zr (0.47), Kaolinite (0.46)	Fe_2O_3 (0.93)
F3	12.2	Cr (0.77), Gibbsite (0.7)	SiO_2 (0.51), Kaolinite (0.46)
F4	15.5	Mn (0.93), Ba (0.88), Co (0.65), Ce (0.69)	
F5	12.8	TiO_2 (0.45), P_2O_5 (0.54), Zr (0.58), Nb (0.75), Quartz (0.48)	
F6	12.5	Sr (0.84), La (0.83), V (0.43)	

with hematite, reflecting the patterns of vermiform facies. The correlation matrix indicates that LOI is correlated to each trace element. This factor opposes ferricretes of high plateaux to the other ferricretes. Factor 2 contributing to 17.5% of the explained variance separates a group composed of Al_2O_3, SiO_2 and kaolinite with Zr exhibiting positive loadings, from Fe_2O_3 with a negative loading. This factor accounts on the undifferentiated ferruginization process of clayey matrices in all ferricrete facies, and also the Al-substitution in Fe-oxihydroxides (Beauvais, 1991). Factor 3 representing 12.2% of the explained variance opposes positive loadings on gibbsite and Cr to negative loadings on kaolinite and SiO_2 reflecting the contrast between gibbsite and kaolinite formation processes in the protopisolitic facies. Examination of the correlation shows that gibbsite is relatively correlated to LOI ($r = 0.31$). Factor 4 contributing to 15.5% of the explained variance shows high positive loadings on Mn, Ba, Ce and Co, describing the secondary development of Mn-oxyhydroxides, effective in protopisolitic and vermiform facies. The analysis of correlations reveals two distinct trends separated by a threshold in Mn-content. When Mn-content is lower than 800 ppm, intercorrelations between Mn, Ba, Co and Ce do not exist, and positive correlations appear between Sr, Ba, La and Ce, while the global relationship revealed by the factor 4 is only effective when Mn-content is higher than 800 ppm. Factor 5 representing 12.8% of the explained variance express the geochemical patterns of residual heavy minerals as shown by the positive loadings on TiO_2, P_2O_5, Zr and Nb with quartz, while Factor 6 contributing to 12.5% of the explained variance exhibits positive loadings on Sr, La and V (Table 2),

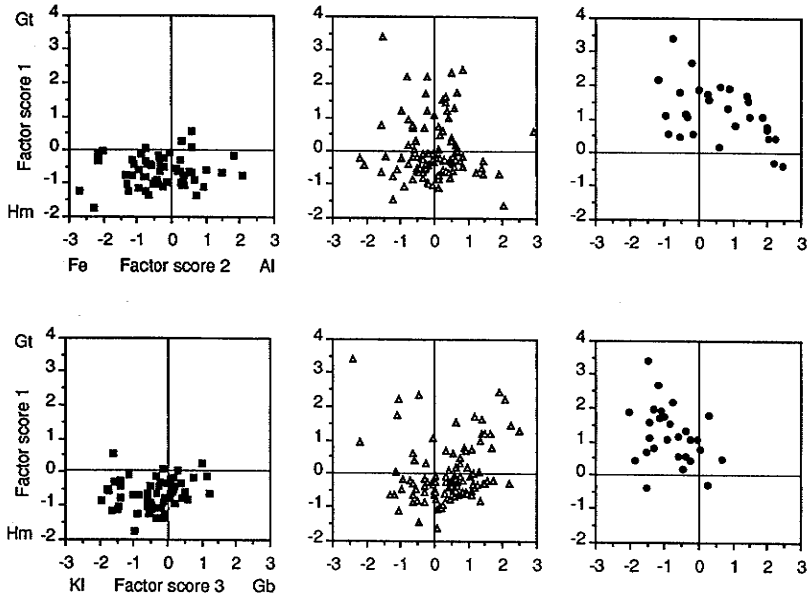

Fig. 8. Petrological differentiation pattern of ferricrete categories reflected by (a) the first factor score diagram F1 vs. F2, and (b) the second factor score diagram, F1 vs. F3 (■ massive and protonodular facies of high plateaux; △ protopisolitic facies of hillslopes and low plateaux; ● vermiform facies of low plateaux; Gt = Goethite; Hm = Hematite; Kl = Kaolinite; Gb = Gibbsite).

that reflects higher abundance of relics of feldspars and micas. The first four factors contributing to 74.7% of the explained variance are loaded by chemical elements showing relationships with minerals depending on lateritic weathering processes, while both factors 5 and 6 representing 25.3% of the explained variance are loaded by chemical elements with no clear affinities to the lateritic mineral phases. These two factors may account on some parent rock inheritance which is better expressed in ferricretes of high plateaux than in those of hillslopes and low plateaux (Fig. 7).

The projections of ferricrete samples on the factor diagrams F1 versus F2 and F1 versus F3 show the main differentiation trends within and between the ferricrete categories (Fig. 8). Three distinct petrological paths are expressed by the factorial axes corresponding to the contrasts goethite/hematite, alumina/iron oxide, and gibbsite/kaolinite. The first diagram of factor scores, F1 versus F2, highlights differences in ferruginization processes discriminating the hematitic ferricretes of high plateaux from the vermiform facies of low plateaux which exhibit another trend between two end-members, ferruginous-goethitic and aluminous-kaolinitic (Fig. 8a). This also may account on the development of goethitic rims and cortex in kaolinitic matrix of vermiform facies as well as around hematitic nodules of protopisolitic facies. The second diagram of factor scores, F1 versus F3, confirms the results of the Fig. 4, showing different contrasts between the petrological differentiation patterns of the three ferricrete categories. The ferricretes of high plateaux are represented by an hematite–kaolinite pattern, while the protopisolitic and vermiform ferricretes of hillslopes and low plateaux are mainly characterized by a goethite–gibbsite and a goethite–kaolinite pattern respectively (Fig. 8b). In both factorial diagrams, the protopisolitic ferricrete facies define a wide domain ranging from the ferricretes of high plateaux to the vermiform ferricretes of low plateaux.

6. Discussion

Our results document that the differentiation patterns and distribution of ferricretes in the Haut-Mbomou region may be governed by interactions between geomorphic and hydroclimatic processes, once the weathering profiles are sufficiently developed on parent amphibole schists. Although less advanced stages of weathering strongly depend on parent rock type (Leprun, 1979; Zeegers and Leprun, 1979; Matheis, 1981; Ambrosi and Nahon, 1986; Nahon, 1991; Tardy, 1993), the influence of hypothetic lithologic variations on relatively old ferricretes is unlikely in our study area. It has been shown that the iron-richness and evolution degree (i.e., age) of similar ferricretes of West Africa tended to blur parent rock signatures (Tardy et al., 1988a; Boeglin and Mazaltarim, 1989; Roquin et al., 1990). In our field area, the differentiation patterns of ferricretes follow the geomorphic evolution of landscape depending on climatic variations to humid or to dry tendencies. Climatic factors continuously model the landforms, modifying the slope gradients, the biological patterns and drainage conditions in soil profiles, which, in turn, influence the way the ferricretes evolve. The actual climatic conditions favour the petrological transformations of ferricretes wherever the forest grows and the water is seasonally retained on concave surfaces, inviting to consider the

influence of water activity and organic matter in mineralogical patterns of ferricretes (Tardy and Nahon, 1985; Beauvais and Tardy, 1993; Tardy, 1993). The high plateau ferricretes mainly composed of poorly hydrated minerals, hematite and kaolinite, generally do not show such transformations, except the protonodular exhibiting secondary goethitic rim around hematitic nodules or gibbsite within the ferruginous matrices. In contrast, protopisolitic and vermiform ferricretes richer in hydrated minerals gibbsite and goethite, respectively, exhibit further petrological variations. As a fact, the vestiges of massive hematitic facies within the protopisolitic layers of hillslopes indicate pedogenetic and morphogenetic relations between high plateaux and hillslopes. In this way, the ferricretes of high plateaux are older than the other facies, and their petrological patterns may reflect past hydroclimatic conditions, while the facies of hillslopes and low plateaux exhibit mineralogical patterns related to actual geomorphic and climatic conditions. The transformation of hematite into goethite is conditioned by a dissolution–reprecipitation mechanism (Schwertmann and Taylor, 1977), while the transformation of kaolinite into gibbsite obeys to a desilication mechanism. However, these mechanisms depend on both water activity and partial pressure of carbon dioxyde produced by the mineralization of organic matter (Tardy, 1993), such as

$$CHOH + O_2 = CO_2 + H_2O \quad (2)$$

So, the transformation of hematite and kaolinite under both hydration and redox process can be described by the following global reactions

$$\underset{\text{(hematite)}}{Fe_2O_3} + CO_2 + 2H_2O = 2\underset{\text{(goethite)}}{FeOOH} + HCOOH + \tfrac{1}{2}O_2 \quad (3)$$

$$\underset{\text{(kaolinite)}}{Si_2Al_2O_5(OH)_4} + CO_2 + 2H_2O = 2\underset{\text{(gibbsite)}}{Al(OH)_3} + 2SiO_2(aq.) + HCOOH + \tfrac{1}{2}O_2 \quad (4)$$

Both field observations and results support this model, whose the above equations are likely involved in the differentiation patterns of protopisolitic facies, and to a lesser extent, in protonodular of high plateaux. However, the formation of gibbsite in the both facies is further conditioned by a relatively good drainage on plan surfaces located at the edges of high plateaux, and on hillslopes and low plateaux overhanging the valley heads. The petrological patterns of ferricretes developed on the planconvex surfaces of high plateaux further reveal that dehydration and oxydation processes have characterized the ferruginization of kaolinite booklets, by preserving a residual fraction of heavy minerals containing Ti, Zr and Nb, and silicate minerals bearing Sr, La and V. The petrological patterns of vermiform and protopisolitic facies further suggest that local hydrodynamic conditions relative to concave surfaces of low plateaux and hillslopes periodically liable to floodings may also influence the trace element behaviour. Indeed, those landsurfaces exhibit much more concavities than the high plateaux, and they are also covered by termitaria composed of reworked clayey–silty materials undergone to surface erosion processes.

Previous studies carried out in similar environments of West Africa have shown that the termitaria materials contained quartz and heavy minerals as ilmenite and zircon, and

that they have been likely transported upward by termites through connected macropores from underlying mottled and saprolite layers (Eschenbrenner, 1987; Freyssinet, 1990). The vermiform facies exhibiting such connected macropores are potential places for termite activity. In fact, the development of secondary goethite with Mn, Cu, Ni, Zn, Co, Sc, Y and Yb through illuviated clayey matrices of vermiform facies can be enhanced by the presence of organic matter (Kämpf and Schwertmann, 1983; Boski and Herbosch, 1990) yielding hydromorphic conditions, which prevail on concave surfaces of hillslopes and low plateaux (Beauvais, 1991). Both hydrodynamical and hypothetic biophysical processes control redox conditions which determine the trace element behaviour and their relation to lateritic minerals. Thus, this could explain that Ti, Zr and Nb are depleted in protopisolitic and vermiform ferricretes, while Ba, Ce and Co are correlated to Mn-oxyhydroxides. This geochemical association is common in lateritic soils (Taylor, 1968; Childs, 1975) evolving under limited geochemical conditions of Eh and pH (Parc et al., 1989; Braun et al., 1990). However, outside those conditions, Mn is depleted, and a correlation between Ba, Ce, Sr and La appears, reflecting unweathered relics of micas and feldspars.

Therefore, we are inclined to infer that the actual distribution of ferricrete in the Haut-Mbomou region is the result of a long time evolution of complex weathering and geomorphic processes driven by the downward reduction of the regolith along with climatic evolution from past-drier to actual-wetter conditions. In turn, that leads to the progressive disappearance of high plateau ferricretes, and hence, to the loss of parent rock signatures.

7. Conclusion

Our results indicate that the regional distribution of different ferricrete facies developed on tectonically stable cratons reflects the interplay between weathering and erosion processes of thick and old lateritic profiles rather than any variety of parent rocks. Petrological and geomorphological patterns of ferricrete facies as well as the behaviour of trace elements among the different minerals sustain this interpretation revealing that high plateau ferricretes could be the oldest, still preserving some geochemical signature of amphibole schists. If so, the hillslopes and low plateaux ferricrete facies might be younger, deriving from a long time evolution of the landscape under the effects of hydroclimatic and geomorphic changes, that tend to blur the parent rock inheritance. Although we do not deny the role of parent rock in the first stage of development of lateritic weathering profiles, we also believe that variations of climatic and geomorphic processes over several million years may influence both the regional distribution and petrological pattern of many old ferricretes widespread on ancient tropical shields.

Acknowledgements

This work was supported by the "Institut Français de Recherche Scientifique pour le Développement en Coopération" and the research program PIRAT (ORSTOM/INSU-

CNRS). We thank the "Centre de Géochimie de la Surface" at the University of Strasbourg (France) for mineralogical and geochemical analyses. The first author is indebted to the "Laboratoire de Pétrologie de la Surface" at the University of Poitiers for facilities in preparing a previous version of this paper. We also thank Vincent Eschenbrenner and Boris Volkoff for helpful critiques of a manuscript draft. Discussions with Dr. Yves Boulvert are appreciated. Dr. Kroonenberg and Dr. Franzmeier are also acknowledged for their useful critiques on the paper.

References

Ambrosi, J.P. and Nahon, D., 1986. Petrological and geochemical differentiation of lateritic iron crust profiles. Chem. Geol., 57: 371–393.

Beauvais, A., 1991. Paléoclimats et dynamique d'un paysage cuirassé du Centrafrique. Morphologie, Pétrologie et Géochimie. Ph.D. Thesis, Univ. Poitiers, 317 pp. (microfilmed).

Beauvais, A. and Colin, F., 1993. Formation and transformation processes of iron duricrust systems under tropical humid environment. Chem. Geol., 106: 77–101.

Beauvais, A. and Tardy, Y., 1993. Degradation and dismantling of iron crusts under climatic changes in Central Africa. Chem. Geol., 107: 277–280.

Boeglin, J.L. and Mazaltarim, D., 1989. Géochimie, degrés d'évolution et lithodépendance des cuirasses ferrugineuses de la région de Gaoua au Burkina-Faso. Sci. Géol. Bull. Strasbourg, 42: 27–44.

Boski, T. and Herbosch, A., 1990. Trace elements and their relation to the mineral phases in the lateritic bauxites from southeast Guinea Bissau. Chem. Geol., 82: 279–297.

Boulvert, Y., 1976. Type de modelé cuirassé. Intérêt morphopédologique des "lakérés". Finesse, précision de la télédétection. Relations avec le tapis végétal (région de Dembia). Rev. Photo Interprétation, Technip, Paris, Vol. 4, pp. 18–29.

Boulvert, Y., 1986. Carte phytogéographique de la République Centrafricaine à 1/1 000 000. ORSTOM, Paris, Notice Explicative No. 104, 132 pp.

Boulvert, Y., 1996. Etude géomorphologique de la République centrafricaine. Carte à 1/1 000 000 en deux feuilles ouest et est. Thèse Univ., Dijon, Notice Explicative No. 110, ORSTOM, Paris, 259 pp.

Braun, J.J., Pagel, M., Muller, J.P., Bilong, P., Michard, A. and Guillet, B., 1990. Cerium anomalies in lateritic profiles. Geochim. Cosmochim. Acta, 54: 781–795.

Brimhall, G.H. and Dietrich, W.E., 1987. Consecutive mass balance relations between chemical composition, volume, density, porosity, and strain in metasomatic hydrochemical systems: results on weathering and pedogenesis. Geochim. Cosmochim. Acta, 51: 567–587.

Butt, C.R.M., 1987. A basis for geochemical exploration models for tropical terrains. Chem. Geol., 60: 5–16.

Butt, C.R.M. and Zeegers, H., 1989. Classification of geochemical exploration models for tropically weathered terrains. J. Geochem. Explor., 32: 65–74.

Childs, C.W., 1975. Composition of iron–manganese concretions from New-Zealand soils. Geoderma, 13: 141–152.

Colin, F. and Vieillard, P., 1991. Behaviour of gold in the lateritic environment: weathering and surface dispersion of residual gold particles, at Dondo Mobi, Gabon. Appl. Geochem., 6: 279–290.

Colin, F., Brimhall, G.H., Nahon, D., Lewis, C.J., Baronnet, A. and Danti, K., 1992. Equatorial rain forest lateritic mantles: a geomembrane filter. Geology, 20: 523–526.

Davies, T.C. and Bloxham, T.W., 1979. Heavy metal distribution in laterites, southwest of regent, Freetown igneous complex, Sierra Leone. Econ. Geol., 74(3): 638–644.

Delvigne, J., 1965. Pédogenèse en zone tropicale. La formation des minéraux secondaires en milieu ferrallitique. Mém. ORSTOM, Paris, Vol. 13, 177 pp.

Donkin, M.J. and Fey, M.V., 1991. Factor analysis of familiar properties of some Natal soils with potential for afforestation. Geoderma, 48(3/4): 297–304.

Eschenbrenner, V., 1987. Les glébules des sols de Côte d'Ivoire. Thèse ès Sci., Univ. Bourgogne, Dijon, 496 pp. (unpublished).

Franquin, P., Diziain, P., Cointepas, J.P. and Boulvert, Y., 1988. Agroclimatologie du Centrafrique. Coll. Init. Docum. Techniques, ORSTOM, Paris, Vol. 71, 522 pp.

Freyssinet, P., 1990. Géochimie et minéralogie des latérites du sud-Mali. Evolution des paysages et prospection géochimique de l'or. Ph.D. Thesis, Univ. Strasbourg, Mém. B.R.G.M., Orléans, Vol. 203, 269 pp.

Freyssinet, P., Lecomte, P. and Edimo, F., 1989. Dispersion of gold and base metals in the Mborguéné lateritic profile, East Cameroun. J. Geochem. Explor., 31: 99–116.

Kämpf, N. and Schwertmann, U., 1983. Goethite and hematite in climosequence in southern Brazil and their application in classification of kaolinitic soils. Geoderma, 29: 27–41.

Lebart, L., Morineau, A. and Fénélon, J.P., 1979. Traitement des données statistiques. Dunod, Paris, 510 pp.

Lecomte, P. and Colin, F., 1989. Gold dispersion in a tropical rainforest weathering profile at Dondo Mobi, Gabon. J. Geochem. Explor., 34: 285–301.

Leprun, J.C., 1979. Les cuirasses ferrugineuses des pays cristallins de l'Afrique occidentale sèche. Genèse. Transformation. Dégradation. Mém. Sci. Géol. Strasbourg, Vol. 58, 224 pp.

Litaor, M.I., Dan, Y. and Koyumdjisky, H., 1989. Factor analysis of a lithosequence in the northeastern Samaria steppe (Israel). Geoderma, 44: 1–15.

Matheis, G., 1981. Trace element patterns in lateritic soils applied to geochemical exploration. J. Geochem. Explor., 15(1–3): 471–480.

Matheis, G. and Pearson, M.J., 1982. Mineralogy and geochemical dispersion in lateritic soil profiles of northern Nigeria. Chem. Geol., 35: 129–145.

Mazaltarim, D., 1989. Géochimie des cuirasses ferrugineuses et bauxitiques de l'Afrique de l'Ouest et Centrale. Ph.D. Thesis, Univ. Strasbourg, 260 pp. (unpublished).

Mestraud, J.P., 1982. Géologie et ressources minérales de la République Centrafricaine. Etat des connaissances fin 1963. Mém. B.R.G.M., Orléans, Vol. 60, 185 pp.

Millot, G., 1970. Geology of Clays. Springer Verlag, Heidelberg, 429 pp.

Mosser, C., 1980. Etude géochimique de quelques éléments traces dans les argiles des altérations et des sédiments. Sci. Géol. Mém., Strasbourg, Vol. 63, 229 pp.

Nahon, D., 1976. Cuirasses ferrugineuses et encroûtements calcaires au Sénégal occidental et en Mauritanie. Systèmes évolutifs: géochimie, structures, relais et coexistence. Sci. Géol. Mém. Strasbourg, Vol. 44, 232 pp.

Nahon, D., 1986. Evolution of iron crusts in tropical landscapes. In: S.M. Coleman and D.P. Dethier (Editors), Rates of Chemical Weathering of Rock and Minerals. Academic Press, pp. 169–191.

Nahon, D.B., 1991. Introduction to the Petrology of Soils and Chemical Weathering. Wiley, New York, 313 pp.

Nalovic, L., 1977. Recherches géochimiques sur les éléments de transition dans les sols. Etude expérimentale de l'influence des éléments traces sur le comportement du fer et l'évolution des composés ferriques au cours de la pédogenèse. Trav. Doc. ORSTOM, Paris, Vol. 66, 235 pp.

Parc, S., Nahon, D., Tardy, Y. and Vieillard, P., 1989. Estimated solubility products and fields of stability for cryptomelane, nsutite, birnessite and lithiophorite based on natural lateritic weathering sequences. Am. Mineral., 74: 466–475.

Roquin, C., Dandjinou, T., Freyssinet, P. and Pion, J.C., 1989. The correlation between geochemical data and spot satellite imagery of lateritic terrain in Southern Mali. J. Geochem. Explor., 32: 149–168.

Roquin, C., Freyssinet, P., Zeegers, H. and Tardy, Y., 1990. Element distribution patterns in laterites of southern Mali: consequence for geochemical prospecting and mineral exploration. Appl. Geochem., 5: 303–315.

SAS (Statistical Analysis System), 1985. User's Guide: Statistics, Version 5. SAS Inst. Inc., Cary, NC, 956 pp.

Schwertmann, U. and Taylor, R.M., 1977. Iron oxides. in: J.B. Dixon, S.B. Weed, J.A. Kittrick, M.H. Milford and J.L. White (Editors), Minerals in Soil Environments. Soil Science Society of America, Madison, WI, pp. 145–180.

Tardy, Y., 1969. Géochimie des altérations. Etude des arènes et des eaux de quelques massifs cristallins d'Europe et d'Afrique. Mém. Serv. Carte Géol., Als. Lorr., Strasbourg, Vol. 31, 199 pp.

Tardy, Y., 1993. Pétrologie des Latérites et des Sols Tropicaux. Masson, Paris, 535 pp.

Tardy, Y. and Nahon, D., 1985. Geochemistry of laterites, stability of Al-goethite, Al-hematite, and

Fe^{3+}-kaolinite in bauxites and ferricretes: an approach to the mechanism of concretion formation. Am. J. Sci., 285: 865–903.

Tardy, Y., Mazaltarim, D., Boeglin, J.L., Roquin, C., Pion, J.C., Paquet, H. and Millot, G., 1988a. Lithodépendance et homogénéisation de la composition minéralogique et chimique des cuirasses ferrugineuses latéritiques. C.R. Acad. Sci. Paris Sér. II, 307: 1765–1722.

Tardy, Y., Melfi, A.J. and Valeton, I., 1988b. Climats et paleoclimats tropicaux périatlantiques. Rôle des facteurs climatiques et thermodynamiques: température et activité de l'eau sur la répartition et la composition minéralogique des bauxites et des cuirasses ferrugineuses, au Brésil et en Afrique. C.R. Acad. Sci. Paris Sér. II, 306: 289–295.

Tardy, Y., Kolbisek, B. and Paquet, H., 1991. Mineralogical composition and geographical distribution of African and Brazilian periatlantic laterites. The influence of continental drift and tropical paleoclimates during the past 150 million years and implications for India and Australia. J. Afr. Earth Sci., 12(1/2): 283–295.

Taylor, R.M., 1968. The association of Mn and Co in soils. Further observations. J. Soil. Sci., 19: 77–80.

Trescases, J.J., 1975. L'évolution géochimique supergène des roches ultrabasiques en zone tropicale. Formation des gisements nickélifères de Nouvelle-Calédonie. Mém. ORSTOM, Paris, Vol. 78, 259 pp.

Zeegers, H. and Leprun, J.C., 1979. Evolution des concepts en altérologie tropicale et conséquences potentielles pour la prospection géochimique en Afrique occidentale soudano-sahalienne. Bull. B.R.G.M. Orléans, 2(2/3): 222–239.

ARTICLE 2

Pergamon

Geochimica et Cosmochimica Acta, Vol. 63, No. 23/24, pp. 3939–3957, 1999

0016-7037/99 $20.00 + .00

PII S0016-7037(99)00173-8

Geochemical balance of lateritization processes and climatic signatures in weathering pro les overlain by ferricretes in Central Africa

ANICET BEAUVAIS*

IRD, Centre D'Ile de France, Laboratoire des Formations Super cielles, 93143 Bondy Cedex, France

(Received December 23, 1998; *accepted in revised form May* 7, 1999)

Abstract—A simple geochemical balance of lateritization processes governing the development of several tens of meters of weathering pro les overlain by ferricretes is estimated on the basis of detailed mineralogical and geochemical data. The lateritic weathering mantle of the "Haut–Mbomou" area in Central Africa is composed of different weathering layers described from the base to the top of vertical pro les as a saprolite, a mottled clay layer, a soft nodular layer, a soft ferricrete, and a ferricrete in which kaolinite, gibbsite, goethite, and hematite occur in various quantities. Incongruent dissolution of kaolinite leads to the formation of gibbsite in the upper saprolite, whereas the hematite does not clearly replace the kaolinite according to an epigene process in the upper ferruginous layers of the pro les. Instead, that kaolinite is also transformed into gibbsite according to an incongruent dissolution under hydrated and reducing conditions induced by a relatively humid climatic pattern. The respective relations of the silica, iron, and aluminum balances and the Al substitution rate of the hematite on the one hand, and of RHG [RHG = 100 (hematite/hematite + goethite)] and the kaolinite on the other hand, to the consumption or the release of protons H^+ permit differentiation of aggrading ferruginization and degradation processes operating in the different lateritic weathering pro les. The Al substitution rate of the Fe–oxyhydroxides varies according to the nature of lateritization processes, e.g., saprolitic weathering and aggrading ferruginization vs. degradation. The observations and results indicate that the ferruginization process of the weathering materials of parent rocks is not a simple ongoing process as often thought. This suggests that the actual lateritic weathering mantle of the Haut–Mbomou area may result from different stages of weathering and erosion during climatic changes. *Copyright © 1999 Elsevier Science Ltd*

1. INTRODUCTION

On tropical African shields, lateritization processes have led to the development of weathering mantles tens of meters thick, often capped with ferricretes, at the expense of all kinds of parent rocks that may re ect a long and complex evolution, including climatic and geomorphic changes (Nahon, 1991; Tardy, 1993; Thomas, 1994; Tardy and Roquin, 1998). The term *ferricrete* must be understood here as ferruginous duricrust instead of iron-cemented conglomerate. It has been assumed that the underlying weathering mantle developed in situ by progressive dissolution of a previous saprolite without allochthonous iron inputs except intrapro le migrations and accumulations, that led the different layers of a weathering pro le to vertically t together during the vertical downward reduction of the regolith (Millot et al., 1976; Nahon, 1976; 1986; Leprun, 1979; Tardy, 1993). Other research based on geomorphological observations also emphasized the mechanical erosion processes, to account for the formation of many ferricretes armoring glacis or slope pediments of western Africa (Vogt, 1959; Michel, 1973; Grandin, 1976; Boeglin, 1990; Bamba, 1996) and etchplains (Thomas, 1965; 1994). Studies focusing on gold behavior in different regions of the African continent have also described the geochemical and the geomorphic processes controlling the detrital ore concentration patterns (Colin et al., 1989; 1992; 1997; Freyssinet et al., 1989; Lecomte and Colin, 1989; Freyssinet, 1990; Colin and Vieillard, 1991; Sanfo et al., 1993; Parisot et al., 1995; Ouangrawa et al., 1996).

The analysis of the geochemical and mineralogical features of lateritic residual formations can improve our understanding of the weathering and lateritization processes. The Haut–Mbomou area in Central Africa at the edge of the rainforest and savannas appears a key area to de ne various lateritic pro le-forming processes (Fig. 1). The aim of this study is twofold: (1) to describe the mineralogical and geochemical pathways of the lateritic weathering layers from the bottom to the top of pro les (Fig. 2); and (2) to derive geochemical balance and the physicochemical mechanisms of the underlying lateritization processes (i.e., saprolitic weathering and ferruginization), that will put forward an evolution model for the actual lateritic weathering mantle of the Haut–Mbomou area.

1.1. Background

It is known that the crystal chemistry of the kaolinite and Fe–oxyhydroxides of lateritic soils re ects the geochemical and physical properties of the medium in which they formed, i.e., past and present pedogenetic conditions (Fitzpatrick and Schwertmann, 1982; Fitzpatrick, 1983; Schwertmann and Kämpf, 1985; Schwertmann and Carlson, 1994; Muller et al., 1995). For instance, the Al substitution rate and crystal size of Fe–oxyhydroxides depend on Eh–pH conditions (Nahon, 1976; Schwertmann et al., 1979; Tardy and Nahon, 1985); pH in uences the dissolution rate of the kaolinite and its behavior within the weathering pro les (Carroll and Walther, 1990; Chorover and Sposito, 1995). Variations of Al substitution rates of Fe–oxyhydroxides may also re ect different iron accumulation processes (Fitzpatrick, 1983).

After the seminal work of Millot and Bonifas (1955) and Millot (1970) on the isovolumetric textural changes during

* (beauvais@bondy.ird.fr).

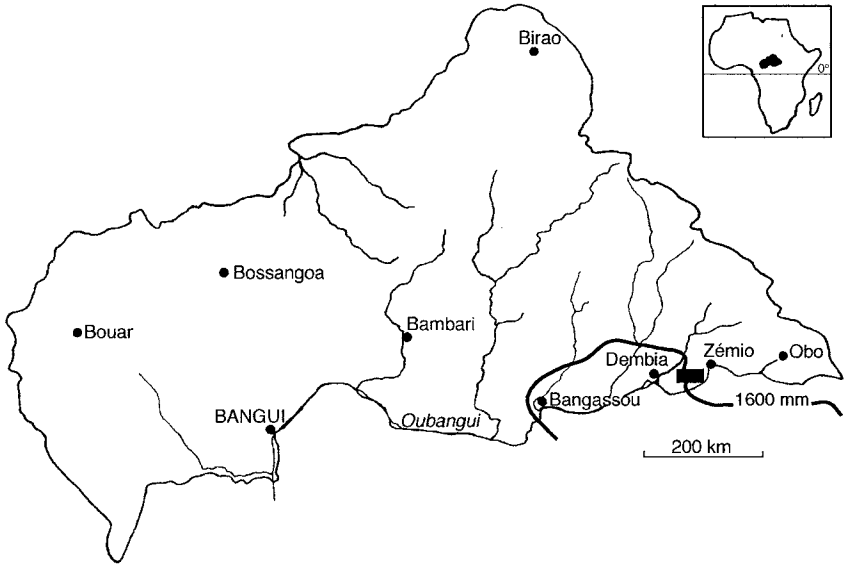

Fig. 1. Location of the study area (black rectangle). The bold curve represents the mean annual rainfall (= 1600 mm).

weathering, Brimhall and Dietrich (1987) formalized a mass balance model relating the chemical composition to the bulk density, volumetric porosity, and strain according to the least mobile element as Zr. However, the correct identi cation of the least mobile element often poses problems because material transfers on hillslope surface with translocations through the pro les and chemical weathering of the element-bearing minerals may invalidate the iso-element method, particularly in the tropical area of Africa (Brimhall et al., 1988; Colin et al., 1992; 1993; Braun et al., 1993). Other models have coupled the stoichiometries of mineral weathering reactions to hydrological and hydrogeochemical data to calculate the mineral weathering rates (Garrels and McKenzie, 1967; Tardy, 1969; Velbel, 1985, 1986). On the basis of the mass transfer principle of Helgeson et al. (1970), Soler and Lasaga (1996) have recently developed a kinetic model to explore the mechanisms of bauxite forma-

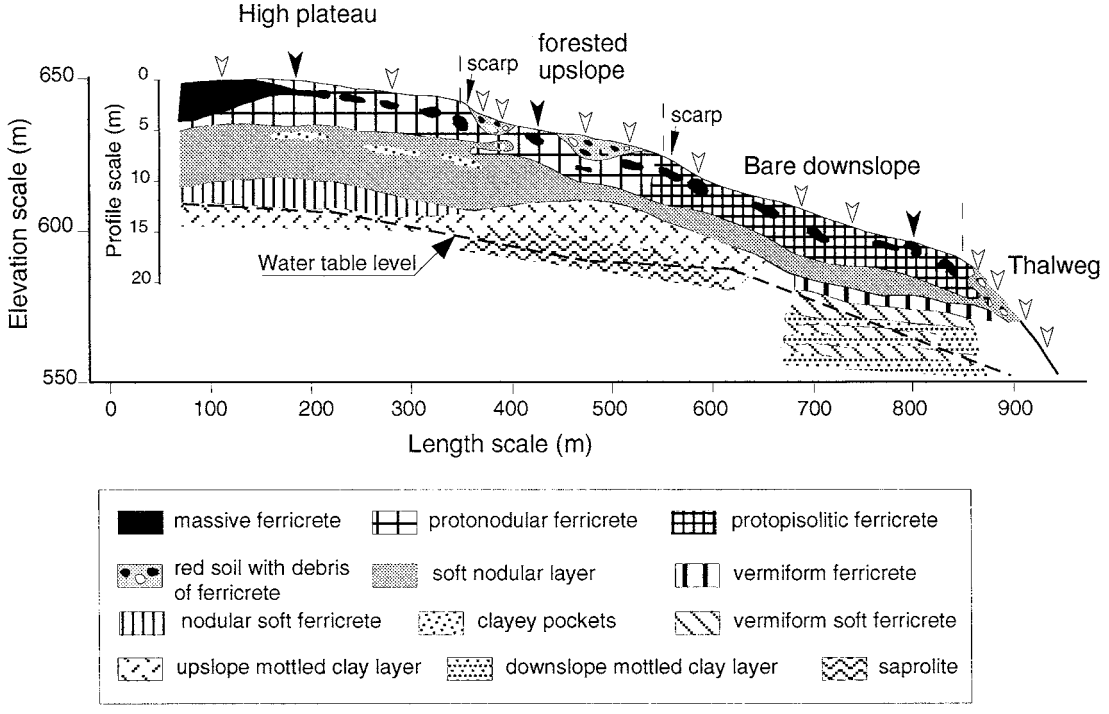

Fig. 2. Sketch of the lateritic weathering toposequence and location of the three analyzed pro les (black arrows; smaller white arrows, other pits).

tion. The validation of the above models by eld observations, however, requires two primary conditions; (1) the availability of a complete weathering pro le from the unweathered parent rock to the topsoil; and (2) geochemical data regarding solutions coming in and getting out of the regolith system. Microprobe analyses of minerals and weathering phases composing the layers of lateritic pro les of western Africa have also proved useful to derive geochemical balances at the scale of mineral assemblages (Ambrosi and Nahon, 1986). A geochemical balance is derived in a similar way but at the scale of the pro les by coupling the results obtained from the bulk chemistry and mineralogy of weathering layers (Beauvais, 1991) and the microprobe analyses of each mineral component.

2. MATERIALS AND METHODS

The study area is located in the "Haut–Mbomou," southeastern Central African Republic (Fig. 1). Plateaus and hillslopes ranging from 650 to 600 m above mean sea level (a.s.l.) are deeply dissected by thalwegs to 570 m a.s.l.—all are covered by a thick lateritic weathering mantle overlain by ferricretes. The geological basement corresponds to the Birrimian Amphibolitic–Pyroxenitic "Complex of Mbomou", which has been tectonically quiet for ~70 My. (Mestraud, 1982; Poidevin, 1991). The humid tropical climate is characterized by a dry season from December to February, a mean annual rainfall of 1600 mm (Fig. 1), a mean annual temperature of 25°C, and a mean annual relative humidity of 80%. The vegetation cover consists of large stretches of grass and bare lands alternating on the plateaus and the hillslopes and by a dense humid forest occupying the valleys and the edges of the highest plateaus.

Sixteen pits were bored through thick lateritic weathering pro les uniformly covered by 3 to 10 m of soft ferricrete and actual ferricrete materials of various petrographic facies depending on the topographic location of the pro le, because the sequence of pits extends across 1 km half drainage divide from a high plateau to a thalweg (Fig. 2). Two scarps of metric height resulting from mechanical erosion processes separate the sequence in three geomorphological units, the high plateau, the forested upslope, and the bare downslope (Fig. 2). The identi cation of parent rocks was impeded either by water occurrences, or by stinking gaseous emanations for the pro les located in the upslope forested area. Methane was detected by smelling, whereas carbon dioxide was identi ed by observing the end of a blazing rope ame up and down when it was shook up and down in the boreholes. However, the compared observations of saprolites in some pits and of rock fragments collected on plateau surfaces and/or thalweg ats indicate an amphibole–schist facies as the most likely parent rock.

2.1. X-ray Diffraction (XRD) and Crystallo-chemical Parameter Calculation

Samples for XRD were sorted and ground, producing a powder with a sieve size of 125 μm. XRD analyses were performed over the range 2 to 80° 2θ using a Cu–Kα radiation, a step size of 1° 2θ/min, and a counting time of 5 s to quickly identify the mineral components of each weathering facies. High-resolution XRD analyses were also made on quasi-pure Fe–oxyhydroxides to calculate their unit-cell parameters by the mean of a statistical re nement program by nonlinear regression (Tournarie, 1969) and to estimate their Al substitution ratios (Schulze, 1982). A Co–Kα radiation was employed over a range 2 to 80° 2θ with a step size of 0.04° 2θ/min and a counting time of 10 s or 20 s with quartz as a standard for adjusting the re ection peaks. The re ections used for all goethite samples were 020, 110, 130, 021, 111, 121, 140, 221, 240, 160, 002, and 061, whereas 012, 104, 110, 113, 024, 116, 214, and 300 re ections were used for the hematite, and even more when further suitable re ections were available. The unit-cell parameters of the Fe–oxyhydroxides may also allow to specify the lateritic weathering processes involved.

The Al substitution of goethites was estimated by a method based on the linear relationship between the unit-cell edge length c for synthetic goethites and different Al substitution rate (Schulze, 1982; 1984; Gerth, 1990). The unit-cell parameter c is estimated using the (hkl) re ections (110) and (111) as,

$$c = \left(\frac{1}{d^2\,(111)} - \frac{1}{d^2\,(110)} \right)^{-1/2} \quad (1)$$

(Norrish and Taylor, 1961; Schulze, 1982). Then, the percentage of mole of AlOOH was calculated from

$$\text{mol\% AlOOH} = 1730 - 572\,c, \quad (2)$$

(Schulze, 1984), which can be used to estimate the Al substitution rate of tropical goethites (Schwertmann and Carlson, 1994).

The Al substitution of hematites was estimated using a correlation between the variations of the unit-cell dimension a and the Al substitution rate for hematite that was empirically demonstrated by,

$$\text{mol\% } Al_2O_3 = 3109 - 617.1\,a, \quad (3)$$

with a estimated from the reticular dimensions $d_{(110)}$ and $d_{(300)}$ (Schwertmann and Kämpf, 1985).

2.2. Microprobe Analysis

Thin sections of each facies including parent rocks were observed using an optical microscope, which allowed to rst describe the texture of minerals and weathering plasmas and then to prepare for their chemical analysis using a microprobe. Scanning electron microscope (SEM) was useful to de ne their crystalline morphology. Microprobe analyses were performed using a Cameca SX-50 analyser. The detection thresholds of the microprobe analyser are ≤50 ppm for the transition elements (Fe, Mn, Cr, and Cu) and ~100 ppm for the other elements (Si, Al, Mg, Ca, Na, K, Ti, P, Ba, Zr, La, and Ce). Only the mean signi cant amounts of some trace elements will be given. The results were used for normative calculation of each mineral in the weathering plasmas, which generally appear as phase mixtures of kaolinite, Fe–oxyhydroxides, and gibbsite but without other minerals. The normative calculation used the number of moles of SiO_2, Al_2O_3, and Fe_2O_3 to estimate the mole percentage fraction (mol%) of minerals (Ambrosi, 1984; Ambrosi and Nahon, 1986; Beauvais, 1991). The Fe substitution ratio of the kaolinite and the Al substitution rates of the Fe–oxyhydroxides were also calculated. If $Al_{(total)} > Si_{(total)}$, the excess of aluminum is incorporated into the hematite or the goethite, the remaining aluminum going to the gibbsite. When $Al_{(total)} < Si_{(total)}$ the excess of silicon means either the incorporation of iron into the kaolinite or free silica.

3. RESULTS AND DISCUSSION

3.1. Parent Rock Petrology

The main minerals of the amphibole–schist parent rock are green hornblendes, plagioclases, and micas as phengites, with secondary minerals as chlorites, epidotes, and garnets, and a little quartz. A summary of their petrographical outlines and an estimation of their mean chemical formula based on at least 5 microprobe analyses for each are given (Fig. 3).

Green hornblendes exhibit prismatic crystals or elongated plate forms. Their composition allows classi cation of them between the actual hornblende, edenite, and pargasite poles according to Deer et al. (1963), but some samples are also close to the tremolite type. Two different types of hornblende were observed: large primary magmatic crystals of actual green hornblende and smaller crystals exhibiting "tooth comb" habit re ecting uralitization process of primary pyroxenes. The mean chemical composition of actual green hornblende is $(Si_{6.36}\ Al_{1.64})\ (Al_{1.07}\ Ti_{0.07}\ Mg_{2.0}\ Fe_{1.86})\ (Fe_{0.075}\ Mn_{0.02}\ Ca_{1.74}\ Na_{0.16})\ Na_{0.52}\ K_{0.1}\ O_{22}\ (OH)_2$, which is an intermediary composition between hornblende and magnesian hastingsite (Leake, 1978). In contrast, the mean chemical composition of

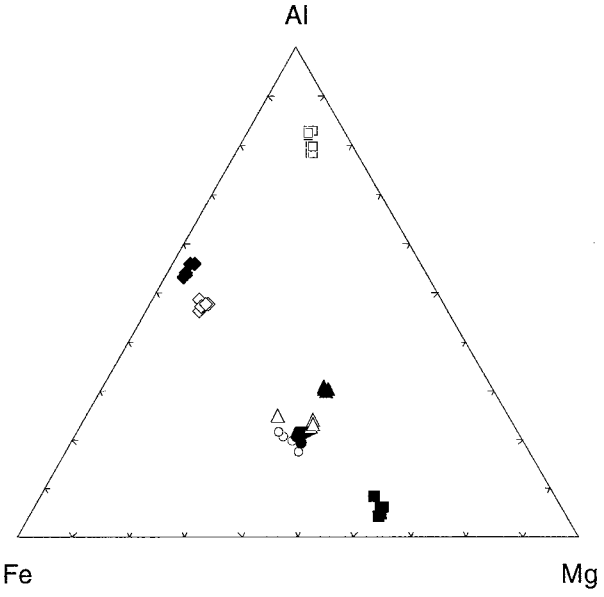

Fig. 3. Geochemical composition of parent rock minerals in an Al–Mg–Fe ternary diagram (black circles, green hornblende; white circles, amphibole from pyroxene uralitization; black squares, actinolite; white squares, phengite; black triangles, chlorite from mica weathering; white triangles, brunsvigite type chlorite; white diamonds, garnet; black diamonds, weathered garnet).

amphibole produced from uralitization of pyroxenes is $(Si_{6.74}\ Al_{1.26})\ (Al_{0.99}\ Ti_{0.03}\ Mg_{1.96}\ Fe_{2.02})\ (Fe_{0.08}\ Mn_{0.03}\ Ca_{1.72}\ Na_{0.17})\ Na_{0.3}\ K_{0.08}\ O_{22}\ (OH)_2$, indicating a ferrous edenite-type hornblende according to Leake (1978). Actinolite was also analysed in a early weathered amphibole–schist. It is less aluminous and less ferriferous but more magnesian than the other amphibole types; its mean structural formula is $(Si_{7.68}\ Al_{0.32})\ (Al_{0.32}\ Ti_{0.04}\ Cr_{0.02}\ Mg_{3.05}\ Fe_{1.57})\ (Fe_{0.05}\ Mn_{0.03}\ Ca_{1.79}\ Na_{0.13})\ Na_{0.05}\ K_{0.01}\ O_{22}\ (OH)_2$ (Fig. 3).

Plagioclases are often saussuritized and form large areas associated with green hornblendes. Their mean formula was calculated as $(Si_{2.97}\ Al_{0.03})\ (Al_{0.98}\ Fe_{0.02})\ Ca_{0.01}\ Na_{1.04}\ O_8$, indicating an albite type.

Micas are fairly well represented in the amphibole–schist rock, exhibiting small plates of 50 to 150 μm. There are phengite-type white micas with a mean structural formula of $(Si_{6.55}\ Al_{1.45})\ (Al_{3.3}\ Ti_{0.03}\ Fe_{0.29}\ Mg_{0.38})\ Mg_{0.11}\ Na_{0.13}\ K_{1.71}\ Ba_{0.03}\ O_{20}\ (OH)_4$.

Chlorites generally result from mica weathering. Their mean chemical composition indicates a diabantite type (Foster, 1962) as is shown by the mean structural formula, $(Si_{6.68}\ Al_{1.32})\ (Al_{3.27}\ Ti_{0.02}\ Fe_{3.22}\ Mg_{4.31}\ Mn_{0.03})\ Ca_{0.07}\ K_{0.22}\ O_{20}\ (OH)_{16}$ (Fig. 3). Other chlorite exhibit curved slats, radially growing and forming typical aggregates in unweathered rock sample. Those are more ferrous and magnesian but less siliceous, close to a brunsvigite type (Foster, 1962) as shown by the mean structural formula $(Si_{5.57}\ Al_{2.43})\ (Al_{2.79}\ Ti_{0.01}\ Fe_{4.35}\ Mg_{4.62}\ Mn_{0.03})\ Ca_{0.01}\ K_{0.01}\ O_{20}\ (OH)_{16}$.

Epidotes appear either as automorphous crystals or resulting from saussuritization process of plagioclases. The mean chemical composition of automorphous epidote crystals is $Si_{3.04}\ (Al_{2.41}\ Ti_{0.01}\ Fe_{0.54})\ Mn_{0.01}\ Mg_{0.01}\ Ca_{1.98}\ O_{12}\ (OH)$, whereas that of the epidote resulting from the saussuritization of the plagioclases is $Si_{3.07}\ (Al_{2.58}\ Ti_{0.01}\ Fe_{0.36}\ Mg_{0.01}\ Mn_{0.01})\ Ca_{1.93}\ O_{12}\ (OH)$.

Garnets are present as automorphous hexagonal porphyroblasts with cross-sections of 2 to 3 mm, cutting across the association amphibole–plagioclase–micas. Their chemical analyses indicate an intermediary composition between almandine (60%), grossular (19%), pyrope (13%), and spessartine (8%) as shown by the mean structural formula $Si_{3.03}\ (Al_{1.97}Ti_{0.01})\ (Fe_{1.79}\ Mg_{0.4}\ Ca_{0.57}\ Mn_{0.23})\ O_{12}$. When the amphibole–schist rock starts to weather, the above mean composition changes to $Si_{3.09}\ (Al_{1.97}Ti_{0.01})\ (Fe_{1.51}\ Mg_{0.12}\ Ca_{0.88}\ Mn_{0.34})\ O_{12}$ (Fig. 3). Besides being more hydrated, the weathered garnets become richer in calcium (31% grossular) and in manganese (12% spessartine) whereas they have less ferrous (53% almandine) and less magnesian (4% pyrope).

3.2. Petrology of Lateritic Weathering Pro les

Field observations revealed ve different layers in the pro les; a saprolite, a mottled clay layer, a soft ferricrete and/or a soft nodular layer, and a ferricrete, the thickness of which spatially varies (Fig. 2). According to the nomenclature established by Tardy (1993), four distinct ferricrete facies were identi ed depending on the geomorphic location; massive and protonodular on the high plateaus and the forested upslopes, protopisolitic and vermiform on the bare downslopes (Beauvais, 1991; Beauvais and Roquin, 1996). The mineralogical and geochemical features of each layer, their variations from the bottom to the top of pro les of the high plateau and the hillslope are described (Fig. 2).

3.2.1. High plateau pro le

Only three layers were identi ed in the pro le of the high plateau. The top of a mottled clay layer occurs at 10 to 12 m, the lower part being underwater, overlain by $\sim$7 m of soft nodular layer and 3 to 4 m of ferricrete with a massive and/or a protonodular facies (Fig. 2).

The soft nodular layer consists of centimetric-size purple reddish nodules embedded in a ne clay–ferruginous matrix with aggregates of 3 to 5 mm. Microscopic observations reveal a red–yellow micronodular matrix structure with micronodules of approximately 50 to 100 μm. On average, it is composed of 18% kaolinite, 44% gibbsite, and 38% goethite substituted by 13 to 19 mol% AlOOH as estimated by the method of Schulze (1984). Additionally, this matrix contains 1.5% TiO_2, 0.14% P_2O_5, and 0.1% CuO, and it is richer in alumina than the ferruginous plasma composing the embedded nodules (Fig. 4A). The richness in alumina is mostly re ected by gibbsite crystallizations forming either from Al absolute accumulation in voids or from incongruent dissolution of kaolinite within the weathering plasmas in which the SEM morphology (Fig. 5A and B) recall what was previously observed in Cameroonese lateritic pro les by Muller (1987). Two types of nodules were distinguished, elongated and round polyhedric. Viewed at the optical microscope, the elongated nodules are composed of numerous kaolinite "booklets" of 10 to 20 μm embedded in a red hematitic plasma, making them appear ferruginized (Fig. 6). In fact, further SEM observations reveal that the hematite

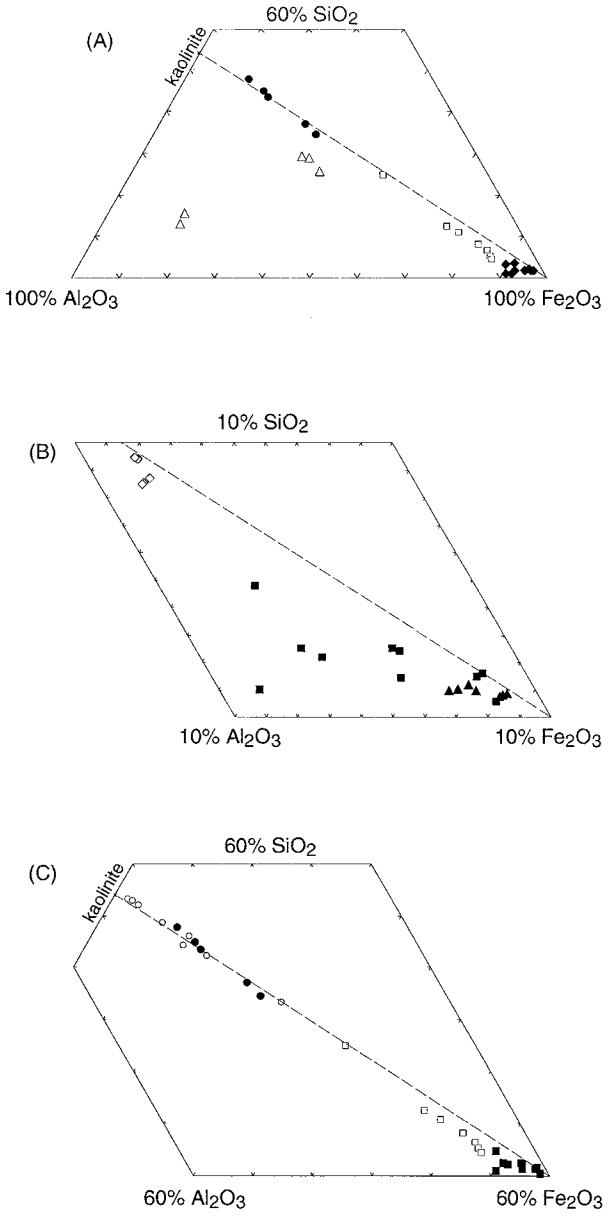

Fig. 4. Geochemical composition of the weathering minerals and plasmas in the different layers of the high plateau pro le in SiO_2–Al_2O_3–Fe_2O_3 ternary diagrams (soft nodular layer analyses in (A) and (C): white triangles, micronodular matrix; black circles, kaolinite of "booklets" in nodules; white squares, hematite of "booklets" in nodules; black diamonds, goethite of cortexes around nodule; ferricrete analyses in (B) and (C): white diamonds, goethite of matrix; black triangles, hematite of matrix; white circles, kaolinite of "booklets"; black squares, hematite of kaolinite "booklets").

does not simply replace kaolinite through epigene processes. Instead, it develops by epitaxy either on (001) plans parallel to *c*-axis of kaolinite "booklets" packing, or it exhibits round "almond" habits of 2-μm diameter on (hk0) plans (Fig. 5C and D). Microprobe analyses reveal that TiO_2 and P_2O_5 increase with increasing ferruginization, and a mean Al substitution of 2.4 mol% Al_2O_3 for the hematite, although the calculation from the unit-cell dimensions $a = 5.04 \pm 0.001$ Å and $c = 13.8 \pm 0.003$ Å does not show any Al substitution when applying equation (3). Even the apparently pure kaolinite "booklets" display some quantity of hematite (Fig. 4A), that is no wonder as the volume analysed by the microbeam equals 1 μm^3, a size similar to that of the hematite spots (Fig. 5C and D). In round polyhedric nodules, hematite is mixed with small size kaolinite of 1 μm (Fig. 5E), which may result from the dissolution–precipitation process of previous kaolinite booklets (Ambrosi and Nahon, 1986). These nodules consist of a mixture of hematite and goethite, as it was observed under re ected light optical microscopy, the goethite spots appearing gray while the hematite is white. Additionally, secondary goethite is developed as rims and cortexes around the two types of nodules. That goethite is substituted by 10 mol% AlOOH, as estimated from microprobe analyses. It also contains 0.17% Mn_2O_3, 0.2% CuO, and 0.26% P_2O_5, and it is more ferruginous than the hematite of the kaolinite "booklets" composing the core of the elongated nodules (Fig. 4A). At the bottom of the soft nodular layer, a nodular soft ferricrete facies was forming by iron absolute accumulation as re ected by secondary goethite crystals growing perpendicularly to the void edges or developing around the primary hematitic nodular domains (Fig. 5F). The unit-cell dimensions of that goethite are $a = 4.53 \pm 0.002$ Å, $b = 9.76 \pm 0.003$ Å, and $c = 2.97 \pm 0.001$ Å, implying an Al substitution of approximately 27 mol% AlOOH according to Eqn. 2. Further, the lower part of the soft nodular layer is also a place for a mineral paragenesis made up of lithiophorite and cerianite (Fig. 7A and B), that re ects speci c redox conditions (Parc et al., 1989; Braun et al., 1990). Higher in the soft nodular layer at the transition with the ferricrete, is a level characterized by very hydrated clayey pockets with few nodules, that was previously interpreted as an iron-depleted facies (Beauvais, 1991). This layer is composed of 64% kaolinite, 20% goethite substituted by 16 mol% AlOOH, and 16% hematite substituted by 9 mol% Al_2O_3.

The ferricrete of massive and/or protonodular facies mainly consists of intimately mixed ferruginous and clay plasmas composed of hematite and kaolinite. SEM observations reveal "cauli ower" habits for the hematitic plasma, which coats inherited primary or neoformed oriented kaolinite platelets of 1 to 2 μm (Fig. 8A and B), that recalls what was seen in the round polyedric nodules of the underlying layer. This ferruginous plasma is indeed composed of 99% hematite substituted by 1.5 mol% Al_2O_3 (Fig. 4B), and 0.19% TiO_2, 0.23% P_2O_5, and 0.11% CuO. The unit-cell dimensions of that hematite are $a = 5.11 \pm 0.001$ Å and $c = 14 \pm 0.004$ Å. The kaolinite of "booklets" is, on average, substituted by 2.4 mol% Fe_2O_3. It exhibits primary mineral habits looking like micas (Fig. 8A), which is consistent with the fact it still contains small quantities of alkalis and alkaline–earths, indicating some inheritance of a previous saprolitic material. Some kaolinite "booklets" exhibit an excess of alumina due to gibbsite crystallizations; they also contain less iron than those of elongated nodules of the soft nodular layer (Fig. 4C). The hematite associated with that kaolinite (Fig. 8A) exhibits an Al substitution higher than that contained into the elongated nodules of the underlying soft nodular layer; it is also more Al substituted than that associated with neoformed small-size kaolinite (Fig. 8B); on average, it is substituted by 4.2 mol% Al_2O_3, against 2.4 and 1.5, respectively (Fig. 4B and C). Further, that hematite also contain

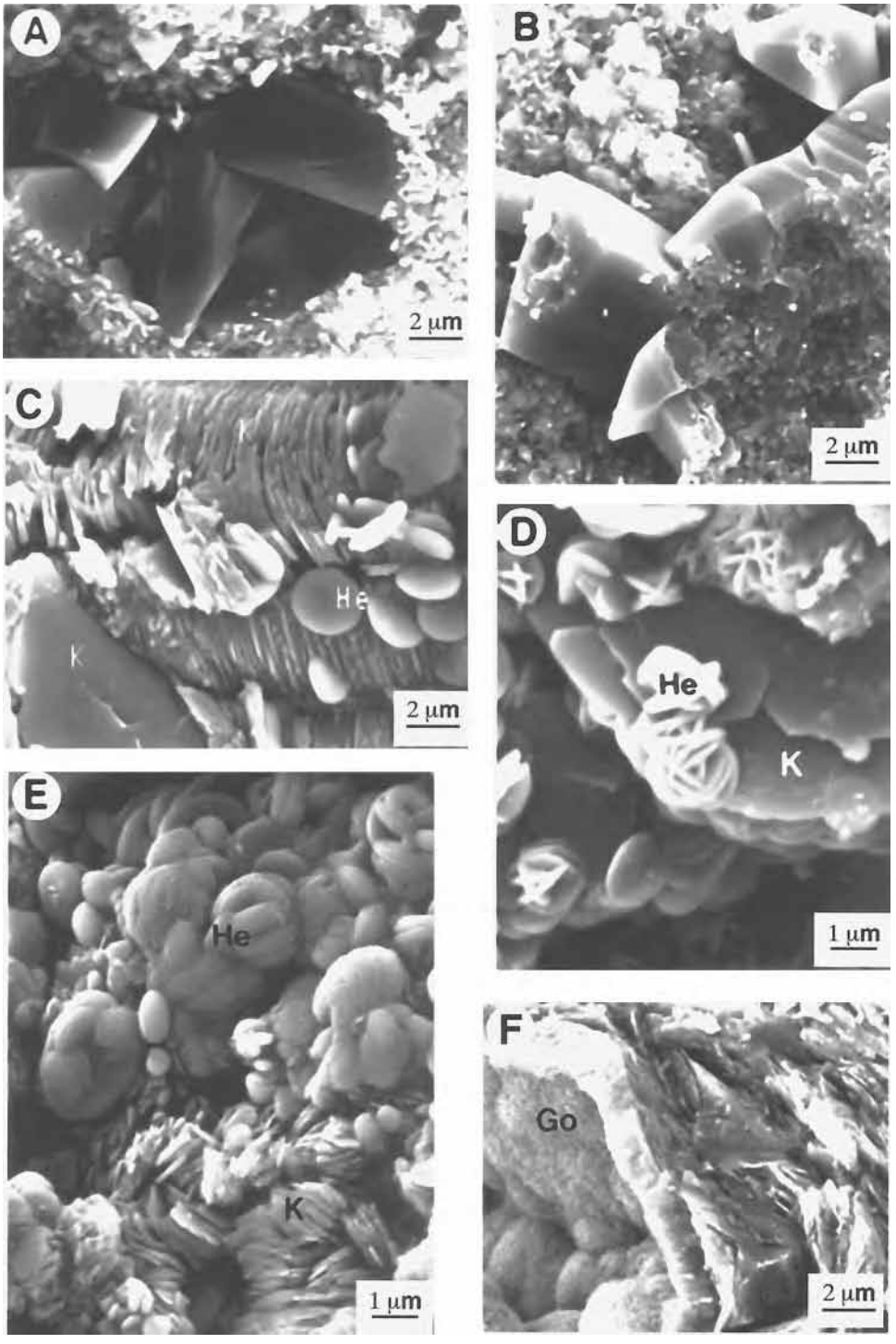

Fig. 5. SEM photomicrographs in the soft nodular layer of a high plateau pro le: (A) Secondary gibbsite crystal development in voids of the clay ferruginous matrix. (B) Gibbsite crystal formed from the incongruent dissolution of kaolinite. (C) Hematite crystals that exhibit either an “almond” habit of 2 mm with an epitaxic development on (001) plans of kaolinite “booklets,” or (D) a “rosette” habit on (110) plans of kaolinite platelets, both in an elongated nodule. (E) Hematite with small size kaolinite in a round polyhedric nodule. (F) Cutan of goethite developing perpendicularly to the void edges in an elongated nodule. (He, hematite crystals; K, kaolinite platelets; Go, goethitic cutan).

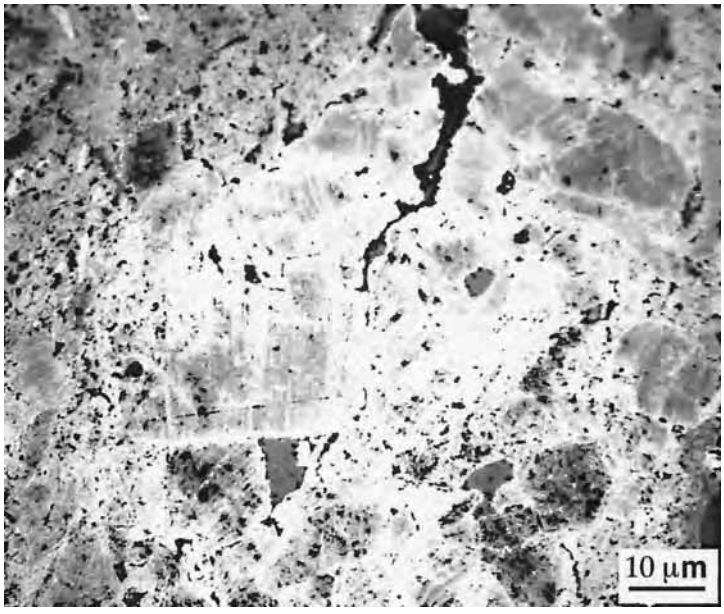

Fig. 6. Optical photomicrograph of kaolinite "booklets" in light gray and hematite in white embedded in the clay ferruginous matrix of an elongated nodule of the soft nodular layer of high plateau pro le.

0.23% TiO_2, 0.1% Cr_2O_3, 0.17% CuO, and 0.5% P_2O_5. Gibbsite crystals and secondary goethitic plasmas were also observed within vacuolar voids of 10 μm affecting the clay–ferruginous plasmas (Fig. 8C). In addition to developing through the porosity, secondary goethite also coats primary inherited kaolinitic structures (Fig. 8D). Microprobe analyses of this goethite reveal mean amounts of 1.61% TiO_2, 0.1% Cr_2O_3, 0.21% Ce_2O_3, and 0.23% P_2O_5. Its unit-cell dimensions are $a = 4.56 \pm 0.009$ Å, $b = 9.93 \pm 0.002$ Å, and $c = 3.01 \pm 0.007$ Å, implying a substitution of ~22 mol% AlOOH.

In summary, the geochemical patterns of the high plateau pro les are governed by the association of kaolinite and Fe–oxyhydroxides in all structures. SEM observations show that the kaolinite is not clearly ferruginized by the hematite according to an epigene process as it was described in other pro les of western Africa (Ambrosi et al., 1986); instead, the two minerals appear closely associated. Aluminum is segregated, leading to gibbsite formation in the micronodular plasmas of the matrix embedding the ferruginous nodules. To a certain degree the kaolinite–gibbsite mineralogy controls the Al substitution of Fe–oxyhydroxides. The secondary goethite of cortexes developed around the nodules is less Al substituted than the goethite neoforming at the bottom of the soft nodular layer. Hematite and secondary goethite of ferricrete are more Al substituted than those of the soft nodular layer.

3.2.2. Hillslope pro les

Five layers were identi ed in the pro les of the hillslope (Fig. 2); in the upslope pro le, a saprolite occurring at 10 to 12 m, ~4 m of mottled clay layer, ~3 to 5 m of soft nodular layer and ~3.5 m of protonodular ferricrete; in the downslope pro le, a mottled clay layer occurring at ~11 m, ~8 m of soft ferricrete layer with a vermiform facies, 1 to 2 m of soft nodular layer, and ~3 m of protopisolitic ferricrete. It is worth mentioning that the ferricrete layer contains some decimetric size relics of massive ferricrete similar to that described in the high plateau pro le.

The saprolite of the upslope pro le consists of a clayey plasma composed of 95% kaolinite substituted by 2 mol% Fe_2O_3 and 5% SiO_2 as relic quartz. This plasma exhibits small-size kaolinite (≤ 2 μm) and kaolinite "booklets" of 50 to 100 μm; it also contains 0.1% MgO, 0.1% CaO, and trace of Mn and Cu (0.07% for each), which likely re ects the pseudomorphic weathering of amphiboles, micas, and chlorites by kaolinite (Fig. 9A). The clayey plasma is mixed with a diffuse ferruginous plasma composed of 83% goethite substituted by 15 mol% AlOOH, 15% gibbsite, and 2% kaolinite (Fig. 10). Additionally, this goethitic plasma contains 0.75% P_2O_5, 0.14% Ce_2O_3, and 0.91% TiO_2. Higher in the layer, the clayey plasma is transformed into plasmas made up of halloysite and gibbsite (Fig. 9B and C). This latter contains minor silicon and iron (Fig. 10), and potassium and barium, which indicates it may also derive from the late weathering of phengites. In addition, a secondary gibbsite is associated with Al–goethite in sites where relic micas are still present (Fig. 9D); it invades all the previous kaolinite–goethite matrices (Fig. 9E). This gibbsite is much less siliceous and less ferruginous than the rst one (Fig. 10). Al substitution of the goethite derived from microprobe analyses is ~20 mol% AlOOH.

The mottled clay layer exhibits various petrographic organizations. In the upslope pro le, the bottom layer is a "patchwork" of a red goethitic plasma in which gibbsitic microdomains are differentiated, a white ocherous clayey plasma with large kaolinite "booklets" inherited from the saprolite, and a brown–orange pedoturbed plasma composed of kaolinite and goethite. The ferruginous plasma of the upslope layer consists of 86% goethite, 13% gibbsite, and only 2% kaolinite (Fig. 10). It also contains 0.48% TiO_2, 0.41% P_2O_5, and 0.1% CuO.

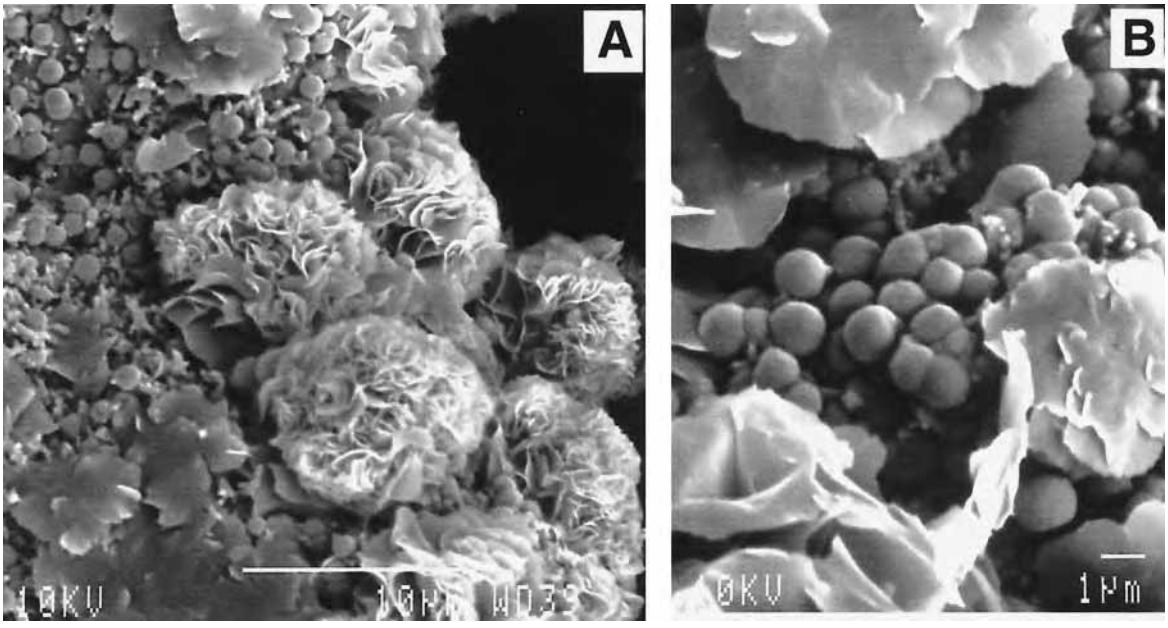

Fig. 7. SEM photomicrographs at the bottom of the soft nodular layer: (A) paragenesis of intertwinned akes of lithiophorite and round "pills" of cerianite. (B) details of the two habits.

Goethite is substituted by 12 mol% AlOOH according to the Eqn. 2, which is a little lower than the substitution derived from the microprobe analyses; this may likely account for a little gibbsite because it is little different from that of the saprolite (Fig. 10). In the downslope pro le, the mottled clay is mainly composed of a gray–white clayey plasma in which a brown–orange ferruginous plasma differentiates. The clayey plasma consists of 70% kaolinite substituted by 3 mol% Fe_2O_3, and 30% goethite (Fig. 11A). Besides exhibiting an excess of silica, it also contains 1.27% Na_2O, 3.14% MgO, and 0.25% CaO, which re ects some relic felspars and epidotes. The ferruginous plasma is composed of 75% goethite substituted by 17 mol% AlOOH and 25% pure kaolinite (Fig. 11A). It also contains 1.4% TiO_2, 0.2% Cr_2O_3, 0.22% P_2O_5, and 0.13% CuO. The Al substitution of the goethite calculated from microprobe analyses is similar to that estimated from Eqn. 2, which ranges from 13 to 19 mol% AlOOH. Although the hematitic domains are not well developed in this layer, a thorough microscopic analysis has revealed hematite substituted by 8 mol% Al_2O_3 (Fig. 11B) and containing 0.35% Cr_2O_3 and 0.15% La_2O_3. Secondary goethite, however, develops at the periphery of these hematitic domains as well as in vacuolar pores; it is only substituted by 6 mol% AlOOH (Fig. 11B) and contains 0.6% P_2O_5 and 0.3% CuO.

The soft ferricrete and ferricrete with a vermiform facies are only developed in the downslope pro le. Both consist of an isotropic brown plasma in which some anisotropic orange spots are differentiated. The vermiform soft ferricrete is crossed by numerous tubular voids of centimetric size that are lled by a gray–white crypto–crystalline clayey plasma in which many ferri–argilans are differentiated, which may indicate clay illuviation processes. Goethite dominates over the hematite, and its Al substitution ranges from 1 to 7 mol% AlOOH (Fig. 11A). Hematitic nodules are rare and only located higher in the vermiform ferricrete at the transition with the soft nodular layer. They are isolated within the goethitic plasma and often surrounded by secondary goethite whose the unit-cell dimensions are $a = 4.62 \pm 0.002$ Å, $b = 9.95 \pm 0.004$ Å, and $c = 3.04 \pm 0.001$ Å. Hematite is substituted by 6 mol% Al_2O_3 whereas secondary goethite is substituted by about 12 mol% AlOOH (Fig. 11B).

The soft nodular layer consists of nodules whose the edges are jagged. As in the high plateau pro le they exhibit an hematitic core outlined by a goethitic rim. No microprobe analyses have been done on weathering plasmas and minerals composing the matrix and nodules of this layer. On average, it is made up of 40% kaolinite, 35% goethite substituted by 12 mol% AlOOH, 15% hematite substituted by 4 mol% Al_2O_3, and 10% gibbsite (Beauvais, 1991).

The protonodular and protopisolitic ferricretes of the hillslope pro les consist of hematitic nodules surrounded by goethitic rims embedded in an indurated clay ferruginous matrix whose the porosity is lled by secondary gibbsite crystals larger than 10 μm (Fig. 12A and B). The matrix of the protopisolitic ferricrete of the downslope pro le indeed corresponds to a plasma made up of only 6% kaolinite, 42% goethite, and 52% gibbsite (Fig. 13A) and it also contains 2.53% TiO_2, 0.15% La_2O_3, and 0.29% P_2O_5. The primary goethite of the matrix is substituted by 15 mol% AlOOH, whereas the secondary goethite developing around the nodules is substituted by approximately 8 mol% AlOOH (Fig. 13B). It also contains 0.23% P_2O_5 and 0.1% CuO. The hematite exhibits two different morphologies: it is either associated with kaolinite or it develops across the primary structure as secondary crystallizations exhibiting "cauli ower" habits (Fig. 12C). This hematite is less aluminous than that associated with the kaolinite of the protonodular ferricrete in the upslope pro les (1 mol% Al_2O_3 instead of 4.4) (Figs. 10 and 13B); its unit-cell dimensions are $a = 5.098 \pm 0.003$ Å and $c = 13.922 \pm 0.007$ Å. The kaolinite "booklets" of the protonodular ferricrete of the upslope pro le

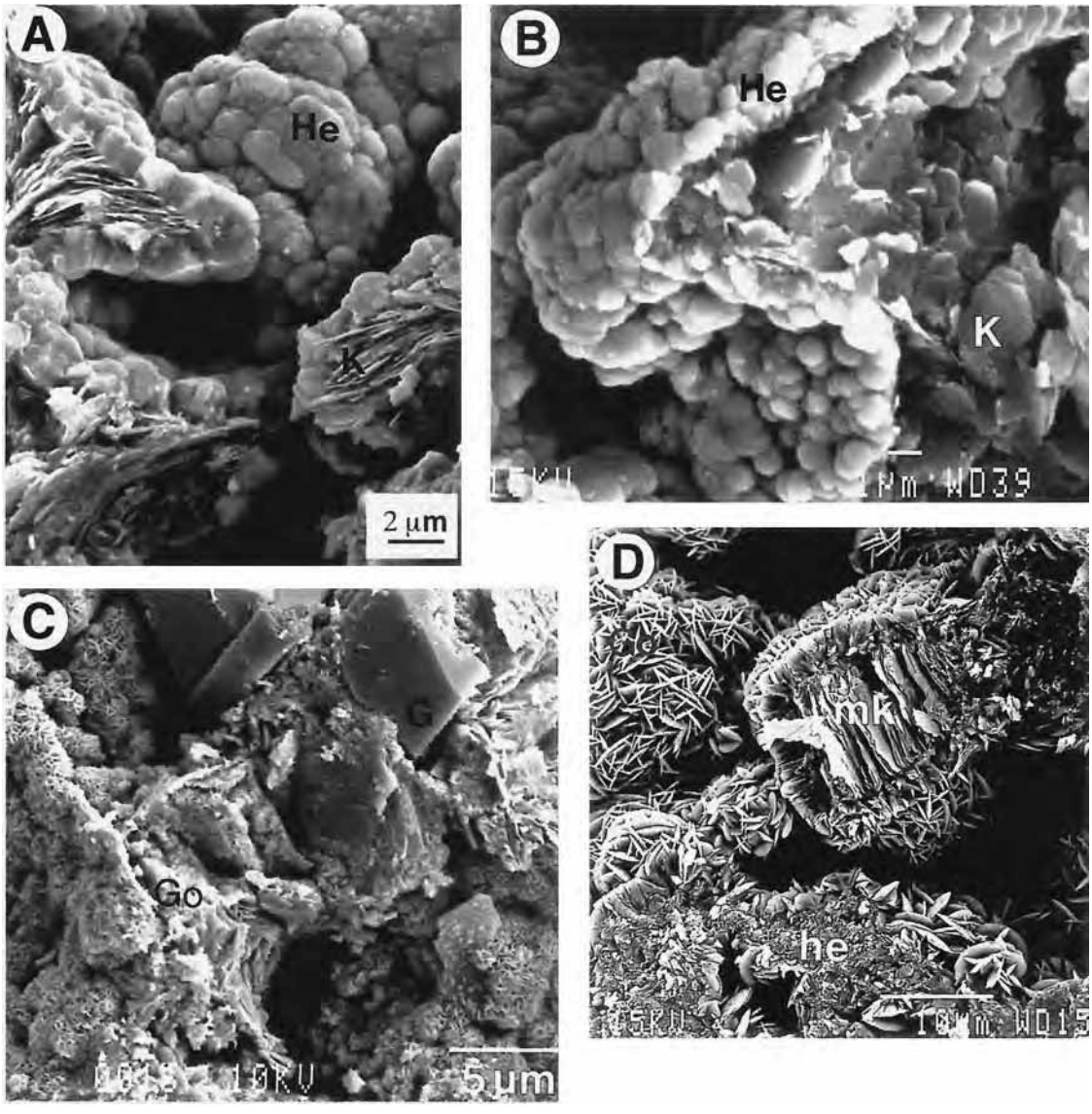

Fig. 8. SEM photomicrographs in the ferricrete of the high plateau pro le: (A) and (B) Intertwinned hematite crystals with a "cauli ower" habit coating kaolinite with an inherited primary structure or the edge of voids in a clayey plasma made up of small size kaolinite respectively (He, hematite crystals; K, kaolinite). (C) Gibbsite and goethite secondary development in the matrix of a round polyhedric nodular domain (G, gibbsite; Go, goethite). (D) Intertwinned akes of secondary goethite (Go) developing around the void edges and the primary structures (he, hematitic matrix; mk, inherited kaolinitized mica).

are barely ferruginous, substituted on average by 2 mol% Fe_2O_3 (Fig. 10). The ferruginization leads to an increase of TiO_2 (0.32% against 0.09%), P_2O_5 (0.71% against 0.13%), and CuO (0.13% against 0.09%). The unit-cell dimensions of the hematite associated with the kaolinite "booklets" are $a = 5.046 \pm 0.001$ and $c = 13.777 \pm 0.004$.

In summary, the kaolinitic lower part of the saprolite of the upslope pro le preserves the parent rock textures while the gibbsitic upper part deletes it. The downslope pro le is characterized by a ongoing ferruginization process from the kaolinitic gray–white plasma of the mottled clay layer to the goethitic or hematitic plasmas of the vermiform soft ferricrete (Fig. 11A and B), which re ects the absolute iron accumulation within the porosity lled by illuviated clayey matrices, leading to less Al substituted iron oxyhydroxides with a dominance of the goethite over the hematite. The protopisolitic ferricrete of the downslope pro le is characterized by aluminous plasmas and by automorphous gibbsite crystallizations, that tends to increase the Al substitution of the goethite rather than that of the hematite (Fig. 13B).

3.3. Geochemical Balance of Lateritization Processes

Two lateritization processes thus control the petrological differentiation patterns of the pro les, weathering in the saprolite and ferruginization in the rest of the pro les. As the weathering in the saprolite preserves the original parent rock textures, one has estimated the isovolumetric chemical balance

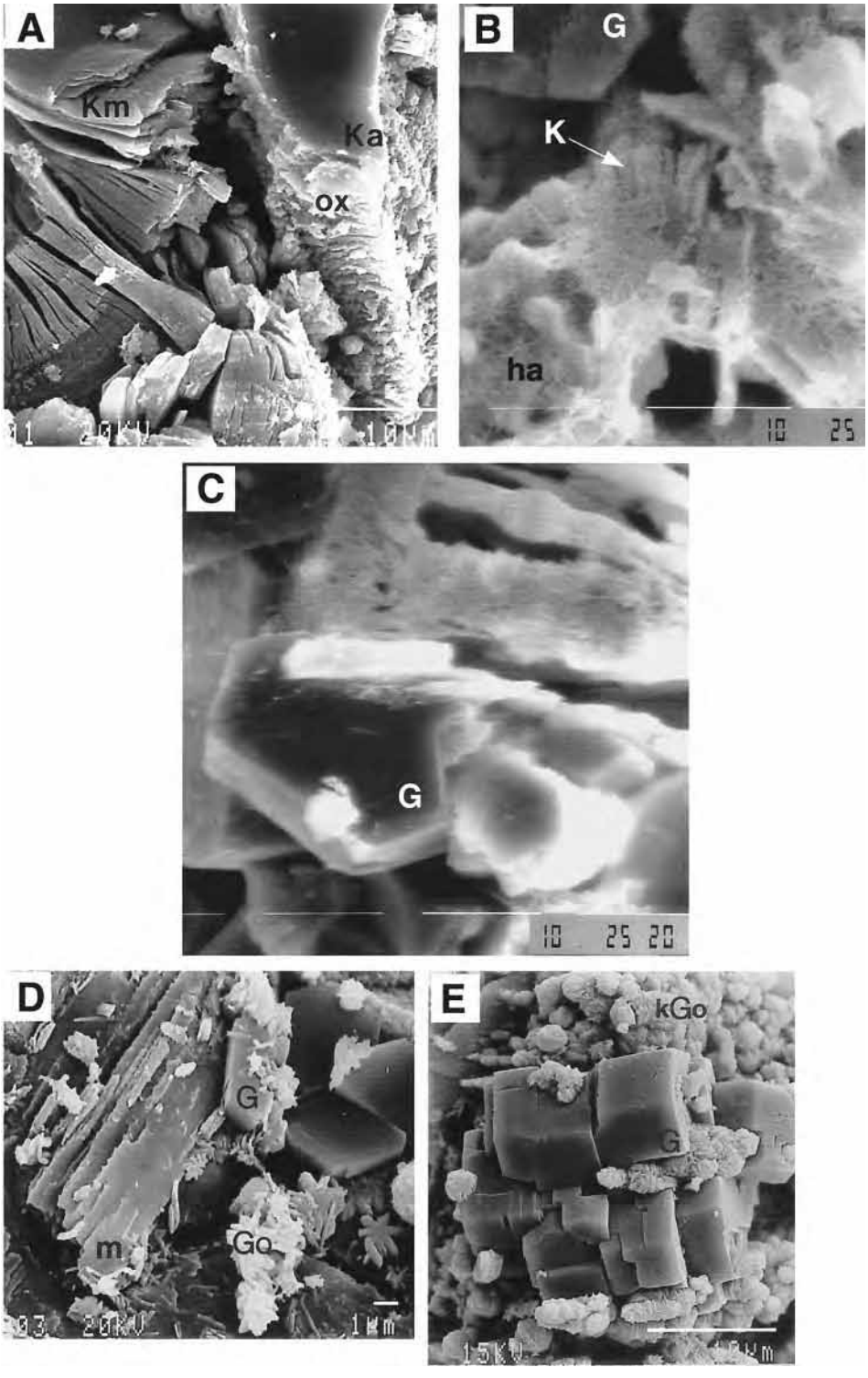

Fig. 9. SEM photomicrographs in the saprolite of the upslope pro le: (A) Pseudomorphic replacement of primary minerals by kaolinite and goethite. (B) Transformation of kaolinite into halloysite and gibbsite. (C) Incongruent transformation of kaolinite into gibbsite. (D) Secondary gibbsite development in voids affecting the goethitic ferruginous plasma. (E) Finely crystallized gibbsite from the incongruent dissolution of kaolinite within the clay ferruginous plasma (Km, kaolinite from micas; Ka, kaolinite from amphibole; ox, iron oxyhydroxide; K, kaolinite; ha, halloysite; G, gibbsite; m, relic micas; Go, goethite; kGo, kaolinite–goethite plasma).

in a way similar to that proposed by Millot (1970), Gardner et al. (1978), and Ambrosi and Nahon (1986). Therefore, the bulk and grain density (ρb and ρg) the porosity (p) the mineralogical and bulk chemical compositions of each weathering and ferruginization layer (Beauvais, 1991) were used with the normative calculations derived from the microprobe analyses of weathering minerals and plasmas to assess a geochemical balance for bulk samples of 1000 cm^3. The Fe–Al substitution rates were also taken into account in the geochemical balance calculations.

3.3.1. Geochemical balance of weathering processes

The isovolumetric weathering process as stressed in the upslope pro le leads to the development of 1000 cm^3 of saprolite characterized by $\rho b = 1.47$ g/cm^3, $\rho g = 2.32$ g/cm^3, and $p = 0.35$ at the expenses of 1000 cm^3 of amphibole–schist, composed of 50% amphibole, 25% albite, 10% phengite, 5% chlorite, 5% epidote, and 5% garnet with $\rho b = 2.94$ g/cm^3, $\rho g = 3$ g/cm^3, and $p = 0.02$. This transformation implies the partial leaching of silica, that allows the formation of 65% kaolinite substituted by 2 mol% Fe_2O_3, while iron and aluminum are relatively enriched to form 30% goethite substituted by 15 mol% AlOOH and 5% gibbsite. The respective mean bulk chemical composition of the parent minerals were estimated from the different formulas previously reported. The isovolumetric weathering of the rock by the saprolite is thus described by

$$\begin{aligned}&1.75\ \text{amphibole} + 2.45\ \text{albite} + 0.69\ \text{phengite}\\&+ 0.22\ \text{chlorite} + 0.33\ \text{epidote} + 0.39\ \text{garnet} + 36.1\ H_2O\\&+ 1.78\ O_2 + 21.89\ H^+\\&+ 2.79\ Fe^{2+} \Rightarrow 4.26[Si_2Al_{1.96}Fe_{0.04})O_5\ (OH)_4]\\&+ 9.2[(Fe_{0.85}Al_{0.15})OOH] + 0.96\ \text{gibbsite} + 18.77\ H_4SiO_4\\&+ 1.22\ Al^{3+} + 5.51\ Mg^{2+} + 4.02\ Ca^{2+} + 3.42\ Na^+\\&+ 1.33\ K^+, \qquad (4)\end{aligned}$$

meaning that 100% (Mg, Ca, Na, K), 69% silica, and 10% Al are released, whereas 35% Fe is relatively accumulated. The saprolitization of the parent rock likely happened under humid and hot conditions, such as those created by a tropical humid climate, implying high soil water uxes and organic carbon. Such conditions may have effectively favored the co-formation of Al–goethite and gibbsite with kaolinite at the expense of the parent silicate minerals.

Upwards to the transition with the mottled clay layer, the former kaolinitic saprolite is transformed into a more gibbsitic layer composed of 48% gibbsite, 36% goethite substituted by 20 mol% AlOOH, and 16% Fe–kaolinite with $\rho b = 1.5$ g/cm^3, $\rho g = 2.3$ g/cm^3, and $p = 0.35$. This part of the pro le is characterized at once by pedoturbed structures changing the geometry of the porosity and thus deleting the parent rock textures and by the hydration–oxidization of the organic matter re ected by gaseous emanations composed of CO_2 and CH_4 as previously mentioned. Under those more reducing and hydrated conditions the kaolinite effectively transforms into gibbsite according to the geochemical reaction,

$$\begin{aligned}&4.26\ \text{Fe–Kaolinite} + 9.2\ \text{Al–goethite} + 0.96\ \text{gibbsite}\\&+ 25.19\ H_2O + 0.88\ Fe^{3+} + 2.78\ Al_{3+} \Rightarrow 1.05\ \text{Fe–Kaolinite}\\&+ 11.04[(Fe_{0.80}Al_{0.20})OOH] + 9.2\ \text{gibbsite} + 6.42\ H_4SiO_4\\&+ 10.98\ H^+. \qquad (5)\end{aligned}$$

It follows from Eqn. 5 that 75% silica is released, while 21% Al and 10% Fe are gained. This con rms that the transformation of kaolinite into gibbsite is primarily a desilication process under relatively acid pH conditions. The aluminum is also enriched from absolute accumulations as proved by the secondary gibbsite crystallizations within the voids where the water activity is high. Conditions of low pH and high water and Al activities also allow goethite with a relatively high Al substitution to be preserved along with the gibbsite (Fitzpatrick and Schwertmann, 1982).

3.3.2. Geochemical balance of ferruginization processes

The ferruginization process stimulates the formation of hematite and goethite. Assuming that it is an ongoing process, it concerns the formation of mottled clay layers, soft nodular layers and/or soft ferricretes, and nally the actual ferricrete (Nahon, 1991; Tardy, 1993). It was also de ned as the epigene replacement of kaolinite by hematite, a general process governing the formation of ferruginous nodules and ferricretes (Nahon et al., 1977; Tardy and Nahon, 1985; Ambrosi et al., 1986; Nahon, 1986).

The ferruginization process in the mottled clay layer is commonly characterized by the hematite formation in mottles made up of kaolinite and goethite inherited from the underlying saprolite (Tardy and Nahon, 1985; Ambrosi and Nahon, 1986). In the upslope pro le, the hematitic ferruginization starts modestly since the mottled clays are composed of 50% kaolinite, 35% goethite substituted by 12 mol% AlOOH, 5% hematite, and 10% gibbsite with $\rho b = 1.54$ g/cm^3, $\rho g = 2.57$ g/cm^3, and $p = 0.40$. The formation of the mottled clays at the expense of the saprolite can be described by

$$\begin{aligned}&4.26\ \text{Fe–kaolinite} + 9.2\ \text{Al–goethite} + 0.96\ \text{gibbsite}\\&+ 5.49\ H_2O + 2.65\ Fe^{3+} \Rightarrow 3.02\ \text{kaolinite}\\&+ 9.91\ [(Fe_{0.88}Al_{0.12})OOH] + 0.96\ \text{hematite} + 1.77\ \text{gibbsite}\\&+ 2.48\ H_4SiO_4 + 2.88\ H^+ + 1.69\ Al^{3+}, \qquad (6)\end{aligned}$$

implying that 29% silica and 16% Al are released while 25% Fe is gained. The loss of Al is limited because the kaolinite is slightly dissolved whereas gibbsite forms.

The ferruginization process under the ferricretes of high plateau and upslope pro les is also characterized by further iron accumulations in the clay–ferruginous material of the mottled clay layer leading to the development of the soft nodular layer. In the upslope pro le, this layer contains, on average, 40% kaolinite substituted by 2 mol%, 35% goethite substituted by 12mol% AlOOH, 15% hematite substituted by 4 mol% Al_2O_3 and 10% gibbsite, with $\rho b = 1.95$ g/cm^3, $\rho g = 3.01$ g/cm^3, and $p = 0.35$. It may develop according to the geochemical reaction,

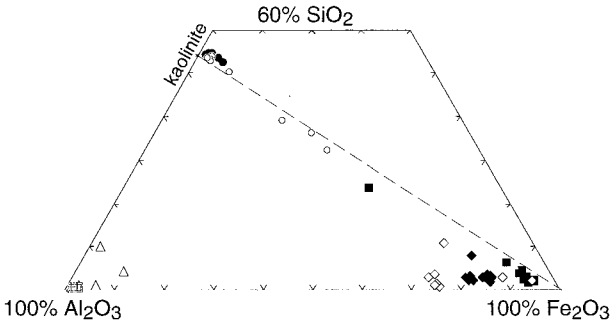

Fig. 10. Geochemical composition of weathering mineral and plasmas in different layers of the upslope profile of hillslope in SiO_2–Al_2O_3–Fe_2O_3 ternary diagram (black circles, kaolinitic plasma of saprolite; black and white diamonds, goethitic plasma of saprolite and mottled clays, respectively; white triangles and crossed squares, primary and secondary gibbsite, respectively in saprolite; white circles and black squares, kaolinite and hematite of "booklets" respectively in ferricrete).

$$3.02\ \text{kaolinite} + 9.91\ \text{Al–goethite} + 0.96\ \text{hematite} + 1.77\ \text{gibbsite} + 6.3\ H_2O + 3.59\ Fe^{3+} \Rightarrow 2.62\ \text{kaolinite} + 10.74\ [(Fe_{0.88}Al_{0.12})OOH] + 2.49\ [(Fe_{1.92}Al_{0.08})O_3] + 1.92\ \text{gibbsite} + 0.8\ H_4SiO_4 + 9.72\ H^+ + 0.35\ Al^{3+}, \quad (7)$$

showing that 13% silica and 4% Al are released while 25% Fe is gained. Reactions in Eqns. 6 and 7 indicate that the increase in iron due to the formation of hematite is low. The pedogenic environment prevailing in the mottled clay and the soft nodular layers of the forested upslope profile is characterized by hydrated and reducing conditions that favor the development of Al–goethite over the hematite.

In the high plateau profile the soft nodular layer richer in purple reddish hematitic nodules is composed of about 28% kaolinite, 23% goethite substituted by 12 mol% AlOOH, 34% hematite substituted by 5 mol% Al_2O_3, and 15% gibbsite with $\rho b = 2.48$ g/cm^3, $\rho g = 2.97$ g/cm^3, and $p = 0.16$. The development of the soft nodular layer from a mottled clay layer presumed to have a composition similar to that of the upslope profile can thus be described by,

$$3.02\ \text{kaolinite} + 9.91\ \text{Al–goethite} + 0.96\ \text{hematite} + 1.77\ \text{gibbsite} + 29.04\ H_2O + 1.46\ Al^{3+} + 14.68\ Fe^3 \Rightarrow 2.37\ \text{kaolinite} + 9.12\ [(Fe_{0.88}Al_{0.12})OOH] + 9.10\ [(Fe_{1.9}Al_{0.1})O_3] + 3.72\ \text{gibbsite} + 1.3\ H_4SiO_4 + 48.42\ H^+, \quad (8)$$

meaning that 22% silica is released while 14% Al and 58% Fe are gained. The hematitic ferruginization is so pronounced here, relative to the upslope profile, though the secondary Al–goethite and gibbsite are still well preserved, implying that the gains of Al and a part of Fe may result from absolute accumulation processes. Even though the mottles of the mottled clay layer truly transform into elongated nodules according to an aggrading hematitic ferruginization process (Tardy and Nahon, 1985), the occurrence of round polyhedric nodules and iron-depleted clayey pockets in the upper part of the soft

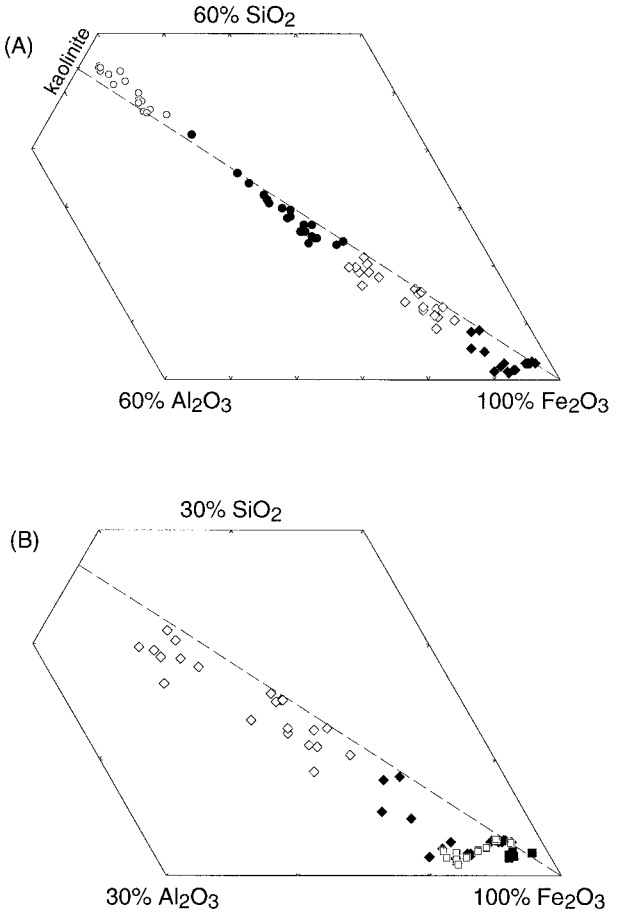

Fig. 11. Geochemical composition of weathering minerals and plasmas in different layers in the lower part (mottled clay and vermiform soft ferricrete and ferricrete layers) of the downslope profile of hillslope in SiO_2–Al_2O_3–Fe_2O_3 ternary diagrams (white circles, gray–white clayey plasma; black circles, brown orange ferruginous plasma in (A); in (A) and (B) white diamonds, goethitic plasma of vermiform ferricrete; black diamonds, secondary goethite of mottled clays; white squares, hematitic plasma of mottled clays; black squares, secondary hematite of vermiform ferricrete).

nodular layer also suggest that this part of the profile could originate from the chemical degradation of the overlying ferricrete likely because of a change of climatic conditions (Beauvais and Tardy, 1991). This degradation facies is on average composed of 64% kaolinite, 20% of goethite substituted by 16 mol% AlOOH and 16% hematite substituted by 9 mol% Al_2O_3 with $\rho b = 2.35$ g/cm^3, $\rho g = 2.85$ g/cm^3, and $p = 0.17$. The local degradation of the soft nodular layer can thus be described by the following geochemical reaction

$$2.37\ \text{kaolinite} + 9.12\ [(Fe_{0.88}Al_{0.12})OOH] + 9.10\ [(Fe_{1.9}Al_{0.1})O_3] + 3.72\ \text{gibbsite} + 5.96\ H_4SiO_4 + 2.25\ Al^{3+} + 26.37\ H^+ \Rightarrow 5.35\ \text{kaolinite} + 7.83\ [(Fe_{0.84}Al_{0.16})OOH] + 4.23\ [(Fe_{1.82}Al_{0.18})O_3] + 25.37\ H_2O + 11.04\ Fe^{3+}, \quad (9)$$

meaning that 56% silica and 18% Al are relatively concentrated

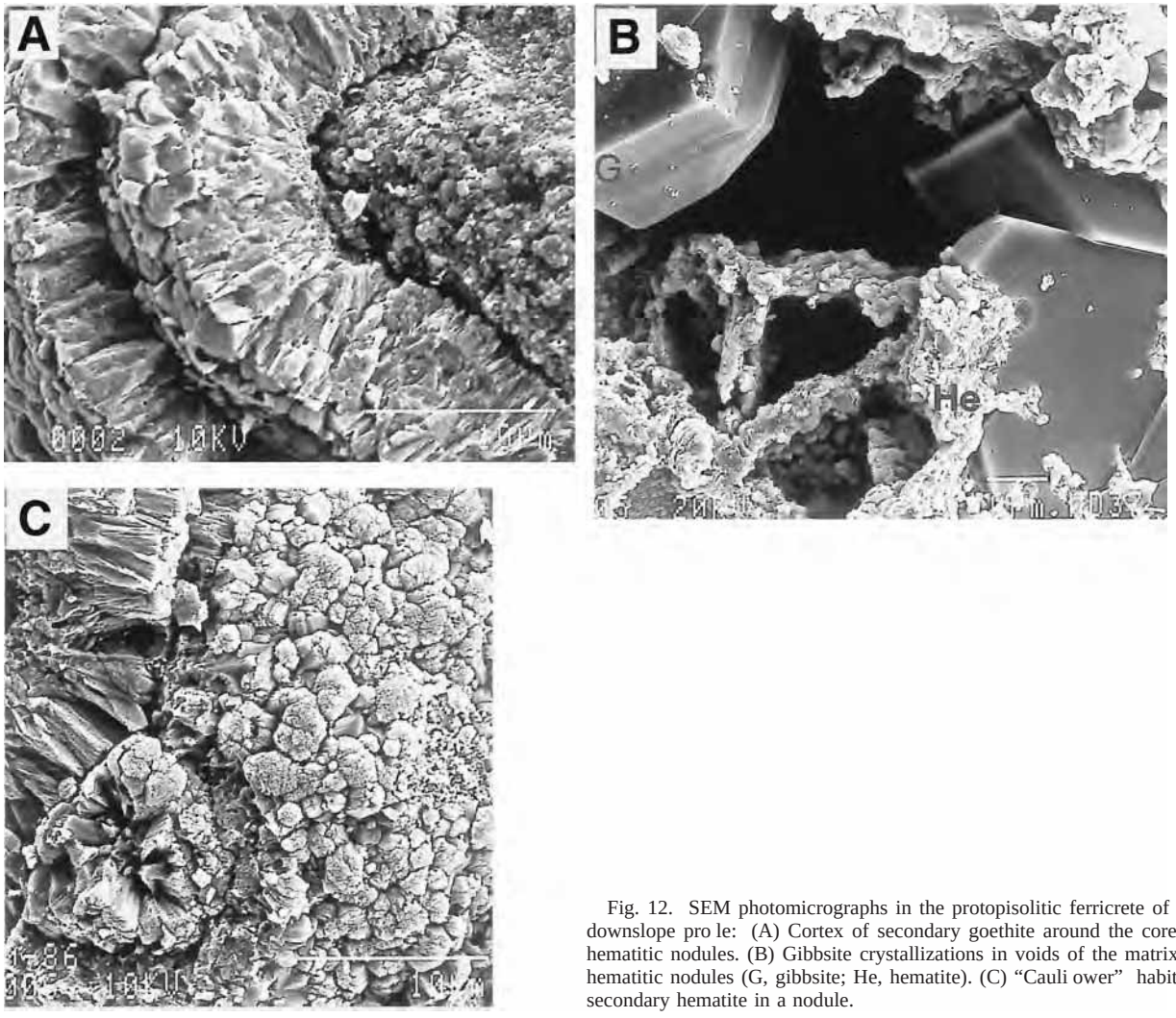

Fig. 12. SEM photomicrographs in the protopisolitic ferricrete of the downslope pro le: (A) Cortex of secondary goethite around the core of hematitic nodules. (B) Gibbsite crystallizations in voids of the matrix in hematitic nodules (G, gibbsite; He, hematite). (C) "Cauli ower" habit of secondary hematite in a nodule.

while 44% Fe is released. This result combined with the petrological observations indicate that the released iron probably migrates downwards and precipitates at the bottom of the soft nodular layer or the top of the mottled clay layer to form a goethitic nodular soft ferricrete (Beauvais, 1991). This facies is on average made up of 30% kaolinite, 60% goethite substituted by about 27 mol% AlOOH, only 5% hematite substituted by 2 mol% Al_2O_3 and 5% gibbsite with $\rho b = 2.65$ g/cm^3, $\rho g = 3.13$ g/cm^3, and $p = 0.15$. The geochemical reaction for this secondary ferruginization process at the top of the mottled clay layer can be written as,

$$\begin{aligned} &3.02 \text{ kaolinite} + 9.91 \text{ Fe–goethite} + 0.96 \text{ hematite} \\ &+ 1.77 \text{ gibbsite} + 24.52\ H_2O + 3.94\ Al^{3+} \\ &+ 9.61\ Fe^{3+} \Rightarrow 2.57 \text{ kaolinite} + 24.07\ [(Fe_{0.73}Al_{0.27})OOH] \\ &+ 1.35\ [(Fe_{1.96}Al_{0.04})O_3] + 1.25 \text{ gibbsite} + 0.9\ H_4SiO_4 \\ &+ 40.65\ H^+, \end{aligned} \quad (10)$$

implying the release of 15% silica and a gain of 30% Al and 47% Fe. The resulting nodular soft ferricrete is formed in part by Fe and Al absolute accumulations that leads to the formation of Al–goethite associated to gibbsite instead of hematite under conditions of high water and Al activity. The reactions shown in Eqns. 8 to 10 describe the superimposition of two opposite mechanisms re ecting different pedoclimatic environments. First the hematitic nodules have been formed by an aggrading ferruginization process under contrasted climatic conditions, i.e., characterized by alternating wet and dry seasons. Second, those nodules were degraded under more humid conditions as those prevailing today, and the resulting loss of iron accumulated at the base of the soft nodular layer to form a goethitic nodular soft ferricrete. During that evolution, the Al substitution of the different generations of goethite varied according to the variations of pH and activities of silica and aluminum (Fitzpatrick and Schwertmann, 1982; Schwertmann and Kämpf, 1985; Tardy and Nahon, 1985).

The ferruginization process under the ferricretes of downslope pro les is dominated by the goethite development over the hematite. The mottled clay layer and the vermiform soft ferricrete may appear like a nodular facies under way to forming as described by Tardy and Nahon (1985) , but the comple-

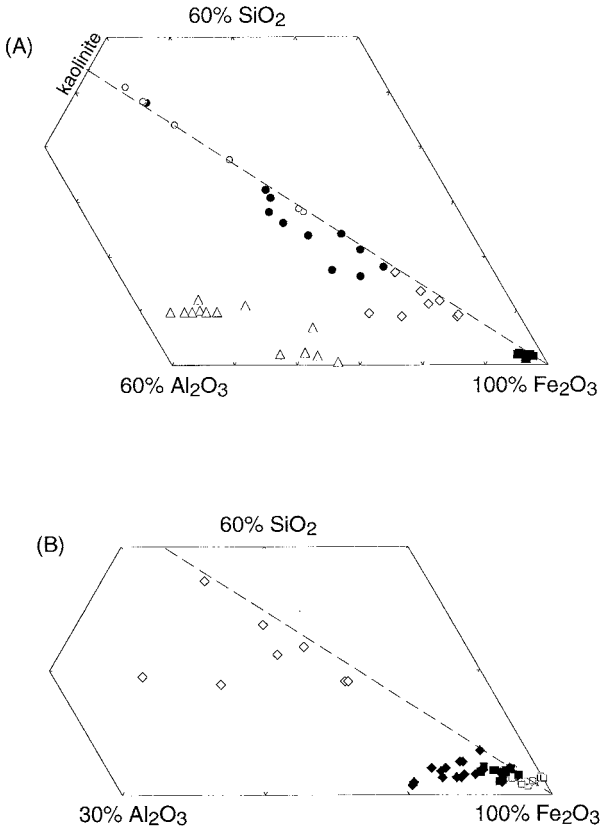

Fig. 13. Geochemical composition of weathering minerals and plasmas in different layers of the upper part (soft nodular and protopisolitic ferricrete layers) of the downslope pro le of hillslope in SiO_2–Al_2O_3–Fe_2O_3 ternary diagrams (white triangles, matrix embedding nodules; black circles, kaolinite of "booklets"; white circles, brown–orange plasma; white squares, hematite of kaolinite "booklets"; black diamonds, primary goethitic plasma; black squares, secondary hematite; white diamonds, secondary goethite).

tion of such a process seems to be delayed by local hydromorphic conditions re ected by bleached clayey matrices resulting from iron and kaolinite dissolution–precipitation processes. Such geochemical conditions favor the development of the goethite over the hematite, which only forms diffuse patches through the most concentrated goethitic domains. In the downslope pro les, the mottled clay layer is on average composed of 74% kaolinite substituted by 3 mol% Fe_2O_3, 23% goethite substitued by 17 mol% Al OOH, and 3% hematite substituted by 8 mol% Al_2O_3, with $\rho b = 1.66$ g/cm^3, $\rho g = 2.46$ g/cm^3, and $p = 0.32$. It may result from dissolution–precipitation processes of a previous mottled clay layer supposed to be similar to that of the upslope pro le, that can be described as,

$$\begin{aligned}&3.02\ \text{kaolinite} + 9.91\ \text{Fe–goethite} + 0.96\ \text{hematite}\\&+ 1.77\ \text{gibbsite} + 4.1\ H_4SiO_4 + 2.2\ Al^{3+}\\&+ 2.46\ H^+ \Rightarrow 5.07\ [(Si_2Al_{1.94}Fe_{0.06})O_5OH_4]\\&+ 7.38\ [(Fe_{0.83}Al_{0.17})OOH] + 0.65\ [(Fe_{1.84}Al_{0.16})O_3]\\&+ 9.25\ H_2O + 3.02\ Fe^{3+},\end{aligned} \tag{11}$$

meaning that 40% silica and 20% Al are gained while 28% Fe is released. This reaction effectively accounts for dissolution–precipitation processes of the kaolinite and iron with an increase of pH and silica activity that leads to the formation of iron–depleted gray–white clay matrices.

Then, after short distance migrations of Fe^{2+}, iron precipitates as goethite under higher water activity and partial pressure of oxygen within the tubules and vacuoles crossing the bleached matrices of the mottled clay layer. This Fe accumulation process concerns the development of a goethitic soft ferricrete made up of 60% Fe–kaolinite, 35% goethite substituted by 12 mol% AlOOH and 5% hematite substituted by 6 mol% Al_2O_3, with $\rho b = 2$ g/cm^3, $\rho g = 2.55$ g/cm^3, and $p = 0.21$, according to the geochemical reaction,

$$\begin{aligned}&5.07\ [(Si_2Al_{1.94}Fe_{0.06})O_5OH_4] + 7.38\ [(Fe_{0.83}Al_{0.17})OOH]\\&+ 0.65\ [(Fe_{1.84}Al_{0.16})O_3]\\&+ 13.08\ H_2O + 6.57\ Fe^{3+} \Rightarrow 4.78\ \text{Fe–kaolinite}\\&+ 13.05\ [(Fe_{0.88}Al_{0.12})OOH + 1.26\ [(Fe_{1.88}Al_{0.12})O_3]\\&+ 0.58\ H_4SiO_4 + 18.93\ H^+ + 0.2\ Al^{3+}.\end{aligned} \tag{12}$$

That implies a loss of 6% SiO_2 and 2% Al and a gain of 47% Fe. The vermiform soft ferricrete effectively results from dissolution–precipitation processes of iron through the illuviated bleached matrices and the macroporosity rather than from a simple ferruginization of the kaolinite. The two mechanisms described by the reactions in Eqns. 11 and 12 are maintained by an hydromorphic environment where the silica activity and pH are relatively high, that leads to the formation of goethite rather than hematite, both exhibiting high Al substitution (Fitzpatrick and Schwertmann, 1982).

The ferruginization process in the ferricrete is characterized by more hematite than goethite. In the high plateau pro le the massive ferricrete is on average composed of 31% kaolinite substituted by 2 mol% Fe_2O_3, 19% goethite substituted by 20 mol% AlOOH, 38% hematite substituted by 3 mol% Al_2O_3, and 10% gibbsite with $\rho b = 2.75$ g/cm^3, $\rho g = 3.35$ g/cm^3, and $p = 0.18$. The development of such a ferricrete at the expense of the underlying soft nodular layer should be described by

$$\begin{aligned}&2.37\ \text{kaolinite} + 9.12\ \text{Al–goethite} + 9.1\ \text{Al–hematite}\\&+ 3.72\ \text{gibbsite} + 0.38\ H_4SiO_4\\&+ 3.39\ H^+ \Rightarrow 2.56\ [(Si_2Al_{1.96}Fe_{0.04})O_5(OH)_4]\\&+ 7.35\ [(Fe_{0.08}Al_{0.2})OOH] + 2.42\ \text{gibbsite}\\&+ 9.93\ [(Fe_{1.94}Al_{0.06})O_3] + 8.43\ H_2O + 0.95\ Al^{3+}\\&+ 0.08\ Fe^{3+},\end{aligned} \tag{13}$$

implying that 7% silica are gained and 9% Al are released whereas Fe remains constant although its balance appears slightly negative. This means that the previously assumed ongoing ferruginization process does not result in the aggrading ferruginization of the soft nodular layer to the actual massive ferricrete with some necessary collapse (Beauvais and Colin, 1993). Instead, this is the degradation of the ferricrete that likely induces the formation of the upper part of the soft nodular layer, which is itself affected by degradation processes as described by the reaction in Eqn. 9. In fact, the petrological

features reported above as the kaolinite–hematite paragenesis suggest that the massive ferricrete of the high plateau could directly derive from the ferruginization of a saprolitic material, once located upper in the regolith (Tardy, 1993). In that case, the geochemical reaction can be written as,

$$4.26\ \text{Fe–kaolinite} + 9.2\ \text{Al–goethite} + 0.96\ \text{gibbsite} + 28.77\ H_2O + 17.26\ Fe^{3+} \Rightarrow 2.56\ \text{Fe–kaolinite} + 7.35\ \text{Al–goethite} + 9.93\ \text{Al–hematite} + 2.42\ \text{gibbsite} + 3.4\ H_4SiO_4 + 48.21\ H^+ + 1.19\ Al^{3+}, \quad (14)$$

meaning that 40% silica and 11% Al are released whereas 68% Fe is gained. Although the ferricrete is rich in hematite it remains ~60% kaolinite. A small proportion of Al is released since the ferricrete also contains Al–goethite and secondary gibbsite, which are in fact signatures of post-humid climatic conditions with relatively low pH and good drainage.

In the upslope pro le the protonodular ferricrete is composed of 22% kaolinite substituted by 2 mol% Fe_2O_3, 29% goethite substituted by 12 mol% AlOOH, 33% hematite substituted by 4 mol% Al_2O_3 and 15% gibbsite with $\rho b = 2.59$ g/cm^3, $\rho g = 3.14$ g/cm^3, and $p = 0.17$. The geochemical balance accounting for the development of that ferricrete facies from the aggrading ferruginization of the underlying soft nodular layer can be expressed as,

$$2.62\ \text{kaolinite} + 10.74\ \text{goethite} + 2.49\ \text{hematite} + 1.92\ \text{gibbsite} + 24.43\ H_2O + 2.18\ Al^{3+} + 11.11\ Fe^{3+} \Rightarrow 1.84\ [(Si_2Al_{1.96}Fe_{0.04})O_5(OH)_4] + 11.36\ [(Fe_{0.88}Al_{0.12})\ OOH] + 8.73\ [(Fe_{1.92}Al_{0.08})O_3] + 3.67\ \text{gibbsite} + 1.56\ H_4SiO_4 + 39.87\ H^+, \quad (15)$$

meaning that 30% silica are released while 23% Al and 41% Fe are gained. The gain of Al re ects the secondary gibbsite crystallizations, while a part of the iron contained in the protonodular ferricrete may also come from the degradation of a previous massive ferricrete similar to that of the high plateau (Fig. 2).

In the downslope pro le the protopisolitic ferricrete is made up of 16% kaolinite substituted by 2 mol% Fe_2O_3, 18% goethite substituted by 12 mol% AlOOH, 44% hematite substituted by 1 mol% Al_2O_3, and 23% gibbsite for $\rho b = 2.59$ g/cm^3, $\rho g = 3.07$ g/cm^3, and $p = 0.15$. If the relationship between the underlying vermiform soft ferricrete and this facies is real, the geochemical reaction describing this ferruginization process can be written as,

$$4.78\ \text{Fe–kaolinite} + 13.05\ \text{Al–goethite} + 1.26\ \text{Al–hematite} + 34.19\ H_2O + 15.86\ Fe^{3+} \Rightarrow 1.37\ [(Si_2Al_{1.96}Fe_{0.04}] + 7.22\ [(Fe_{0.8}Al_{0.2})OOH] + 5.76\ \text{gibbsite} + 11.92\ [(Fe_{1.98}Al_{0.02})O_3] + 6.82\ H_4SiO_4 + 43.2\ H^+ + 1.46\ Al^{3+}, \quad (16)$$

implying that 71% silica and 13% Al are released while 53% Fe is gained. This protopisolitic ferricrete is the poorest in kaolinite and the richest in hematite. Gibbsite likely formed from hydration and desilication processes of the kaolinite. Although an aggrading ferruginization process according to the model proposed by Nahon (1976, 1986) and Ambrosi and Nahon (1986) cannot be disproven, one can also consider that a part of Fe could have been imported according to a process similar to that described above for the ferricrete of the upslope pro le (Fig. 2).

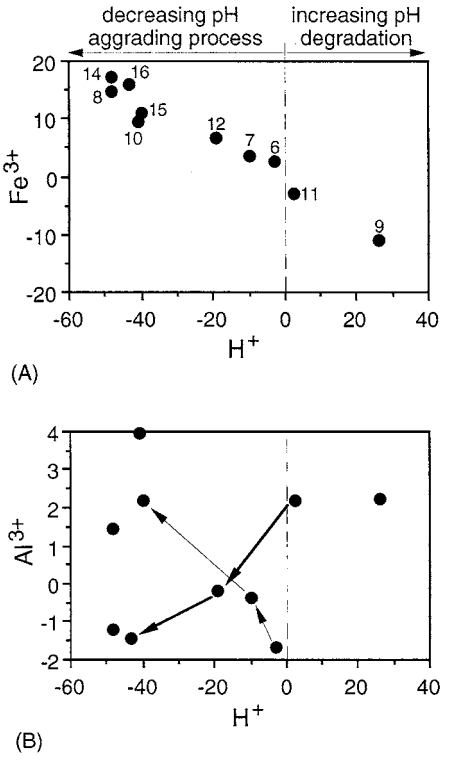

Fig. 14. (A) Iron and (B) aluminum geochemical balances as functions of consumed or released protons H^+ (the number relate to the geochemical reactions in text; the dash line represents the boundary between aggrading and degradation processes for a nil proton balance; the thin arrows within the diagram indicate the evolution in the upslope pro le according to the reactions in Eqns. 6, 7, and 15, whereas the bold arrows relate to the evolution in the downslope pro le described by the reactions in Eqns. 11, 12, and 16).

3.4. Geochemical Patterns of Ferruginization Processes

The results obtained from the geochemical reactions in Eqns. 6 to 16 allow (1) to analyse the effect of the ferruginization processes on the behavior of different geochemical and mineralogical quantities as a function of the consumption or release of H^+, that traduces an increase or a decrease of pH (Figs. 14 and 15), and (2) to discuss the way the kaolinite is dissolved during the ferruginization processes (Fig. 16). The stronger the release of H^+, thus the lower is the pH, the higher is the quantity of water consumed, the better are the drainage conditions and the highest is the iron gain (Fig. 14A). This characterizes the aggrading ferruginization processes governing the development of the hematite with a low Al substitution in the upper well oxidized parts of the pro les or the neoformation of the goethite with a high Al substitution in the lower more

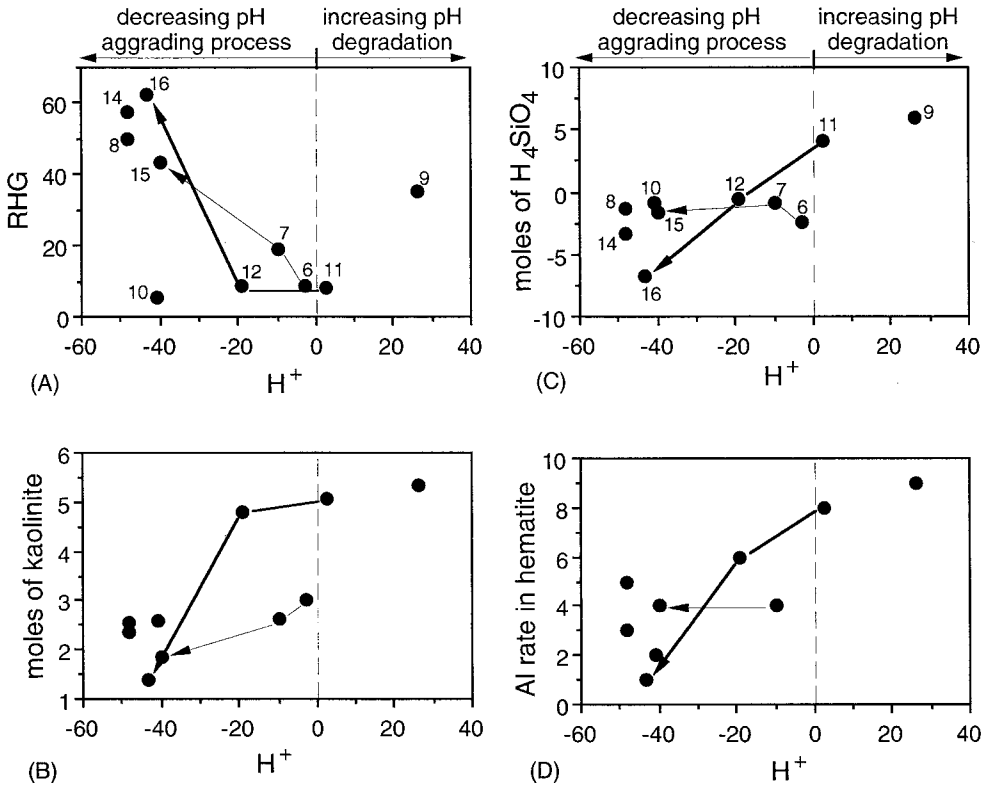

Fig. 15. Evolution of (A) RHG, (B) the kaolinite amount, (C) the dissolved silica, and (D) the Al substitution rate of hematite as functions of consumed or released protons H^+ [RHG= 100 *(hematite/hematite + goethite)]; see Fig. 14 for the other explanations).

hydrated parts where the Al activity is high (Figs. 14B and 15A and D). When the system loses iron as in the reactions Eqns. 9 and 11, both H^+ and dissolved silica are consumed (Figs. 14A and 15C). This effectively happens when the degradation driven by iron dissolution–precipitation mechanisms operates, stimulating the neoformation of kaolinite and goethite with minor Al substitution instead of hematite and gibbsite (Fig. 15A–C). When the silica balance ≥ 0 with increasing pH, the hematite is more aluminous in the degradation facies (Fig. 15C and D), while the less aluminous hematite is developed in layers, which are also the poorest in kaolinite (Fig. 15B and D), that could appear contradictory with the idea of an epigene replacement of the kaolinite by the hematite (Nahon et al., 1977; Tardy and Nahon, 1985; Nahon, 1986). The aluminum balance of the hillslope pro les is contrasted because it depends on the dissolution rate of kaolinite and on the ability of gibbsite to crystallize. In the upslope pro le, the aluminum increases as the pH lowers whereas it decreases in the downslope pro le (Fig. 14B), where the dissolution of kaolinite goes faster than in the upslope pro le (Fig. 15B and C). In this pro le gibbsite continously increases from the mottled clays to the ferricrete (Fig. 16A). In fact, kaolinite is better correlated to gibbsite rather than to hematite (Fig. 16A and B) suggesting that it was less ferruginized by hematite according to an epigene process than it underwent an incongruent dissolution wherever the gibbsite formed.

3.5. Climatic Evolution Patterns of the Lateritic Weathering Mantle

It was proposed that mineralogical variations of bauxites and ferricretes could re ect climate and palaeoclimate changes driven by the continental drift in Africa and Brazil (Tardy et al., 1988, 1991; Tardy and Roquin, 1998). For instance, a bauxite mainly composed of gibbsite and goethite should be formed under humid conditions while a ferricrete rich in hematite and kaolinite should re ect drier climatic conditions. This study's observations and results suggest that the lateritic weathering mantle of the Haut–Mbomou area in Central Africa could have undergone the effects of chemical and mechanical erosion processes according to climatic changes. Under the effect of a climatic change from humid to drier conditions a presumably thick saprolite layer made up of kaolinite and goethite could have been oxidized and ferruginized to form a massive ferricrete, i.e., the parent ferricrete, since this latter is mainly composed of bundles of kaolinite booklets similar to those of the actual underlying saprolite but shrouded in an hematitic cement, instead of being dissolved and replaced by hematite according to epigene processes. As those climatic conditions persisted, the weathering rate of the parent material decreased while the ferruginization front went down into the saprolite favoring the development of mottled clay and soft nodular layers between the saprolite and the ferricrete, with a dominance of the hematite over the goethite. This initial lateritic

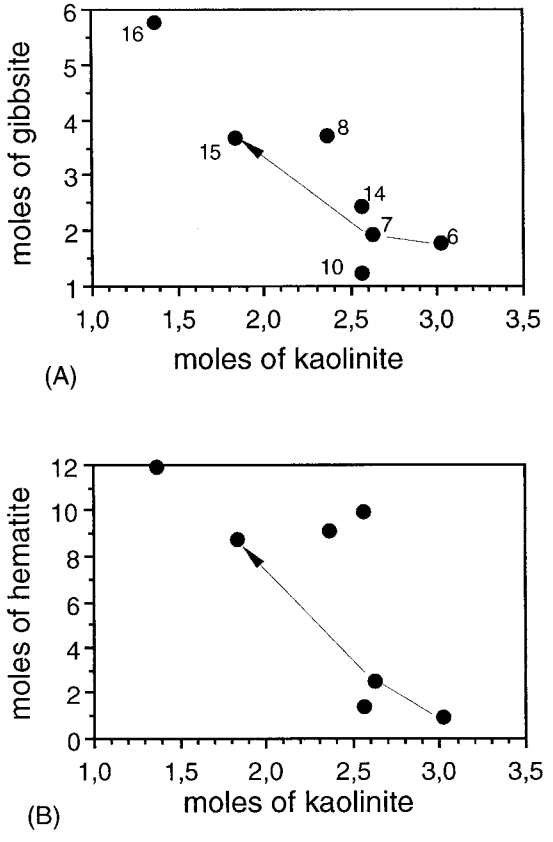

Fig. 16. Variations of (A) gibbsite and (B) hematite amounts as functions of the kaolinite amount (see Fig. 14 for the explanations).

weathering mantle overlain by the parent massive ferricrete is actually only preserved on the high plateau and its edges suggesting that it could then have undergone further weathering and erosion processes on the hillslopes under the in uence of alternating humid and drier climates. A return to more humid conditions could have set off the degradation of the parent ferricrete under the combined effects of the humidity and the organic matter oxidization (Beauvais and Tardy, 1991; Tardy, 1993). This mechanism is likely re ected (1) by the Fe-depleted clayey pockets and the numerous round polyhedric nodules occurring at the base of this ferricrete and the top of the underlying soft nodular layer in the high plateau pro le, and (2) the occurrences of Al–goethite and gibbsite with hematite and kaolinite in the ferricrete and in the nodules of the soft nodular layer. Degradation of the parent ferricrete resulted in Fe and Al release that led to intrapro le migrations and absolute accumulations of secondary Al–goethite with relatively high Al substitution and associated gibbsite lower in the pro les, in particular at the top of the saprolite of the upslope pro le and at the base of the soft nodular layer of the high plateau pro le where a nodular soft ferricrete rich in Al–goethite neoforms. A new evolution towards drier climatic conditions rst stimulated mechanical erosion processes of the parent ferricrete degradation products that is re ected by geomorphic patterns as, (1) the two discrete scarps incising the hillslope topography and (2) the numerous blocks of parent ferricrete spread around. Those climatic conditions should have gone on to allow the aggregation–ferruginization of the remaining lateritic products on hillslopes that form the actual protopisolitic ferricrete embedding parent ferricrete relics. Today the actual subhumid conditions further stimulate the inner chemical degradation of the ferricretes around the high plateaus where a ring of forest develops. Those conditions also maintain an hydromorphic environment in the downslope pro les making the mottled clays and the vermiform soft ferricrete to look like a pseudo-gley. The clayey matrices are bleached, the iron dissolution–precipitation processes are stimulated, Al substitution of the Fe–oxyhydroxides increase and goethite dominates over hematite.

4. CONCLUSION

In the Haut–Mbomou area, a simple geochemical balance of lateritization processes based on petrological observations indicates that the ferruginization of the weathering materials of amphibole–schist rocks does not appear as a simple on-going process from the bottom to the top of the pro les. Instead, the actual lateritic weathering mantle could result from different stages of weathering–erosion process according to climatic changes, which determine the aggrading ferruginization or degradation processes of ferricretes. The aggrading ferruginization leads either to the formation of hematite with low Al substitution under dehydration, oxidization and low pH conditions, or to the neoformation of goethite with high Al substitution in which the water and aluminum activities are high and the redox potential is lowered. The degradation processes favor the development of goethite at the expenses of hematite, and they are traced by relatively high Al substitution, in particular for relic hematite. The massive ferricretes of the high plateaus are the oldest, appearing to be relics of past drier climates. These ferricretes could result from the ferruginization of previous saprolites because they still contain numerous kaolinite booklets, which are not clearly ferruginized by the hematite according to epigene processes but simply embedded in an hematitic ferruginous cement. The relatively low Al substitution of the hematite could also preclude the hypothesis of the epigene replacement. The ferricretes of the hillslopes could derive at least pro parte from the degradation and the erosion of the previous massive ferricretes during the downward reduction of the regolith under the effects of climatic changes from dry to humid. They are, however, richer in goethite and gibbsite, whereas hematite and kaolinite could be relics of past drier climates. The geomorphological patterns of the landforms and the petrological features of the underlying lateritic weathering mantle could be in that way good signatures of climatic changes.

Acknowledgments—Grateful thanks to Ph. Karcher (“Centre de Géochimie de la Surface,” Strasbourg, France) for his technical support during SEM observations. I also thank two anonymous for their useful review of the paper. This work was carried out in part thanks to the nancial support of the research program PIRAT from INSU (CNRS) and ORSTOM. This is a contribution from IRD (RED-UR062).

REFERENCES

Ambrosi J.–P. (1984) Pétrologie et géochimie d’une séquence de pro ls latéritiques cuirassés ferrugineux de la région de Diouga, Burkina Faso. 3rd Cycle Thesis, Univ. Poitiers, France, 225 pages.
Ambrosi J.–P. and Nahon D. (1986) Petrological and geochemical

differentiation of lateritic iron crust pro les. *Chem. Geol.* **57,** 371–393.

Ambrosi J.–P., Nahon D., and Herbillon A. J. (1986) The epigene replacement of kaolinite by hematite in laterite—Petrographic evidence and the mechanisms involved. *Geoderma* **37,** 283–294.

Bamba O. (1996) L'or disséminé dans les albitites birimiennes de Larafella (Burkina Faso). Evolution dans les latérites et les cuirasses ferrugineuses. Ph. D. Thesis, Univ. Aix-Marseille III, France.

Beauvais A. (1991) Paléoclimats et dynamique d'un paysage cuirassé du Centrafrique. Morphologie, Pétrologie et Géochimie. Ph. D. Thesis, Univ. Poitiers, France.

Beauvais A. and Colin F. (1993) Formation and transformation processes of iron duricrust systems in tropical humid environment. *Chem. Geol.* **106,** 77–151.

Beauvais A. and Roquin C. (1996) Petrological differentiation patterns and geomorphic distribution of ferricretes in Central Africa. *Geoderma* **73,** 63–82.

Beauvais A. and Tardy Y. (1991) Formation et dégradation des cuirasses ferrugineuses sous climat tropical humide, à la lisière de la forêt équatoriale. *C. R. Acad. Sci., Paris, Sér. II* **13,** 1539–1545.

Boeglin J.–L. (1990) Evolutions minéralogiques et géochimique des cuirasses ferrugineuses de la région de Gaoua (Burkina Faso). Ph. D. Thesis, Univ. Strasbourg, France.

Braun J.–J., Pagel M., Herbillon A., and Rosin C. (1993) Mobilization and redistribution of REEs and thorium in syenitic lateritic pro le: A mass balance study. *Geochim. Cosmochim. Acta* **57,** 4419–4434.

Braun J.–J., Pagel M., Muller J. P., Bilong P., Michard A., and Guillet B. (1990) Cerium anomalies in lateritic pro les. *Geochim. Cosmochim. Acta* **54,** 781–795.

Brimhall G. H. and Dietrich W. E. (1987) Constitutive mass balance relations between chemical composition, volume, density, porosity, and strain in metasomatic hydrochemical systems: Results on weathering and pedogenesis. *Geochim. Cosmochim. Acta* **51,** 567–587.

Brimhall G. H., Lewis C. J., Ague J. J., Dietrich W. E., Hampel J., Teague T., and Rix P. (1988) Metal enrichment in bauxites by deposition of chemically mature aeolian dust. *Nature* **333,** 819–824.

Carroll S. A. and Walther J. V. (1990) Kaolinite dissolution at 25°, 60° and 80°C. *Am. J. Sci.* **290,** 797–810.

Chorover J. and Sposito G. (1995) Dissolution behavior of kaolinitic tropical soils. *Geochim. Cosmochim. Acta* **59,** 3109–3121.

Colin F., Alarcon C., and Vieillard P. (1993) Zircon: An immobile index in soils? *Chem. Geol.* **107,** 273–276.

Colin F., Brimhall G. H., Nahon D., Lewis C. J., Baronnet A., and Danti K. (1992) Equatorial rain forest lateritic mantles: A geomembrane lter. *Geology* **20,** 523–526.

Colin F., Lecomte P., and Boulangé B. (1989) Dissolution features of gold particles in a lateritic pro le at Dondo–Mobi, Gabon. *Geoderma* **45,** 241–250.

Colin F., Sanfo Z., Brown E., Bourles D., and Minko E. (1997) Gold: A tracer of the dynamics of tropical laterites. *Geology* **25(1),** 81–84.

Colin F. and Vieillard Ph. (1991) Behavior of gold in the lateritic environment: Weathering and surface dispersion of residual gold particles at Dondo–Mobi, Gabon. *Appl. Geochem.* **6,** 279–290.

Deer W. A., Howie R. A., and Zussman J. (1963) Chain silicates. In *Rock Forming Minerals*, vol. 2 (eds.), p. 273. Longmans.

Fitzpatrick R. W. (1983) Iron compounds as indicators of pedogenetic processes: Examples from the southern hemisphere. In *Iron in Soils and Clay Minerals* (eds. J. W. Stucki et al.), pp. 351–396.

Fitzpatrick R. W. and Schwertmann U. (1982) Al-substituted goethite: An indicator of pedogenic and other weathering environments in South Africa. *Geoderma* **27,** 335–347.

Foster M. D. (1962) Interpretation of the composition and a classi - cation of chlorites. *U.S. Geol. Surv., Prof. Paper* **414A,** 1–33.

Freyssinet, P. (1990) Géologie et minéralogie des latérites du Sud–Mali. Evolution des paysages et prospection géochimique de l'or. PhD. Thesis, Univ. Strasbourg, France.

Freyssinet, P., Lecomte, P., and Edimo F. (1989) Dispersion of gold and base metals in the Mborguéné lateritic pro le, East Cameroun. *J. Geochim. Explor.* **31,** 99–116.

Gardner L. R., Kheoruenromne I., and Chen H. S. (1978) Isovolumetric geochemical investigation of a buried granite saprolite near Columbia, SC, U.S.A. *Geochim. Cosmochim. Acta* **42,** 417–424.

Garrels R. M. and Mackenzie F. T. (1967) Origin of the chemical compositions of some springs and lakes. In *Equilibrium Concepts in Natural Water Systems* (ed. W. Stumm), Am. Chem. Soc. Adv. in Chemistry Ser. **67,** 222–242.

Gerth J. (1990) Unit-cell dimensions of pure and trace metal-associated goethites. *Geochim. Cosmochim. Acta* **54,** 363–371.

Grandin G. (1976) Aplanissements cuirassés et enrichissement des gisement de manganèse dans quelques régions d'Afrique de l'Ouest. *Mém. ORSTOM*, Paris, France, **82**, 275.

Helgeson H. C., Brown T. H., Nigrini A., and Jones T. A. (1970) Calculation of mass transfer in geochemical processes involving aqueous solutions. *Geochim. Cosmochim. Acta* **34,** 569–592.

Leake B. E. (1978) Nomenclature of amphiboles. *Am. Mineral.* **63,** 1023–1052.

Lecomte P. and Colin F. (1989) Gold dispersion in a tropical rain forest weathering pro le at Dondo–Mobi, Gabon. *J. Geochem. Explor.* **34,** 285–301.

Leprun J.–C. (1979) Les cuirasses ferrugineuses des pays cristallins de l'Afrique occidentale sèche—Genèse, transformations, dégradation. *Mém. Sci. Géol.*, Strasbourg, France, **58,** 24.

Mestraud J. L. (1982) Géologie et ressources minérales de la République Centrafricaine (Etat ds connaissances à la n 1963). *Mém. BRGM*, Orléans, France, **60,** 186.

Michel P. (1973) Les bassins des euves Sénégal et Gambie. Etude géomorphologique. *Mém. ORSTOM*, Paris, France, **63,** 752.

Millot G. (1970) *Geology of clays: Weathering, sedimentation, geochemistry*. Springer, 429 pp.

Millot G. and Bonifas M. (1955) Transformations isovolumétrique dans les phénomènes de latéritisation et de bauxitisation. *Bull. Serv. Carte Géol. Als. Lorr.*, Strasbourg, France, **8,** 3–10.

Millot G., Bocquier G., and Paquet H. (1976) Géochimie et paysages tropicaux. *La Recherche*, Paris, France, **7,** 236–244.

Muller J.–P. (1987) Analyse pétrologique d'une formation latéritique meuble du Cameroun. Essai de traçage d'une différenciation supergène par les paragénèses minérales secondaires. Ph.D. Thesis., Univ. Paris VII, France.

Muller J.–P., Manceau A., Calas G., Allard T., Ildefonse P., and Hazemann J.–L. (1995). Crystal chemistry of kaolinite and Fe–Mn oxides: Relation with formation conditions of low temperature systems. *Am. J. Sci.* **295,** 1115–1155.

Nahon D. (1976) Cuirasses ferrugineuses et encroûtements calcaires au Sénégal Occidental et en Mauritanie. Systèmes évolutifs: Géochimie, structures, relais et coexistence. *Mém. Sci. Géol*. Univ. Strasbourg, France, **44,** 232.

Nahon D. (1986) Evolution of iron crusts in tropical landscapes. In: *Rates of Chemical Weathering of Rocks and Minerals* (eds. S. M. Coleman and D. P. Dethier), pp. 169–191. Academic Press.

Nahon D. (1991) *Introduction to the petrology of soils and chemical weathering*. John Wiley, p. 313.

Nahon D., Janot C., Karpoff A.M., Paquet H., and Tardy Y. (1977) Mineralogy, petrography and structures of iron crusts (ferricretes) developed on sandstones in the western part of Senegal. *Geoderma* **19,** 263–277.

Norrish K. and Taylor R. M. (1961) The isomorphous replacement of iron by aluminium in soil goethites. *J. Soil. Sci.* **12,** 294–306.

Ouangrawa M., Grandin G., Parisot J. C., and Baras E. (1996) Dispersion mécanique de l'or dans les matériaux de surface: Exemple du site aurifère de Piéla, Burkina Faso. *Pangea* **25,** 25–40.

Parc S., Nahon D., Tardy Y., and Vieillard Ph. (1989) Estimated solubility and elds of stability for cryptomélane, nsutite, birnessite and lithiophorite based on natural lateritic weathering sequences. *Amer. Mineral.* **74,** 466–475.

Parisot J.–C., Ventose V., Grandin G., Bourges F., Debat P., Tollon F., and Millo L. (1995) Dynamique de l'or et d'autre minéraux lourds dans un pro l d'altération cuirassé du Burkina Faso, Afrique de l'Ouest. Intérêt pour l'interprétation de la mise en place des matériaux constituant les cuirasses de haut-glacis. *C. R. Acad. Sci., Paris, Sér. IIa* **321,** 295–302.

Poidevin J.–L. (1991) Les ceintures de roches vertes de la République Centrafricaine (Bandas, Boufoyo, Bogoin et Mbomou)—Contribution à la connaissance du Précambrien du Nord du craton du Congo. Ph. D. Thesis, Univ. Clermont–Ferrand II, France.

Sanfo Z., Colin F., Delaune M., Boulangé B., Parisot J.–C., Bradley R.,

and Bratt J. (1993) Gold: A useful tracer in subsahelian laterites. *Chem. Geol.* **107,** 323–326.

Schulze D. G. (1982) The identi cation of iron oxides by differential X-ray diffraction and the in uence of aluminum substitution on the structure of goethite. Ph. D. Thesis, Technische Universität München, Freising–Weihenstephan, Germany.

Schulze D. G. (1984) The in uence of aluminum on iron oxides. VIII. Unit-cell dimensions of Al-substituted goethites and estimation of Al from them. *Clay Clay Miner* **32,** 36–44.

Schwertmann U. and Carlson L. (1994) Aluminum in uence on iron oxides: XVII. Unit-cell parameters and aluminum substitution of natural goethites. *Soil Sci. Soc. Am. J* **58,** 256–261.

Schwertmann U., Fitzpatrick R. W., Taylor R. M., and Lewis D. G. (1979) The in uence of aluminum on iron oxides. Part II. preparation and properties of Al-substituted hematites. *Clay Clay Miner* **27,** 105–112.

Schwertmann U. and Kämpf N. (1985) Properties of goethite and hematite in kaolinitic soils of southern and central Brazil. *Soil Sci.* **139,** 344–350.

Soler J. M., and Lasaga A. C. (1996) A mass transfer model of bauxite formation. *Geochim. Cosmochim. Acta* **60,** 4913–4931.

Tardy Y. (1969) Géochimie des altérations. Etude des arènes et des eaux de quelques massifs cristallins d'Europe et d'Afrique. *Mém. Serv. Carte Géol. Alsace Lorraine, Strasbourg, France,* **31,** 199.

Tardy Y. (1993) *Pétrologie des latérites et des sols tropicaux*. Masson, Paris, p. 535.

Tardy Y., Kolbisek B., and Paquet H. (1991) Mineralogical composition and geographical distribution of African and Brazilian periatlantic laterites. The in uence of continental drift and tropical palaeoclimates during the past 150 million years and implications for India and Australia. *J. Afr. Earth Sci.* **12,** 283–295.

Tardy Y., Mel A.J., and Valeton I. (1988) Climats et paléoclimats tropicaux périatlantiques. Rôle des facteurs climatiques et thermodynamiques: Température et activité de l'eau sur la répartition et la composition minéralogique des bauxites et des cuirasses ferrugineuses, au Brésil et en Afrique. *C. R. Acad. Sci., Paris, Sér. II* **306,** 289–295.

Tardy Y. and Nahon D. (1985) Geochemistry of laterites, stability of Al–goethite, Al–hematite and Fe^{3+}–kaolinite in bauxites and ferricretes: An approach to the mechanism of concretion formation. *Am. J. Sci.* **285,** 865–903.

Tardy Y. and Roquin C. (1998) *Dérive des continents, Paléoclimats et altérations tropicales*. Editions BRGM, Orléans, France, p. 473.

Thomas M. F. (1965) An approach to some problems of landform analysis in tropical climates. In *Essays in Geography for Austin Miller* (eds. J. B. Whittow and P. D. Wood), pp. 118–144. University of Reading.

Thomas M. F. (1994) *Tropical geomorphology in the tropics. A study of weathering and denudation in low latitudes*. p. 460. John Wiley.

Tournarie M. (1969) Evaluation optimale des inconnus d'un système statique non linéaire, I. Prinicpe et théorie. *J. Phys.* **30,** 737–751.

Velbel M. A. (1985). Geochemical mass balances and weathering rates in forested watersheds of the southern blue ridge. *Am. J. Sci.* **285,** 904–930.

Velbel M. A. (1986). The mathematical basis for determining rates of geochemical and geomorphic processes in small forested watersheds by mass balance: Examples and implications. In *Rates of Chemical Weathering of Rock and Minerals* (eds. S. M. Coleman and D. P. Detheir), 439–451. Academic Press.

Vogt J. (1959). Aspects de l'évolution morphologique récente de l'Ouest Africain. *Ann. Géogr. Fr.* **68,** 367, 193–206.

ARTICLE 3

Clays and Clay Minerals, Vol. 50, No. 3, 314–330, 2002.

IN SITU CHARACTERIZATION AND DIFFERENTIATION OF KAOLINITES IN LATERITIC WEATHERING PROFILES USING INFRARED MICROSPECTROSCOPY

ANICET BEAUVAIS[1],* AND JACQUES BERTAUX[2]

[1] Cerege-IRD, UR-037, Europôle Méditerranéen de l'Arbois, B.P. 80, 13545 Aix-en-Provence Cedex, France
[2] IRD, UR-055, Centre d'Ile de France, LFS, 32 avenue Henri Varagnat, 93143 Bondy Cedex, France

Abstract—Lateritic weathering kaolinites have been characterized *in situ* and differentiated for the first time by means of infrared microspectroscopy (IRMS). Four classical OH-stretching bands have been observed in the Fourier transform infrared (FTIR) spectra, at 3695, 3668, 3650 and 3620 cm^{-1}, denoted ν_1, ν_2, ν_3 and ν_4, respectively, plus a band at 3595 cm^{-1} associated with the octahedral substitution of Fe^{3+} for Al^{3+}. Infrared microspectroscopy of thin-sections of lateritic weathering profiles provides useful information on the types of kaolinite present in different horizons of the profile. The spectra obtained from large well-ordered kaolinite crystals look like those obtained by diffuse reflectance in that, compared with the KBr disk spectra of <2 μm powders, bands at 3668 and 3650 cm^{-1} are enhanced, and the strong absorption of KBr disks at 3695 cm^{-1} is replaced by a broad weaker band from 3700−3680 cm^{-1}. In laterites, these large well-ordered kaolinites often exhibit a band at 3595 cm^{-1} indicative of significant Fe^{3+} substitution for Al^{3+} in the structure. The IR microspectra obtained from regions of small, more poorly-ordered kaolinites do not differ so markedly from that of KBr disks. All show enhanced absorption around 3650 cm^{-1} compared with well-ordered kaolinites, indicating that the disorder is due, at least in part, to domains of dickite-like and/or nacrite-like stacking in their structure. The 3595 cm^{-1} band is always weaker than that of the well-ordered kaolinite in the same profile. The IRMS data from well-characterized reference kaolinites show that the ratio $A\nu_2/A\nu_3$ is a pertinent IR order index for kaolinites. The larger this index, the larger is the area of the 3595 cm^{-1} band, and the larger and the more ordered is the kaolinite sample. It is suggested that the diversity of FTIR spectra observed reflects intergrowths of kaolinite-dickite polymorphs, or at least mixtures of high- and low-defect kaolinites which are frequently encountered in the lateritic geosphere rather than pure kaolinitic phases. The largest kaolinites having secondary crystallized in voids are the most ordered and the most ferruginous and have been considered as useful mineralogical tracers of the recent evolution of old lateritic terrains.

Key Words—Dickite, Infrared Microspectroscopy, Kaolinite, Lateritic Weathering, Longitudinal Optical Mode, Structural Order, Transverse Optical Mode

INTRODUCTION

Kaolinite is a ubiquitous clay mineral in lateritic weathering profiles developed at the expense of many kinds of parent rocks in tropical areas (Millot, 1970; Murray, 1988). The crystal chemistry of kaolinite is, however, very complex. For instance, it has been shown that its structural order index depended on defect centers and substitution of Fe^{3+} for Al^{3+} in the octahedral sites, and that these reflected various geochemical conditions of the medium in which it crystallized (Hinckley, 1963; Angel *et al.*, 1974; Jones *et al.*, 1974; Meads and Malden, 1975; Rengasamy, 1976; Mendelovici *et al.*, 1979; Mestdagh *et al.*, 1980, 1982; Cases *et al.*, 1982; Brindley *et al.*, 1986; Giese, 1988; Muller and Calas, 1989; Muller *et al.*, 1995). Different generations of kaolinite and kaolin polymorphs characterized by their own crystal chemical properties may effectively develop in the same weathering profile according to specific structural and textural patterns (Cantinolle *et al.*, 1984; Ambrosi and Nahon, 1986; Muller and Bocquier, 1987; Nahon, 1991). It has long been accepted that weathering matrices with inherited parent-rock structure generally contain well-crystallized kaolinite with low Fe substitution, while clayey matrices with blurred parent-rock structure embed poorly-crystallized kaolinite with higher Fe substitution (Herbillon, 1980; Didier *et al.*, 1983; Cantinolle *et al.*, 1984; Muller and Bocquier, 1987). The aim of this work is to characterize *in situ* different types of standard kaolinite along with kaolinites of lateritic origin on polished thin-sections by means of the infrared microspectroscopy (IRMS), and to try relating the crystal chemical characteristics of the second ones to the geochemical conditions of the medium in which they crystallized.

Background

In past decades, numerous studies made progress in understanding the relations between the kaolinite structure and its infrared (IR) spectroscopic signatures. Pertinent data in the mid-IR range were obtained especially in the region of the OH-stretching vibrations, *i.e.* between 3550 and 3750 cm^{-1}. Indeed, OH bands are very sensitive probes for distinguishing between kaolin clay minerals and for determining their structure

* E-mail address of corresponding author:
beauvais@arbois.cerege.fr

(Farmer, 1964, 1974, 1998, 2000; Farmer and Russell, 1964; Ledoux and White, 1964; Parker, 1969; Rouxhet *et al.*, 1977; Cruz-Cumplido *et al.*, 1982; Brindley *et al.*, 1986; Prost *et al.*, 1989; Johnston *et al*., 1990; Frost and Van der Gaast, 1997). As the kaolinite unit-cell contains only four different OH groups (Bish, 1993), the IR spectra of kaolinites obviously exhibit four OH-stretching bands at frequencies of 3695, 3668, 3650 and 3620 cm^{-1}, which were denoted ν_1, ν_2, ν_3 and ν_4, respectively (Farmer 1998; Frost and Johansson, 1998). The three higher frequency bands, ν_1, ν_2 and ν_3, have been assigned to the three inner-surface hydroxyls on the layer surface, here termed the OuOH groups, while ν_4 at ~3620 cm^{-1} stands for the inner hydroxyls, *i.e.* the InOH groups (Ledoux and White, 1964; Rouxhet *et al.*, 1977; Johnston *et al.*, 1990). Another OH-stretching band denoted ν_5 was also designated near 3685 cm^{-1} by using Raman spectroscopy (Wiewióra *et al.*, 1979; Johnston *et al.*, 1985; Frost and Van der Gaast, 1997; Farmer, 1998). The occurrence of the 3685 cm^{-1} band was recently ascribed to a transverse optical (TO) vibration involving the in-phase stretching vibration of the three inner-surface hydroxyls in the unit-cell. This vibration gives rise to ν_1 at 3695 cm^{-1} in KBr disk spectra (Farmer, 1998, 2000). The bands resulting from the vibration of the OuOH groups, including ν_5, are generally attributed to coupled in-phase and out-of-phase inner surface hydroxyls (Rouxhet *et al.*, 1977; Brindley *et al.*, 1986; Frost and Van der Gaast, 1997; Farmer, 1998).

Empirical tests from XRD and IR spectroscopy analyses have long been applied to assess the crystallinity of kaolinite; after Brindley *et al*. (1986), we will use structural order or disorder rather than good or poor crystallinity. For instance, the hydroxyls absorption patterns of kaolinites have been shown to reflect the degree of structural disorder (Barrios *et al.*, 1977; Prost *et al.*, 1989). Among them, the ratio between the integrated intensity, *i.e.* the area, of OH-stretching bands at 3668 cm^{-1} and 3650 cm^{-1} empirically documents the structural order or disorder of kaolinite (Farmer, 1974; Mestdagh *et al.*, 1982; Brindley *et al.*, 1986). An IR spectrum of a poorly-ordered kaolinite effectively presents a poorly-resolved ν_2 OH-stretching band. Brindley *et al.* (1986) showed that the wavenumber of ν_1 decreased with the width at half-height of ν_4 as the structural order measured by the Hinckley index increased. On the basis of Rietveld refined structural data, this finding was, however, questioned (Plançon *et al*., 1988, 1989). Farmer and Russell (1964) and Prost *et al.* (1989) argued that IR spectra of poorly-crystallized kaolinites revealed the existence of dickite- and nacrite-like configurations whose proportion increased with increasing structural disorder.

Most previous IR spectroscopic techniques required the mechanical extraction of clay fractions, but this is not the best way to distinguish clay minerals according to their various sizes and morphologies. What one generally analyzes with classical transmission IR on KBr powder pellets of weathering materials is a mixture of well-ordered and poorly-ordered small-size kaolinites. It has been also suggested that pressing kaolinite particles when making KBr pellets had an effect on the intensities of the OH-stretching bands (Bell *et al.*, 1991), that is avoided when using IRMS. The advantage of IRMS is its ability to analyze a limited zone in a thin-section, selecting either single flakes of kaolinite 'booklets' or a population of optically similar small kaolinites. Soil scientists make much use of thin-sections to describe soil profiles, and the recent development of IR microscopes makes it possible to measure a spot as small as 20 μm either in transmission or in reflection mode. Very few studies, however, have explored the capacity of the IRMS technique for the *in situ* characterization of clays in soils. Rintoul and Fredericks (1995) used reflection-mode IRMS for studying bauxitic pisoliths. Johnston *et al*. (1990) obtained indirect information on the OH structure of single crystals of dickite and kaolinite using a polarizing IR microspectrometer. They showed that the intensities of the 3620 and 3668 cm^{-1} bands were influenced by rotation of the electrical vector around the *c* axis in the *ab* plane of a single crystal of kaolinite, whereas the intensity of the 3650 cm^{-1} band was not changed. They concluded that all OuOH are oriented almost perpendicular to the octahedral sheet, while the InOH are sub-parallel to the sheets, pointing at the octahedral vacancy, later confirmed by Farmer (1998, 2000). We present new insights on the application of IRMS in transmission mode for the *in situ* characterization of different types of kaolinites in thin-sections. We believe that IRMS is a suitable technique for studying the hydroxyl region of kaolinites from lateritic soil profiles even with large amounts of Fe oxyhydroxides.

MATERIALS AND TECHNIQUE

Samples

Kaolinites from reference standards and from tropical soils were investigated *in situ* in thin-sections by IRMS. The reference samples are of different origins and exhibit varying size and structural order (Table 1). Two specimens of well-ordered hydrothermal kaolinites, DCV, a pure sample (Allard, 1994) and GB1, from France and Great Britain, respectively; five sedimentary kaolinites, among them, two well-ordered samples, A1, from Manaus in Brazil and, KGa1, from Georgia in the USA, and three more disordered samples, KGa2, FU7 and FBT2, from Georgia in the USA and France, respectively; and one soil kaolinite, B4, from Manaus in Brazil (Table 1). Soil kaolinites were also analyzed from samples collected in three lateritic weathering profiles belonging to the same topographical sequence in south-eastern Central African Republic (Figure 1). Detailed petrological and geochemical studies of the profiles have been reported (Beauvais, 1991, 1999; Beauvais and

Table 1. Characterization of kaolinite specimens.

Sample	Reference or source	Location	R2	E_{120K}
(1) A1 <20 μm	Lucas *et al*., 1987	Manaus (b) Brazil	0.7	9.3
(2) DCV >2μm	Gaite *et al*., 1993	Aveyron (a) France	1.35	3.1
(3) GB1	Cases *et al*., 1982	Cornwall (a) Great Britain	1.13	6.2
(4) KGa1	van Olphen and Fripiat 1979	Georgia (b) USA	1.03	6.2
(5) KGa2	van Olphen and Fripiat 1979	Georgia (b) USA	0.69	10
(6) FU7	Cases *et al*., 1982	Charentes (b) France	0.23	14
(7) FBT2 <38 μm	Delineau *et al*., 1994	Charentes (b) France	0.44	14.2
(8) B4 <20 μm	Lucas *et al*., 1987	Manaus (c) Brazil	0.23	12.6

Numbers in parentheses refer to the spectra of Figures 5 and 6
(a) hydrothermal; (b) sediment; (c) soil.
R2 = XRD disorder index of Liétard (Cases *et al*., 1982)
E_{120K} = EPR disorder index measured at 120 K (Gaite *et al*., 1997; Balan *et al*., 1999)

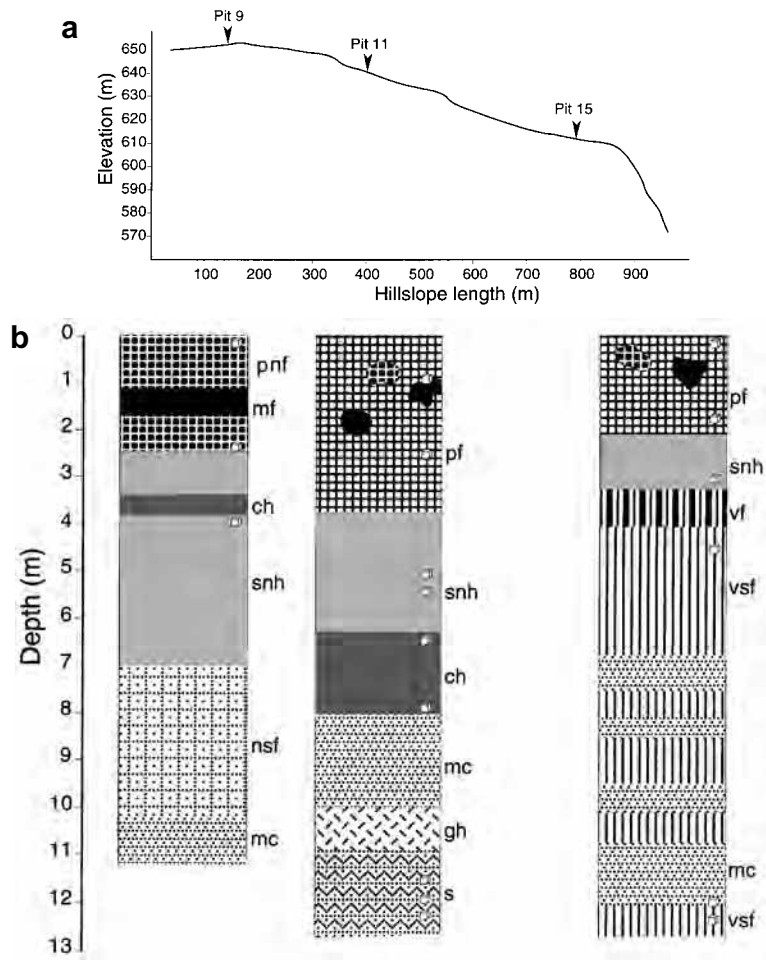

Figure 1. (a) Topographic location of the lateritic weathering profiles in which kaolinites were analyzed by IRMS. (b) Descriptive sketch of the profiles in the Central African Republic (the small cubes represent samples in which thin polished sections have been made for the IRMS analysis; s = saprolite; gh = gibbsitic horizon; mc = mottled clays; ch = clayey horizon; snh = soft nodular horizon; nsf = nodular soft ferricrete; vsf = vermiform soft ferricrete; vf = vermiform ferricrete; mf = massive ferricrete; mnf = metanodular ferricrete; pf = protopisolitic ferricrete). The different ferricrete facies were defined by Tardy (1993).

Colin, 1993). From the bottom to the top of the profiles, five standard horizons were observed, a saprolite, a mottled clayey horizon, a soft nodular horizon, a soft ferricrete and a ferricrete (Figure 1). Notice that the ferricrete is geochemically degraded and progressively replaced by micronodular soft soils wherever the forest is developing (Beauvais and Tardy, 1991). The soft nodular horizons contain lithorelic nodules with the parent-rock structure, and pedorelic nodules with a soil structure as previously described by Beauvais (1991). Kaolinite was analyzed in each horizon. It is associated with goethite, hematite and gibbsite in various proportions depending on the horizon facies, *i.e.* the location in the profiles (Figure 1b). In saprolite, ferruginous nodules and ferricrete matrices with preserved parent-rock structure, the kaolinite platelets of 10–20 μm are stacked as 'booklets' of 40–50 μm in size accross the *c* axis (Figure 2). The making of thin-sections thus leads to a variety of kaolinite 'booklets' orientations according to the three crystallographic axes, *a*, *b*, *c*. In all the profile horizons except the saprolite, the kaolinites of crypto-crystalline clay-ferruginous matrices without parent-rock structure, are smaller, 1–2 μm in size (Figure 3). These two kinds of kaolinite are supposed to have different crystal chemical characteristics reflecting different geochemical properties of the medium in which they have been formed.

Experimental procedure

Well-characterized reference kaolinites were first analyzed using KBr pellets. The samples were ground mechanically with small agate balls in an agate vial under acetone and in a refrigerated area at 4°C in order to prevent heating and structural changes of particles. A particle size <2 μm was required to avoid excessive scattering of IR radiation. The powder was carefully mixed by hand with KBr in an agate mortar. A dilution of 0.25% was used for all samples studied. Weighing was done within a dry atmosphere, with an accuracy of 10^{-5} g. A 300 mg pellet, 13 mm in diameter, was prepared by pressing the mixture in a vacuum die, with up to 8 tons cm^{-2} of compression. The pellets were oven dried for two days at 110°C before data acquisition.

Transmission Fourier transform IR (FTIR) spectra of these KBr pellets were recorded at room temperature on a Perkin-Elmer FT 16 PC spectrometer in the 4000–250 cm^{-1} energy range with a 2 cm^{-1} resolution. The beam crossing the KBr pellet has an approximate diameter of 8 mm, so that this method can be considered as IR macrospectrometry in relation to the IR microspectrometry technique described below. For each spectrum, 50 scans were cumulated. Absorbance was computed relative to a background of sample holder containing a pure KBr pellet.

Infrared absorption spectra of kaolinites from thin-sections were obtained by transmission at room temperature. The spectra were recorded with a Bruker A 590 microscope coupled with an equinox 55 Bruker FTIR spectrometer in the frequency range 6000–1500 cm^{-1}.

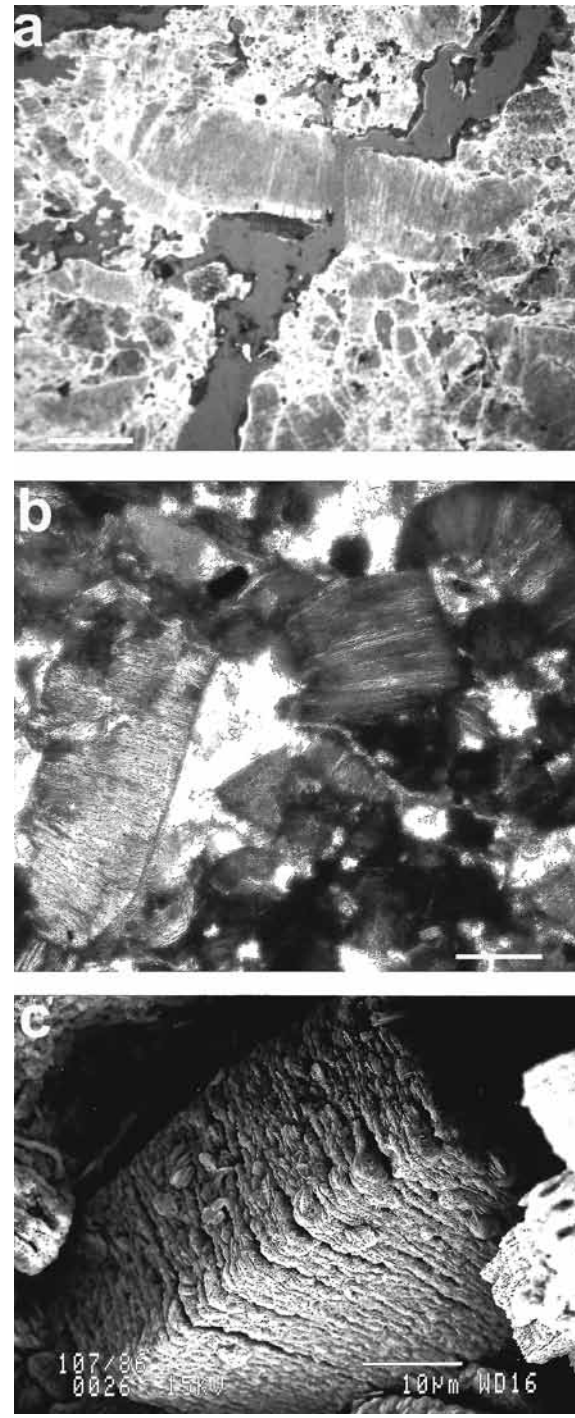

Figure 2. Large secondary kaolinite 'booklets' crystallized in large voids of ferruginous matrices of nodules and ferricrete. (a) Under reflected light optical microscope (scale bar = 10 μm). (b) Under polarized optical microscope and partially replaced by gibbsite crystals (scale bar = 5 μm). (c) Under scanning electron microscope coated by iron oxyhydroxides (scale bar = 10 μm).

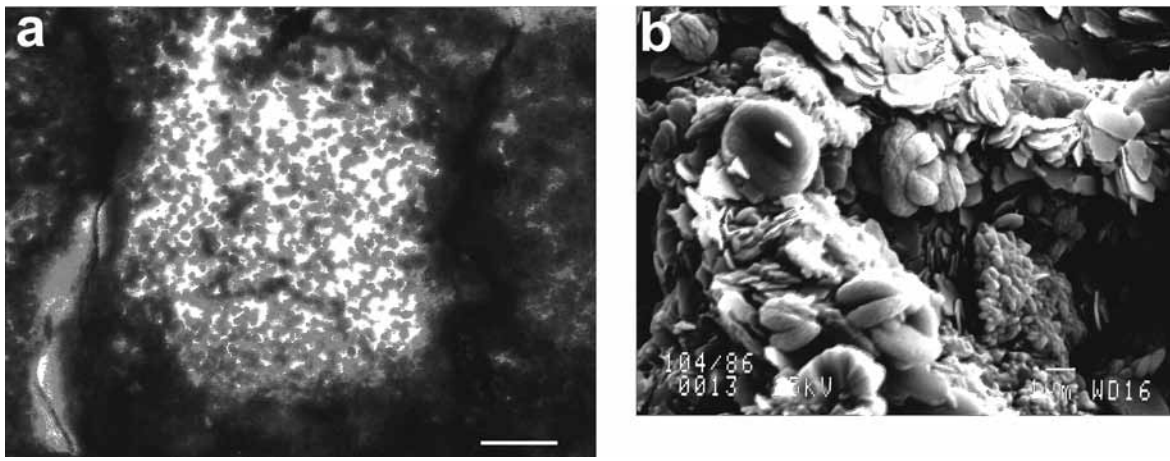

Figure 3. Small-size kaolinites associated with micronodular hematite in nodules and ferricrete of the high plateau profile. (a) Viewed under polarized optical microscope (scale bar = 5 μm). (b) Under scanning electron microscope (scale bar = 1 μm). Note the small hexagonal flakes of well-crystallized kaolinite and the 'doughnut' habit of hematite, these latter corresponding to several coalesced micronodules of hematite in Figure 3a.

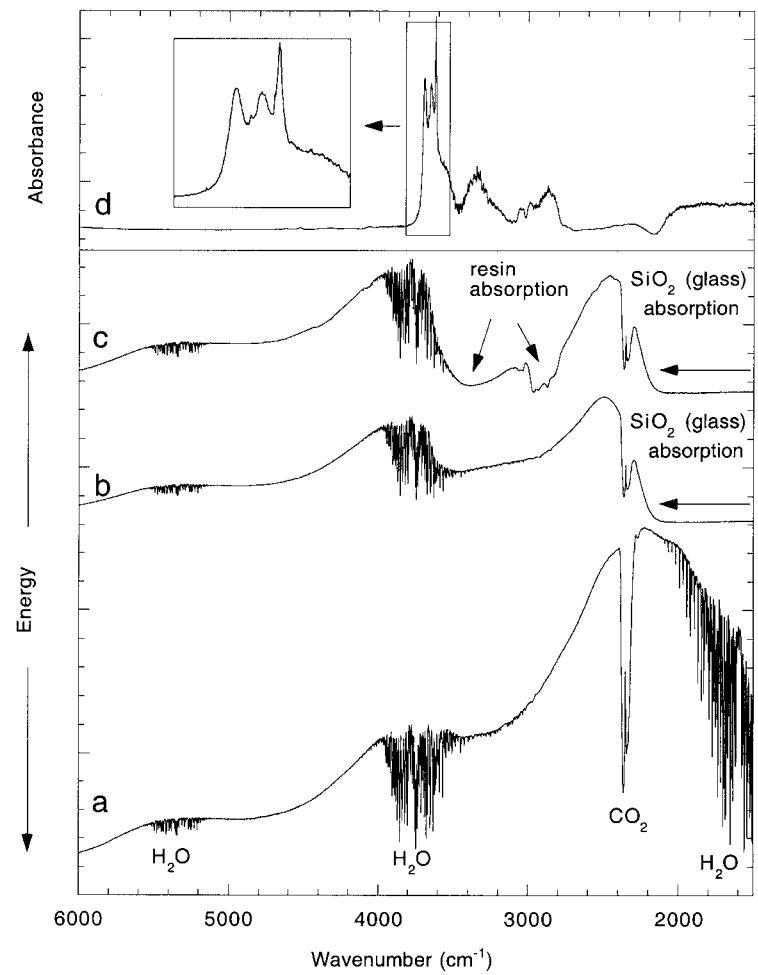

Figure 4. IR microspectrometry transmission measurements through a thin-section. a, b and c are single-channel measurements through a 50 μm spot of air, glass slide and glass slide plus resin, respectively. The resulting curves show the variation of energy in arbitrary unit *vs*. wavelength given as its inverse, the wavenumber. The narrow absorption bands due to atmospheric H_2O and CO_2 are shown in curve a. d is the IRMS spectrum of clays in a thin-section of soil, with an enlargement of the OH-stretching region.

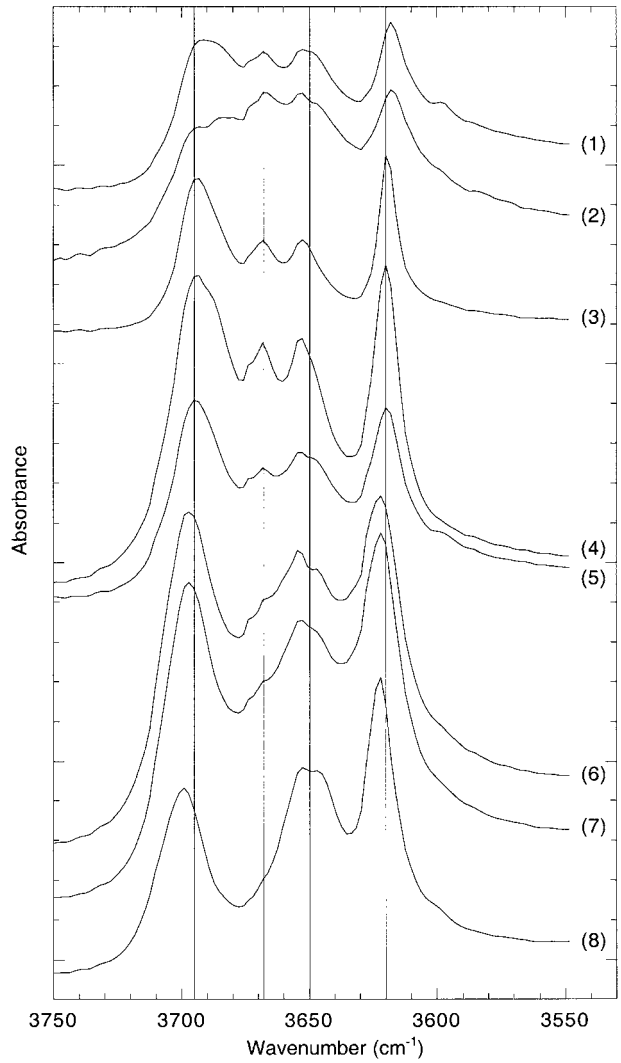

Figure 5. IRMS spectra of the well-characterized reference kaolinites in thin-sections. The numbers refer to sample numbers in Table 1. The vertical lines represent the standard centered absorption-band positions of well-ordered kaolinites, ν_1 at 3695 cm^{-1}, ν_2 at 3668 cm^{-1}, ν_3 at 3650 cm^{-1} and ν_4 at 3620 cm^{-1}.

This configuration used a Globar source and a liquid N_2-cooled narrow-band mercury-cadmium telluride (MCT) detector to optimize the response in the OH-stretching region (Johnston *et al*., 1990). The beam size was reduced to a diameter of 50 μm, *i.e.* an area of 1962.5 μm^2 was analyzed which includes several kaolinite flakes in the case of 'booklets' (Figure 2), or a mixture of numerous smaller kaolinites, $\leqslant 2$ μm, with Fe oxyhydroxides in the case of clay-ferruginous matrices (Figure 3). Preliminary test measurements were made with a spectral resolution at 2 or at 4 cm^{-1}, and the co-addition of 300 or 100 scans, respectively. As no significant changes in absorption band characteristics were detected, the spectra were recorded by the accumulation of 100 scans at a resolution of 4 cm^{-1}. The aperture of the microscope is either filled with the (110), (010) or (110) faces of the kaolinite crystals stacked as 'booklets' along the *c* axis that results from different cut planes used to make the thin-sections (Figure 2). Although we did not use a polarization system, perhaps we should consider that the resulting different orientations of the kaolinite 'booklets' to the incident IR beam could give rise to variations in intensities of the OH-stretching bands, similar to those observed when applying a polarization system (Johnston *et al*., 1990, 1998). Kaolinite books with different orientations regarding the *c* axis also result in various Raman spectra (Frost and Van der Gaast, 1997). Unfortunately, we do not have any means to accurately determine the orientations of 'booklets' in the thin-sections.

The *in situ* measurements were made on soil thin-sections, 30 μm thick, mounted, after impregnation with resin, on a glass slide and subsequently polished. Glass slides, *i.e.* amorphous silicate, are transparent to the IR

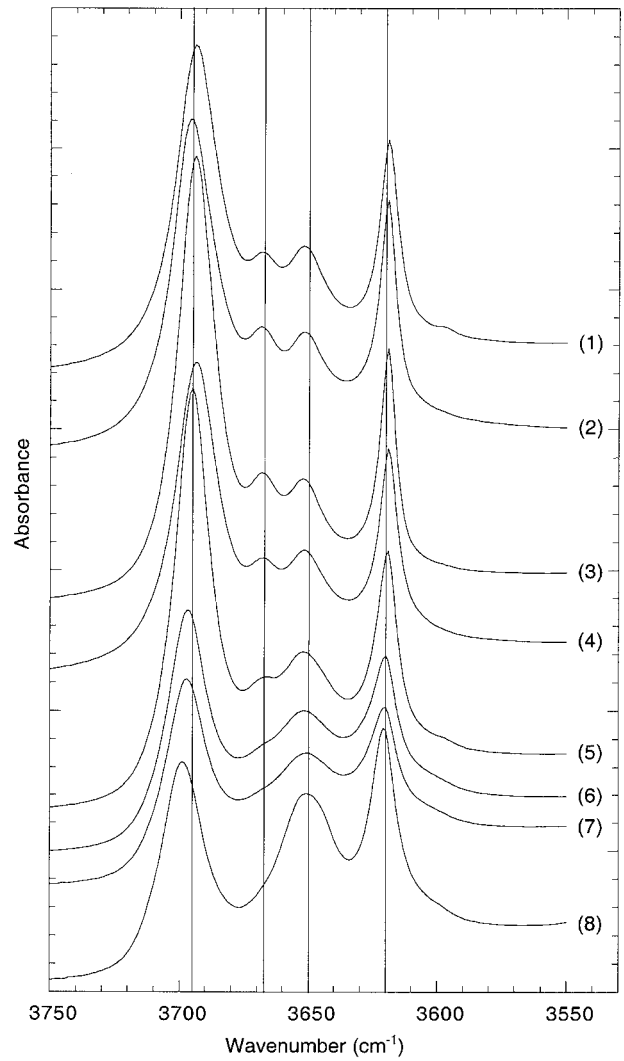

Figure 6. IR spectra of the well-characterized reference kaolinites in KBr pellets (numbers and vertical lines as in Figure 5).

radiation above 2500 cm^{-1}, where no absorption due to SiO_4 tetrahedra occurs; this still allows a thorough observation of the OH region between 3500 and 3800 cm^{-1} (Figure 4). The level of energy received by the MCT detector when no thin-section is crossed allows the measurement of IR absorption between 6000 and 1500 cm^{-1} (Figure 4a), with a maximum of energy, *i.e.* best signal to noise ratio, between 1500 and 2500 cm^{-1}. The glass slide absorbs all the energy below 2200 cm^{-1} (Figure 4b), while additional absorption due to the resin of the thin-section occurs around 2800–3000 cm^{-1} and as a broad band centered at 3400 cm^{-1} (Figure 4c). Finally, the only remaining energy available for a measurement through a thin-section lies between 2250 and 2750 cm^{-1} and above a frequency of 3500 cm^{-1} over which the OH-stretching vibrations of clays absorb the IR radiation, so that the spectra have been expanded between 3570 and 3750 cm^{-1} (Figure 4d). All transmission-absorption spectra measured on thin-sections were referenced against a measurement of the absorption solely due to the glass slide and the epoxy resin used to make the thin-sections (Figure 4c).

The baseline of each IR and IRMS spectrum was corrected by using the interactive mode of the Bruker OPUS software, meaning that a third-order polynomial was applied; after which, the envelopes of the identified OH-absorption bands were decomposed into Lorentzian components. Experimental and calculated spectra were fitted by a least-squares procedure using the Marquardt-Levenberg algorithm (Marquardt, 1963). The band component analyses were based on the objective observation of four to five absorption bands in each spectrum and on the best resulting RMS error, which was generally $\leqslant 0.05$. The area of each band was calculated as a percentage of the total OH-stretching area between 3550 and 3750 cm^{-1}.

Table 2. Location and description of kaolinite samples in the high plateau profile (P9) analyzed by IRMS.

Sample	Horizon (depth)	Texture description
104-2n (1)	Soft nodular (4 m)	Light yellow internodular clay-ferruginous matrix
104-1 (2)	as above	Orange clay-ferruginous plasma in a pedorelict ferruginous nodule
104-12 (3)	as above	Orange clay-ferruginous internodular matrix
104-11 (4)	as above	Kaolinite 'booklet' within a hematitic lithorelict nodule (see Figure 7c)
104-5 (5)	as above	as above
104-4 (6)	as above	as above
107_4 (1)	Ferricrete (2.5 m)	yellow cryptocrystalline internodular matrix (see Figure 8c)
107_10 (2)	as above	as above
107-0n (3)	as above	Clay-ferruginous matrix within a lithorelict nodule
107-3 (4)	as above	Orange matrix within a nodule (see Figure 8c,d)
107_29 (5)	as above	as above
107_8 (6)	as above	Secondary kaolinite 'booklet' within a hematitic nodule (see Figure 2)
107_2 (7)	as above	White kaolinite 'booklet' within a lithorelict nodule (see Figure 7d)
107_1 (8)	as above	Kaolinite 'booklet' coated by orange ferruginous oxy-hydroxides within a lithorelict nodule (see Figure 7e,f)
107_7 (9)	as above	Small size kaolinite coated with micronodular hematite (see Figures 3 and 8a)
110-0 (1)	Ferricrete (0.10 m)	Small-size kaolinite within a pedorelict nodule
110-1 (2)	as above	Small-size kaolinite within a nodule's yellow rim (see Figure 8b)
110-2n (3)	as above	as above
110-10 (4)	as above	Mixture of 'booklets' and small size kaolinites
110-8 (5)	as above	Kaolinite 'booklet' within a lithorelict nodule
110-11 (6)	as above	as above
110-7 (7)	as above	as above
110-13 (8)	as above	Kaolinite with inherited mica structure (see Figure 8b)

Numbers in parentheses refer to spectra in Figure 10a–c

RESULTS AND DISCUSSION

Kaolinites from standard references

Kaolinites from well-characterized standard references (Table 1) have been analyzed in thin-section by IRMS. The resulting spectra of relatively well-ordered, (1) to (4), and disordered, (5) to (8), kaolinites are presented in Figure 5 and compared to those obtained with IR spectroscopy on KBr pellets (Figure 6). Four classical absorption bands at 3695, 3668, 3650 and 3620 cm^{-1}, *i.e.* ν_1, ν_2, ν_3 and ν_4, respectively, are observed (Figures 5 and 6). Additional weaker bands are, however, also detected, at 3685 and 3645 cm^{-1}, plus a pair of very weak frequencies around 3670 cm^{-1} in the

Table 3. Location and description of kaolinite samples in the upslope profile (P11) analyzed by IRMS.

Sample	Horizon facies (depth)	Texture description
186-1 (1)	Saprolite (12 m)	Small size kaolinite with goethite
186-2 (2)	as above	as above
19-1 (3)	Saprolite (11.5 m)	as above
17-0 (4)	as above	Kaolinitic plasma with booklets (see Figure 7b)
17_3 (5)	as above	Kaolinite booklets
17_5 (6)	as above	Mixture of large and small size kaolinites (see Figure 7a)
17_6 (7)	as above	Kaolinitic plasma with smaller size kaolinite
17_7B (8)	as above	kaolinite 'booklet'
27-3 (3)	Mottled clays (8 m)	Red clay-ferruginous plasma
31-1 (1)	as above	
61-1 (2)	Soft nodular (5 m)	Pink clay matrix
33-6 (4)	Idem (5.5 m)	Clay-ferruginous matrix embedding nodules
33-8 (5)	as above	Ferruginous nodule
33-9 (6)	as above	as above
69-2 (1)	Ferricrete (1 m)	Orange-brown matrix embedding nodules
66-1 (2)	as above (2.5 m)	Clay-ferruginous matrix embedding nodules
69-1 (3)	as above (1 m)	Clay-ferruginous yellowish plasma
66-4 (4)	as above (2.5 m)	Clay-ferruginous matrix embedding nodules
66-2 (5)	as above	Clay plasma within a nodule

Numbers in parentheses refer to spectra of Figure 9a–c

Table 4. Location and description of kaolinite samples in the downslope profile (P15) analyzed by IRMS.

Sample	Horizon facies (depth)	Texture description
78-0 (1)	Soft ferricrete (12.5 m)	Yellow rim around a black nodular domain
79-2 (2)	Mottled clays (12 m)	White crypto-crystalline clayey plasma (see Figure 8e)
79-5 (3)	as above	as above
85 (4)	Soft ferricrete (8.6 m)	Orange clay-ferruginous matrix
91-2 (5)	as above (4.5 m)	White-yellowish clay matrix
94-4 (7)	Soft nodular (3.05 m)	Red-orange plasma at the edge of void crossing the matrix
96-9 (8)	Ferricrete (2.05 m)	Yellow clay matrix
96-10 (9)	as above	Orange clay-ferruginous plasma in a pedorelict nodule
96-6 (11)	as above	Kaolinite booklet
96-13 (12)	as above	as above
96-15 (13)	as above	Many kaolinite booklets
100-0 (6)	Ferricrete (0.10 m)	Yellow clay-ferruginous matrix embedding hematitic nodules (see Figure 8f)
100-13 (10)	as above	Small size kaolinite coated with micronodular hematite within a pedorelict nodule
100-9 (14)	as above	Kaolinite inside a hematitic nodule

numbers in parentheses refer to spectra of Figure 11

IRMS spectra (Figure 5). According to V.C. Farmer (pers. comm.), these can result from diffusely scattered and/or specularly reflected radiations entering the spectrometer because of the wide angles of convergence and divergence of the incident and collected radiations, respectively. It is a characteristic of reflectance spectra that weak absorption bands are enhanced, whereas strong absorption bands are replaced by a region of high reflectivity extending from the transverse to the longitudinal frequencies (Farmer, 2000); *e.g.* from 3685 to 3697 cm^{-1}. From the well-ordered to the disordered kaolinite, one observes on both figures, a shift of ν_1 and ν_4 to higher wavenumbers, and an aditional weak absorption band at ~3597 cm^{-1} in spectra (1), (2), (5) and (8), of samples A1, DCV, KGa2 and B4, respectively (Figures 5 and 6). That latter band results from Al-Fe substitution in the octahedra of the kaolinite structure, and can be denoted as ν_{Fe}. Spectrum (8) of B4 is almost like a spectrum of dickite, with only three absorption bands, the first being centered at ~3700 cm^{-1}. This could support the idea that a poorly-ordered kaolinite would be an intergrowth of kaolinite- and dickite-like structures (Farmer and Russell, 1964; Barrios *et al*., 1977; Lombardi *et al*., 1987; Prost *et al*., 1989). The resemblance between the IR and IRMS spectra (Figures 5 and 6) has motivated the application of the IRMS technique to kaolinite samples of soil thin-sections.

Kaolinites of lateritic weathering profiles

Lateritic weathering kaolinites have been examined in each petrographical facies of three different vertical profiles, as described above (Figure 1; Tables 2–4). Two kinds of kaolinite were analyzed using IRMS: large (10–20 μm) crystals stacked as 'booklets' in saprolite (Figure 7a,b), and also in lithorelic ferruginous nodules, (either as secondary crystallizations or intimately associated with Fe oxyhydroxides (Figures 2, 7c–f)); and small ($\leqslant$2 μm) randomly-oriented kaolinites in crypto-crystalline clay-ferruginous matrices inside or around ferruginous nodules (Figures 3, 8a to d and 8f), or also in illuviated gray-white clay deposits filling large elongate voids looking like 'socks' (Figure 8e). These two types of kaolinite were observed throughout the three profiles, from the saprolite to the ferricrete, within the clay-ferruginous matrices and the nodules (Tables 2 to 4); and they have been distinguished according to their respective IRMS spectrum (Figures 9 to 11). In Figures 9 to 11, examples of spectra are presented for the different kaolinite crystal sizes of different weathering facies in upslope (pit 11), high plateau (pit 9) and downslope (pit 15) profiles (Figure 1). The numerous IRMS spectra presented account for the diversity of clay textures observed in the thin-sections (Tables 2–4; Figures 2, 3, 7 and 8).

Examination of the different spectra in the OH-stretching region ranging from 3550 to 3750 cm^{-1} reveals the four classical bands represented by vertical straight lines in Figures 9 to 11, which correspond to the four well-known OH-stretching bands, ν_1, ν_2, ν_3 and ν_4 at ~3695, 3668, 3650 and 3620 cm^{-1}, respectively. As already noted, weak absorptions ascribed to TO mode are also observed (Figures 9 to 11). These bands will not be considered in the curve-fitting procedure. In the following, some representative types of large-size and small-size kaolinites are described with their respective FTIR spectrum in the OH-stretching region ranging from 3550 to 3750 cm^{-1}.

Large-size kaolinites. Kaolinites from the saprolite of the upslope profile, P11, derive from the pseudomorphic weathering of parent minerals like amphiboles, plagio-

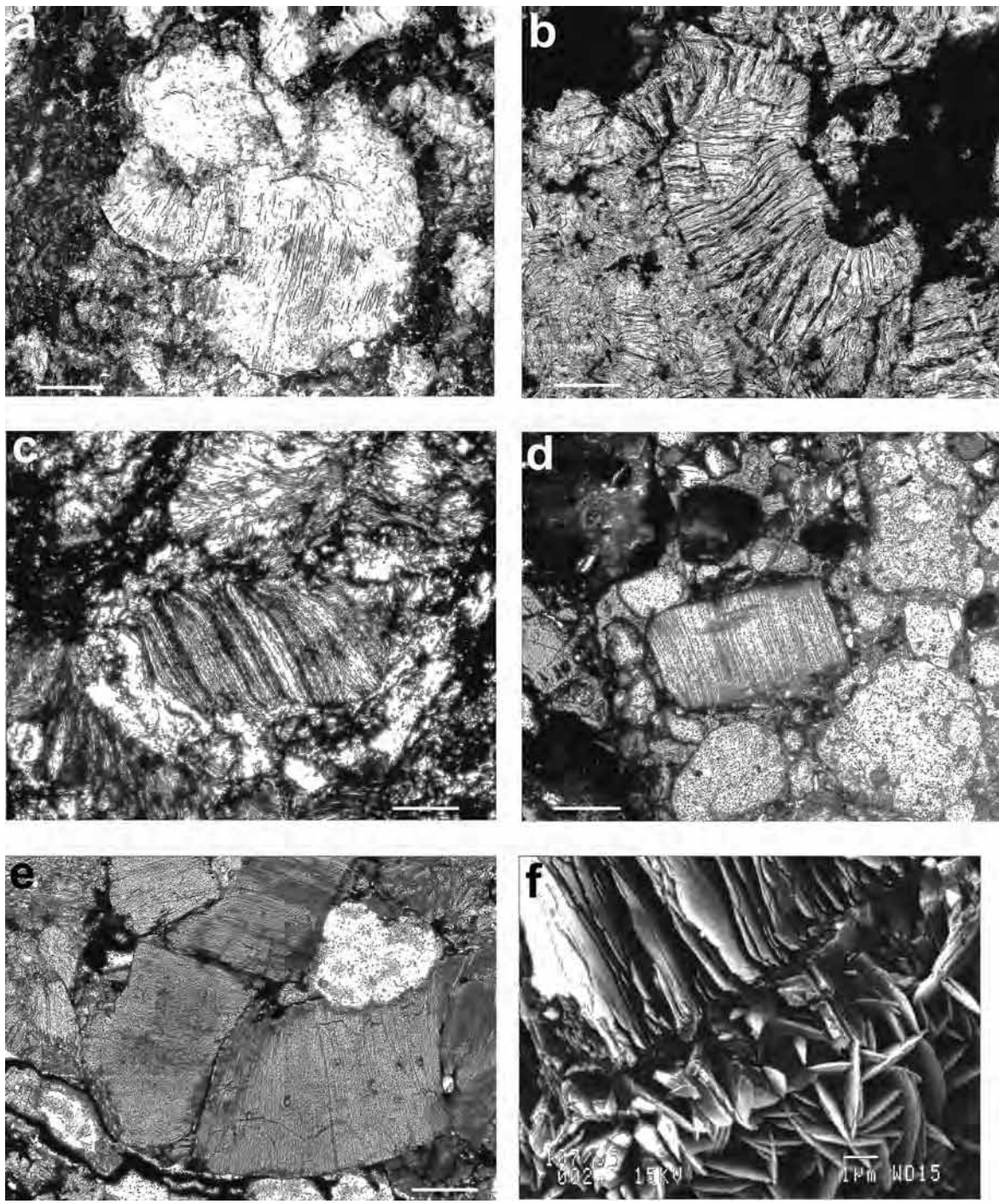

Figure 7. Large-size well-crystallized kaolinites: (a) and (b) in the saprolite of the upslope profile (scale bar = 10 μm); (c) in the soft nodular horizon with more or less ferruginous coatings (scale bar = 5 μm); (d) and (e) in the ferricrete of the high plateau profile (scale bar = 10 μm). (a) to (e) Polarized optical micrographs and (f) scanning electron micrograph of kaolinite 'booklets' coated by goethite crystals in the ferricrete of the high plateau profile (scale bar = 1 μm).

clases, chlorites, epidotes and phengites (Beauvais, 1999). Although the volume of parent minerals is preserved, the kaolinites may have different sizes and morphologies (Figure 7a,b) and exhibit different IRMS spectra labeled 4 and 6 for the larger ones and 3 for the smaller ones in Figure 9a. The spectra labeled 4, 5 and 6 in Figure 10a correspond to large-size kaolinite 'booklets' inside lithorelic nodules of the soft nodular horizon of the high plateau profile (Figure 10c). The large kaolinite 'booklets' of Figure 7d–f in the ferricrete of the high plateau

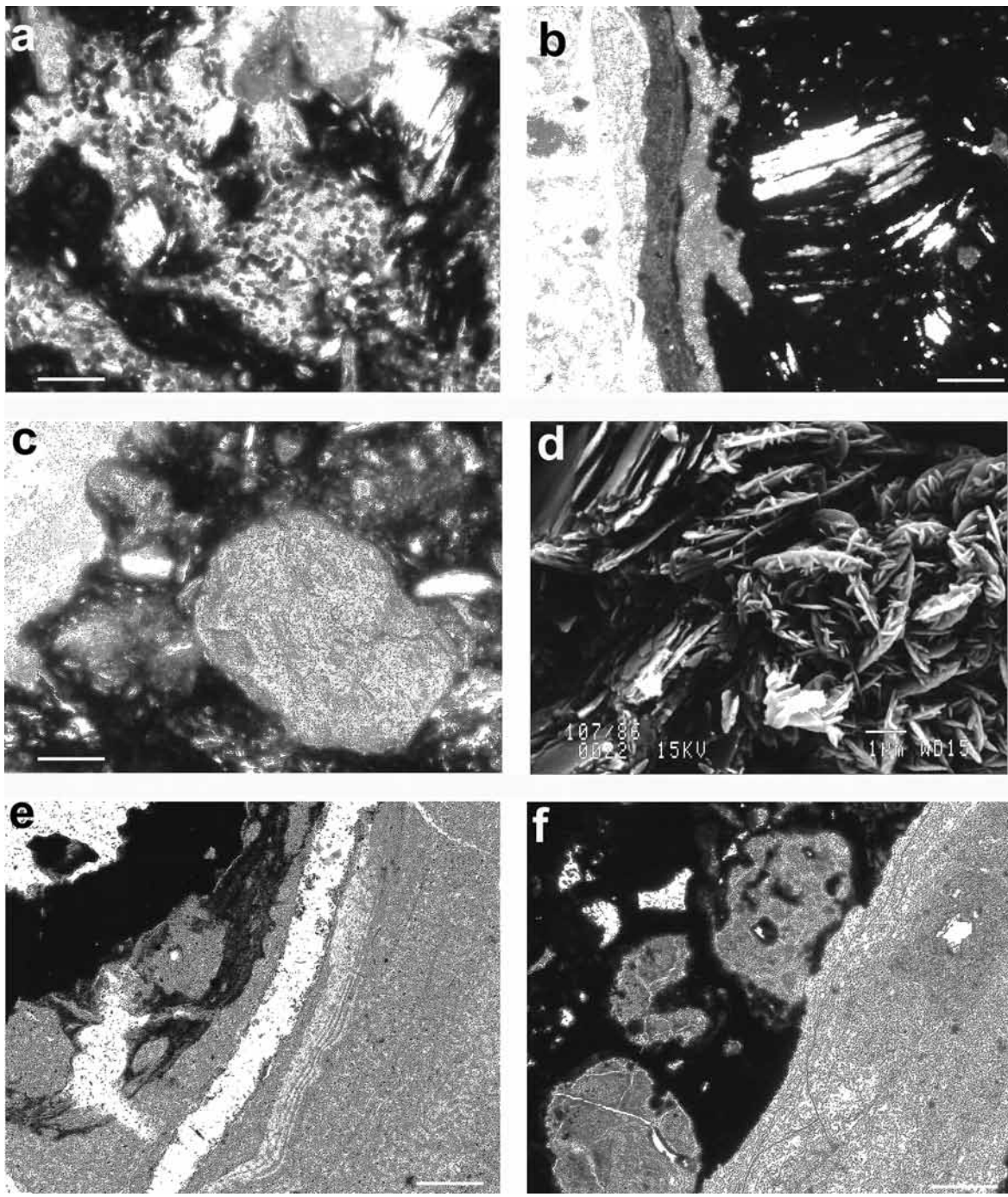

Figure 8. Small-size kaolinites in the ferricrete of the high plateau profile. (a) Well-crystallized, associated with micronodular hematite (scale bar = 5 µm). (b) Poorly-crystallized within yellow crypto-crystalline clay ferruginous matrices (lighter left part of the photomicrograph) around a ferruginous nodule containing a kaolinite 'booklet' with inherited micas structure (scale bar = 10 µm). (c) Within orange matrices in nodules (light gray in the center of the photomicrograph) (scale bar = 5 µm). (d) Scanning electron micrograph of small size kaolinites with goethite (scale bar = 1 µm). (e) In the downslope profile, poorly-crystallized kaolinite in illuviated clay material filling a large void in the soft ferricrete (scale bar = 10 µm). (f) In a yellow clay ferruginous matrix (light gray, right-hand side of the photomicrograph) enclosing a nodule of the ferricrete (scale bar = 10 µm).

profile exhibit spectra labeled 7 and 8 in Figure 10b, respectively, while the secondary kaolinite 'booklets' crystallized in voids (Figure 2) have a spectrum labeled 6 in Figure 10b. Large kaolinite with inherited mica structure (Figure 8b) in ferricrete at the top of the high plateau profile gives spectrum 8 in Figure 10c.

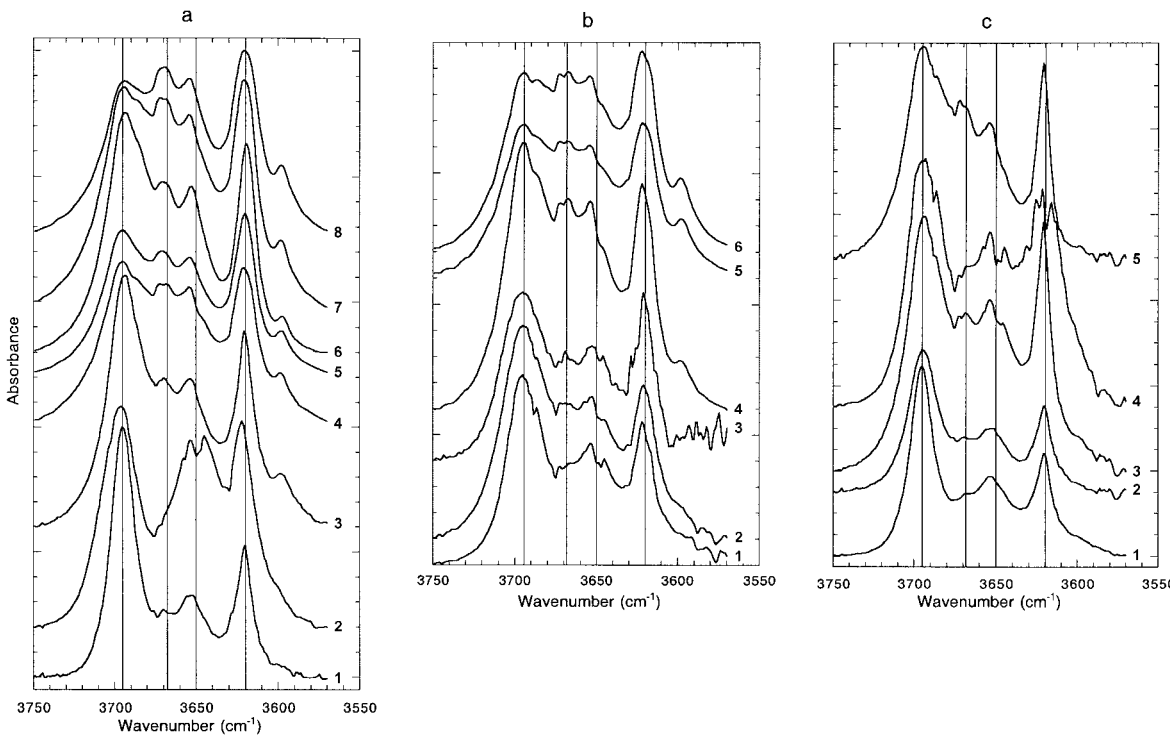

Figure 9. IRMS spectra of the two types of kaolinite in the upslope profile, pit 11; (a) in the saprolite horizon (1–3 = small-size kaolinites; 4–8 = large-size kaolinites); (b) in the mottled clays and soft nodular horizons (1–3 = small-size kaolinites; 4–6 = large-size kaolinites); (c) in the ferricrete horizon (1–4 = small-size kaolinites; 5 = large-size kaolinites). See Figure 5 for an explanation of the vertical lines.

Large-size kaolinites exhibit various IRMS spectra according to the differences in band intensities of the inner-surface hydroxyls (Figures 9–11). These are characterized by five bands, ν_2 standing for the 3668 cm^{-1} band is particularly well resolved. A band at ~3595 cm^{-1} assigned as ν_{Fe} has been also detected, reflecting structural Fe^{3+} substituting for Al^{3+}. The intensity of this well-known vibration band is generally in proportion to the Fe^{3+} substitution rate for Al^{3+} in octahedral sites of the kaolinite structure (Mestdagh *et al.*, 1980; Cases *et al.*, 1982; Delineau *et al.*, 1994). A frequency attributed to TO mode of the in-phase OH-stretching vibration also occurs at ~3685 cm^{-1}.

Small-size kaolinites. Small-size kaolinites associated with micronodular hematite in ferricrete of high plateau profiles (Figures 3 and 8a) give rise to spectrum 9 in Figure 10b. Small-size kaolinites of crypto-crystalline clay-ferruginous plasma inside nodules of ferricrete (Figure 8c) give spectrum 4 in Figure 10b. Ferruginous nodules of ferricretes are generally embedded into a crypto-crystalline yellow clay-ferruginous matrix (Figure 8b,c,f), the kaolinite of which is very small, $\leqslant 1$ μm. That kaolinite is characterized by IRMS spectra labeled 1 and 2 in Figure 10b, 2 in Figure 10c or 6 in Figure 11. Small-size kaolinites may also have been translocated by illuviation processes through large pores and voids of the soft ferricrete in the downslope profile. Such a clay material is typically oriented (Figure 8e) and has spectra labeled 2 or 3 in Figure 11.

Small-size kaolinites have spectra indicating they are poorly-ordered, with a good resolution of bands at 3700, 3654 and 3620 cm^{-1} but with ν_2 of large-size kaolinite being weak or absent. The band ν_{Fe} is commonly present but weaker than in spectra of large-size kaolinites (Figures 9–11). Some spectra also exhibit an additional band at ~3645 cm^{-1}. Such a frequency has been reported in Raman spectra of coarsely-crystalline dickite by Johnston *et al.* (1998). In the IRMS spectra of small poorly-ordered kaolinites, the bands at 3654 and 3645 cm^{-1} could arise from regions of dickite- and nacrite-like stacking, respectively (Farmer and Russell, 1964; Barrios *et al.*, 1977; Lombardi *et al.*, 1987; Prost *et al.*, 1989), or at least from the mixture of high- and low-defect kaolinites (Johansson *et al.*, 1998).

Before differentiating each kaolinite type by band area measurements, we should point to some obvious differences between the two types. From the small-size to the large-size kaolinites, there is an increasing intensity of the band at 3668 cm^{-1}, ν_2, a decreasing intensity of the band at 3695 cm^{-1}, ν_1, and the occurrence of a well-resolved band at ~3595 cm^{-1}, ν_{Fe}, this last band being very poorly expressed in the spectra of small-size kaolinites (Figures 9–11). Some

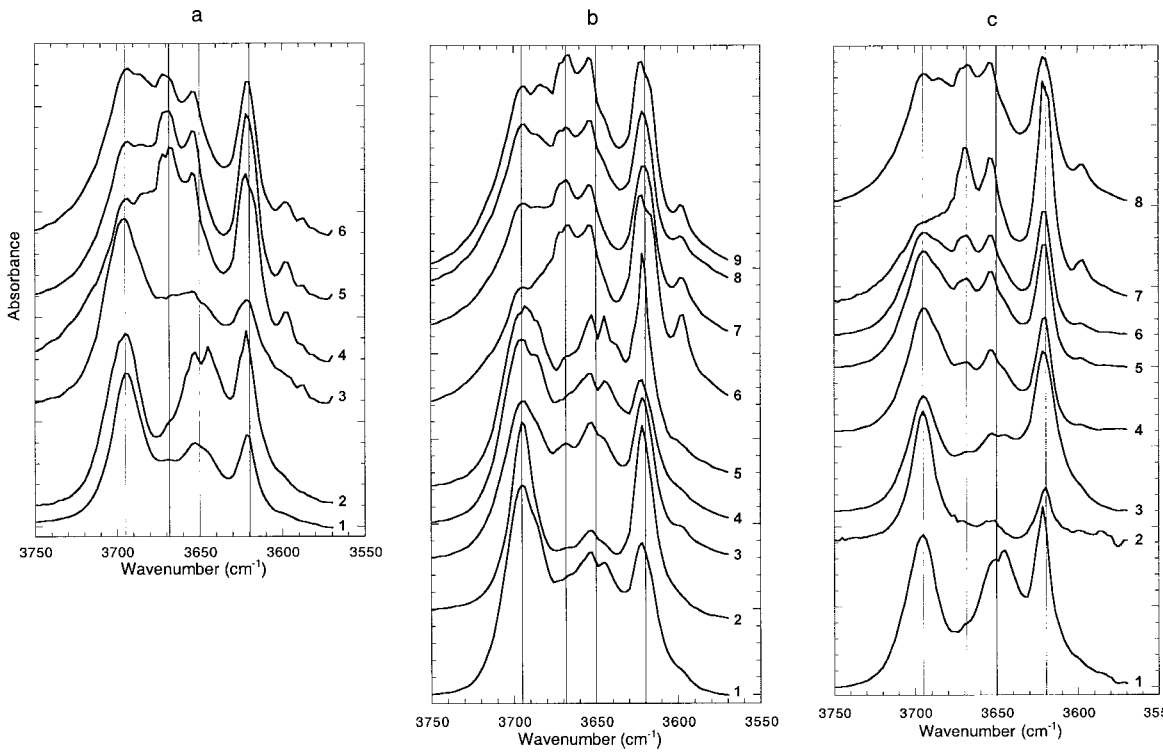

Figure 10. IRMS spectra of the two types of kaolinite in the high plateau profile, pit 9; (a) in the soft nodular horizon (1–3 = small-size kaolinites; 4–6 = large-size kaolinites); (b) at 2 m depth in the ferricrete horizon (1–5 = small-size kaolinites; 6–9 = large-size kaolinites); (c) at 0.10 m depth in the ferricrete horizon (1–4 = small-size kaolinites; 5–8 = large-size kaolinites). See Figure 5 for an explanation of the vertical lines.

large-size kaolinites also show a LO/TO pair in the 3668–3670 cm^{-1} region, while many small-size kaolinites exhibit a band at 3645 cm^{-1} near ν_3.

Large-size vs. small-size kaolinites. Only the significant linear relationships between the band areas have been examined to distinguish the large-size from the small-size kaolinites. Five bands were used for the decomposition, ν_1, ν_2, ν_3, ν_4 and ν_{Fe} when it was necessary. As ν_1, ν_2 and ν_3 in well-ordered kaolinites have been ascribed to coupled in-phase and out-of-phase inner surface hydroxyls (Rouxhet *et al*., 1977; Frost and van der Gaast, 1997; Farmer, 1998), the relationships between the areas of these three absorption bands were examined. The plot of the area of ν_2, ($A\nu_2$), against the area of ν_1, ($A\nu_1$), discriminates the two groups of kaolinite, with the large-size kaolinites characterized by $15 < A\nu_2 < 31$ and $18 < A\nu_1 < 50$, while the small-size kaolinites have $4 < A\nu_2 < 18$ and $35 < A\nu_1 < 53$ (Figure 12).

The plot of the area of ν_2 against that of ν_3 also obviously discriminates large-size from small-size kaolinites around an area ratio of ν_2 over ν_3 equal 1 (Figure 13a). The area of the 3668 cm^{-1} band (ν_2) and more generally the ratio of the areas of ν_2 and ν_3 reflects the structural order-disorder of the kaolinite, *i.e.* $A\nu_2/A\nu_{3(\text{disordered kaolinites})} \leqslant 1 \leqslant A\nu_2/A\nu_{3(\text{ordered kaolinites})}$ (Cases *et al*., 1982; Brindley *et al*., 1986). This is confirmed by Figure 14, where the reference kaolinites exhibit good correlations between the disorder indexes R2 and E_{120K} given in the Table 1 and the ratio $A\nu_2/A\nu_3$, this effectively being a reliable IR order index for the kaolinites. Well-ordered kaolinites are characterized by the highest values of R2 and $A\nu_2/A\nu_3$, and the lowest E_{120K}, whereas the disordered kaolinites exhibit low R2, high E_{120K}, and low $A\nu_2/A\nu_3$ (Table 1, Figure 14). According to Figure 13b, large kaolinites are characterized by a ratio $A\nu_2/A\nu_3$ ranging from 0.81 to 1.84, while it averages ~0.5, ranging from 0.09 to 0.81, for small kaolinites (Figure 13b). This implies that large-size kaolinites are well ordered whereas most small-size kaolinites are rather disordered. Based on results obtained from IR spectroscopy on KBr pellets, it has, however, long been thought that the more structural defects a kaolinite contained, the more it incorporated octahedral Fe^{3+}, and thus, the more it was disordered (Mestdagh *et al*., 1980; Cases *et al*., 1982). Our results, however, show quite a different trend, with a significant positive correlation between the areas ratio $A\nu_2/A\nu_3$ and $A\nu_{Fe}$, the latter being larger for the large kaolinites than for the smaller ones (Figure 13b). This means that, under natural lateritic conditions, large-size kaolinites stacked as 'booklets' can crystallize in large voids from Fe-rich (Si, Al) solutions and have crystal chemical characteristics of

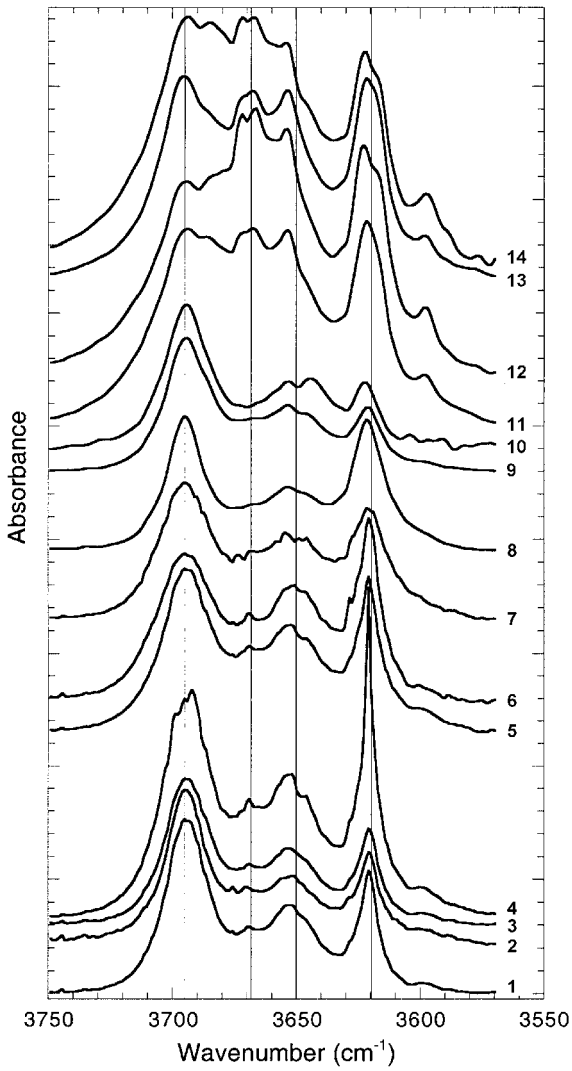

Figure 11. IRMS spectra of the two types of kaolinite from the mottled clays and the soft ferricrete at the bottom to the ferricrete horizon at the top of the downslope profile, pit 15 (1–10 = small-size kaolinites; 11–14 = large-size kaolinites). See Figure 5 for an explanation of the vertical lines).

well-ordered kaolinite, whereas small-size kaolinites can be poorly ordered and poor in Fe. These results show that the quantity of Fe in the octahedral structure of kaolinite is not simply related to the IR order index, $A\nu_2/A\nu_3$, and thus to the structural order of the kaolinite. Well-ordered kaolinites with structural Fe have been synthetized (Petit and Decarreau, 1990), and this is also consistent with the positive relation of $A\nu_2/A\nu_3$ to $A\nu_{Fe}$ (Figure 13b).

For small-size kaolinite, the areas of ν_2 and ν_{Fe} are not correlated, indicating that if these kaolinites are all the more disordered as the area of ν_2 is reduced, they can exhibit various amounts of Fe substitution for Al (Figure 13b). Low-defect or less-disordered kaolinites can incorporate large amounts of Fe, meaning that the relation between the octahedral substitution of Fe^{3+} for

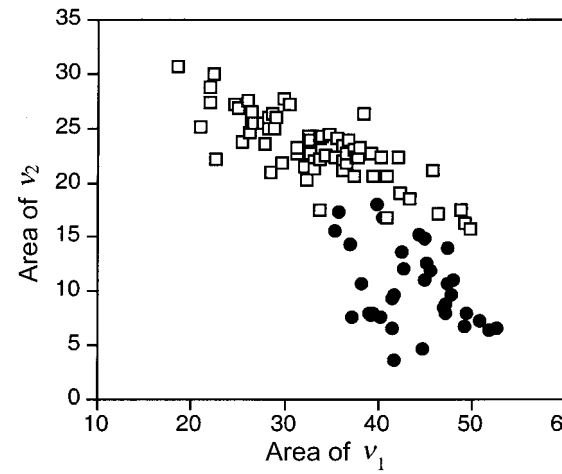

Figure 12. Relationships between the band intensities of the inner surface hydroxyls, $A\nu_2$ *vs.* $A\nu_1$ (open squares = kaolinite 'booklets'; filled circles = small-size kaolinites).

Al^{3+} and the proportion of structural defects and/or stacking faults is not as obvious as previously believed. Large-size and small-size kaolinites probably have different growth kinetics and thermodynamics that control the amount of structural defects on the one hand, and the amount of structural Fe on the other hand, without any simple relationship between one and the other.

To summarize, the two kaolinite groups have been clearly distinguished using band area measurements (Figures 12,13). The large-size kaolinites are all the more ordered as the areas of ν_2, ν_{Fe} and the ratio of the areas ν_2:ν_3 are all large. The crystal chemical characteristics of the best-ordered kaolinites agree well with the results published by Petit and Decarreau (1990) on Fe^{3+}-doped kaolinites obtained from synthesis products. The small-size kaolinites are all the more disordered as the area of ν_2 andν_{Fe} are low, and as the area of ν_1 and ν_3 are, on average, relatively higher than those of the large-size kaolinites (Figures 12,13a). No particular differences were found within the same group of kaolinites, large or small, according to the different horizons of the same weathering profile; this limits the interpretation of the results in terms of geochemical process signatures.

We have, however, noticed that, within the group of large-size kaolinite stacked as 'booklets', a majority of those exhibiting the highest $A\nu_2/A\nu_3$ and $A\nu_{Fe}$ (Figure 13b) have secondary crystals of gibbsite in large voids (Figure 2). This requires percolation of Fe-rich (Si, Al) solutions through the weathering profiles; such solutions are likely in a semi-humid wooded environment with high organic-matter contents (Beauvais and Tardy, 1991). Under such pedoclimatic conditions, the geochemical degradation of the upper ferruginous horizons, *i.e.* the ferricretes, effectively permits the partial release of Fe with Al and silica (Beauvais, 1999). It was recently suggested that the actual weathering profiles have undergone past pedoclimatic changes that could explain the variety of weath-

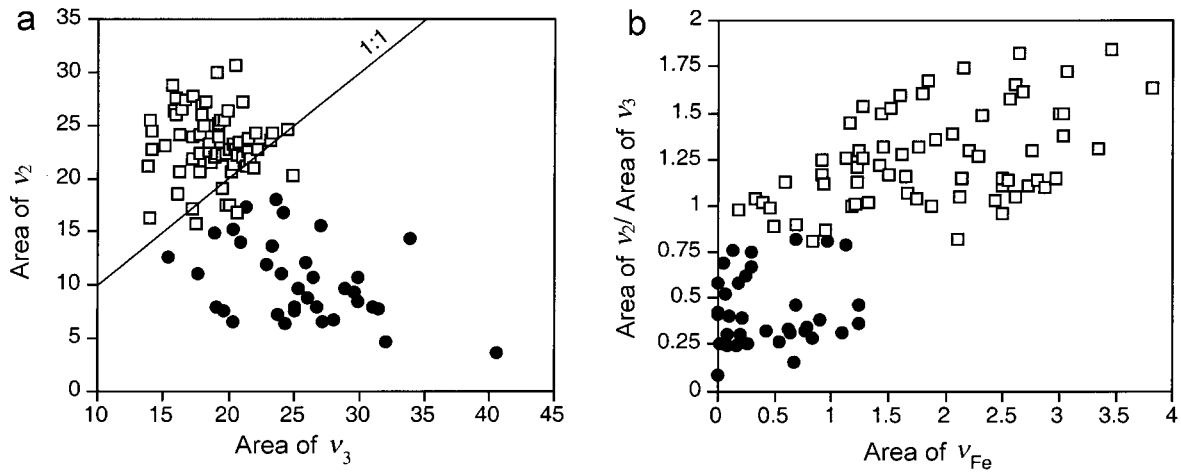

Figure 13. Relationships between the band intensities of the inner surface hydroxyls. (a) $A\nu_2$ *vs.* $A\nu_3$; the 1:1 straight line is for $A\nu_2 = A\nu_3$. (b) $A\nu_2/A\nu_3$ *vs.* $A\nu_{Fe}$ at 3595 cm^{-1} (see Figure 12 for an explanation of the symbols).

ering facies and kaolinites as well (Beauvais, 1999). No obvious crystal chemical differences have, however, been noted between the kaolinite 'booklets' of the saprolite and those observed in the nodules of the soft nodular horizon or in the hematitic matrices of the ferricrete. Our results mean that perhaps some kaolinite 'booklets' of the matrices of the upper ferruginous horizons could have been inherited from previous saprolitic materials (Beauvais, 1999), while the secondary kaolinite 'booklets' associated with gibbsite crystals in large voids crossing the primary structures could be good mineralogical tracers of the ferricrete degradation described earlier (Beauvais and Tardy, 1991; Beauvais, 1999). Further IRMS investigations would, however, be necessary to differentiate better the different types of kaolinite 'booklets', and to relate their OH absorption band patterns to specific geochemical processes.

CONCLUSIONS

Infrared microscopy is a valuable technique for measuring *in situ* the OH-absorption bands of selected kaolinites directly on soil thin-sections. Although the low frequencies of the IR spectrum of kaolinite are perturbed by the presence of glass, resin and glue used in preparing the thin-sections, the information contained in the OH-stretching region is of sufficient quality to distinguish different kinds of kaolinite. Contributions of this technique with respect to the KBr pellets method are (1) the *in situ* analysis of clay minerals within oriented undisturbed rock samples, and (2) the differentiation of well-ordered and poorly-ordered kaolinites according to their respective size and texture in the rock sample. The IRMS results show that the ratio of the integrated intensities of ν_2 at 3668 cm^{-1} over ν_3 at 3650 cm^{-1}, $A\nu_2/A\nu_3$, remains a good index of structural order for the kaolinites. Lateritic weathering kaolinites could be intergrowths of kaolinite- and dickite-like structures or at least mixtures of low- and high-defect kaolinites whether they are large or small, the relative contribution of which reflecting various geochemical, thermodynamic and/or growth kinetics conditions controlling the kaolinite formation. Clay mixtures are quite likely in the studied weathering profiles in which recent evolution can be traced from secondary kaolinite 'booklets', which are the best ordered and more ferruginous.

ACKNOWLEDGMENTS

This work is dedicated to the late Prof. Ph. Ildefonse. It is a contribution from IRD (UR 037 and UR055) and Cerege. Dr T. Allard and the LMC laboratory (University of Paris 6 and 7) are gratefully aknowledged for providing us with reference kaolinites. Dr V.C. Farmer and an anonymous referee are acknowledged for their useful critiques of a previous version. The authors are particularly grateful to Dr V.C. Farmer for providing them with a reprint of his recent publication and for his invaluable comments throughout the review process.

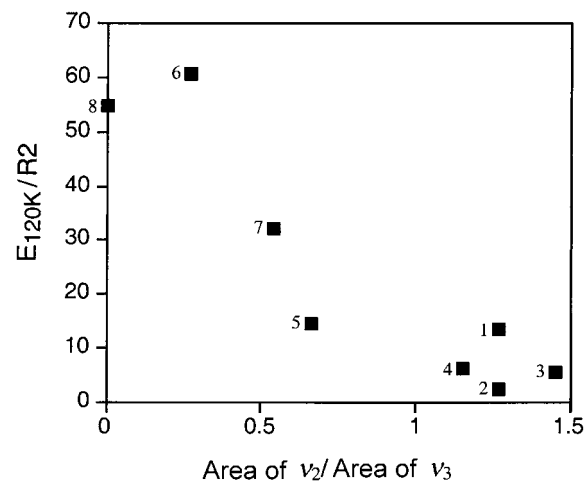

Figure 14. Relationships between the ratio of the disorder indexes, E_{120K}/R2, and $A\nu_2/A\nu_3$ for the well-characterized reference kaolinites (see Table 1 for an explanation of E_{120K} and R2, and for the numbers attached to the filled squares).

REFERENCES

Allard, T. (1994) La kaolinite: un dosimètre des rayonnements naturels. Application au traçage de migrations anciennes de radioéléments dans la géosphère. Ph.D. thesis, Université de Paris VII, Paris, France, 205 pp.

Ambrosi, J.-P. and Nahon, D. (1986) Petrological and geochemical differentiation of lateritic iron crust profiles. *Chemical Geology*, **57**, 371–393.

Angel, B.R., Jones, J.P.E. and Hall, P.L. (1974) Electron spin resonance studies of doped synthetic kaolinite. I. *Clay Minerals*, **10**, 247–255.

Balan, E., Allard, Th., Boizot, B., Morin, G. and Muller, J.-P. (1999) Structural Fe^{3+} in natural kaolinites: new insights from electron paramagnetic resonance spectra fitting at X and Q-band frequencies. *Clays and Clay Minerals,* **47**, 605–616.

Barrios, J., Plançon, M., Cruz, I. and Tchoubar, C. (1977) Qualitative and quantitative study of stacking faults in a hydrazine treated kaolinte – Relationship with the infrared spectra. *Clays and Clay Minerals,* **25**, 422–429.

Beauvais, A. (1991) Paléoclimats et dynamique d'un paysage cuirassé du Centrafrique. Morphologie, Pétrologie et Géochimie. Ph.D. thesis, Université de Poitiers, Poitiers, France, 317 pp.

Beauvais, A. (1999) Geochemical balance of lateritization processes and climatic signatures in weathering profiles overlain by ferricretes in Central Africa. *Geochimica et Cosmochimica Acta,* **63**, 3939–3957.

Beauvais, A. and Colin, F. (1993) Formation and transformation processes of iron duricrust systems in tropical humid environment. *Chemical Geology*, **106**, 77–151.

Beauvais, A. and Tardy, Y. (1991) Formation et dégradation des cuirasses ferrugineuses sous climat tropical humide, à la lisière de la forêt équatoriale. *Comptes Rendus de l'Académie des Sciences, Paris,* Séries II, **13**, 1539–1545.

Bell, V.A., Citro, V.R. and Hodge, G.D. (1991) Effect of pellet pressing on the infrared spectrum of kaolinite. *Clays and Clay Minerals,* **39**, 290–292.

Bish, D.L. (1993) Rietveld refinement of the kaolinite structure at 1.5 K. *Clays and Clay Minerals,* **41**, 738–744.

Brindley, G.W., Kao C.-C., Harrison, J.L., Lipsicas, M. and Raythatha, R. (1986) Relation between structural disorder and other characteristics of kaolinites and dickites. *Clays and Clay Minerals,* **34**, 239–249.

Cantinolle, P., Didier, P., Meunier, J.-D., Parron, C., Guendon, J.-L., Bocquier, G. and Nahon, D. (1984) Kaolinites ferrifères et oxyhydroxydes de fer et d'alumine dans les bauxites des Canonettes (S.E. de la France). *Clay Minerals*, **19**, 125–135.

Cases, J.-M., Liétard, O., Yvon, J. and Delon, J.-F. (1982) Etude des propriétés cristallochimiques, morphologiques, superficielles de kaolinites désordonnées. *Bulletin de Minéralogie*, **105**, 439–455.

Cruz-Cumplido, M., Sow, C. and Fripiat, J.J. (1982) Spectre infrarouge des hydroxyles, cristallinité et énergie de cohésion des kaolins. *Bulletin de Minéralogie*, **105**, 493–498.

Delineau, T., Allard, T., Muller, J.-P., Barres, O., Yvon, J. and Cases, J.-M. (1994) FTIR reflectance *vs*. EPR studies of structural iron in kaolinites. *Clays and Clay Minerals,* **42**, 308–320.

Didier, P., Nahon, D., Fritz, B. and Tardy, Y. (1983) Activity of water as a geochemical controlling factor in ferricretes. A thermodynamic model in the system kaolinite Fe-Al oxyhydroxides. *Sciences Geologiques,* **71**, 25–44.

Farmer, V.C. (1964) Infrared absorption of hydroxyls groups in kaolinite. *Science*, **145**, 1189–1190.

Farmer, V.C. (1974) *The Infrared Spectra of Minerals*. Monograph **4.** The Mineralogical Society, London, 539 pp.

Farmer, V.C. (1998) Differing effects of particle size and shape in the infrared and Raman spectra of kaolinite. *Clay Minerals*, **33**, 601–604.

Farmer, V.C. (2000) Transverse and longitudinal crystal modes associated with OH stretching vibrations in single crystals of kaolinite and dickite. *Spectrochimica Acta*, **56A**, 927–930.

Farmer, V.C. and Russell, J.D. (1964) The infrared spectra of layer silicates. *Spectrochimica Acta*, **20**, 1149–1173.

Frost, R.L. and Johansson, U. (1998) Combinations bands in the infrared spectroscopy of kaolins – a drift spectroscopic study. *Clays and Clay Minerals,* **46**, 466–477.

Frost, R.L. and Van der Gaast, S.J. (1997) Kaolinite hydroxyls – a Raman microscopy study. *Clay Minerals*, **32**, 471–484.

Gaite, J.-M., Ermakoff, P. and Muller, J.-P. (1993) Characterization and origin of two Fe^{3+} EPR spectra in kaolinite. *Physics and Chemistry of Minerals*, **20**, 242–247.

Gaite, J.-M., Ermakoff, P., Allard, Th. and Muller, J.-P. (1997) Paramagnetic Fe^{3+}: a sensitive probe for disorder in kaolinite. *Clays and Clay Minerals,* **45**, 496–505.

Giese, R.F., Jr. (1988) Kaolin minerals. Structures and stability. Pp. 29–66 in: *Hydrous Phyllosilicates* (S.W. Bailey, editor). Reviews in Mineralogy, **19**. Mineralogical Society of America, Washington, D.C.

Herbillon, A.J. (1980) Mineralogy of oxisols and oxic materials. Pp. 109–126 in: *Soils with Variable Charge* (B.K.G. Theng, editor). New Zealand Society of Soil Science, Wellington, New Zealand.

Hinckley, D.N. (1963) Variability in "crystallinity" values among the kaolin deposits of the coastal plain of Georgia and South Carolina. Pp. 229–235 in: *Proceedings of the 11th National Clay Conference, Ottawa* (A. Swineford, editor). Pergamon Press, New York.

Johansson, U., Holmgren, A., Forsling, W. and Frost, R. (1998) Isotopic exchange of kaolinite hydroxyl protons: a diffuse reflectance infrared Fourier transform spectroscopy study. *Analyst,* **123**, 641–645.

Johnston, C.T., Sposito, G. and Birge, R.R. (1985) Raman spectroscopy study of kaolinite in aqueous suspension. *Clays and Clay Minerals,* **33**, 483–489.

Johnston, C.T., Agnew, S.F. and Bish, D.L. (1990) Polarized single-crystal Fourier-transform infrared microscopy of Ouray dickite and Keokuk kaolinite. *Clays and Clay Minerals,* **38**, 573–588.

Johnston, C.T., Helsen, J., Schoonheydt, R.A., Bish, D.L. and Agnew, S.F. (1998) Single-crystal Raman spectroscopic study of dickite. *American Mineralogist*, **83**, 75–84.

Jones, J.P.E., Angel, B.R. and Hall, P.L. (1974) Electron spin resonance studies of doped synthetic kaolinite. II. *Clay Minerals*, **10**, 257–270.

Ledoux, R.L. and White, J.L. (1964) Infrared study of selective deuteration of kaolinite and halloysite at room temperature. *Science*, **145**, 47–49

Lombardi, G., Russell, J.D. and Keller, W.D. (1987) Compositional and structural variations in the size fractions of a sedimentary and a hydrothermal kaolin. *Clays and Clay Minerals,* **35**, 321–335.

Lucas, Y., Chauvel, A. and Ambrosi, J.-P. (1987) Processes of aluminium and iron accumulation in latosols developed on quartz-rich sediments from central Amazonia (Manaus, Brazil). Pp. 289–299 in: *Proceedings of the International Meeting on Geochemistry of the Earth Surface and Processes of Mineral formation, Granada, Spain* (R. Rodríguez-Clemente and Y. Tardy, editors). Madrid: Consejo Superior de Investigaciones Cientificas; Paris: Centre National de la Recherche Scientifique (CNRS).

Marquardt, D.W. (1963) An algorithm for least-squares estimation of nonlinear parameters. *Journal of the Society*

of Industrial Applied Mathematics, **11**, 431–441.

Meads, R.E. and Malden, P.S. (1975) Electron-spin resonance in natural kaolinites containing Fe^{3+} and other transition metal ions. *Clay Minerals*, **10**, 313–345.

Mendelovici, E., Yariv, S.H. and Villalba, R. (1979) Iron-bearing kaolinite in Venezuelan laterite. I. Infrared spectroscopy and chemical dissolution evidence. *Clay Minerals*, **14**, 323–331.

Mestdagh, M.M., Vielvoye, L. and Herbillon, A.J. (1980) Iron in kaolinite: II. The relationship between kaolinite crystallinity and iron content. *Clay Minerals*, **15**, 1–13.

Mestdagh, M.M., Herbillon, A.J., Rodrique, L. and Rouxhet, P.G. (1982) Evaluation du rôle du fer structural sur la cristalinité des kaolinites. *Bulletin de Minéralogie*, **105**, 457–466.

Millot, G. (1970) *Geology of Clays: Weathering, Sedimentation, Geochemistry*. Springer, New York, 429 pp.

Muller, J.-P. and Bocquier, G. (1987) Textural and mineralogical relationships between ferruginous nodules and surrounding clayey matrices in a laterite from Cameroon. Pp. 186–194 in: *Proceedings of the International Clay Conference, Denver, 1985* (L.G. Schultz, H. van Olphen and F.A. Mumpton, editors). The Clay Minerals Society, Bloomington, Indiana.

Muller, J.-P. and Calas, G. (1989) Tracing kaolinites through their defect centers: kaolinite paragenesis in a laterite (Cameroon). *Economic Geology*, **84**, 694–707.

Muller, J.-P., Manceau, A., Calas, G., Allard, T., Ildefonse, Ph. and Hazemann, J.-L. (1995) Crystal chemistry of kaolinite and Fe-Mn oxides: relation with formation conditions of low temperature systems. *American Journal of Science*, **295**, 1115–1155.

Murray, H.H. (1988) Kaolin minerals: their genesis and occurrences. Pp. 67–90 in: *Hydrous Phyllosilicates* (S.W. Bailey, editor). Reviews in Mineralogy, **19.** Mineralogical Society of America, Washington, D.C.

Nahon, D. (1991) *Introduction to the Petrology of Soils and Chemical Weathering*. John Wiley, New York, 313 pp.

Parker, T.W. (1969) Classification of kaolinites by infrared spectroscopy. *Clay Minerals*, **8**, 19–35.

Petit, S. and Decarreau, A. (1990) Hydrothermal (200°C) synthesis and crystal chemistry of iron rich kaolinites. *Clay Minerals*, **25**, 181–196.

Plançon, A., Giese, R.F. and Snyder, R. (1988) The Hinckley index for kaolinites. *Clay Minerals*, **23**, 249–260.

Plançon, A., Giese, R.F., Snyder, R., Drits, V.A. and Bookin, A.S. (1989) Stacking faults in the kaolin-group minerals: defect structures of kaolinite. *Clays and Clay Minerals*, **37**, 203–210.

Prost, R., Dameme, A., Huard, E., Driard, J. and Leydecker, J.-P. (1989) Infrared study of structural OH in kaolinite, dickite, nacrite and poorly crystalline kaolinite at 5 to 600°K. *Clays and Clay Minerals*, **37**, 464–468.

Rengasamy, P. (1976) Substitution of iron and titanium in kaolinites. *Clays and Clay Minerals*, **24**, 264–266.

Rintoul, L. and Fredericks, P.M. (1995) Infrared microspectroscopy of bauxitic pisoliths. *Applied Spectroscopy*, **49**, 1608–1616.

Rouxhet, P.G., Samadacheata, N., Jacobs, H. and Anton, O. (1977) Attribution of the OH stretching bands of kaolinite. *Clay Minerals*, **12**, 171–179.

Tardy, Y. (1993) *Pétrologie des Latérites et des Sols Tropicaux*. Masson, Paris, 535 pp.

Van Olphen, H. and Fripiat, J.-J. (1979) *Data Handbook for Clay Minerals and other Non-metallic Minerals.* Pergamon Press, Oxford, UK, 346 pp.

Wiewióra, A., Wieckowski, T. and Sokolowska, A. (1979) The raman spectra of kaolinite subgroup minerals and of pyrophyllite. *Archiwum Mineralogiczne*, **135**, 5–14.

(*Received 3 January 2001; revised 9 November 2001; Ms. 511*)

VOLET II

VOLET II - STRUCTURE GEOELECTRIQUE DES ALTERATIONS LATERITIQUES ET MORPHOGENESE

Les structures des manteaux d'altération latéritique sous-tendant des surfaces de type "glacis" ferrugineux étagés ont été imagées en 2-D par des méthodes géophysiques de tomographie de résistivité électrique (ERT) et géoradar (GPR). Le but était de définir les relations morphogénétiques entre deux systèmes d'altération cuirassés étagés dans une région (Sénégal Oriental) où les transferts latéraux de matériaux latéritiques ont été non négligeables dans le développement des manteaux d'altération et l'évolution des surfaces porteuses (Michel, 1973).

1. TEST DE LA METHODE DE TOMOGRAPHIE DE RESISTIVITE ELECTRIQUE

La tomographie de résistivité électrique (ERT) a été testée au Sénégal Oriental sur des manteaux d'altération latéritique développés sur roches granitiques et métamorphiques, dont la succession des horizons est révélée par des coupes de route et des profils excavés (Ritz et al., 1999).

Sur substrat granitique, le profil géoélectrique montre un manteau d'altération hétérogène pour lequel la résistivité apparente varie rapidement au sein d'un même horizon. Les variations latérales des propriétés électriques sont moins prononcées sur substrat schisteux que sur granite.

Dans les deux zones, le matériel sec proche de la surface est très résistant. Il s'agit de la cuirasse ferrugineuse dont la résistivité varie de 3000 à 30000 Ohm.m reflétant des variations latérales et verticales de faciès qui dépendent de la fabrique (texture) et de la richesse en fer. Les horizons de carapace ferrugineuse ont quant à eux des résistivités de l'ordre de 1000 Ohm.m. La seconde couche, intermédiaire, à faible résistivité (20-100 Ohm.m) contient de l'argile et de petites quantités d'eau. La troisième couche très résistive correspond au substrat géologique non altéré.

La comparaison des données géo-électriques avec les informations pétrographiques montre que la méthode ERT peut être utilisée comme un outil d'exploration rapide et efficace pour cartographier en continu les altérations latéritiques épaisses des domaines tropicaux.

2. STRUCTURE DES ALTERATIONS LATERITIQUES ET MORPHOGENESE

La tomographie de résistivité électrique a été employée pour étudier plus en détail la structure du manteau d'altération latéritique développé sur bedrock granitique au Sénégal Oriental et ses relations géométriques avec la géomorphologie et les structures hydrogéologiques (Beauvais et al., 1999 ; 2003).

Les données obtenues à partir d'un dispositif cross-borehole entre deux profils espacés de 10 m d'une part, et les mesures effectuées *in situ* sur les aquifères, et sur le granite affleurant dans les thalwegs d'autre part, ont été intégrées dans les modèles inverses pour obtenir des résultats plus précis sur les domaines de résistivité réelle des différentes couches d'altération. Les images dérivant de la modélisation inverse renseignent sur les relations géométriques entre les différentes couches, en particulier celles des aquifères avec le bedrock et la surface du sol (Beauvais et al., 1999).

Les relations géométriques entre les topographies discordantes du bedrock et de la surface du sol indiquent qu'une partie du manteau d'altération actuel est d'origine allochtone, ce qui est aussi corroboré par les observations pétrographiques faites sur les profils excavés (puits). La topographie actuelle du bedrock en dômes de granite sain et sillons d'altération résulte de processus d'altération différentielle (Beauvais et al., 2003). Les caractères géomorphologiques des versants résultent en revanche de processus d'érosion et-ou de l'altération latéritique de matériel remanié (pédiments) qui a finalement conduit au développement de cuirasses polygéniques sur des surfaces d'aplanissement étagées bien différenciées.

3. APPLICATION COMBINEE DE L'ERT ET DU GPR

La tomographie de résistivité électrique (ERT) a été combinée au géo-radar (GPR) pour (1) étudier dans le détail la structure de deux systèmes latéritiques étagés sur roche granitique, et (2) définir leurs relations morphogénétiques (Beauvais et al., 2004).

Le GPR fournit des données haute résolution sur les horizons ferrugineux indurés de surface (cuirasse + carapace), les horizons sous-jacents argileux (saprolite) limitant la profondeur d'investigation. Les discontinuités des réflexions détectées sur les enregistrements géoradar, correspondent à des teneurs contrastées en fer et argile des matériaux d'altération latéritique superposés, ainsi qu'à des taux différenciés de porosité et de concentration en kaolinite. L'ERT à 1.5 m d'espacement inter électrodes et le GPR permettent des investigations sur les

horizons ferrugineux indurés jusqu'à des profondeurs comparables. Les épaisseurs d'horizons estimées à partir des profils ERT et GPR correspondent assez bien à celles qui sont mesurées directement dans les profils.

Les images ERT et GPR rendent bien compte de la variabilité des faciès d'altération latéritique identifiés dans les puits foncés sur chaque surface étagée, moyen et haut glacis (Michel, 1973), lesquelles ont été modelées à la fois par des processus d'altération et de ferruginisation, puis d'érosion, ce qui a permis le développement de profils d'altération latéritique plus ou moins matures ou évolués. La surface du moyen glacis, la plus jeune, a subi seulement une phase d'altération et de développement de la cuirasse, alors que celle du haut glacis, la plus vieille, a subi deux phases des mêmes processus (Michel, 1973 ; Grandin, 1976 ; Beauvais, 1999). Le front de ferruginisation a effectivement pénétré plus profondément dans les profils du haut glacis que dans ceux du moyen glacis, comme en atteste les résistivités électriques élevées et les pseudos réflexions radars à des profondeurs de 8-10, corroborées par une épaisseur équivalente des horizons ferrugineux dans ces profils m du haut glacis. En revanche, la pseudosection ERT du moyen glacis montre une couche résistante relativement peu épaisse pour la cuirasse au-dessus d'une couche peu résistante plus épaisse de saprolite. Le profil GPR pour cette surface montre aussi un contact bien marqué à une profondeur de 5 m entre la cuirasse et les horizons peu ferrugineux argileux.

4. REEVALUATION DES PROCESSUS D'ALTERATION LATERITIQUE

Les profils géo-électriques fournissent des images 2-D de la structure des profils d'altération latéritique, des circonvolutions des fronts d'altération et par conséquent de la topographie du bedrock. En y intégrant la topographie de surface, on dispose ainsi d'images précises de versants de plusieurs centaines de mètres sur des manteaux d'altération de plusieurs dizaines de mètres. Cependant, l'imagerie géo-électrique seule ne permet pas une compréhension univoque des objets examinés. Couplée à des puits de forages, et au géoradar, elle s'avère être un complément indispensable pour évaluer les processus supergènes (altération, ferruginisation et érosion) responsables de la géomorphologie des versants étudiés. Les relations spatiales entre les topographies de surface et du bedrock permettent notamment de discuter les processus d'altération *in situ*, responsables du développement autochtone des manteaux d'altération, et les processus d'érosion responsables du transfert de produits d'altération allochtone sur les versants et de leur accumulation sur des profils tronqués de

l’aval avant leur reprise dans une nouvelle phase d’altération-ferruginisation (Beauvais et al., 1999 ; 2003).

Il est suggéré que les changements climatiques et leurs conséquences sur les processus d’altération et d’érosion sont responsables de l’évolution long terme des paysages du Sénégal Oriental.

5. ARTICLES SCIENTIFIQUES DU VOLET II

4 articles (Sénégal Oriental) : structure 2-D des manteaux d’altération, mécanismes, évolution et morphogenèse tropicale.

Journal of Applied Geophysics (Ritz et al., 1999) : Tomographie de Résistivité Electrique (ERT), tests en environnement latéritique sur deux types de substratum géologique.

Earth & Planetary Science Letters (Beauvais et al., 1999) : Tomographie de Résistivité Electrique (ERT), relations spatiales entre la topographie des versants et celle du bedrock, évolution géomorphologique d'un paysage latéritique.

Earth Surface Processes and Landforms (Beauvais et al., 2003) : Tomographie de Résistivité Electrique de l’altération différentielle d’un granite post-tectonique au sein d’un complexe de roches vertes.

Geoderma (Beauvais et al., 2004) : ERT et GPR combinés, investigation de deux systèmes cuirassés étagés et emboîtés, et relations morphogénétiques.

ARTICLE 4

ELSEVIER

Journal of Applied Geophysics 41 (1999) 335–344

JOURNAL OF APPLIED GEOPHYSICS

Electrical imaging of lateritic weathering mantles over granitic and metamorphic basement of eastern Senegal, West Africa

Michel Ritz [a,*], Jean-Claude Parisot [a], S. Diouf [b], A. Beauvais [c], F. Dione [b], M. Niang [b]

[a] *ORSTOM, Département des Ressources Minérales, BP1386, Dakar, Senegal*
[b] *UCAD, Département de Géologie, Dakar, Senegal*
[c] *ORSTOM, Centre D'Ile de France, UR062-RED, 32 av. Henri Varagnat, Bondy, France*

Received 6 July 1998; accepted 10 February 1999

Abstract

The electrical properties of several tens of metres of lateritic weathering mantle were investigated by using electrical resistivity tomography (ERT) in two basement areas of eastern Senegal. The field survey was conducted along two profiles providing continuous coverage. Colour-modulated pseudosections of apparent resistivity vs. pseudo-depth were plotted for all survey lines, giving an approximate image of the subsurface structure. In the area underlain by granitic basement, the pseudosection suggests a very inhomogeneous weathered layer in which the apparent resistivity changes more rapidly than thickness. In the second area, underlain by schists, the lateral changes in electrical properties are less pronounced than those of the granitic area. Interpretation of 2D Wenner resistivity data yielded considerable detail about the regolith, even without pit information. In both areas, the near-surface topsoil comprising undersaturated lateritic material is highly resistive. The intermediate layer with low resistivities (e.g., 20–100 Ωm) contains clays including small quantities of water. The third, highly resistive layer reflects the granitic basement. Comparison of ERT survey results with pit information shows general agreement and suggests that ERT can be used as a fast and efficient exploration tool to map the thick lateritic weathering mantle in tropical basement areas with hard rock geology.

Keywords: Electrical imaging; Tropical weathering; Saprolite; Iron crust; Two-dimensional resistivity models; Senegal

1. Introduction

Overburden cover is common in most parts of the world. In eastern Senegal and other tropical regions, the overburden mostly consists of a thick lateritic weathering mantle. The landscape of eastern Senegal is characterized by large flattened surfaces deeply dissected by erosion processes. These surfaces are generally covered by iron crusts under which develop thick clay-rich weathering material. The thickness of these horizons can exceed several tens of meters depending on the nature of the fresh rock and the geomorphological situation (Blot et al., 1976; Leprun, 1979). A knowledge of the weathering layers and processes is important in groundwater prospecting, evaluation of the mineral poten-

* Corresponding author. Tel.: +221-832-34-80; Fax: +221-832-43-07; E-mail: ritz@dakar.orstom.sn

0926-9851/99/$ - see front matter
PII: S0926-9851(99)00008-7

tial, and geologic mapping (Palacky and Kadekaru, 1979; Hazell et al., 1992). Geophysical surveys can play a major role in the acquisition of such a knowledge. Recent works have shown that the application of direct current (DC) resistivity methods can reveal details of the weathered zone (Robain et al., 1996). In general, DC resistivity soundings in such geological setting show a basic three-layer geoelectrical succession with a low resistive clay-rich saprolite layer sandwiched between much more resistive materials corresponding to the iron crust and basement. However, sampling limitations or incorrect interpretation of data have frequently led to unsatisfactory results because of (i) the presence of lateral resistivity variations within layers which are not horizontally disposed and of (ii) the excessive depth of weathering.

DC surveys are designed to discriminate between anomalies reflecting subsurface electrical resistivity contrasts associated with lithologic and/or hydrologic characteristics. The interpretation of the resistivity sounding data is usually made assuming a stratified earth (Keller and Frischknecht, 1966; Koefoed, 1979) and can only provide the parameters of a horizontally layered model with limited resolution. Spatial variations of earth materials or topographic effects, however, invalidate such assumptions.

In several parts of West Africa (Delaitre, 1993; Tardy, 1993), significant spatial variations have been reported in the lithologic characteristics of weathering profiles. Hence, the highly heterogeneous nature of the overburden implies that situations could arise in which the 1D layered models do not account for realistic geologic structures. This implies that at least 2D information is required.

In areas where complex geology renders conventional DC methods inadequate and where it is necessary to have a continuous cover, the 2D resistivity imaging process can be used for a more accurate delineation of subsurface structures. The electrical resistivity tomography (ERT) method (Griffiths and Barker, 1993) differs from the DC survey in using a multielectrode array system and in recording the maximum number of independent measurements on the array. The purpose of this work was thus to investigate whether ERT could provide accurate information on the weathered layers developed upon the basement in selected areas of eastern Senegal. The surveys were conducted at locations where the geology is well-known from the observation of pits and road cuts, so interpreted data could be compared to this information.

2. Geological and weathering setting of investigated areas

The investigated area is located in eastern Senegal 800 km southeastern of the capital Dakar where two sites have been chosen within lower Proterozoic formations (Fig. 1).

At Tenkoto, a topographic sequence of pits has been set up from a gently sloping plateau covered by an iron crust to a thalweg (Fig. 1a). The geophysical profile is paralleled 30 m from the topographic sequence of pits. The fresh rock is a granite with biotites and amphiboles. The pits were dug to a depth of 7–12 m in a clayey layer including water (Fig. 2a–b). At the bottom of pits, the top of the saprolite contains some decimetric to metric size blocks of unweathered granite which were also observed in the thalweg flats. This saprolite is overlain by a 0.5-m thick mottled clay layer containing many pebbles of angular quartz and round ferruginous nodules. This level actually undergoes further digging for gold artisanal exploration. Above this is the soft iron crust, a low hardened ferruginous level, 2.5 m to 3.5 m thick, which is formed by gravels and ferruginous nodules embedded in a soft matrix. This soft iron crust is covered by a very hardened massive iron crust, 3.5 to 5 m thick (Fig. 2a). The ferruginous levels exhibit rapid lateral variations in hardening and thickness. Locally, the matrix is softer around cracks and fissures that reflects the degradation and the

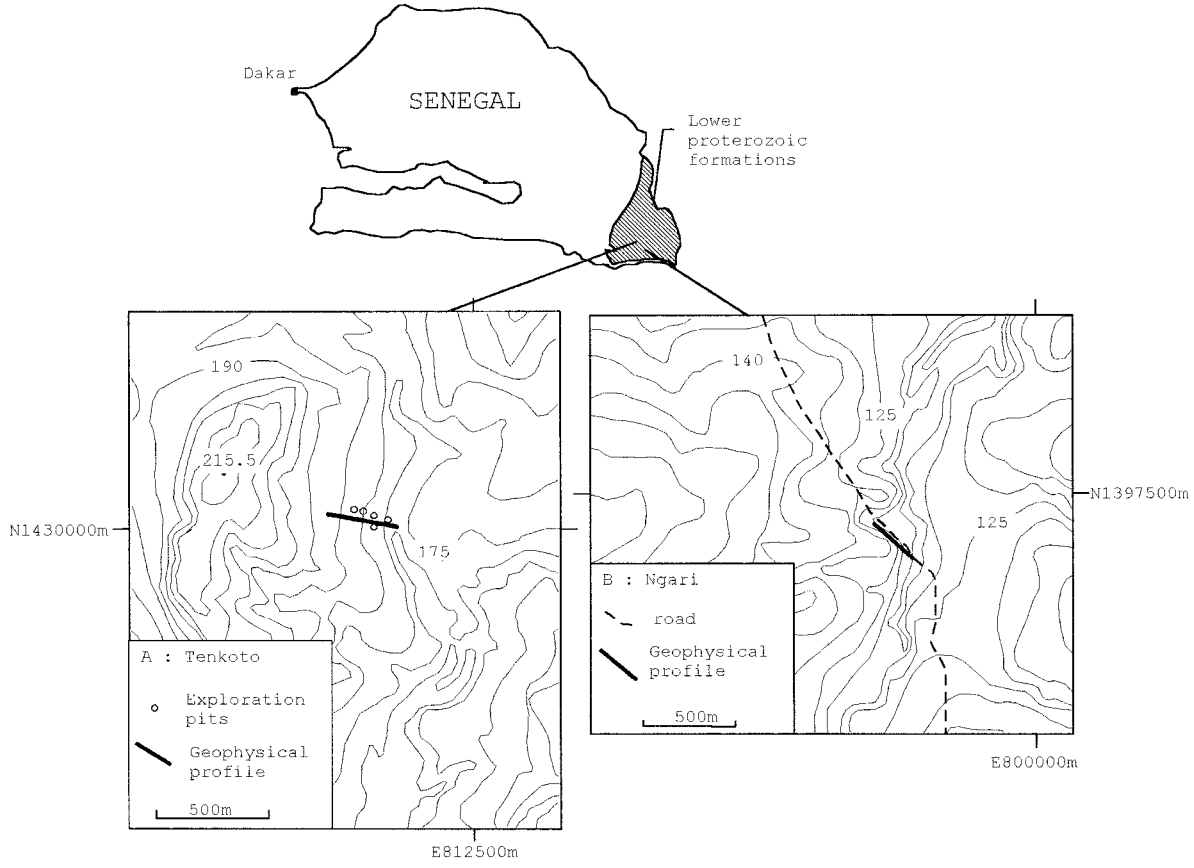

Fig. 1. Topographic location maps of the geophysical profiles (a) at Tenkoto with pits and (b) at Ngari with the road cut. The contour lines are to 5 m intervals. UTM coordinates.

disaggregation of the iron crust whose thickness ranges from 1 to 2.5 m on slopes (Fig. 2b).

At Ngari, a road cuts the lateritic plateau providing an exposure of 12 m thick over a length of 100 m (Fig. 1b). The geophysical profile is paralleled 30 m inside the plateau from the road cut. The weathering process affects schists belonging to a proterozoic metasedimentary series (Birimian). A thick clayey horizon is observed from 6 m to the base of the cut including a saprolite covered by a 1-m thick mottled clay layer (Fig. 2c). A ferruginous horizon is composed of a 2-m thick soft iron crust covered by 4 m of an iron crust which shows marks of dismantling characterized by ferruginous nodules embedded in a clayey–ferruginous soft matrix (Fig. 2c). This disaggregated facies occurs at the base of the iron crust as well as on edges of the plateau where it is often mixed with a linear horizon of pebbles originating from the bending of a quartz vein. Sideways, the ferruginous horizon is cut by the slope of the plateau. The slopes are covered by a colluvial horizon formed by iron crust debris embedded in a clay–ferruginous matrix (Fig. 2c).

The direct observation of pits and road cut does not determine the fresh rock, its topography and the possible geological discontinuity as variations of facies or presence of quartz veins. Such informations are nevertheless of great interest (i) for a better knowledge of the geology, (ii) for understanding the geochemical and physical processes governing the formation of these lateritic weathering profiles, and (iii) for a better

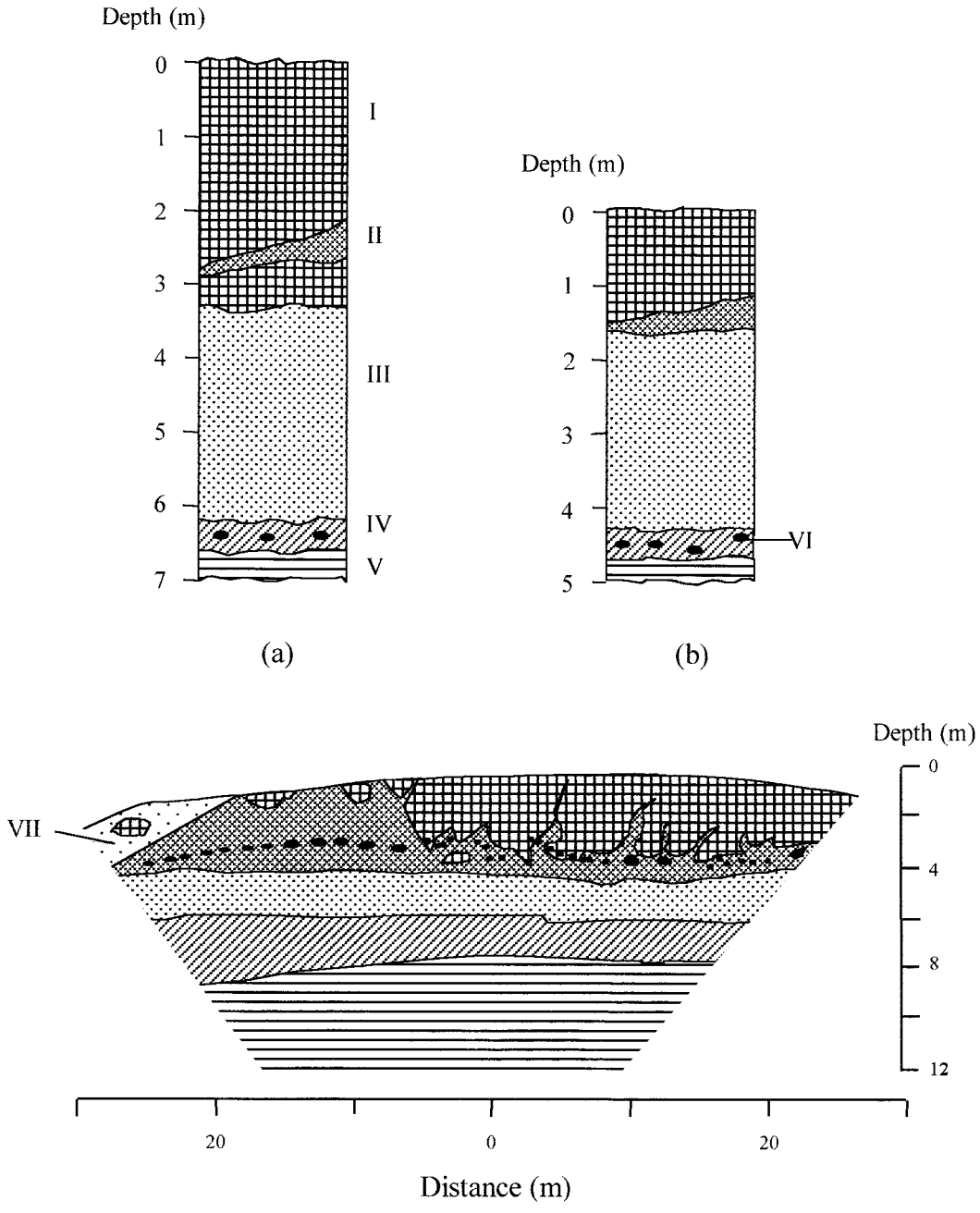

Fig. 2. Lithologic sections of two pits within the Tenkoto area. (a) Weathering profile on the plateau. (b) Weathering profile on the slope. (c) Sketch of the overburden across the Ngari area (I = iron crust; II = disaggregated iron crust; III = soft iron crust; IV = mottled clay layer; V = saprolite; VI = angular quartz and debris of iron crust; VII = colluvial material).

interpretation of the underlying geomorphic processes.

3. Geoelectrical method

The 2D resistivity data were recorded using the ABEM Lund Imaging System with an array of 64 steel electrodes. The survey was carried out along two profiles to examine the ERT response under different geological situations and their effectiveness for providing quantitative information on the weathering mantle. Electrical measurements (Fig. 3) are made on a straight line with a constant spacing using a computer-controlled multichannel resistivitymeter (Griffiths et al., 1990). To obtain good topsoil layer information, it is practice to employ more than one inter-electrode spacing during surveying. The unit electrode spacing determines the length of the profile, the depth of investigation, and the resolution. The short spacing, e.g., 0.5–1 m, will give more detailed information on the upper part of the weathering profile, while the larger spacings, e.g., 3–5 m, have been used to investigate the deeper zones such as the saprolite and the bedrock. A Wenner electrode configuration was employed. The data are classically presented in the form of pseudosections (Edwards, 1977), which give an approximate picture of the subsurface resistivity. Inversion of the data is required to obtain a vertical true resistivity section through the underlying structure (Beard et al., 1996; Loke and Barker, 1996). The field data depicted as contoured pseudoresistivity sections were inverted using the least-squares method as described by Loke (1997). Furthermore, the topographic variations have been incorporated in the inversion processing. The resulting pseudosections of apparent resistivities do not necessarily indicate gradual change of resistivity, implying to carefully compare the resistivity data with the pit observations. Though the inversion method is fast and accurate for simple 2D structures, it does not always give unique and precise limits of bodies of small size.

4. Results and discussion

4.1. Tenkoto profile

Fig. 4 represents the apparent resistivity and the true resistivity images in the upper 5 m of the weathering zone for the granitic area of Tenkoto with an electrode spacing of 0.5 m. Fig. 4b shows a 2-m thick surface layer having resistivities above 10 000 Ωm, that corresponds

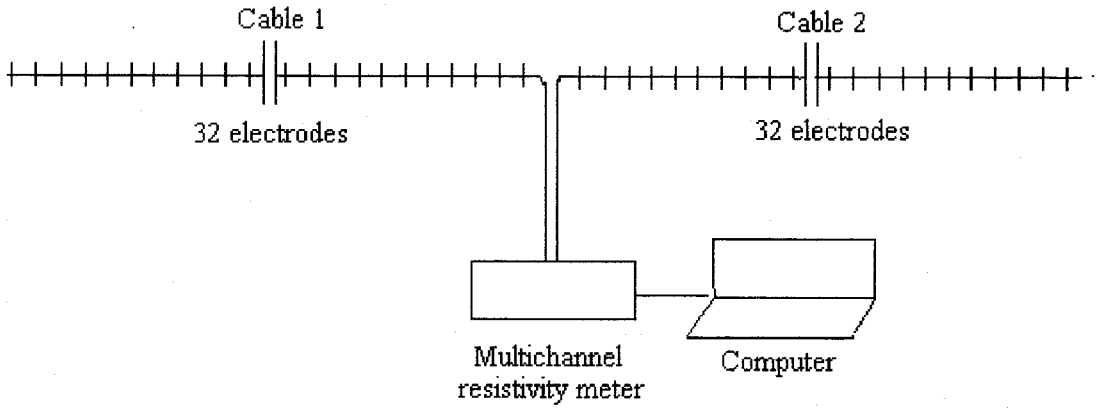

Fig. 3. Schematic layout of the electrical resistivity tomography (ERT) experiment to image the lateritic weathering mantles. Sixty-four electrodes were arranged at equal spacings along a straight line. The cables are connected to a multichannel resistivity meter which is controlled by a computer.

to a very hardened iron crust. The heterogeneity of resistivity is greatest within this layer suggesting lateral variations of hardening and facies.

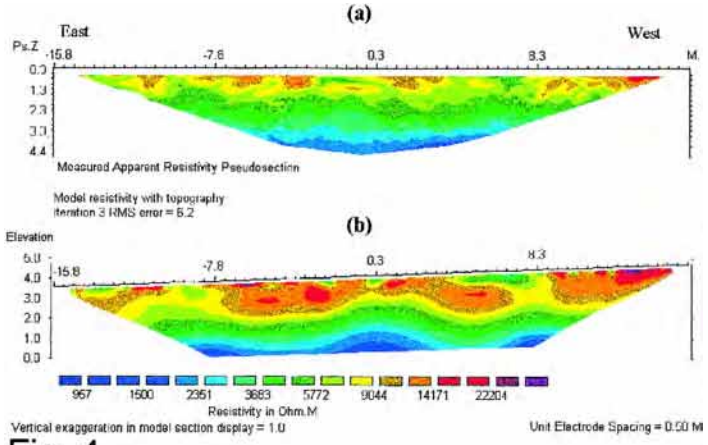

Fig. 4

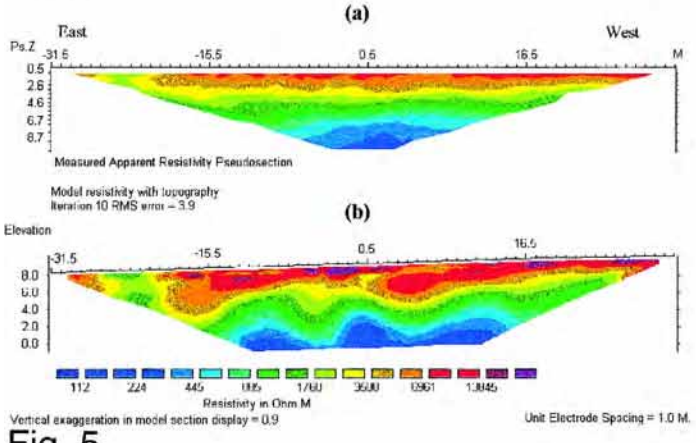

Fig. 5

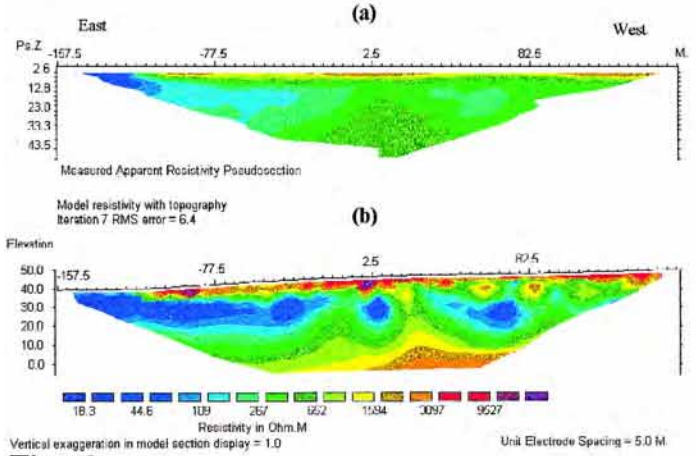

Fig. 6

With an electrode spacing of 1 m (Fig. 5), both depth of investigation and profile length increase, but details of the surface layer are fading compared to the Fig. 4. This section emphasizes even so the heterogeneity of the iron crust. A low resistivity zone of 100 Ωm occurs at depth corresponding to the saprolite. The soft iron crust is characterized by resistivities ranging from 1000 to 3000 Ωm. The scarp underlining the edge of the plateau is marked by a decrease of resistivities between −21 m and −26 m that corresponds to the dismantling of the iron crust (Fig. 5b).

The pseudoresistivity and the inversion for an electrode spacing of 5 m allow a larger view of the weathering mantle (Fig. 6). Fig. 6b shows the high-resistivity surface layer, corresponding to the iron crust. The resistivity, however, decreases of about 10 Ωm in the eastern part of the section. This likely reflects the boundary between the iron crust and the clay-rich weathering material into which freshwater originating from the stream close to the resistivity profiling can infiltrate. At this scale, the geoelectrical distinction between the soft iron crust and the overlying iron crust is not clear. On the other hand, the zone of low resistivity characterizing the saprolite is well-defined, though it seems to be perturbed by a narrow resistivity discontinuity between positions 17.5 and 22.5 m, dividing the area into an eastern and a western zone having similar resistivities. The low resistivities occurring in the eastern zone have been first related to freshwater infiltrations feeding a perched water table which may evaporate during the dry season. Such zones of low resistivity are thus more likely associated with a relatively high clay component. Even a small quantity of water in clay materials increases the cation exchange capacity of clays (Keller and Frischknecht, 1966). As a result, the resistivity of the pore fluid can be significantly lowered. Clays can retain water by capillary action due to their fine-grained texture and this also results in a lowering of the resistivity. Beneath, the saprolite resistivities increase progressively to values above 3000 Ωm. This is likely an indication of a transition from the saprolite to the granitic sand then to the unweathered granite basement. A sharp and narrow high-resistivity area ranging from 650 to 1100 Ωm ascends from the bedrock to the saprolite, that can indicate either a strong irregularity of the bedrock or a geological structure like a quartz vein. The results from the granitic area suggest a lateritic weathering mantle of about 40 m thick from the unweathered bedrock to the surface.

4.2. Ngari profile

Figs. 7 and 8 show the results of 2D resistivity surveying at Ngari with electrode spacings of 0.9 and 3 m, respectively. The pseudosection reveals a decrease of the apparent resistivity with depth (Fig. 7). Fig. 7b shows a well-defined top layer with resistivities above 5000 Ωm corresponding to the iron crust of 2–4 m thick. The lower boundaries of the iron crust and of the soft ferruginous horizon correspond to resistivities of 2500 Ωm and 900 Ωm, respectively. To the west from position 12.1 m, these layers are no longer detected. Fig. 6b suggests that intermediate resistivities below 300 Ωm exist at depth of 7–8 m from position −14 m to position 6.7 m. Westward of the position 6.7, the top of this layer is, however, displaced

Fig. 4. (a) Observed apparent resistivity pseudosection at Tenkoto with an electrode spacing of 0.5 m together with (b) the 2D inversion model section.

Fig. 5. Same as for Fig. 4 with an electrode spacing of 1 m.

Fig. 6. Same as for Fig. 4 with an electrode spacing of 5 m.

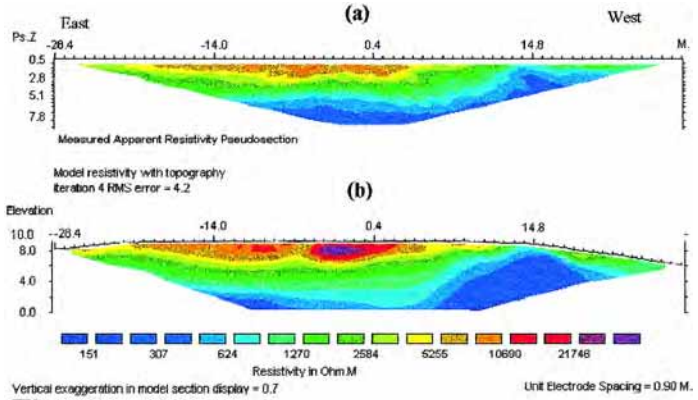

Fig. 7

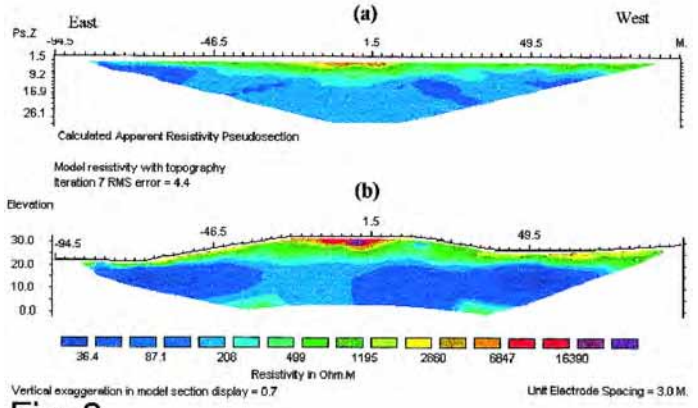

Fig. 8

Fig. 7. (a) Observed apparent resistivity pseudosection at Ngari with an electrode spacing of 0.90 m together with (b) the 2D inversion model section including the topography.

Fig. 8. Same as for Fig. 7 with an electrode spacing of 3 m.

towards the surface, that corresponds to the scarp where the iron crust is disaggregated.

The pseudosection with an electrode spacing of 3 m indicates a nonlayered subsurface electrical structure (Fig. 8). The range of apparent resistivities is comparable with that observed at Tenkoto (Fig. 6), but with a higher limit for the minimum values of apparent resistivities. Fig. 8b shows a thin surface layer with resistivities above 5000 Ωm located at the summit of the plateau, between positions −22 and 10, where the iron crust occurs. The resistivity of that surface layer, however, decreases towards the edges of the section to values of about 2000 Ωm, that characterizes colluvial materials resulting from the destruction of the iron crust in the course of hillslope erosion processes. Below this is a quasi-continuous layer of around 1000 Ωm which could be related to the basis of the ferruginous horizon. A broad zone of 30–200 Ωm, corresponding to the saprolite layer, extends across the entire profile, and becomes more conductive towards the flanks (Fig. 8b). The zones of lowest resistivities can readily be explained by a higher clay content or a higher groundwater content, or any combination of both. The thickness of this layer is not resolved because of the relatively short profile length. At

Ngari, the saprolite layer probably has a thickness of at least 25 m and could be thicker than at Tenkoto.

5. Concluding remarks

The above examples show that the ERT method is well-suited to analyse the inner structure of lateritic overburden, because it gives not only a resistivity value depending on the physical, chemical, and hydrological parameters of the different layers, but it also provides information upon specific geoelectrical heterogeneity of the investigated zone and, thus, upon the lithological variations. Precise identification of the lithology is, however, not possible on the basis of resistivity data alone; correlation with pits is required.

The two study sites present many similarities. The resistivity of the iron crust ranges from 3000 to 30 000 Ωm, indicating lateral variations of facies. Direct field observations allow to correlate zones of very high resistivities to most iron crust facies, while the zones of lower resistivities can be related to the disaggregated iron crust whose matrix is softer. At the two sites, the soft iron crust exhibits comparable resistivities about 1000 Ωm.

In agreement with field observations, variations of resistivity show that the transition from the fresh rock to the saprolite is progressive, while the transition between the saprolite and the ferruginous horizons is more rapid.

The variations of resistivity within each horizon give also interesting indications. The low and variable resistivities in the saprolite may be due to facies changes and/or changes in water content. In fact, the very low resistivity of the saprolite (< 30 Ωm) can be interpreted as a fully saturated layer since it is connected to streams, that is confirmed by the presence of water at the bottom of Tenkoto well and at the base of Ngari profiles. Considering the geological context at Tenkoto, two explanations for the increase of resistivity in connection with the fresh rock can be proposed: (i) it is either related to a quartz vein since a layer containing numerous angular quartz debris has been observed beneath the iron crust, or (ii) it indicates a dome of fresh rock which is a structure frequently encountered in granitic areas and, often visible in the thalweg flats. In fact, 3D surveying with multielectrode arrays will be necessary to choose between these two hypotheses. This work is actually under process.

The maximum of detail is obtained for most ferruginous horizons developing between 0 and 5 m which were analyzed with a small electrode spacing of 0.5 or 1 m. Though the dismantling horizon of quartz vein occurs at depth ranging from 3 to 6 m, it is, however, not detected. Instead, it is defined as discontinuous objects of small size (< 40 cm) presenting a low contrast of resistivity with the surrounding material.

ERT gives a good image of the main weathering horizons which show similar geoelectrical characteristics in the two studied areas. Our results provide useful indications on the thickness, variations of facies and the nature of contacts between the different formations.

References

Beard, L.P., Hohmann, G.W., Tripp, A.C., 1996. Fast resistivity/IP inversion using a low-contrast approximation. Geophysics 61, 169–179.

Blot, A., Leprun, J.C., Pion, J.C., 1976. Originalité de l'altération et du cuirassement des dykes basiques dans le massif de granite de Saraya (Sénégal oriental). Bull. Soc. Geol. France 7, 45–49.

Delaitre, E., 1993. Etude des latérites su Sud-Mali par la méthode de sondage électrique. PhD thesis, Strasbourg University.

Edwards, L.S., 1977. A modified pseudosection for resistivity and induced-polarization. Geophysics 42, 1020–1036.

Griffiths, D.H., Barker, R.D., 1993. Two-dimensional resistivity imaging and modelling in areas of complex geology. J. Appl. Geophys. 29, 211–226.

Griffiths, D.H., Turnbull, J., Olayinka, A.I., 1990. Two-dimensional resistivity mapping with a computer-controlled array. First Break 8, 121–129.

Hazell, J.R.T., Cratchley, C.R., Jones, C.R.C., 1992. The

hydrogeology of crystalline aquifers in northern Nigeria and geophysical techniques used in their exploration. In: Wright, E.P., Burgers, W.G. (Eds.), Hydrogeology of Crystalline Basement Aquifers in Africa. Geological Society Special Publication, No. 66, pp. 155–182.

Keller, G.V., Frischknecht, F.C., 1966. Electrical methods in geophysical prospecting. Pergamon, Oxford.

Koefoed, O., 1979. Geosounding Principles: 1. Resistivity Sounding Measurements. Elsevier, Amsterdam.

Leprun, J.C., 1979. Les cuirasses ferrugineuses des pays cristallins de l'Afrique occidentale sèche. Genèse. Transformation-dégradation. Mémoire Sciences Géologiques, Vol. 58, Strasbourg University.

Loke, M.H., Barker, R.D., 1996. Rapid least-squares inversion of apparent resistivity pseudosections by a quasi-Newton method. Geophys. Prosp. 44, 131–152.

Loke, M.H., 1997. RES2DINV software user's manual.

Palacky, G.J., Kadekaru, K., 1979. Effect of tropical weathering on electrical and electromagnetic measurements. Geophysics 44, 69–88.

Robain, H., Descloitres, M., Ritz, M., Atangana, Q.Y., 1996. A multiscale electrical survey of a lateritic soil in the rain forest of Cameroon. J. Appl. Geophys. 34, 237–253.

Tardy, Y., 1993. Pédologie des latérites et des sols tropicaux. Masson, Paris.

ARTICLE 5

ELSEVIER

Earth and Planetary Science Letters 173 (1999) 413–424

EPSL

www.elsevier.com/locate/epsl

Analysis of poorly stratified lateritic terrains overlying a granitic bedrock in West Africa, using 2-D electrical resistivity tomography

Anicet Beauvais [a,*], Michel Ritz [b], Jean-Claude Parisot [b], Michel Dukhan [b], Christian Bantsimba [b,c]

[a] *IRD, Département RED, UR-062, Centre d'Ile de France, 32 avenue Henri Varagnat, 93143 Bondy Cedex, France*
[b] *IRD, Département RED, UR-062, Centre de Hann, B.P. 1386, Dakar, Senegal*
[c] *IRD, Département RED, UR-062, UCAD, Département de Géologie, Dakar, Senegal*

Received 11 June 1999; revised version received 1 October 1999; accepted 1 October 1999

Abstract

Two-dimensional electrical resistivity tomography has been employed to investigate the subsurface structure of a thick lateritic weathering mantle overlying a granitic bedrock in southeastern Senegal. The resistivities were measured along two kilometric pro les insuring continuous coverage. Exploration pits exposed the different weathering layers, i.e., a saprolite, a mottled zone, a soft ferricrete and a ferricrete, whose respective thicknesses were used to constrain the measured apparent resistivity, despite their spatial variations. Colour-modulated pseudo-sections of apparent resistivity versus pseudo-depth including the groundsurface topography clearly show spatial variations in electrical properties of the weathering layers since their apparent resistivity changes faster than their respective thickness. The data from a cross-borehole survey along with estimates of resistivity for aquifers and granite were integrated into the pseudo-sections to provide more useful results about the real resistivity ranges of the weathering layers. The resulting geo-electrical images document the geometric relations between the different layer boundaries, in particular those of the aquifers with the bedrock and groundsurface topographies. The spatial relationships between the granitic bedrock and groundsurface topographies suggest that a large part of the actual lateritic weathering mantle is allochthonous. This also implies that the actual topography of the bedrock surface was mainly shaped by weathering processes while the hillslope geomorphic patterns result from erosion processes or lateritic weathering of reworked materials leading to ferricrete development according to the different landforms observed. It is suggested that climatic changes were implied in the landscape evolution of our study area.

Keywords: resistivity; tomography; weathering; saprolite; laterites; geomorphology; Senegal

1. Introduction

Lateritic overburden of tropical areas has been developed on many kinds of parent rocks under the effect of weathering processes. At least one third of the Earth's surface has undergone lateritic weathering processes that have led to the formation of laterites, i.e., tropical soils, bauxites and ferricretes, since the Mesozoic [1–6]. Such residual formations commonly exhibit thicknesses of several tens of metres with a complex layer organization due to vertical

* Corresponding author. Tel.: +33-1-4802-5500; Fax: +33-1-4847-3088; E-mail: beauvais@bondy.ird.fr

0012-821X/99/$ – see front matter
PII: S0012-821X(99)00245-9

and lateral variations of the geochemical and physical properties of each weathering layer [5,7]. The factors and processes governing these variations have been studied in detail in West and Central Africa on the basis of petrographical observations in pits, and of mineralogical and geochemical data [8–14]. Although such studies are useful in understanding the mechanisms of formation and transformation of the weathering layers and facies at the scale of vertical pro l es, they do not provide a full knowledge of the weathering mantle, its thickness and 2-D layer organization including the geometry of the saturated domains and of the water tables [15]. Also they do not allow the interpretation of the underlying lithologic and hydrologic processes at the scale of inter uves of kilometric size. Such a knowledge is however needed in groundwater prospecting, mineral exploration and geologic mapping in the tropical shields [16,17].

The aim of our study is to provide geo-electrical sections of the lateritic overburden along a complete inter uv e in order to obtain a 2-D integrated image of the geomorphological and hydrogeological structures that can document the relationships between the layer boundaries of the lateritic weathering mantle and the bedrock and groundsurface topographies.

Direct-current (DC) resistivity methods are usually applied to detect subsurface geologic and/or hydrologic anomalies. They also provide a coarse geo-electrical image of the soil surface layers and of the weathered zone [15]. The resulting 1-D models roughly display three geo-electrical layers assuming a strati ed earth [18,19], with a low-resistivity layer attributed to a saprolite layer sandwiched between two resistive layers corresponding to the underlying unweathered bedrock and to the overlying ferruginous layers, e.g., the ferricrete. *Ferricrete* is used here as a generic term for ferruginous duricrust independently of the staked processes [5,7]. The deep and old weathering mantles capped with ferricretes can however exhibit signi - cant lithological variations [5,20].

The application of the electrical resistivity tomography (ERT) method has proved useful to investigate the complex 2-D organization of poorly strati ed lateritic overburden [21,22]. Two-D models resulting from ERT applications are more appropriate to investigate the deep weathering mantles since they are able to document at once the vertical and lateral variations of resistivity, whereas 1-D models from the DC method are based on limited measurements of the apparent resistivity and thus only display the coarse geo-electrical contrasts.

2. Site description

The eld work was done at Tenkoto within a gold mining prospecting area in southeastern Senegal (Fig. 1). The geological basement of this area is composed of early Palaeoproterozoic formations including a greenstone belt surrounding a granitic batholith intrusion (Fig. 1A). The study is focused on the granitic intrusion overlain by a thick lateritic weathering mantle capped with ferricrete. On the basis of petrographical observations in pits, the ferricrete layer is thought to result, in large measure, from the erosion and redisposition of an earlier lateritic weathering mantle developed on the greenstones [23]. That interpretation was, however, contradicted by later researchers who argued that the lateritic weathering pro les have been developed in situ on parent rock without any allochthonous deposits [8,9]. These two opposed interpretations imply that the hillslope shape is mainly controlled by either mechanical erosion or geochemical weathering processes depending on whether one considers the rst or the second proposition. One hopes to obtain useful data from ERT to resolve this issue.

The geomorphology of the greenstones area consists of steep hills, one of them bearing a ferricrete thought to be of Pliocene age [23] (Fig. 1). The hills dominate a geomorphologic system of plateaus and glacis on the granitic batholith corresponding to the ‘High-Glacis’ and ‘Middle-Glacis’, respectively, as de ne d by Michel [23]. Granite domes and boulders outcrop in the thalwegs around the village of

Fig. 1. (A) Location and geomorphological characteristics of the study area. According to Michel [23], the probable limit of the granitic batholith within the greenstone area is delineated by the curved line; black star stands for Tenkoto village. (B) Topographic cross section according to the dashed line in (A).

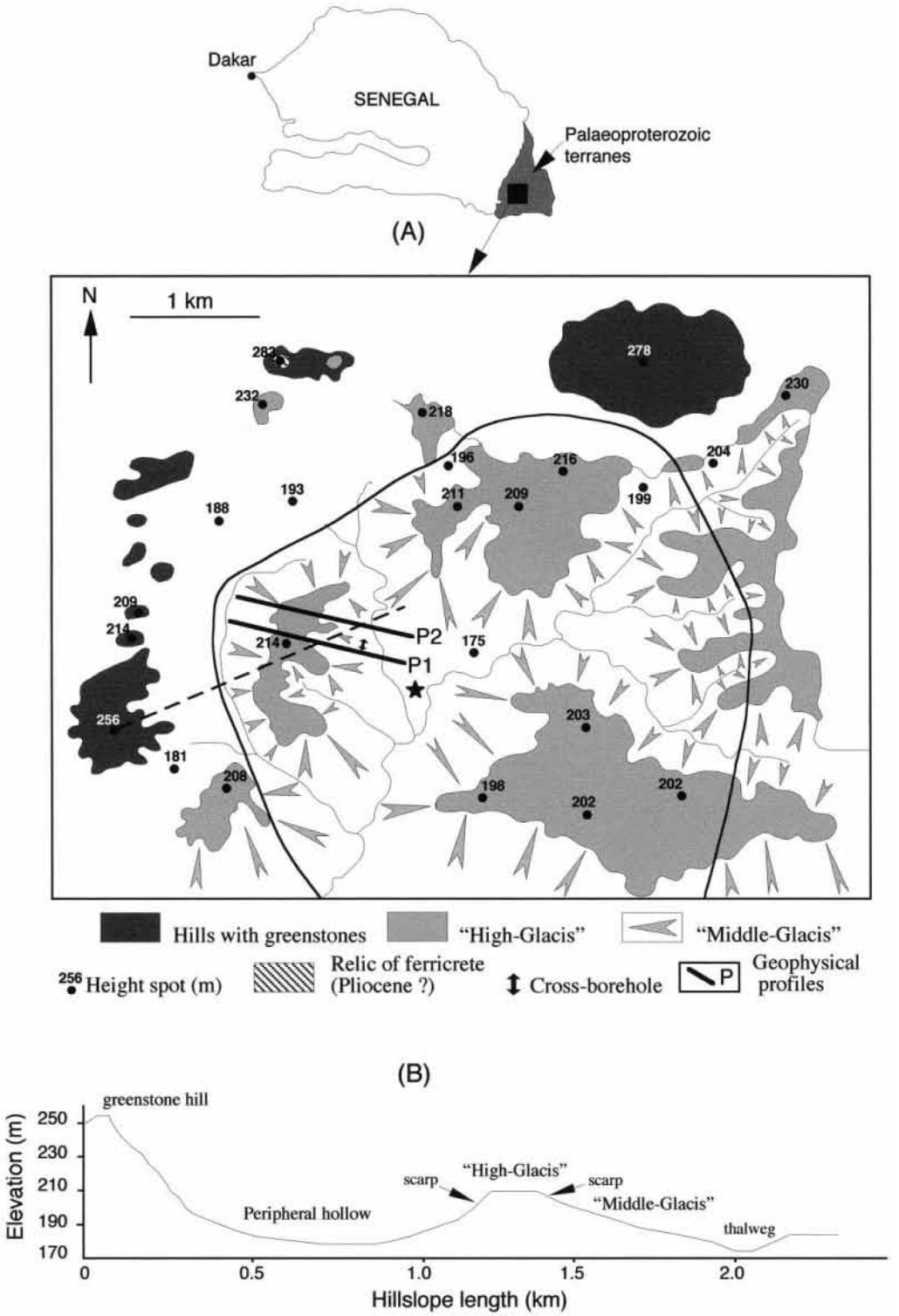
Dakar
SENEGAL
Palaeoproterozoic terranes
(A)
N
1 km
278
230
232
218
204
196
216
193
211
209
199
188
209
214
214
P2
P1
175
256
203
181
208
198
202
202
Hills with greenstones
"High-Glacis"
"Middle-Glacis"
256 Height spot (m)
Relic of ferricrete (Pliocene ?)
Cross-borehole
P
Geophysical profiles
(B)
greenstone hill
Elevation (m)
250
230
210
190
170
scarp
"High-Glacis"
scarp
"Middle-Glacis"
Peripheral hollow
thalweg
0
0.5
1.0
1.5
2.0
Hillslope length (km)

Tenkoto. The highest hills culminate around 255–285 m, while 'High-Glacis' and 'Middle-Glacis' stand at 200–215 m and 175–195 m, respectively (Fig. 1). A wide peripheral hollow in which one can find debris and blocks of greenstones and ferricrete lies down between the 'High-Glacis' and the greenstone hills (Fig. 1B). This area underwent and still undergoes active gold artisanal prospecting using pits dug along the thalwegs as well as intensive exploration by a multinational mining company. The thalwegs are flat and they were completely dry during the geo-electrical survey. Four standard layers were observed from the bottom to the top of pits: a saprolite, a mottled zone, a soft ferricrete, and a ferricrete which can present degradation facies resulting from the disaggregation of the matrix. This profile layout was used to calibrate the geo-electrical measures, in particular those obtained by the cross-borehole configuration.

The climate is seasonal tropical with a wet season from April–May to September–October and a dry season for the rest of the year. The mean annual rainfall is 1200–1300 mm, the mean annual temperature is ~28°C while the mean annual relative air humidity is ~50%. The vegetation consists of a semi-humid savanna with an alternation of wood and Graminaceae domains.

3. Geo-electric method

The ERT method was applied to provide useful information about the ranges of resistivity, ρ, for each layer composing the geo-electrical structure that best characterizes the lateritic weathering mantle. A 2-D resistivity tomography was obtained by employing the ABEM Lund Imaging System using a multi-electrode Wenner configuration with an array of 64 steel electrodes. Two profiles of 1420 m length oriented S70°E and spaced 200 m apart were investigated (Fig. 1A). They cross the 'High-Glacis' and the 'Middle-Glacis'. Profile II crosses the gently sloping north edge of the 'High-Glacis'. The unit electrode spacing was 10 m that provided a global view of hundred metres thickness of geological structures. Such a disposition is effectively appropriate to investigate the spatial relations between the layer boundaries and the groundsurface topography. Each profile was partitioned into three sections with two overlappings of 24 electrodes, i.e., 240 m. The topography of the profiles was obtained using a clinometer with measurements every 10 m and less when it was necessary. The electrical measures were made using a computer-controlled multichannel resistivity-meter located in the middle of the 64 electrodes configuration, implying that, for each section of 640 m length, the first electrode is positioned at −315 m while the last one is at 325 m [24]. The apparent resistivity data were inverted using a least-square method to obtain a pseudo-resistivity section of the underlying structures including the topographic variations [25–27]. The gradual changes of resistivity does not necessarily indicate gradual changes of the geophysical properties of the weathering layer and facies, impeding useful selection of the layer boundaries.

That has led us to carry out a cross-borehole survey between two pits spaced 10 m apart, with an electrode spacing of 0.5 m (Fig. 2). The electrodes were set up on the pit walls and in the groundsurface making an inverted U-shape electrode bridge. The cross-borehole data inversion provided the true resistivity range of the different weathering layers previously described in the pits. The resistivity of the granite was estimated using in situ measurements with small Wenner layouts while the water conductivity was directly measured in pits recently bored.

Then, the new resistivity data were incorporated into the previous inverted pseudo-resistivity sections to obtain a 2-D geo-electrical image of the lateritic weathering mantle with relatively precise limits between resistivity domains representing the different weathering layers. These geo-electrical images document on the spatial relationships between the layers, their boundaries and the topographic groundsurface, that can provide useful data to reconcile previous interpretations [8,9,23].

4. Results and discussion

4.1. Electrical resistivity tomography of the lateritic weathering mantle

The field cross-borehole results are shown in Fig. 2. The 2-D cross-borehole image obtained be-

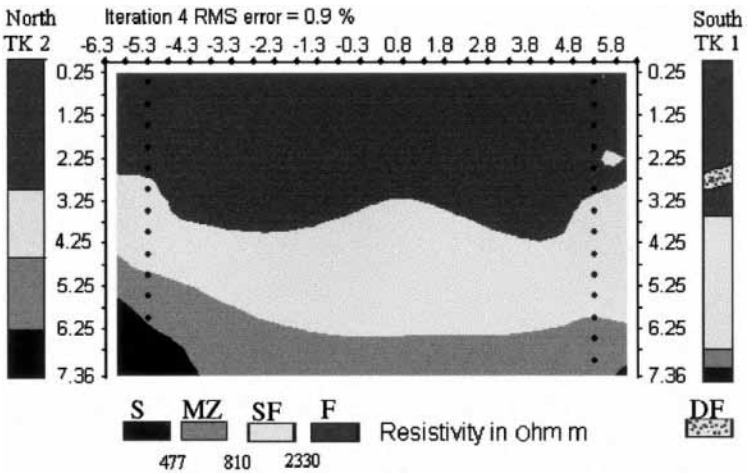

Fig. 2. Correlation between lithology of two pits (*TK 1* and *TK 2*) and the model obtained after the inversion of the cross-borehole data set. A spacing between the electrodes (dots) of 0.5 m was used. *S* = saprolite; *MZ* = mottled zone; *SF* = soft ferricrete; *F* = ferricrete; *DF* = disaggregated ferricrete. Horizontal and vertical scales in metres. Numbers below boxes are resistivities in ohm m.

tween two pits is consistent with the eld observations, allowing the geo-electrical distinction of the ferricrete with $\rho > 2330$ ohm m (Ω m) from the soft ferricrete with $810 < \rho < 2330$ Ω m, and the mottled zone of $477 < \rho < 810$ Ω m from the saprolite whose $\rho < 477$ Ω m (Fig. 2). Notice that the degradation zone within the ferricrete exhibits a resistivity similar to the soft ferricrete.

2-D inversion sections of pro l es I and II exhibit considerable details of the weathering layer organization (Fig. 3). This gure basically shows three layers with the rst and third having relatively high resistivities, $\rho > \sim 800$ Ω m. The high resistivity is interpreted to characterize the ferruginous layers and the more or less weathered granite, respectively. The intermediate layer of lower resistivity represents the saprolite. The highest surface resistivities were measured on the topographic heights, and they seem to be thicker in the rst pro l e than in the second one along a section ranging from ~325 to 645 m (Fig. 3). Discontinuities of saprolite resistivity are detected in pro l e I at 5 m, 395 m, and 705–715 m (Fig. 3A). These discontinuities are also detected in pro le II at 5 m, 325 m and 355 m (Fig. 3B). They occur just above relatively sharp highs of the resistive deep layer re ecting the unweathered granite, in particular at 5 and 325 m in the second pro l e (Fig. 3B). Between 5 and 325 m, the deep highly resistive layers attributed to the bedrock are indeed shallower in the second pro le than in the rst one (Fig. 3). On the other hand, the highly resistive layers lie deeper in the second pro l e between ~645 and 965 m, making the low-resistivity layers look thicker (Fig. 3B). Layers of very low resistivity ranging from 7 to 40 Ω m at the two extreme ends of the pro l es re e ct saturated domains, i.e., between −285 and −115 m, and between 945 and 1045 in pro l e I (Fig. 3A), and between −25 and 285 m, 5 and 185 m, and 875 and 1065 m in pro l e II (Fig. 3B).

4.2. Aquifers and granite resistivities

On the basis of in situ measurements, the weathered granite is characterized by $710 < \rho < 1700$ Ω m while the unweathered granite has $\rho > 3140$ Ω m. Laboratory measurements show a mean clay content of ~30% in the pits located downslope of the 'Middle-Glacis' where the mean porosity is ~40%. The analysis of water in the pits provides a mean resistivity of 155 Ω m. These informations along with the assumption that the saprolite is roughly homogeneous were used to derive an empirical relation from the generalized Archie law [28] in order to delineate the boundaries of saturated domains in the saprolite and around the thalwegs. A more accurate estimate for the upper limit of the saturated domain resistivity is obtained by correcting for the clay contribution [25]. This relation to the ERT results indicates that a

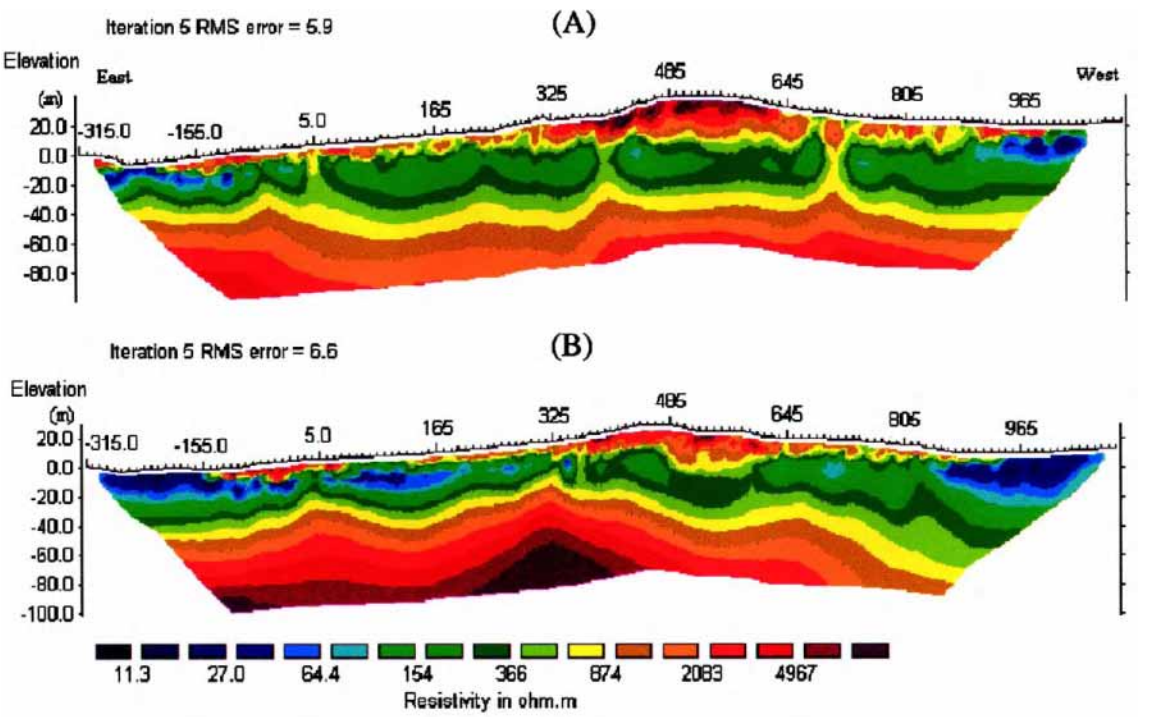

Fig. 3. 2-D inversion results including the topography with an electrode spacing of 10 m for (A) pro le I and (B) pro le II. Vertical exaggeration in models is 2.0.

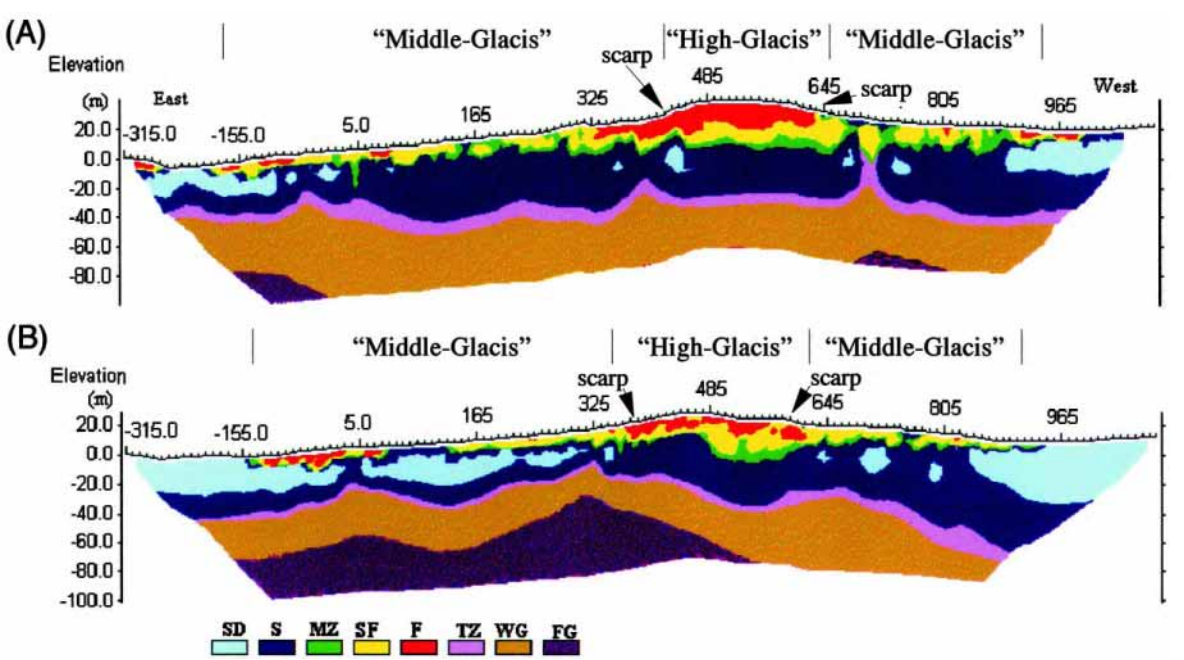

saprolite with a mean porosity of ~40%, containing ~30% clay and saturated by fluids with a mean resistivity of 155 Ω m can be reasonably described by $\rho = 130$ Ω m.

4.3. Geometric relations between the layer boundaries and the groundsurface

Integrated cross sections were obtained from the interpreted ERT and cross-borehole data incorporating the aquifers and granite resistivities. These sections result in identifying eight resistivity layers as, a saturated domain, a saprolite, a mottled zone, a soft ferricrete, a ferricrete, a transition zone, a more or less weathered granite, and an unweathered granite (Fig. 4).

The first profile roughly exhibits a smooth bedrock topography while the second shows a more convex bedrock surface. Between −315 and 325 m, the bedrock appears shallower in the second profile than in the first one, suggesting that the bedrock topography is sloping to the southeast, while the weathering mantle thickens to that direction (Fig. 4). The highs of the bedrock surface in the second profile spatially correspond to zones of degradation of the ferricrete at 325–335 m and to a thinning of the saprolite separating a stream saturated zone from a domain of saturated saprolite between 5 and −15 m on the 'Middle-Glacis' (Fig. 4B).

The upper saprolite boundary is very corrugated in the first profile where it is overlain by a thin mottled zone, the layer boundaries being roughly parallel (Fig. 4A). The two weathering layers are shallower beneath the 'Middle-Glacis' than beneath the 'High-Glacis' over which the ferricrete and soft ferricrete layers are the thickest (Fig. 4). At 405 m and 705 m in the first section (Fig. 4A) and at 325 m in the second section (Fig. 4B), the bedrock surface highs or granitic domes corresponding to thinnings or discontinuities of saprolite are located just underneath the scarps that likely spring from degradation and partial removing of the overlying ferricrete at the edges of the 'High-Glacis'. On the other hand, the bedrock hollows correspond to weathering layer thickenings over which the ferruginous layers are also well developed, i.e., the ferricrete.

The groundsurface and bedrock topographies are controlled by weathering and erosion processes that determine the geomorphic patterns and the hydrodynamics of the underlying lateritic weathering mantle.

4.4. Geomorphic patterns vs. bedrock topography

The relationships between the groundsurface and the bedrock topographies are more clearly defined in Fig. 5 which is derived from Fig. 4. The vertical axis was expanded by a factor of ~3 to emphasize discrete groundsurface planforms of decametric size. At this length scale, convex bedrock domes correspond to groundsurface concavities while some topographic convexities overlie bedrock concavities as hollows. At the scale of hundreds of metres, the slope gradients for the two topographies are also negatively correlated (Fig. 5). At the whole profile scale, the bedrock and groundsurface topographies are effectively not parallel at all.

It was suggested that many tropical landscapes have undergone geomorphic modifications under the influence of climatic changes which control the balance between the weathering and erosion [1–6,23,29–34]. We also believe that climatic fluctuations were implied in the landscape evolution of southeastern Senegal; humid episodes favoured the rocks' weathering and the formation of ferricretes while the resulting landscape was eroded and dissected during dry periods, leading to new landforms, e.g., to the shaping of the 'High-Glacis' and 'Middle-Glacis' (Fig. 6). Fig. 6 represents the sequence of climate-depending processes that should have shaped the landforms of Tenkoto area. The previous lateritic weathering mantle developed in situ over the greenstone and the granitic bedrock was so eroded under semi-arid to

Fig. 4. Lithostratigraphic cross sections across the Tenkoto area based on ERT and cross-borehole data and physical parameters as discussed in the text: (A) profile I; (B) profile II. *SD* = saturated domain, $\rho < 130$ Ω m; *S* = saprolite, $130 < \rho < 477$ Ω m; *MZ* = mottled zone, $477 < \rho < 810$ Ω m; *SF* = soft ferricrete, $810 < \rho < 2330$ Ω m; *F* = ferricrete, $\rho > 2330$ Ω m; *TZ* = transition zone, $417 < \rho < 713$ Ω m; *WG* = less or more weathered granite, $710 < \rho < 3100$ Ω m; *FG* = fresh granite, $\rho > 3140$ Ω m. Vertical exaggeration in cross sections is 2.0.

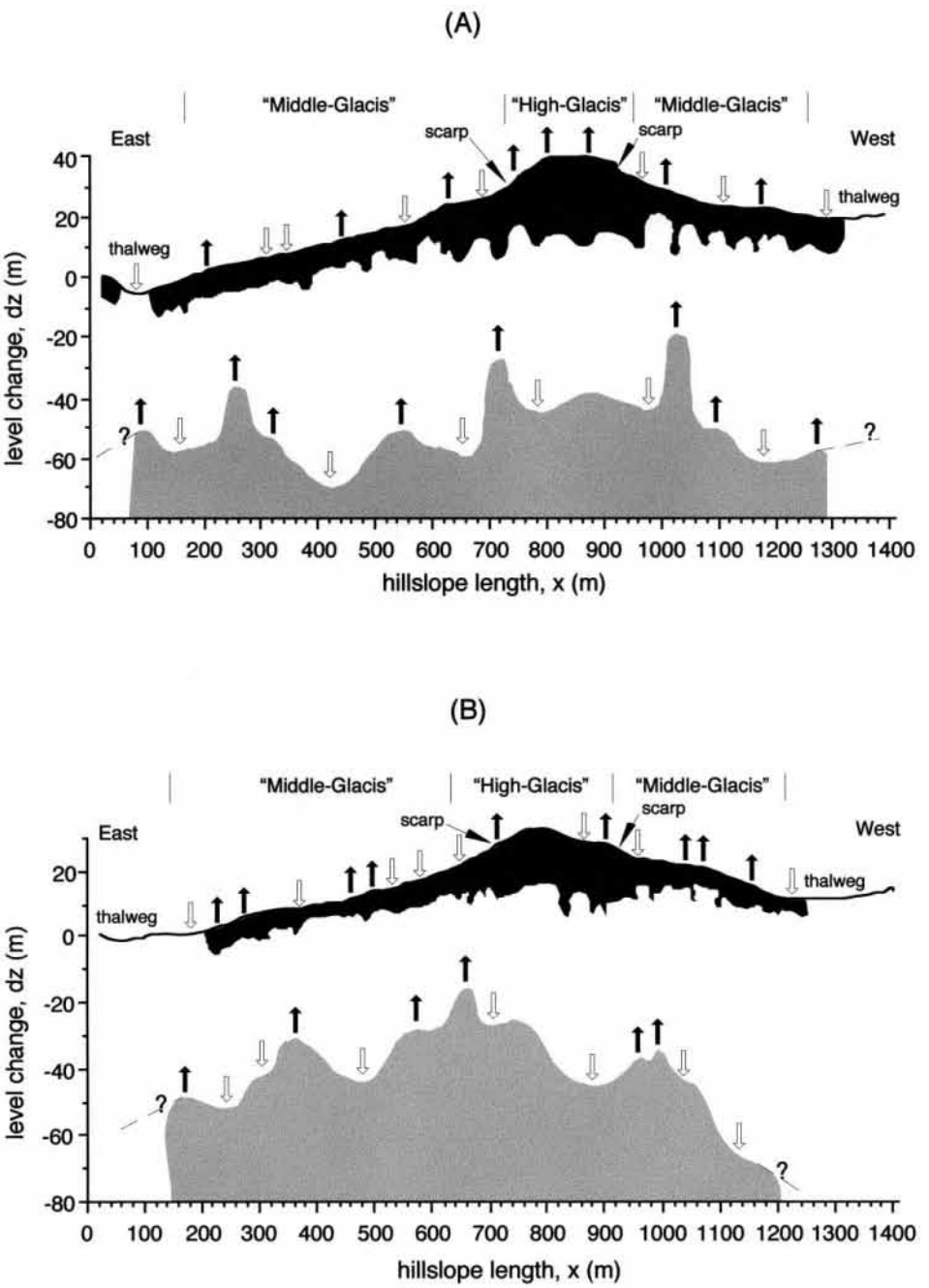

Fig. 5. Geomorphologic cross sections across the Tenkoto area derived from Fig. 4 after expansion of the vertical axis by a factor of ~3: (A) pro le I; (B) pro le II. Upper dark grey layer = soft ferricrete + ferricrete with $\rho > 810\ \Omega$ m; lower light grey layer = weathered and unweathered granite with $\rho > 710\ \Omega$ m; the space between the two layers is occupied by the saprolite + the mottled clay layer with $130 < \rho < 810\ \Omega$ m, and by the saturated domain with $\rho < 130\ \Omega$ m; black arrows = convex and plan-convex landforms + bedrock domes; white arrows = concave and plan-concave landforms + bedrock hollows.

arid climatic conditions, stripping and exposing some parts of the granitic bedrock, while the weathering pro l e capped with a thick ferricrete was partially preserved on greenstone (Fig. 6A). The resulting etched surface [31] probably exhibited concave and convex forms that controlled the accumulation patterns of the material eroded from the lateritic weathering pro- l es developed on the surrounding greenstones [23] (Fig. 6A,B); a relic of such pro les capped with a purple reddish massive ferricrete is still observable on the hill culminating at 283 m in the greenstone area (Fig. 1B). Coarse detritic materials embedding ferricrete debris with a similar petrographical facies have been observed over a thickness of ~15 m in the 'High-Glacis' pro l es [23] (Fig. 6C,D). Furthermore, the groundsurface of the peripheral hollows is strewn with blocks of that ferricrete and greenstone. Also, a part of the clay fraction of the ne detritic material should have been imported from the saprolite of the previous greenstone pro l es.

Most of the coarse and ne materials rst settled within the granitic bedrock concavities nearest to the western greenstones. Thick lateritic weathering pro les have been effectively developed above bedrock hollows in which the bulk of the eroded material coming from the surrounding greenstone hills should have been deposited (Fig. 6B–D). The resulting landforms carrying thick ferricretes are more convex than concave (Fig. 5). The ferricrete of the 'High-Glacis' is however less preserved, because it is more disaggregated in the second geo-electrical pro le than in the rst one. This can re ect the lesser thickness of the weathering pro l e since the bedrock slopes to the southeast while the groundsurface of the 'High-Glacis' slopes to the north, both with a gradient of ~4% (Figs. 4 and 5). The bedrock surface is effectively shallower in the second pro le than in the rst one.

Under seasonal tropical conditions, the actual lateritic weathering mantle appears differentially eroded generating different topographic forms carrying distinct weathering facies: convex forms with thick ferricretes on the 'High-Glacis', plan-concave forms with soft ferricrete and/or mottled clays, and fairly concave forms with shallow mottled clays and saprolite, both being mainly developed on the 'Middle-Glacis', excepting the geomorphic scarps delimiting the 'High-Glacis' (Fig. 4). These scarps located just above bedrock domes present concavities with relatively small curvature radius, that may indicate the partial removal of the weathering mantle, and thus the thinning of the weathering pro l es (Fig. 5). Thin pro l es capped with a thin ferricrete or at best with a soft ferricrete are more sensitive to the erosion processes that create plan-concave landforms rather than convex. The 'Middle-Glacis' exhibits a succession of discrete concave and plan-convex forms that can re- e ct short distance transfers and deposits of colluvial materials which were effectively observed [23]. In such a way, the hillslope shape as a whole can be at once weathering and transport limited [30]. The convex 'High-Glacis' covered by thick ferricretes arises from creep processes, while the plan-concave slopes result from sheetwash and overland ow [30], which tend to truncate the weathering pro l es. The above landforms and the physical properties of the associated materials are also able to control the permeability and thus the underlying hydrodynamics.

4.5. Hydrodynamics of the lateritic weathering mantle

The hydrodynamic processes are controlled by the groundsurface and bedrock topographies, and also by the physical properties of the materials, e.g., the porosity depending on clay and iron contents but also on size and content of residual quartz. Convex hillslope units with ferricrete generate divergent runoff while concave units favour the concentration of water as well as its in ltration since they result from the degradation of the ferricrete exhuming more porous mottled clays and saprolite. Beneath the resulting scarps, sharp bedrock domes act as structural thresholds generating divergent water uxes and thus limiting the weathering processes, while adjacent concave bedrock forms as hollows concentrate the water ux es enhancing the bedrock weathering (Fig. 5). These processes seasonally repeat so that the bedrock weathering process can be construed as a self-organized geochemical system. During the rainy season, a continuous saturated level in the saprolite of the second pro le from −315 to 345 m just underneath the eastern scarp (Fig. 4B) would also be expected. Under seasonal tropical conditions, signi cant variations of the water table level can lead to underground dissolution processes [31], that could

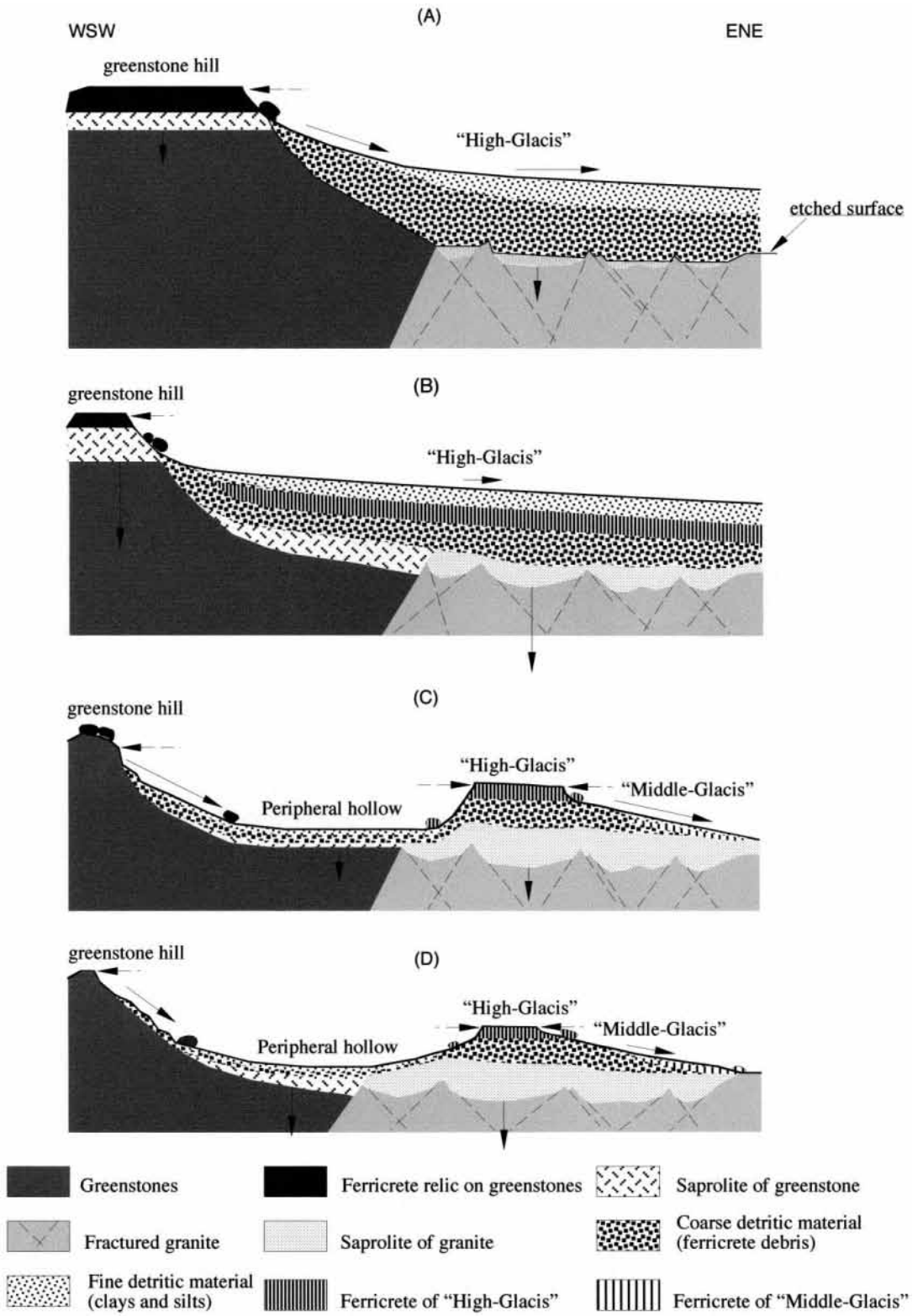
(A)
WSW
ENE
greenstone hill
"High-Glacis"
etched surface
(B)
greenstone hill
"High-Glacis"
(C)
greenstone hill
"High-Glacis"
"Middle-Glacis"
Peripheral hollow
(D)
greenstone hill
"High-Glacis"
"Middle-Glacis"
Peripheral hollow
Greenstones
Ferricrete relic on greenstones
Saprolite of greenstone
Fractured granite
Saprolite of granite
Coarse detritic material (ferricrete debris)
Fine detritic material (clays and silts)
Ferricrete of "High-Glacis"
Ferricrete of "Middle-Glacis"

also explain why the ferricrete of the 'High-Glacis' appears more disaggregated in the second pro l e than in the rst one (Figs. 4 and 5).

5. Conclusion

2-D electrical resistivity tomography has proved useful in analyzing the layer organization of thick lateritic weathering mantles. Results from the ERT and cross-borehole methods along with the estimates of the aquifers and granitic rock resistivities provide constrained resistivity ranges for each weathering layer, i.e., the unweathered and weathered bedrock, the saturated and unsaturated saprolite, the mottled zone, the soft ferricrete and the ferricrete. That has also allowed useful description of the relationships between the layer boundaries, in particular between the granitic bedrock and the groundsurface topographies. The hillslope geomorphic patterns result from mechanical erosion processes of allochthonous material accumulated over an undulated granitic surface whose topography was shaped by previous climatic weathering processes. The spatial relationships between the bedrock and groundsurface topographies thus indicates that the hillslope shape results from both mechanical erosion and weathering processes re ecting climatic and geomorphic changes. Hence, the electrical resistivity tomography is a useful tool for earth investigations —it is also promising for mining and groundwater prospecting.

Acknowledgements

We gratefully thank J.-M. Wackerman for conductivity measurements in the pits and G. Grandin for helpful criticism on a previous version and advised hints for Figs. 1, 5 and 6. This work was na ncially supported by the 'Institut de Recherche pour le Développement', IRD (AB 662102, RED-UR06). Criticism and remarks from Pr. C.R. Twidale and an anonymous reviewer have been also appreciated. *[RV]*

Fig. 6. Sketch of weathering–erosion processes that should have governed the shaping of Tenkoto area landscape as a function of climatic changes: (A) semi-arid to arid climate; (B) humid seasonal tropical climate; (C) dry seasonal tropical to semi-arid climate; (D) actual seasonal tropical climate. Horizontal or oblique plain arrows = mechanical erosion with lateral transport of material; vertical plain arrows = rock weathering with thickening of the pro le; dashed arrows = scarp retreat; the length of the arrows stands for the magnitude of processes; arbitrary scale for thicknesses; the topographic pro le in (D) is that of Fig. 1B.

References

[1] G. Pedro, Distribution des principaux types d'altération chimique à la surface du globe, Présentation d'une esquisse géographique, Rev. Géogr. Phys. Dyn., Paris 10 (5) (1968) 457–470.

[2] B. Daily, C.R. Twidale, A.R. Milnes, The age of the lateritized summit surface on Kangaroo Island and adjacent areas of South Australia, J. Geol. Soc. Aust. 21 (4) (1974) 187–192.

[3] P. Michel, Cuirasses bauxitiques et ferrugineuses d'Afrique Occidentale, Aperç u chronologique, in: Geomorphologie des reliefs cuirassés dans les pays tropicaux chauds et humides, Travaux et Documents de Géographie tropicale, 33, CEGET, CNRS, Bordeaux, 1978, pp. 13–31.

[4] M.I. Bird, A.R. Chivas, Oxygen isotope dating of the Australian regolith, Nature 331 (1988) 513–516.

[5] Y. Tardy, Pétrologie des latérites et des sols tropicaux, Masson, Paris, 1993, 535 pp.

[6] C.R. Twidale, J.A. Bourne, Origin and age of bornhardts, southwest Western Australia, Aust. J. Earth Sci. 45 (1998) 903–914.

[7] D.B. Nahon, Introduction to the Petrology of Soils and Chemical Weathering, Wiley, New York, NY, 1991, 313 pp.

[8] A. Blot, J.C. Leprun, J.C. Pion, Originalité de l'altération et du cuirassement des dykes basiques dans le massif de granite de Saraya (Sénégal oriental), Bull. Soc. Geol. Fr. 7 (1976) 45–49.

[9] J.-C. Leprun, Les cuirasses ferrugineuses des pays cristallins de l'Afrique occidentale sèche, Genèse, Transformation, Dégradation, Mém. Sci. Géol., Strasbourg 58 (1979) 224 pp.

[10] D. Nahon, Cuirasses ferrugineuses et encroûtements calcaires au Sénégal occidental et en Mauritanie, Systèmes évolutifs: géochimie, structures, relais et coexistence, Mém. Sci. Géol., Strasbourg 44 (1976) 232 pp.

[11] D. Nahon, Evolution of iron crusts in tropical landscapes, in: S.M. Coleman, D.P. Dethier (Eds.), Rates of Chemical Weathering of Rock and Minerals, Academic Press, New York, NY, 1986, pp. 169–191.

[12] Y. Tardy, D. Nahon, Geochemistry of laterites, stability of Al-goethite, Al-hematite, and Fe^{3+}-kaolinite in bauxites and ferricretes: an approach to the mechanism of concretion formation, Am. J. Sci. 285 (1985) 865–903.

[13] J.-P. Ambrosi, D. Nahon, Petrological and geochemical

differentiation of lateritic iron crust pro les , Chem. Geol. 57 (1986) 371–393.
[14] A. Beauvais, F. Colin, Formation and transformation processes of iron duricrust systems under tropical humid environment, Chem. Geol. 106 (1993) 77–101.
[15] H. Robain, M. Descloitres, M. Ritz, Q.Y. Atangana, A multiscale electrical survey of a lateritic soil in the rain forest of Cameroon, J. Appl. Geophys. 34 (1996) 237–253.
[16] G.J. Palacky, K. Kadekaru, Effect of tropical weathering on electrical and electromagnetic measurements, Geophysics 44 (1979) 69–88.
[17] J.R.T. Hazell, C.R. Cratchley, C.R.C. Jones, The hydrogeology of crystalline aquifers in northern Nigeria and geophysical techniques used in their exploration, in: E.P. Wright, W.G. Burgers (Eds.), Hydrogeology of Crystalline Basement Aquifers in Africa, Geol. Soc. London, Spec. Publ. 66 (1992) 155–182.
[18] O. Koefoed, Geosounding Principles, 1, Resistivity Sounding Measurements, Elsevier, Amsterdam, 1979, 276 pp.
[19] G.V. Keller, F.C. Frischknecht, Electrical Methods in Geophysical Prospecting, Pergamon, Oxford, 1966, 519 pp.
[20] E. Delaitre, Etude des latérites du Sud-Mali par la méthode de sondage électrique, Ph.D. Thesis, Strasbourg University, Strasbourg, 1993, 193 pp.
[21] D.H. Grif ths, R.D. Barker, Two-dimensional resistivity imaging and modelling in areas of complex geology, J. Appl. Geophys. 29 (1993) 211–226.
[22] M. Ritz, J.-C. Parisot, S. Diouf, A. Beauvais, F. Diome, M. Niang, Electrical imaging of lateritic weathering mantles over granitic and metamorphic basement of eastern Senegal, West Africa, J. Appl. Geophys. 41 (1999) 335–344.
[23] P. Michel, Les bassins des euves Sénégal et Gambie, Etudes géomorphologiques, Mém. ORSTOM, Paris 63 (1973) 1170 pp.
[24] D.H. Grif ths, J. Turnbull, A.I. Olayinka, Two-dimensional resistivity mapping with a computer-controlled array, First Break 8 (1990) 121–129.
[25] L.P. Beard, G.W. Hohmann, A.C. Tripp, Fast resistivity/IP inversion using a low-contrast approximation, Geophysics 61 (1996) 169–179.
[26] M.H. Loke, R.D. Barker, Rapid least-squares inversion of apparent resistivity pseudosections by a quasi-Newton method, Geophys. Prosp. 44 (1996) 131–152.
[27] M.H. Loke, RES2DINV software user's manual, 1997.
[28] A. Hossin, Calcul des saturations en eau par la méthode des ciments argileux (formule d'Archie généralisée), Bull. A.F.T.P., 1960.
[29] G. Grandin, Aplanissements cuirassés et enrichissement des gisements de manganèse dans quelques régions d'Afrique de l'Ouest, Mém. Off. Rech. Sci. Tech. Outre-Mer, Fr. 82 (1976) 275 pp.
[30] M.J. Selby, Hillslope Materials and Processes, Oxford University Press, Oxford, 1993, 451 pp.
[31] M.F. Thomas, Geomorphology in the Tropics, A Study of Weathering and Denudation in Low Latitudes, Wiley, New York, NY, 1994, 460 pp.
[32] A. Beauvais, C. Roquin, Petrological differentiation patterns and geomorphic distribution of ferricretes in Central Africa, Geoderma 73 (1996) 63–82.
[33] Y. Tardy, C. Roquin, Dérive des continents, Paléoclimats et altérations tropicales, BRGM, Orléans, 1998, 473 pp.
[34] A. Beauvais, Geochemical balance of lateritization processes and climatic signatures in weathering pro les overlain by ferricretes in Central Africa, Geochim. Comochim. Acta (1999) in press.

ARTICLE 6

Earth Surface Processes and Landforms
Earth Surf. Process. Landforms **28**, 1071–1080 (2003)
Published online 13 August 2003 in Wiley InterScience (www.interscience.wiley.com). DOI: 10.1002/esp.504

TESTING ETCHING HYPOTHESIS FOR THE SHAPING OF GRANITE DOME STRUCTURES BENEATH LATERITIC WEATHERING LANDSURFACES USING ERT METHOD

ANICET BEAUVAIS,[1,2]* MICHEL RITZ,[2,3] JEAN-CLAUDE PARISOT[2,3] AND CHRISTIAN BANTSIMBA[3,4]

[1] *Cerege-IRD, UR-037, Université d'Aix-Marseille III, Europôle de l'Arbois, BP 80, 13545 Aix-en-Provence Cedex, France*
[2] *IRD, DME, UR-037, BP A5, 98848 Nouméa, New Caledonia*
[3] *IRD, Centre de Hann, BP 1386, Dakar, Sénégal*
[4] *UCAD, Département de Géologie, Dakar, Sénégal*

Received 12 April 2002; Revised 10 January 2003; Accepted 6 February 2003

ABSTRACT

Granite domes, boulders and knobs buried within saprolite have been detected beneath lateritic weathering landsurfaces using 2D electrical resistivity tomography (ERT). This technique provides a valuable means of mapping the bedrock topography and the regolith structures underneath landsurfaces, as it is intrinsically very sensitive to the electrical properties of superimposed pedological, hydrological and geological layers, allowing the determination of their relative geometry and spatial relationships. For instance, 2D inverse electrical resistivity models including topographic data permit the definition of lithostratigraphic cross-sections. It shows that resistive layers, such as the more or less hardened ferruginous horizons and/or the bedrock, are generally well differentiated from poorly resistive layers, such as saprolite, including water-saturated lenses, as has been corroborated by past and actual borehole observations. The analysis of the 2D geometrical relations between the weathering front, i.e. the bedrock topography, and the erosion surface, i.e. the landsurface topography, documents the weathering and erosion processes governing the development of the landforms and the underlying structures, thus allowing the etching hypothesis to be tested. The infiltration waters are diverted by bedrock protrusions, which behave as structural thresholds compartmentalizing the saprolite domain, and also the regolith water table, into distinct perched saturated subdomains. The diverted waters are thus accumulated in bedrock troughs, which behave like underground channels where the saprolite production rate may be enhanced, provided that the water drainage is efficient. If the landsurface topography controls the runoff dynamics, the actual bedrock topography as depicted by ERT imaging influences the hydrodynamics beneath the landsurface. In some way, this may control the actual weathering rate and the shaping of bedrock protrusions as granite domes and knobs within thick saprolite, before their eventual future exposure. Copyright © 2003 John Wiley & Sons, Ltd.

KEY WORDS: electrical resistivity tomography; granite domes; etching; lateritic landsurface

INTRODUCTION

Granitoid inselbergs are very common landforms exposed at the Earth surface, which are thought to have been previously buried within thick saprolite before stripping and exposure, in many cases resulting from etching process (Thomas, 1989a,b). An extensive literature has reported field observations and data on inselbergs and bornhardts. Except for road cuts, deep drillings and/or excavation observations which have revealed domes and/or boulders embedded in thick saprolite (Thomas, 1966a,b, 1994; Boyé and Fritsch, 1973; Twidale, 1990), no studies have really provided a complete 2D image of such structural features underneath the lateritic weathering landsurface. To highlight the subsurface processes at work in the development and shaping of granite domes and/or knobs at the base of regoliths, we have applied 2D electrical resistivity tomography (ERT) with various electrode spacings to lateritic terrains of southeastern Senegal, West Africa. This area provides an interesting case for addressing the issue of the formation of buried inselberg-like structures such as prominent granite bodies, i.e. 'whalebacks', that are actually cropping out in many thalwegs. It has previously been shown that the underground granite bedrock topography was very irregular, exhibiting domes or 'ruwares' and troughs

* Correspondence to: A. Beauvais, IRD, DME, UR-037, BP A5, 98848 Nouméa, New Caledonia. E-mail: anicet.beauvais@noumea.ird.nc

along kilometric ERT profiles oriented N120° and sloped north to south (Beauvais *et al*., 1999). ERT is however a suitable technique for the investigation of buried structures, even those of tropical lateritic terrains (Griffiths and Barker, 1993; Ritz *et al*., 1999). Although real granite inselbergs are present in our study area, we believe that, in such a granitic geological environment, ERT can provide useful 2D images to test the etching process as hypothetically responsible for dome-shaped structure development beneath inherited lateritic landsurfaces.

Granite domes and inselbergs have been observed in many tropical regions, from the dry latitudes in deserts to the humid latitudes in rainforests. This indicates a dependence on climatic change (Garner, 1974; Büdel, 1982; Summerfield, 1991; Selby, 1993; Thomas, 1994). These are generally associated with etchplains, exposed and/or exhumed by repeated stripping of the embedding saprolite (Thomas, 1989a,b, 1994). Differentiated or divergent chemical weathering processes are strongly involved in the shaping of granite dome structures embedded in thick saprolite (Bremer, 1994). Reiterated mechanical erosion processes of a different nature, such as regolith stripping, stream dissection and, more rarely, long-distance scarp retreat, have contributed to exposing the resulting inselbergs at the Earth's surface (Twidale, 1982; Thomas, 1994; Twidale and Bourne, 1998). It has long been known that before being exposed granite inselbergs have been shaped by differential chemical weathering underneath the soil surface (Thomas, 1966a,b; Twidale, 1990). This process is primarily controlled by the endogenetic structure of the granite bedrock as the density distribution of fractures and joints (Thomas, 1966b; Boyé and Fritsch, 1973; Twidale, 1982), and secondarily, by the variation of its petrologic composition (Pye *et al*., 1986). Chemical weathering works down along the joints, disintegrating the granite and breaking it up into fresh individual blocks as boulders and tors floating free in the deeper zone of saprolite. The surface erosion processes mechanically denude the landsurface at a rate depending on climatic conditions, i.e. seasonal tropical, in regions of quiet tectonics (Büdel, 1982). The above-described processes account for the two stages of the development of etchsurfaces. In other words, periods of differential deep weathering isolating protrusions of fresh granite within a thick saprolite, are followed by periods of stripping that can cause the exposition of those protrusions, which could later evolve into bedrock inselbergs dominating lowlands (Thomas, 1989a,b, 1994). We present modern 2D ERT images that account for the actual development of granite dome structures buried within thick regolith underneath stepped landsurfaces covered by ferricrete in southeastern Senegal.

GEOLOGICAL AND FIELD SETTING

In southeastern Senegal, the geological basement is composed of Early Palaeoproterozoic volcano-sedimentary formations, i.e. Birimian, dated from 2·2 Ma, including a greenstone belt surrounding a granite batholith (Figure 1). Granites of syn- and post-tectonic origin are associated with these formations. The Birimian greenstone consists of meta-andesitic lava and meta-tuffs and also of gabbros and pyroxenites. These formations have been effectively intruded by a post-tectonic granite batholith of around 5 km diameter, which is crossed by fractures oriented NW, and by veins of pegmatite, rhyolite and dacite (Figure 1). The granite is mainly composed of 25 per cent quartz, 25 per cent orthoclase, 45 per cent plagioclase, and 5 per cent (biotite + amphibole), while the tuffs are composed of 13 per cent quartz, 5 per cent orthoclase, 55 per cent plagioclase, 20 per cent Fe-Mg minerals and 7 per cent ilmenite, magnetite, hematite and chlorite. The study is focused on the granite intrusion itself, and on the contact between the granite and the tuffs, both being overlain by a thick lateritic weathering mantle capped with ferricrete.

The landscape consists of steep hills on greenstone, dominating a geomorphologic system of two stepped glacis on the granite batholith, which have been named High- and Middle-glacis (Michel, 1973). These two geomorphologic units are covered by ferricrete (Figure 1). The hills culminate around 255–285 m. The highest hill bears a relic of ferricrete thought to be older than the ferricrete developed on the lower glacis as a rectilinear slope (Michel, 1973), whereas fresh or little-weathered mafic rocks crop out on the other hills. High- and Middle-glacis have altitudes of 200–215 m and 175–195 m, respectively (Figure 1). Between hills and lateritic glacis a peripheral hollow at around 180 m has been shaped on meta-andesites and meta-tuff formations, and also on the granite. Many dome-shaped granites crop out in flat thalwegs incising the Middle-glacis slope, while it has previously been shown that the buried granite topography was rather undulating and not parallel to the actual landsurface topography (Beauvais *et al*., 1999).

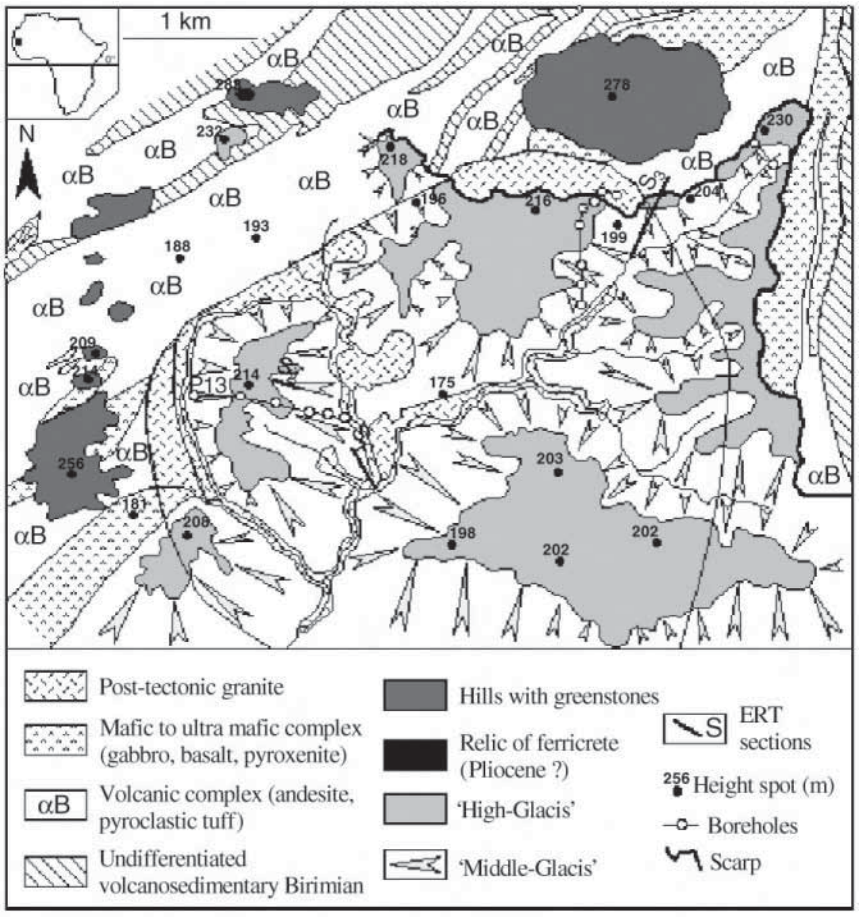

Figure 1. Geological and geomorphological map, and location of the electrical resistivity tomography (ERT) sections, S1, S2 and S3. Reproduced from Beauvais *et al*., 1999, with permission from Elsevier Science

The climate is seasonal tropical with a wet season from June to September and a dry season for the rest of the year. The mean annual rainfall is 1200–1400 mm, the mean annual temperature is *c*. 28 °C while the mean annual relative air humidity is *c*. 50 per cent. The wettest month is August with *c*. 300 mm, while the highest rainfall recorded is 100 mm. The vegetation consists of a semi-humid savannah with an alternation of wood and graminaceae domains.

GEOPHYSICAL TECHNIQUE

A 2D electrical resistivity tomography survey was carried out by combining multichannel direct current (DC) geo-electrical measurements and 2D tomographic inversion techniques (Daily and Ramirez, 1992; Loke and Barker, 1996; Storz *et al*., 2000). An ABEM Lund Imaging System was employed with a Wenner configuration and an array of 64 steel electrodes. Although a dipole–dipole configuration has proved useful in locating buried resistive bodies such as bedrock in weathered terrains (Zhou *et al*., 1999), a Wenner array is more suitable because of the presence of near-surface resistivity variations that otherwise produce noisy data (Griffiths and Barker, 1993). The discontinuous ferricrete surface layer can effectively cause such problems. Three geophysical sections have been obtained (Figure 1). Unit electrode spacings of 5 and 3 m were employed to provide greater detail on the subsurface ferruginous horizons of the regolith, such as the ferricrete and the soft ferricrete, and also to detect the prescence of relatively shallow bedrock structures (Bantsimba, 2001). A unit spacing of 10 m was also used to provide a global view of 100 m thickness of regolith and geological structures. Such a

layout is suitable to examine the bedrock topography as well as the expected geological contacts beneath the landsurface.

The electrical measurements were recorded using a computer-controlled multichannel resistivity meter located in the middle of the 64 electrode configuration. The apparent resistivity data were inverted using a least-square method to obtain a model of the underground geology that yielded the observed distribution of apparent resistivity values (Beard *et al*., 1996; Loke and Barker, 1996; Loke, 1997; Zhou *et al*., 1999). A resistivity section of the underlying structures, integrating the *in situ* resistivity values of the bedrock, the underground water and the different layers of the regolith plus the landsurface topography, was finally obtained. The topography of the profiles was obtained using a clinometer with measurements every 10 m and less when it was necessary. Although a 10 m electrode spacing provides a data resolution lower than a 5 or a 3 m spacing (Zhou *et al*., 1999), the numerous boreholes close to the different geophysical sections (Figure 1) have aided the useful calibration of the geo-electrical models, and thus, their geological interpretation. The major part of those boreholes was previously set and described by BRGM researchers (Michel, 1973); we have dug additional pits for our own purpose (Beauvais *et al*., 1999; Bantsimba, 2001).

RESULTS AND DISCUSSION

Electrical image of the granite–ferricrete unconformity

The geo-electrical section, S1 (Figure 1), was recorded in the downslope part of a glacis slope, i.e. Middle-glacis, including a thalweg where an unconformity was observed between a fresh granite dome outcrop and a ferricrete of equal thickness (Figure 2A). The investigation depth is around 50 m. A relatively good interpretation of the electrical resistivity section can be gained from previously obtained results (Beauvais *et al*., 1999; Bantsimba, 2001). This concerns (i) direct observations in boreholes, (ii) calibrations of the electrical resistivity signal for the different regolith horizons applying a cross-borehole electrical resistivity survey in the same area, and (iii) the *in situ* resistivity measurements of the granite bedrock and of the water conductivity in some boreholes. The spatial variations of resistivity, ρ, thus reflect the superimposition of different geo-electrical layers corresponding to well defined horizons (Figure 2B). The geo-electrical layer comprising the ferricrete and the soft ferricrete is well characterized by $\rho > 1600\ \Omega$m, while the layer defined by $130 < \rho < 1600\ \Omega$m corresponds to the saprolite plus the mottled clays horizon. The weathered granite is characterized by $1600 < \rho < 3250\ \Omega$m, whereas $\rho > 3250\ \Omega$m well described the unweathered granite. The saturated domains of the saprolite have been defined by $\rho \leq 130\ \Omega$m (Figure 2), which has been derived from the generalized Archie law corrected for the clay contribution (Hossin, 1960; Beard *et al*., 1996) as previously explained (Beauvais *et al*., 1999). The above geo-electrical interpretation accounts accurately for the unconformity observed in the field between the granite bedrock and the ferricrete layer on the stream bank between positions 85 and 95 m, where no saprolite is preserved in between the two layers (Figure 2B). This indicates a likely allochthonous origin of the lateritic material forming the ferricrete cap since the latter directly overlies the granite, for which the Fe-content is too low to explain the upper ferruginous accumulation solely by *in situ* geochemical processes. The ferricrete layer protects the Middle-glacis regolith from erosion, but we could imagine that tectonic events such as uplift, and/or climatic changes, would further incise the glacis slope or cause it to retreat, and/or to strip the regolith until the buried granite dome was further exposed. It has recently been shown in the same area that the buried granite protrusions or domes rise up beneath topographical concavities, in particular beneath the scarps located between the High- and the Middle-glacis slope (Beauvais *et al*., 1999), while granite domes are effectively cropping out in most thalwegs (Figure 1). The boundary between the weathered granite and the saprolite is undulating showing a trough and a dome between position 130 and 175 m (Figure 2). Also notice the absence of a saturated domain in the saprolite layer above the bedrock dome in the middle part of Figure 2B around the position 160 m. In contrast, water saturation occurs when the saprolite thickens just above the bedrock troughs between positions 140–150, 180–210 and 275–285 m. The occurrence of water is effective in many boreholes dug around the ERT sections, and was noted by previous researchers (Michel, 1973). Regolith aquifers have been commonly described in various geological environments of many African areas (Enslin, 1961; Tardy, 1969; Blot, 1980; Beauvais, 1999). The detection of water lenses within the regolith is useful to tackle the

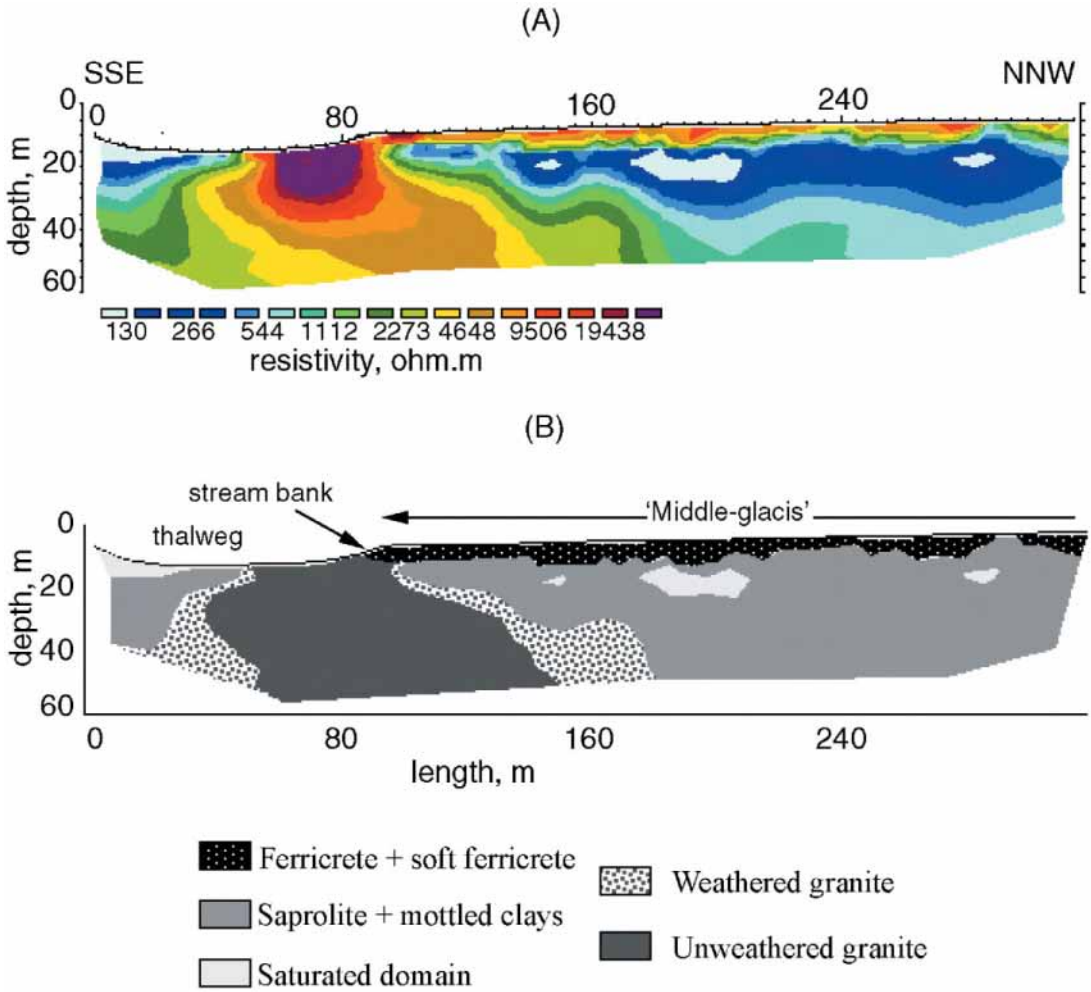

Figure 2. (**A**) 2D inversion results including the landsurface topography with an electrode spacing of 5 m for the electrical resistivity tomography section S1. (**B**) 2D geo-electrical interpretation of (A)

hydrodynamic and differential weathering processes at work in the shaping of the granite topography, in particular, for the genesis of free features like tors and/or boulders within the saprolite.

Geo-electrical image of the upper Middle-glacis slope

A second geo-electrical profile, S2 (Figure 1), was recorded on the upper Middle-glacis slope with an electrode spacing of 3 m that allows an investigation depth of only 15 to 20 m, but provides greater detail of subsurface structures (Figure 3). Such an electrical section allows the differentiation of a consolidated ferricrete of around 2 m thick from a soft ferricrete between positions 0 and 48 m. This geo-electrical section is however especially interesting as it reveals the occurrence of a relic boulder of more or less weathered granite of around 10 m diameter floating free into a relatively thick saprolite. Indeed, the boulder can be defined by resistive layers, $1600 < \rho < 3250\ \Omega$m, embedded in a less resistive domain, $\rho < 1600\ \Omega$m, which can be effectively attributed to saprolite (Figure 3). A previous borehole, P13 (Figure 1), dug on the Middle-glacis landsurface several years ago had revealed the presence of a similar granite boulder at around 10 m depth underneath a saprolite covered with ferruginous horizons as a soft ferricrete and a dismantling horizon with ferricrete debris (Michel, 1973). The consolidated ferricrete layer did not develop between 48 and 100 m as confirmed by the observations made in an actual borehole located at 59 m, which was set at this location to verify the absence of ferricrete. This

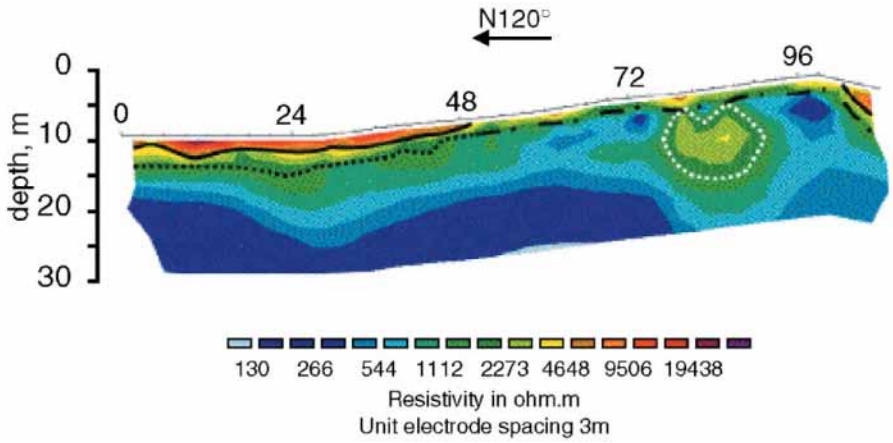

Figure 3. 2D inversion results including the landsurface topography with an electrode spacing of 3 m for the electrical resistivity tomography section S2. The plain black line represents the boundary between the consolidated ferricrete and the soft ferricrete; the stippled black line represents the lower limit of the soft ferricrete; the dashed black line represents the lower limit of the colluvial material, both representing interfaces with the saprolite; the white stippled line represents the contour of the expected granite boulder

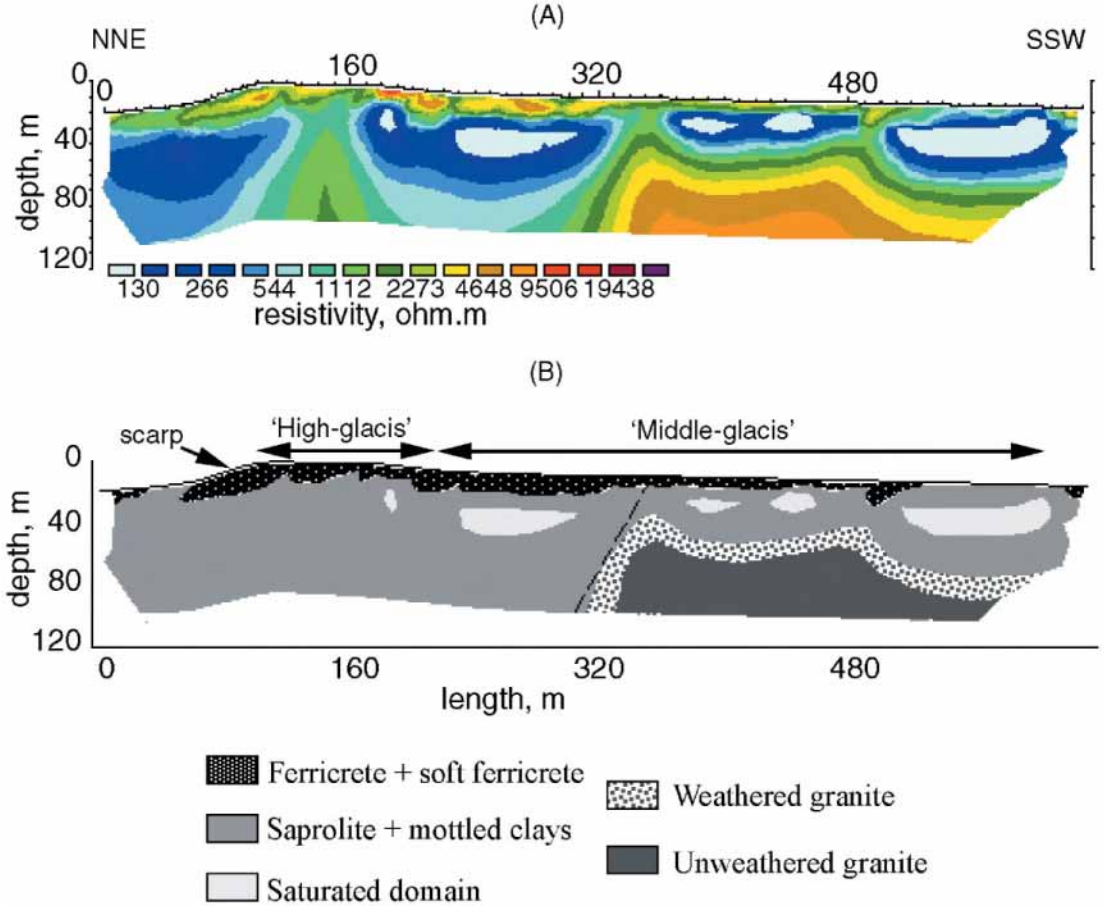

Figure 4. (**A**) 2D inversion results including the landsurface topography with an electrode spacing of 10 m for the electrical resistivity tomography section S3. (**B**) 2D geo-electrical interpretation of (A). The dashed line represents the supposed contact between the tuff and the granite

borehole indeed shows from top to bottom: 0·4 m of humic brown soil with centimetre-sized ferruginous nodules; around 1·5 m of unconsolidated colluvial nodular ferruginous material including 0·3–0·5 m sized free ferricrete blocks and debris; and, a mottled clay horizon occurring at 1·9 m depth (Bantsimba, 2001). Notice that the lower limit of the colluvial ferruginous horizon as delineated from the geo-electrical interpretation and the borehole observation is almost secant to the surface of the expected granite boulder between position 79 and 85 m. These observations sustain the interpretation made for the first geo-electrical section, S1. The colluvial ferruginous material is of allochthonous origin. As previously proposed, such an exogenous material was likely deposited over a previously eroded granite regolith according to climate change (Beauvais *et al*., 1999).

Geo-electrical image of the granite–tuffs contact

A third geo-electrical section, S3 (Figure 1) was obtained across a lithological contact between the granite batholith and tuffs (Figure 4). Using a unit electrode spacing of 10 m, the investigation depth is around 80 m. As above, the resistive layer with $\rho > 1600\ \Omega$m represents the hardened ferruginous horizons as the soft ferricrete and the ferricrete, while the less resistive layer, $130 < \rho < 1600\ \Omega$m, can be attributed to the clayey horizons as the mottled clay layer and the saprolite. Beyond a depth of 20 m, another resistive domain $\rho > 3250\ \Omega$m is clearly visible on the right side of Figure 4 from the position 320 m. This is the geo-electrical signature of the unweathered granite as previously defined (Beauvais *et al*., 1999). The topography of the fresh granite exhibits a knob, which behaves like a structural threshold distributing the percolation waters. Two perched saturated domains containing meteoric waters are effectively developed on both sides of the knob, the largest being in the tuff saprolite (Figure 4B). On the tuff regolith system (left part of Figure 4), the lateritic weathering profile including the ferricrete cap appears thicker than that developed on the granite. In fact, it seems that the less resistive layers sink deeper beyond 80 m. The rate of saprolite production is effectively much higher on tuffs than on granite. On the Middle-glacis, the ferricrete is also thicker on tuffs than on granite. That suggests an autochthonous component for the regolith development, at least for the one developed from the tuffs, even though allochthonous transfers have obviously been involved in the landform development of this area, in particular, that of the granite batholith (Michel, 1973; Beauvais *et al*., 1999) (Figure 2). Except for the saturated domain related to the stream system (right side of Figure 4), the one confined in the tuff saprolite is deeper and more voluminous than that of the granite saprolite. The saprolite of tuffs is richer in kaolinite relatively to quartz than the granite saprolite, and thus, it is less permeable and retains more meteoric water. The relatively shallow saturated domains of the granite saprolite may reflect the occurrence of illuvial clay lenses within the granite saprolite (Figure 4).

In the following, the subsurface processes at work in the shaping of the granite bedrock buried within the regolith are discussed, with an emphasis on the differentiated etching processes that can model at the same time buried granitic features and new landforms.

Differentiated etching processes and landforms evolution

Figure 5 represents a sketch of the modelling of the bedrock topography underneath landsurfaces of south-eastern Senegal under the influence of differentiated erosion and weathering processes. Notice that the runoff is not taken into account, as only the vertical meteoric water fluxes are required to illustrate the differentiation of the weathering processes at work in the shaping of the granite topography. It has been previously suggested that the granite bedrock topography could have experienced partial exposure before burial (Figure. 5A, B) underneath allochthonous lateritic weathering materials including ferricrete debris originating from the older ferricrete-capped weathering profiles developed on the surrounding greenstone hills (Figure 1) (Michel, 1973; Beauvais *et al*., 1999). Such processes result from relatively dry climatic conditions which have resulted in the denudation of the previous lateritic weathering mantles and the modelling of an etchsurface which was finally recovered by allochthonous lateritic materials (Figure 5A, B). Later, under a more humid climate, a ferricrete was developed by reworking Fe-rich lateritic allochthonous materials, while the weathering of the bedrock was reactivated, the original etchsurface being buried in the resulting thick weathering mantle (Figure 5C).

As for many exposed inselbergs, the buried granite domes of southeastern Senegal could thus result from etching processes which are a combination of differentiated bedrock weathering and landsurface denudation (Thomas, 1989a,b, 1994). The magnitude of these processes is determined by the mineralogical and structural

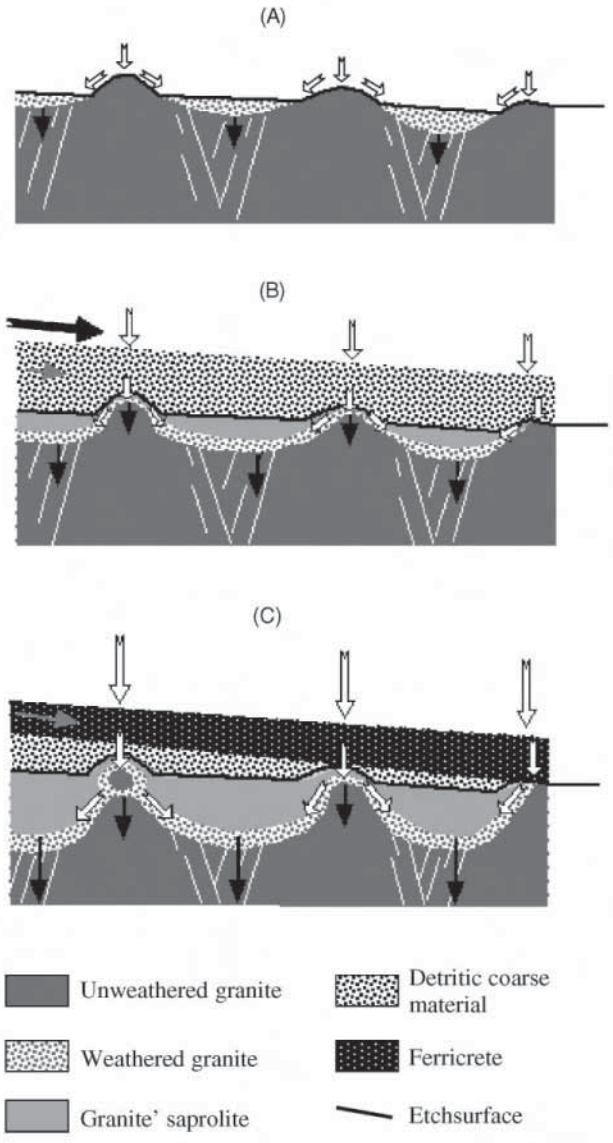

Figure 5. Sketch of the modelling of the granite bedrock in southeastern Senegal. (**A**) Modelling of the etchsurface. (**B**) Accumulation of detritic lateritic material over the original etchsurface. (**C**) Reactivation of the weathering processes and development of a ferricrete reworking the detritic materials. Oblique white lines in the granite represent fractures and joints; broad arrow in (B) represents the transfer-accumulation process of detritic materials; oblique grey arrow represents the migration of Fe-rich solutions contributing to the ferricrete development; white arrows represent the meteoric water fluxes; vertical black arrows represent the lowering of the weathering front; the relative magnitudes of the different processes are indicated by the size of the arrows

patterns of the granite itself, and by climatic and/or tectonic pulsation, respectively (Büdel, 1982; Pye *et al.*, 1986; Summerfield, 1991). The structure and heterogeneous petrologic nature of the granite batholith may effectively induce differentiated weathering patterns able to generate protrusions, knobs and/or domes of fresh granite underneath the landsurface. For instance, differentiated etching processes might have formed the granite boulder detected beneath the Middle-glacis landsurface upslope (Figure 3). Dome-shaped features can also be locally amplified by the proximity of tuffs, the tuffs having been weathered more quickly than the granite in the northeastern zone of our study area (Figure 4). Therefore, the granite knobs and/or domes can further protrude

within the saprolite. Such features might be considered as inherited structural thresholds shedding the percolation water, and thus generating a positive feedback mechanism, thereby protecting themselves from intense chemical weathering (Figure 5). If these divergent water fluxes on the granite knobs may contribute to refill the perched saturated domains identified by ERT in the saprolite, a large part is drained to the bedrock troughs and contributes to efficient weathering (Figure 5B, C). As it was previously shown that the bedrock topography slopes north–south (Beauvais *et al*., 1999), these troughs can be interpreted as underground channels through which the water drainage quality contributes to maintain the weathering processes. The rate of these processes can be increased at the feet of the buried domes and/or knobs (Figure 5C).

Our field observations and interpretations of ERT imaging support the concept of 'divergent weathering' (Bremer, 1994). A 2D image of the first stage of development of granite domes by differential weathering is provided beneath the landsurface before these structural features undergo, perhaps, a future exposure or an exhumation (Twidale, 1981; Twidale and Romani, 1994; Twidale and Bourne, 1998). The exhumation of the granite domes will however depend on the dismantling and erosion of the overlying regolith, in particular, the ferricrete cap, that implies specific tectonic and/or climatic conditions for the future. For instance, the exhumation process of such buried structures might be dependent on new phases of erosion and weathering ferruginization. These new lateritic processes could generate a new lower landsurface, known as the Low-glacis, similar to the one described around 150 km northeastward (Michel, 1973), where true granite 'whaleback' and/or inselbergs effectively rise above an old flattened landsurface assimilated to Low-glacis type landforms (Vogt, 1959). Although no such landform has yet formed in our study area, we recall that the granite bedrock crops out in most thalwegs (Figures 1 and 2B), so that it could be further exposed if conditions for the modelling of a new landsurface were sustained, for instance, conditions favourable to the formation of a Low-glacis landsurface similar to the one widely developed northwards. The most efficient process for shaping the granite dome and inselbergs is however the differential weathering operating within thick saprolite of the actual glacis landsurfaces (Figure 5). Once the granite structures have been exposed their forms change very slowly, their aerial shape being mainly inherited from past conditions which prevailed at the weathering front beneath the previous landsurface (Twidale, 1990). At present, an interesting issue would be to record measurements of the *in situ* production of cosmonuclides such as ^{10}Be and ^{26}Al in quartz grains of both buried and outcropping granite features to verify if the buried ones have effectively experienced exposure before burial (Figure 5A).

CONCLUSION

The ERT technique usefully documents the structure of granite bedrock, and allows distinction of different horizons in the thick regolith, among them the different hardened ferruginous horizons and the perched saturated domains in the saprolite. ERT also provides useful images of granite domes and knobs within thick saprolite beneath the landsurface. These images account for the primary geological structures of, perhaps, incipient future inselbergs before their exposure. If the bedrock topography results from differentiated weathering processes, it may also control the actual hydrodynamics underneath the landsurface once the meteoric waters have been infiltrated. The resulting domes and knobs of granite are structural thresholds distributing the percolation waters towards the bedrock troughs hosting the largest volume of saprolite. We believe such a system to be self-organized in that the more meteoric waters percolate through the regolith, the quicker the perched saprolite domains can be saturated, but the larger is the quantity of water diverted by the knobs that is drained to the underground bedrock channels. This results in an increase in the saprolite production rate, and thus, the deepening of the weathering front that also accentuates the concavity of bedrock furrows. In consequence, the protrusion of the granite knobs is enhanced, preparing in that way an eventual future exhumation, provided that forthcoming tectonic and/or climatic conditions are sustained for shaping new landforms, such as Low-glacis type landsurface.

ACKNOWLEDGEMENTS

This is a contribution of IRD (UR-037). We thank Dr G. Grandin for his critical reading of a previous draft, and two anonymous referees for their critical review.

REFERENCES

Bantsimba C. 2001. *Contribution à la caractérisation des couvertures latéritiques par les imageries électriques et radar, Sénégal Oriental*. Third cycle thesis, UCAD University, Dakar, Senegal.

Beard LP, Hohmann GW, Tripp AC. 1996. Fast resistivity/IP inversion using a low-contrast approximation. *Geophysics* **61**: 169–179.

Beauvais A. 1999. Geochemical balance of lateritization processes and climatic signatures in weathering profiles overlain by ferricrete in Central Africa. *Geochimica and Cosmochimica Acta* **63**(23/24): 3939–3957.

Beauvais A, Ritz M, Parisot J-C, Dukhan M, Bantsimba C. 1999. Analysis of poorly stratified lateritic terrains overlying a granite bedrock in West Africa, using 2-D electrical resistivity tomography. *Earth and Planetary Sciences Letters* **173**: 413–424.

Blot A. 1980. *L'altération climatique des massifs de granite du Sénégal*. Travaux et Documents 114. ORSTOM: Paris.

Boyé M, Fritsch P. 1973. Dégagement artificiel d'un dôme crystallin au Sud-Cameroun. *Travaux et Documents de Géographie Tropicale* (Bordeaux), France **8**: 31–62.

Bremer H. 1994. Soils in tropical geomorphology. *Zeitschrift für Geomorphologie* **38**(3): 257–265.

Büdel J. 1982. *Climatic Geomorphology*. Princeton University Press: Princeton, New Jersey.

Daily W, Ramirez A. 1992. Electrical resistivity tomography of vadose water movement. *Water Resources Research* **28**: 1429–1442.

Enslin JF. 1961. Secondary aquifers in south Africa and the scientific selection of boring sites in them. *International Conference on Hydrology. CCTA Publ. 66, Section 4, Groundwater Hydrology*: 379–389.

Garner HF. 1974. *The Origin of Landscapes – A Synthesis of Geomorphology*. Oxford University Press: New York.

Griffiths DH, Barker RD. 1993. Two-dimensional resistivity imaging in areas of complex geology. *Journal of Applied Geophysics* **29**: 211–226.

Hossin A. 1960. Calcul des saturations en eau par la méthode des ciments argileux (formule d'Archie généralisée). *Bulletin de I'Association Française des Techniciens et Professionnels du Pétrole*.

Loke MH. 1997. *RES2-DINV: Software User's Manual*.

Loke MH, Barker RD. 1996. Rapid least-squares inversion of apparent resistivity pseudosections by a quasi-Newton method. *Geophysical Prospecting* **44**: 131–152.

Michel P. 1973. *Les bassins des fleuves Sénégal et Gambie. Etudes géomorphologiques*. Mémoire 63. ORSTOM: Paris.

Pye K, Goudie AS, Watson A. 1986. Petrological influence on differential weathering and inselberg development in the Kora area of Central Kenya. *Earth Surface Processes and Landforms* **11**: 41–52.

Ritz M, Parisot J-C, Diouf S, Beauvais A, Diome F, Niang M. 1999. Electrical imaging of lateritic weathering mantles over granite and metamorphic basement of eastern Senegal, West Africa. *Journal of Applied Geophysics* **41**: 335–344.

Selby MJ. 1993. *Hillslope Materials and Processes*. Oxford University Press: Oxford.

Storz H, Storz W, Jacobs F. 2000. Electrical resistivity tomography to investigate geological structures of the earth's upper crust. *Geophysical Prospecting* **48**: 455–471.

Summerfield MA. 1991. *Global Geomorphology*. Longman Scientific & Technical: New York.

Tardy Y. 1969. Géochimie des altérations. *Etude des arènes et des eaux de quelques massifs cristallins d'Europe et d'Afrique*. Mémoire 31. Service de la Carte Géologique d'Alsace et de Lorraine: Strasbourg.

Thomas MF. 1966a. Some geomorphological implications of deep weathering patterns in crystalline rocks in Nigeria. *Transactions of the Institute of British Geographers* **40**: 173–193.

Thomas MF. 1966b. The origin of bornhardts. *Zeitschrift für Geomorphologie*, *N. F.* **10**: 478–480.

Thomas MF. 1989a. The role of etch processes in landform development I. Etching concepts and their applications. *Zeitschrift für Geomorphologie N. F.* **33**(2): 129–142.

Thomas MF. 1989b. The role of etch processes in landform development II. Etching and the formation of relief. *Zeitschrift für Geomorphologie N. F.* **33**(3): 257–274.

Thomas MF. 1994. *Geomorphology in the Tropics. A Study of Weathering and Denudation in Low Latitudes*. John Wiley: New York.

Twidale CR. 1981. Inselbergs- exhumed and exposed. *Zeitschrift für Geomophologie, N. F.* **25**(2): 219–221.

Twidale CR. 1982. *Granite Landforms*. Elsevier: Amsterdam.

Twidale CR. 1990. The origin and implications of some erosional landforms. *Journal of Geology* **98**: 343–364.

Twidale CR. Bourne JA. 1998. Origin and age of bornhardts, Southwest Western Australia. *Australian Journal of Earth Sciences* **45**: 903–914.

Twidale CR. Romani JRV. 1994. On the multistage development of etch forms. *Geomorphology* **11**(2): 107–124.

Vogt J. 1959. Aspect de l'évolution morphologique récente de l'Ouest Africain. *Annales Géographique, France*. **367**: 193–206.

Zhou W, Beck BF, Stephenson JB. 1999. Reliability of dipole-dipole electrical resistivity tomography for defining depth to bedrock in covered karst terranes. *Environmental Geology* **39**(7): 760–766.

ARTICLE 7

Available online at www.sciencedirect.com
SCIENCE DIRECT®
Geoderma 119 (2004) 121–132
GEODERMA
www.elsevier.com/locate/geoderma

Combined ERT and GPR methods for investigating two-stepped lateritic weathering systems

Anicet Beauvais[a,b,*], Michel Ritz[a], Jean-Claude Parisot[a], Christian Bantsimba[c], Michel Dukhan[d]

[a] *IRD, DME, UR-037, BP. A5, 98848 Nouméa Cedex, New Caledonia*
[b] *Cerege-IRD, UR-037, Europôle de l'Arbois, BP. 80, 13545 Aix-en-Provence Cedex, France*
[c] *UCAD, Département de Géologie, Dakar, Senegal*
[d] *IRD, US-19, BP. 5045, 34032 Montpellier Cedex, France*

Received 29 January 2003; accepted 26 June 2003

Abstract

Electrical resistivity tomography (ERT) and ground-penetrating radar (GPR) surveys have been carried out in eastern Senegal for investigating two-stepped lateritic systems developed upon crystalline basement rocks. The geo-electrical pseudo-sections derived from ERT data provide a broad view of the lateritic weathering mantle, which is characterised by a decrease in resistivity with increasing depth. High resistivities characterise hardened ferruginous materials, in particular, the ferricrete, while the lower resistivities are related to the clayey horizons such as the saprolite. GPR provides high-resolution and continuous subsurface data on the hardened ferruginous horizons. The underlying clay horizons, however, drastically restricted the investigation depth. An anomalous area showing an obvious disruption of the reflections was detected in one of the radar records, suggesting contrasting iron and clay contents of superimposed lateritic weathering materials with differentiated porosity rate and kaolinite amount. Both ERT and GPR allow quite similar investigation depths of the hardened ferruginous surface horizons. Observations from trial boreholes located near the profiles contribute to better interpretation of the ERT and GPR results. The thickness of the weathering horizons depicted from ERT and GPR data roughly corresponds to that measured in the boreholes. The two geophysical methods are affected in different ways by lateritic terrains, but ERT and GPR surveys combined with borehole observation help to reduce ambiguous geological interpretations. ERT and GPR images show the variability of the lateritic weathering facies identified in the boreholes of each landsurface, 'Middle-' and 'High-glacis', depending on different erosion and weathering-ferruginisation processes that have shaped these landsurfaces and allowed the development of more or less mature underlying lateritic weathering profiles.

Keywords: Electrical resistivity tomography; Ground-penetrating radar; Weathering mantle; Ferricrete; Saprolite

1. Introduction

A thick weathering mantle resulting from lateritization processes conceals large areas of bedrock in tropical regions. Weathering profiles developed upon basement rocks commonly exhibit thickness of sever-

* Corresponding author. IRD, UR-037, BP. A5, 98848 Nouméa Cedex, New Caledonia.
E-mail address: Anicet.Beauvais@noumea.ird.nc (A. Beauvais).

0016-7061/$ - see front matter © 2003 Elsevier B.V. All rights reserved.
doi:10.1016/j.geoderma.2003.06.001

al tens of meters, depending on the nature of the parent rock but also on the geomorphic processes at work in the shaping of the landscape (Nahon, 1991; Tardy, 1993; Grandin, 1976; Thomas, 1994). The components of the weathering profile can be discontinuous with a relatively high lateral variability (Bocquier, 1973; Nahon, 1976; Boulet, 1978; Beauvais, 1999). The understanding of their relative contribution to the global process of the lateritic weathering system is important for a wide variety of geophysical investigations including groundwater prospecting and mineral exploration (Palacky and Kadekaru, 1979; Hazell et al., 1992). The purpose of this study is to apply electrical resistivity tomography (ERT) and ground-penetrating radar (GPR) techniques at the same site for accurately depicting the structure of lateritic weathering mantles developed upon granitic rocks. The comparison of the results obtained by the two methods, with available borehole observations, also allows improvement of the interpretations. In particular, those results can together contribute to a better knowledge of the subsurface processes that have shaped the landsurfaces and generated the diversity of underlying lateritic horizon facies, which have been directly observed in the boreholes.

Direct current (DC) resistivity methods and borehole data have been traditionally used to get information on lateritic terrains and tropical soils. Subsurface properties can be, however, highly variable over short distances and borehole data are restricted to the points

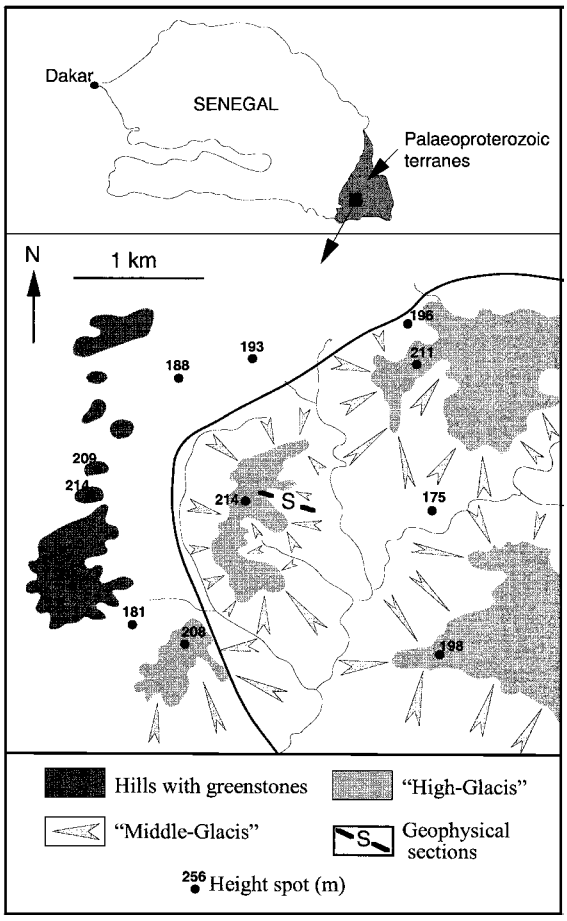

Fig. 1. Study area showing geomorphological patterns, and geophysical profile positions. (The broad envelop is for the boundary of the granite batholith.)

of observation and measurement. The highly heterogeneous nature of the regolith also implies that situations could arise in which the 1-D layered models do not account for realistic geologic structures, rendering conventional DC methods inadequate.

Alternative methods such as ERT and GPR are more suitable to get a continuous cover of the regolith. ERT has been applied to major groundwater exploration problems and to the investigation of areas of complex geology (Griffiths and Barker, 1993; Dahlin and Owen, 1998). GPR has been successfully used in hydrogeological investigations, mapping of bedrock surfaces, and detection of soil horizons (van Overmeeren, 1994; Doolittle and Collins, 1998; Freeland et al., 1998; Aranha et al., 2002). ERT method provides greater depth information than GPR, but it is less portable and does not give unique interpretations. GPR method is a reliable, rapid and economical tool for high-resolution profiling of subsurface structures, but highly conductive horizons, e.g. clay horizons and saline groundwater, generally attenuate radar signals very quickly. The ERT and GPR techniques are also affected in different ways by the geological and environmental noise. It is, however, useful to combine the two methods for providing comprehensive coverage of the investigated sites and for optimising the survey results. We believe that such a combined geophysical approach is suitable to highlight the difference in weathering patterns between two-stepped lateritic landsurfaces of southeastern Senegal (Fig. 1). These lateritic landsurfaces were previously defined as ‘middle-’ and ‘high-glacis’ (Michel, 1973). Both are covered by ferricrete, which overlies relatively thick weathering mantles developed on a post-tectonic granite batholith that intrudes through a volcano-sedimentary basement, including a greenstone belt made up of meta-andesitic tuffs (Fig. 1). We test the usefulness of ERT and GPR techniques to characterise and differentiate the weathering mantles associated to these two landsurfaces.

2. Geophysical techniques

ERT was applied to provide a continuous cover along the profiles and to get quantitative information on the geo-electrical properties of the regolith. A 2-D resistivity tomography was obtained with the ABEM Lund Imaging System with an array of 64 steel electrodes. A Wenner configuration was used with a unit electrode spacing of 1.5 m that is a suitable compromise to obtain enough information on a 15-m thickness with suitable precision. The unit spacing affects the length of the profile, the investigation depth and the resolution. Too large of a unit spacing inevitably leads to a loss of geo-electrical information about the subsurface materials (Ritz et al., 1999). As the hardened ferruginous horizons are relatively thin, the electrodes of the array should be less spaced to get higher vertical and horizontal resolution on those horizons. The ERT method differs from the conventional DC resistivity survey by using a large array of electrodes and by recording the maximum of independent measurements that are possible on the array (Griffiths et al., 1990). ERT data were inverted to produce detailed electrical structures of the cross section below the survey lines, as these are classically presented in the form of pseudo-sections (Edwards, 1977). The measured pseudo-sections including topographic variations were processed with a 2-D inverse modelling technique to give the estimated true resistivities (Loke, 1997). ERT, however, does not provide unique interpretation and is also insensitive to surface layers or features having similar electrical properties.

A pulse EKKO IV radar system with 50-MHz antennas was used in our field investigations. GPR is employed to provide very detailed and continuous images of the subsurface by penetration and reflection of high-frequency electromagnetic waves in the ground (Davis and Annan, 1989; Beres and Haeni, 1991). The success of GPR depends on the permitivity or the dielectric constant contrasts in the ground. Permitivity contrasts between different media determine the amplitude of the reflections (Davis and Annan, 1989). The electrical resistivity of the subsurface horizons also determines the attenuation of the radar signals and thus the penetration depth that can be reached. Areas having highly conductive material such as clayey soil horizons quickly attenuate the signals because of their electrical properties (Jol and Smith, 1991). The use of GPR is indeed inappropriate in areas where the soil resistivity is less than 100 Ω m. The attenuation of the radar signal also increases with increasing antennae frequency (Davis and Annan, 1989). Because emphasis was placed on the penetra-

tion depth rather than resolution, the profiles were measured with 50-MHz antennas, spaced by 0.5 m. The Common mid Point (CMP) technique was used to calculate near-surface average velocities (Annan and Davis, 1976). Lateral changes were not observed from CMP profiles, therefore a constant velocity was used throughout the length of each radar profile. The slope gradient was measured along the profiles using a clinometrer, and the resulting topographic corrections were applied to the radar profiles. The data were processed and plotted using standard procedures (Annan, 1993).

3. Results and discussion

Two longitudinal profiles perpendicular to the contour lines were surveyed applying ERT and GPR methods. The first one extends on a plateau and its scarps assimilated to the 'high-glacis' landsurface, while the second one extends in the mid-part of a piedmont hillslope corresponding to the 'middle-glacis' landsurface (Fig. 1). The nomenclature of previous geomorphologists (Michel, 1973; Grandin, 1976) was adopted for qualifying the glacis type of the two landsurfaces.

3.1. ERT imaging

The measured geo-electrical data were inverted using the interpretation software RES2-DINV (Loke, 1997), implying a nonlinear least-squares optimisation technique to obtain the inversion of measured resistivities (Griffiths and Barker, 1993). The topographic variations have been incorporated in the inversion processing. Notice that the resulting 2-D inverted sections do not necessarily indicate gradual change of resistivity, requiring careful comparison of the resistivity data with available borehole information (Fig. 2).

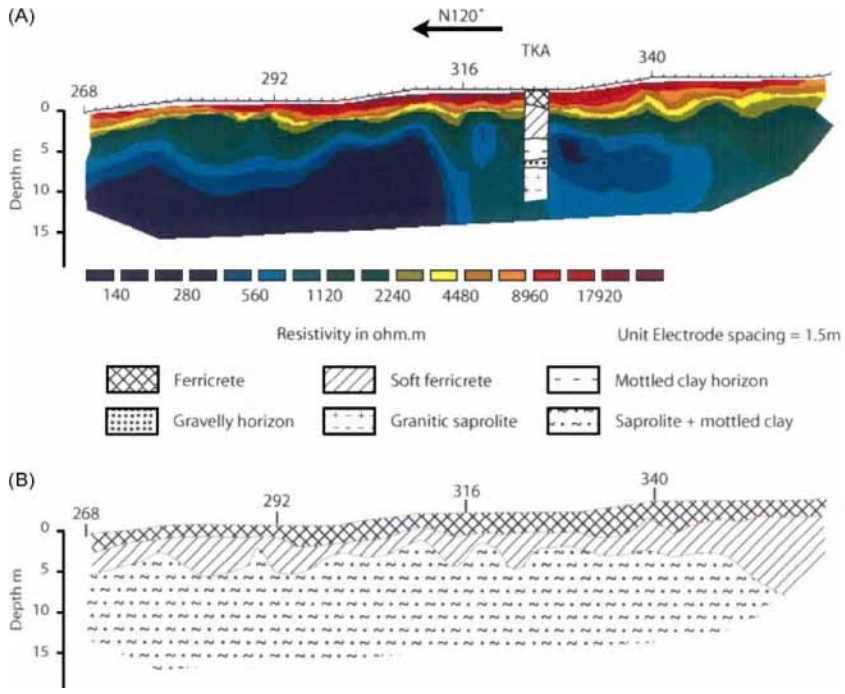

Fig. 2. (A) 2-D Inverted resistivity section from "Middle-glacis" site with an electrode spacing of 1.5 m, and (B) geological interpretation based on the correlation with the lithologic log of a trial borehole, TKA, at position 324. The interpreted section consists of three geo-electrical domains: (1) hardened materials as ferricrete (ρ>4480 Ω m), (2) soft lateritic materials as soft ferricrete + mottled clays (1120 < ρ < 4480 Ω m), and (3) saprolite (ρ < 1120 Ω m.)

3.1.1. 'Middle-glacis' geo-electrical section

The geo-electrical section of the 'middle-glacis' exhibits a relatively thin domain of resistive layers over a thicker one of less resistive layers (Fig. 2A). A trial borehole, TKA, located at position 324 m was described for comparison with interpreted depths from the ERT section. The top layers with resistivities in excess of 4480 Ω m likely correspond to ferruginous hardened horizons (Fig. 2B). At the base of the pseudo-section, the clayey horizons have resistivities ranging from 140 to 1120 Ω m (Fig. 2A and B). Resistivities ranging from 1120 and 4480 Ω m could be attributed to the soft ferruginous horizons such as the soft ferricrete. The decreasing resistivity of the geo-electrical layers with increasing depth might be due to the increasing clay content with depth that also results in higher moisture.

The geo-electrical boundary separating the ferricrete from the underlying soft ferricrete horizon is very tenuous because the ferricrete is thin, only 2-m thick, as defined from the observation of the trial borehole (Fig. 2A), and because the electrical properties of the two ferruginous horizons are generally very similar (Beauvais et al., 1999). The ambiguity in resolving the boundary between the ferricrete and the soft ferricrete was resolved by using a small electrode spacing of 1.5 m. A comparison of interpreted depths with the lithologic log obtained for TKA also reveals a good correspondence between the soft ferricrete horizon and the resistivity layers ranging from 1120 and 4480 Ω m (Fig. 2B). Notice that the gravelly horizon detected in the borehole at the transition between the mottled clays horizon and the saprolite cannot be extrapolated over the entire

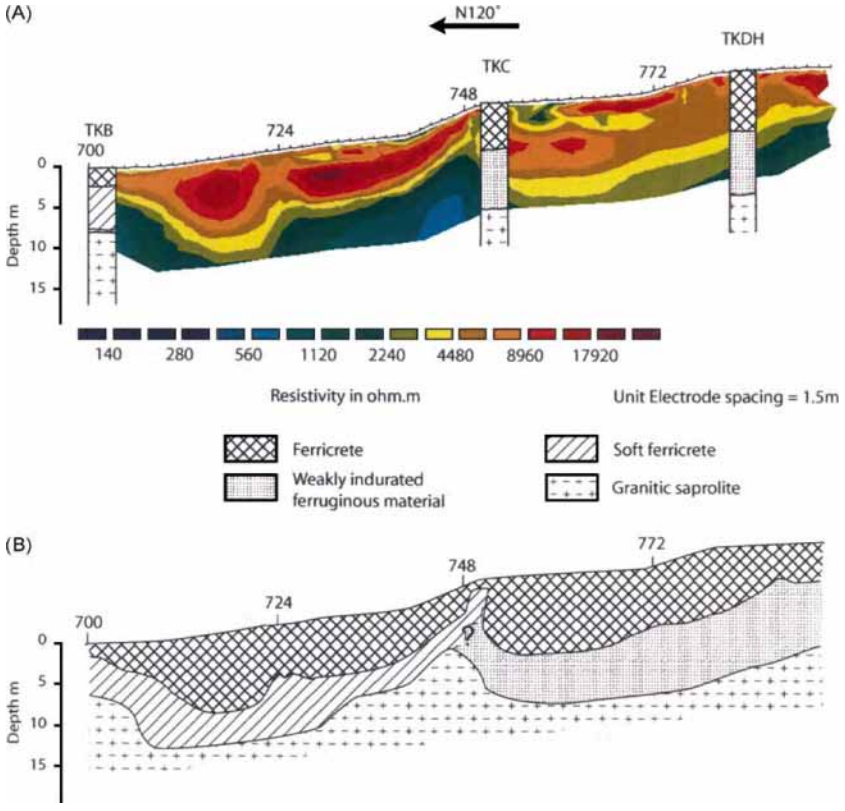

Fig. 3. (A) 2-D inversion model section for the 'High-glacis' landsurface lateritic weathering system with an electrode spacing of 1.5 m. (B) Geological interpretation based on the correlation with the lithologic logs of trial boreholes, TKB, TKC and TKDH, at positions 700, 754 and 786 m, respectively. (See Fig. 2 for the resistivity ranges interpretations.)

section (Fig. 2B). Indeed, it does not correspond to a precise resistivity range for such relatively thin material sandwiched between two poorly resistive clay horizons (Fig. 2A).

3.1.2. 'High-glacis' geo-electrical section

The same logarithmic colour scale is applied to display the 'high-glacis' 2-D resistivity section (Fig. 3A). Although the 'high-glacis' profile exhibits the same overall geo-electrical characteristics, the surface high resistivities attributed to the ferruginous hardened materials are much thicker than those of the 'middle-glacis' profile (Figs. 2A and 3A). High resistivities, above 4480 Ω m, detected in the upper layers are laterally heterogeneous and thicken to the East from positions 748 to 700 m, the scarp at the edge of the 'High glacis' (Fig. 3A). The estimated thickness of the layers varies from a few meters to 8–10 m. In places, a thin very resistive layer, ρ>8960 Ω m, is detected on top of this layer between positions 763 and 775 (Fig. 3A). Below the resistive layer, the other layers are continuous and slightly undulated, while the resistivity decreases progressively to values of 280–560 Ω m. Decrease in resistivity with depth also indicates an increase of clay content with high moisture. The thickness of the geo-electrical layers determined from the ERT data compared to that of the horizons defined in the boreholes, TKB, TKC and TKDH (Fig. 3A) implies resistivity values between 1120 and 4480 Ω m for the ferruginous clayey horizons including the soft ferricrete and the less hardened heterogeneous ferruginous material. The saprolite is thus defined by resistivities lower than 1120 Ω m, while the ferricrete horizon is characterised by ρ>4480 Ω m (Fig. 3B). Three-dimensional effects, however, can lead to ambiguous interpretations of the geo-electrical profiles, thus limiting the efficiency of ERT, requiring the use of another independent geophysical method, such as ground-penetrating radar (GPR), to highlight the 2-D geometry of the hardened ferruginous horizons and their interface with the deeper clay horizons.

3.2. GPR imaging

The two upper bands represent the noise system (Figs. 4 and 5). The propagation velocity through the surface layers was 0.080 m/Ns. During the survey, the hardened surface horizons were dry, while the deep clayey horizons were moist. The radar profiles were also interpreted using additional information from trial boreholes.

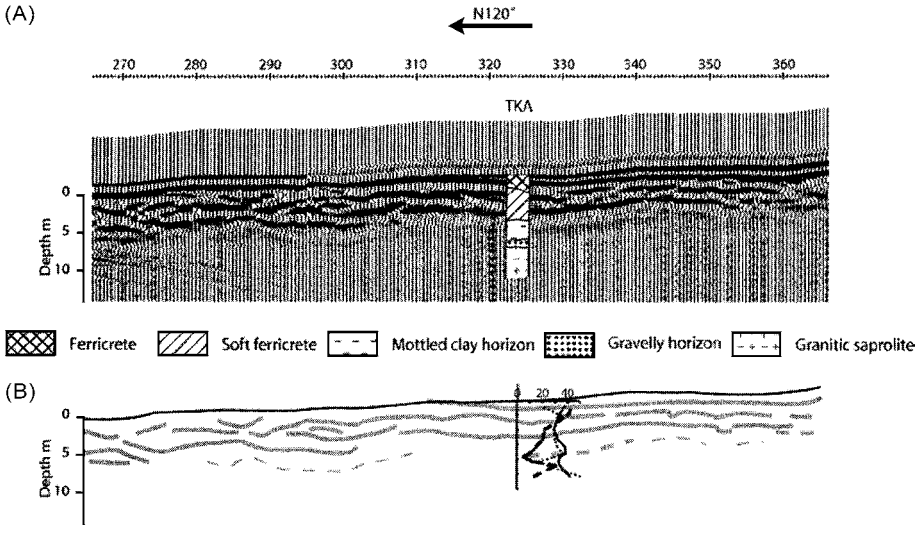

Fig. 4. (A) GPR profile for the 'Middle-glacis' landsurface, and correlation with the lithologic log of the trial borehole TKA. (B) Interpreted georadar reflectors in grey colour superimposed to the kaolinite, Fe_2O_3 and porosity curves for the borehole (broad grey curves = broad reflector; broad dashed grey curves = thin discontinuous reflectors; thin dashed grey curves = very discrete reflectors; stippled curve = kaolinite content; plain curve = porosity rate; bold dashed curve = Fe_2O_3 content).

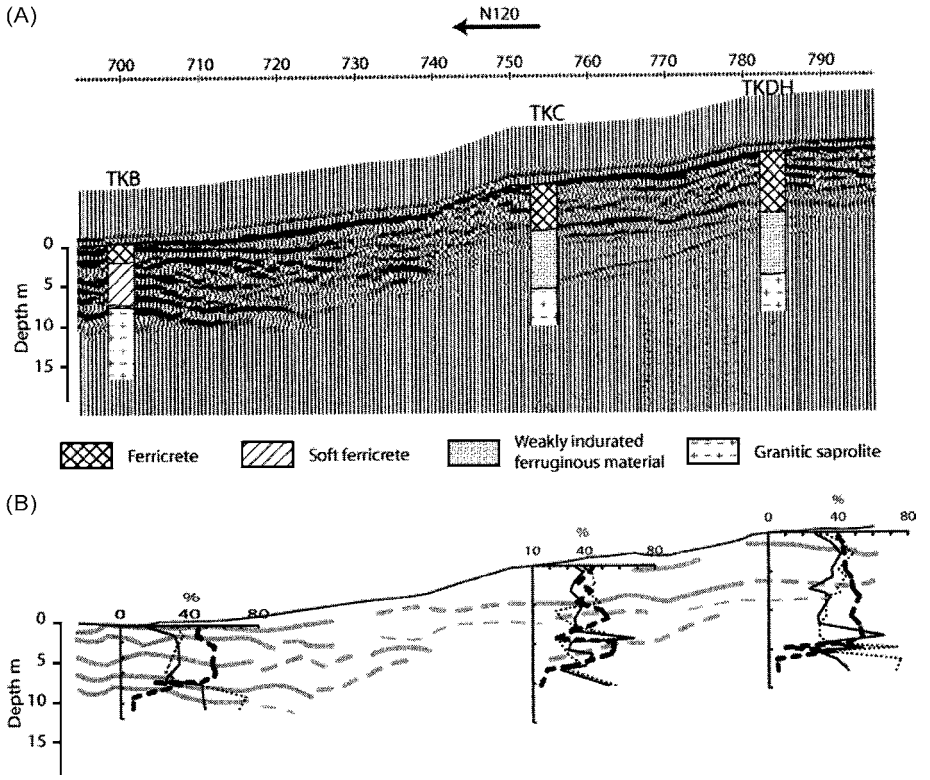

Fig. 5. (A) GPR profile for the 'High-glacis' landsurface and its edge, and correlation with lithologic logs of the trial boreholes, TKB, TKC and TKDH. (B) Interpreted georadar reflectors in grey colour superimposed to the kaolinite, Fe_2O_3 and porosity curves for each borehole (see Fig. 4 for the curves labels explanations).

3.2.1. 'Middle-glacis' georadar profile

The observation depth is at best 5 to 7.5 m in the 'middle-glacis' georadar profile (Fig. 4A). The lack of reflections indicates that the radar signal is attenuated within the mottled clays horizon, while it disappears in the saprolite. The reflection configuration of the radar record is undulated to chaotic and it is interpreted as reflecting buried coarse materials, which have been effectively observed in the trial borehole TKA (Fig. 4A). An interface between ferruginous hardened materials and the clayey horizons has been observed at a depth of about 5 m for TKA. The undulated reflection patterns may thus indicate compact materials, i.e., ferricrete and soft ferricrete, overlying the clayey horizons. In the middle part of the profile, strong reflectors, 1 to 3 m beneath the surface, may suggest abrupt boundaries separating highly contrasted materials in terms of kaolinite content and porosity rate, which effectively control the dielectric constant. In tropical weathering terrains, large variations in the degree of hardness and/or in the clay contents of subsurface materials are commonly observed (Beauvais and Roquin, 1996; Beauvais, 1999). These contrasts can cause strong reflections in the GPR signals. Notice that thin horizons composed of at least 30% clay-size particles can produce high-amplitude reflectors on radar records (Gorin, 1989). Some deepest reflections of higher amplitude may indicate the interface between the clayey and the hardened ferruginous horizons (Fig. 4A).

In 'middle-glacis' georadar profile, the reflector detected at 5 m reflects the difference in Fe_2O_3 and kaolinite contents and porosity between 5 and 8 m. The corresponding decrease in kaolinite and porosity, with an increase of Fe_2O_3 content, effectively leads to a quite discrete reflector at 8 m in the radar profile.

This can be a signature of ferruginous coarse materials in a gravelly horizon observed in the borehole between the mottled clays horizon and the saprolite (Fig. 4B). This horizon cannot be extrapolated with confidence (Fig. 2B). The discrete reflector attributed to this horizon in the GPR record can, however, provide a more precise image of its extension within the regolith of the 'middle-glacis' that the ERT image could not.

3.2.2. 'High-glacis' georadar profile

The GPR record from the 'high-glacis' landsurface and its scarped edge shows significant changes in the reflection pattern over short horizontal distances (Fig. 5A). Fig. 5A is the radar record with logs from trial boreholes, TKB, TKC and TKDH at the same scale. A disruption of reflections occurs in the centre of the radar profile between positions 720 and 750 m and there is an increasing of the reflectivity in the upper part, to the East, across the disruption separating two distinct radar facies. Eastwards, the reflection configuration of the profile is undulated to chaotic, consisting of multiple west-dipping sub-horizontal reflections of high amplitude, which are obliquely truncated (Fig. 5A). The shape of the disruption may suggest changes of lateritic weathering facies in terms of mineralogical and/or physical patterns and/or erosion processes at the edge of the 'high-glacis' landsurface and subsequent accumulation of highly contrasting hardened materials that coarsen toward the disruption. There are some diffraction tails at the ends of the disrupted reflections between 730 and 740 m that could be GPR signatures of coarse ferruginous hardened materials.

In contrast, the GPR signal is more quickly attenuated in the west side of the profile, and the useful thickness for observation seems to be a little thinner than in the east side (Fig. 5A). This facies is less reflective except for some prominent, continuous reflections suggesting an interface between relatively hardened and more clayey materials. The main reflectors extracted from Fig. 5A and the curves of Fe_2O_3 and kaolinite contents and porosity measured in the trial borehole have been drawn in Fig. 5B. The reflector underlined by the first broad line can be seen from position 754 to position 778 m at a depth ranging from 3 to 6.5 m (Fig. 5A and B). Two trial boreholes, TKC and TKDH, located at positions 754 and 786 m, respectively, reveal an interface between a consolidated ferricrete and a more or less hardened ferruginous material at depths of 5 to 7.5 m (Fig. 5A). We therefore interpret this reflector as the lower boundary of the ferricrete. The broad dashed line between positions 786 and 800 m represents a less prominent discontinuous reflector (Fig. 5B). The upper topography of this reflector may be regarded as the lower limit of the ferricrete where the degree of hardness may change abruptly both vertically and laterally. Notice that the topographies of the landsurface and of the reflector are parallel, indicating that the ferricrete has been formed in situ even if it contains some allochtonous elements (Beauvais et al., 1999).

On the whole, the radar record exhibits an attenuated signal as the clay content of the deep horizons increases, limiting the observation depths (Fig. 5B). Hence, the zones where the radar reflections are discrete or absent can be interpreted as representing the saprolite horizons. The broad dashed lines in Fig. 5B represent the position below which the degree of hardness of lateritic materials may strongly vary or diminish.

The radar reflectors may also represent the interface between two very contrasting horizons in terms of Fe_2O_3, kaolinite content and porosity (Fig. 5B). Between positions 700 and 720 m, contrasts in Fe_2O_3, kaolinite and porosity in the TKB profile at the 8-m depth make a strong reflector at the same depth in the radar record (Fig. 5A). The attenuated signal at 6 m between positions 750 and 780 m can be explained by the relatively high frequency variation of Fe_2O_3 and kaolinite contents and of porosity along 10-m thickness in the TKC profile (Fig. 5B). Between positions 740 and 750 m, the radar signal is somewhat noisy. This can be due to technical problems, such as the antennas not being entirely set on the soil because of the very rough surface on the scarp, or to less resistive horizons (Fig. 3), which are likely to contain less ferruginous, less hardened and more clayey materials. This part of the profile corresponds to the edge of the 'high-glacis' landsurface, which has been intensively eroded as it was noted above and as previously reported (Beauvais et al., 1999). Better interpretations can be achieved by combining the ERT and GPR images calibrated with the borehole observations.

3.3. Interpretations from combined ERT and GPR

Integrated cross sections for the two lateritic systems have been obtained from the interpreted ERT and GPR data (Fig. 6). The cross sections show the main radar reflectors, as derived from Figs. 4B and 5B, superimposed on the ERT interpretations based upon comparison with borehole descriptions (Fig. 6).

3.3.1. 'Middle-glacis' lateritic system

As reported above, the results of ERT with an electrode spacing of 1.5 m have shown some obvious resistivity differences that allowed the distinction of a ferricrete and a soft ferricrete horizon. Fig. 6A shows the agreement of the interpreted thickness of the hardened ferruginous horizons from ERT, and validated by the boreholes observations, with the GPR reflectors. Both interpreted ERT and GPR reveal similar depth characterisations of the ferricrete and soft ferricrete horizons. GPR, however, provides discontinuous profiles of the contact of ferricrete surface layer with the soft ferricrete horizon and between the soft ferricrete and the underlying clayey horizons. GPR depicts lateral changes in materials along these interfaces, suggesting lateral variations of hardness and/or weathering facies in terms of variable Fe_2O_3 and clay contents and porosity. The discrete, pseudo-reflector likely corresponds to the gravelly horizon at the transition with the upper saprolite horizon. Thus, a mottled clay horizon can be represented between this coarse material and the soft ferricrete (Fig. 6A), as it was effectively observed in the borehole (Figs. 2A and 4A). Furthermore, this mottled clay horizon contains numerous ferruginous elements of allochtonous origin (Bantsimba, 2001). The interpretation of the domain between the gravelly horizon and the soft ferricrete thus implies that the saprolite extends everywhere below the pseudo-reflector (Fig. 6A).

3.3.2. 'High-glacis' lateritic system

Both GPR and ERT provide similar depth characterisations of the ferricrete horizon (Fig. 6B). The lower reflectors mark quite satisfactorily the base of the ferricrete, while the discrete pseudo-reflectors

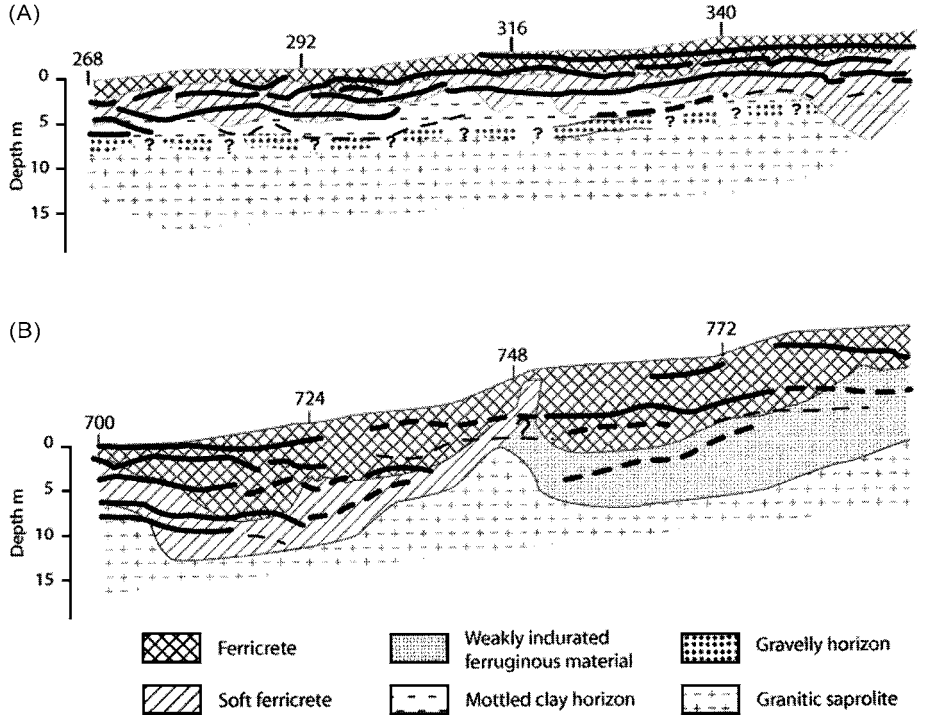

Fig. 6. Superimposition of the extracted georadar reflectors onto the interpreted ERT images. (A) 'Middle-glacis' landsurface. (B) 'High-glacis' landsurface. (See Fig. 4 for the signification of each reflector curves.)

indicate either the soft ferricrete in the left part of Fig. 6B or the less hardened ferruginous material in the right part. There are few discrepancies between the positions of the upper limit of the clayey horizons deduced from GPR data or from the ERT interpretation, particularly in the western part of the profile. This can be explained by the physico-chemical heterogeneity of the ferruginous material identified between the ferricrete and the saprolite, i.e., by the variability of hardness and porosity, and also of composition in Fe_2O_3 and kaolinite (Fig. 5B). In contrast, GPR and ERT interfaces roughly agree in the eastern part of the profile. The ferricrete thickens westwards until about position 720 m, where there is some small disagreement between the GPR and ERT results, in particular at the extremities of the disrupted reflections. This coincides with thick, resistive surface layers that are detected by ERT and that are attributed to hardened ferruginous material (Fig. 6B). Notice the presence of some isolated diffraction features at a depth of about 6.5 m, which may be associated with a relatively high contrast in Fe_2O_3 and kaolinite contents and porosity between the ferruginous and the more clayey horizons in the 'high-glacis' scarp (Fig. 6B). Disparities in the depth distribution extend westwards, and seem to dwindle near position 786 m on the 'high-glacis' landsurface. GPR provides shallow depths, less than 6.5 m for the top of the clayey horizon, which can be more or less ferruginous and thus characterised by discrete reflectors. The depth occurrence of the clay horizon as depicted by ERT is variable over relatively short longitudinal distances, but it varies on a larger thickness, 5 to 10 m, than those obtained with GPR. The area of disparities coincides with a rough surface topography where scarps are prominent geomorphologic features.

ERT and GPR images with the borehole observations are useful to well define the different components of the two lateritic weathering systems, and to interpret each of them as reflecting different subsurface processes.

3.4. Subsurface processes signatures

The ERT and GPR images of the 'middle-' and 'high-glacis' lateritic weathering system can reflect the contrasted history of each landsurface with their terrains in terms of differentiated erosion and weathering processes. By the fact that the two landsurfaces have relatively differentiated ages, the 'middle-glacis', the youngest, underwent only one phase of weathering and ferricrete development, whereas the 'high-glacis', the oldest, has undergone two phases of such processes (Michel, 1973; Grandin, 1976; Beauvais et al., 1999). The ferruginisation front has moved deeper in the 'high-glacis' profiles than in the 'middle-glacis' profiles. The thickness of the 'high-glacis' hardened ferruginous horizons such as ferricrete and soft ferricrete is effectively twice the thickness of the 'middle-glacis' horizons (Fig. 6). Thus, the ERT section of the 'high-glacis' exhibits relatively high resistive layer at depths around 8 to 12 m, while the GPR of this landsurface shows some discrete pseudo-reflectors. The latter are signatures of more or less hardened ferruginous materials at similar depths, whereas the true clay horizons cause the opacity of the georadar signal. In contrast, the ERT section of the 'middle-glacis' shows a relatively thin subsurface domain of resistive layers for the ferricrete over a thick poorly resistive domain for the saprolite. The GPR profile for this landsurface exhibits a sharp contact between the ferricrete, the base of which is effectively marked by a clear reflector and very poorly ferruginous clay horizons, resulting in a truly opaque georadar signal at depths of 5 to 7.5 m.

4. Summary and conclusions

Our results show that combined ERT and GPR investigations are useful to document the structure of tropical soils and subsurface lateritic terrains. The ERT imaging of the two lateritic systems provides information on specific geo-electrical heterogeneity of the main lateritic weathering horizons. Using an electrode spacing of 1.5 m, the near-surface information is precise for the relatively thin and hardened ferruginous horizons of the 'middle-glacis' lateritic system. The GPR signature of lateritic ferruginous horizons is characterised by more or less continuous and parallel reflections of high-amplitude with some diffraction patterns, depending on the variability of the materials compaction and/or hardness. The reflection pattern of the 'middle-glacis' lateritic system is generally less undulated and chaotic than the 'high-glacis'. The radar imaging of the 'high-glacis' system

effectively appears highly heterogeneous, suggesting both lateral and vertical variations of ferruginous and weathering facies in terms of hardness and/or iron and clay contents. The structures related to the eroded and accumulated materials are detected at the scarped edge of the 'high-glacis' landsurface. There are some discrepancies between the position of the interfaces obtained from GPR data and from the ERT interpretations along the profiles. The combination of ERT and GPR results with independent observations and measurements in boreholes provides higher accuracy in depicting the interfaces that roughly correspond to the boundaries of the main weathering horizons. Hence, the combined use of ERT and GPR methods in conjunction with lithologic logs strengthens the geological interpretations by reducing the ambiguous results. This effectively improves the accuracy of the lateral and vertical observations, thus providing a large-scale perspective of the investigated terrains. The variability of the ERT and GPR patterns could be signatures of the time-space-differentiated weathering and ferruginisation processes that have contributed to the contrasted development of the two lateritic weathering systems, 'high-' and 'middle-glacis', reflecting their different evolution patterns and age.

Acknowledgements

This paper is a contribution of UR-037 of the 'Institut de la Recherche pour le Développement' (IRD). Dr. D.H. Griffiths and an anonymous reviewer are greatly acknowledged for their helpful review of the paper.

References

Annan, A.P., 1993. Practical Processing of GPR Data. Sensors and Software.

Annan, A.P., Davis, J.L., 1976. Impulse radar sounding in permafrost. Radio Sci. 11, 383–394.

Aranha, P.R.A., Augustin, C.H.R.R., Sobreira, F.G., 2002. The use of GPR for characterizing underground weathered profiles in the sub-humid tropics. J. Appl. Geophys. 49, 195–210.

Bantsimba, C., 2001. Contribution à la caractérisation des couvertures latéritiques par les imageries électriques et radar, Sénégal Oriental. 3rd Cycle Thesis, UCAD University, Dakar, Senegal.

Beauvais, A., 1999. Geochemical balance of lateritization processes and climatic signatures in weathering profiles overlain by ferricrete in Central Africa. Geochim. Cosmochim. Acta 63 (23/24), 3939–3957.

Beauvais, A., Roquin, J.-C., 1996. Petrological differentiation patterns and geomorphic distribution of ferricretes in Central Africa. Geoderma 73 (1–2), 63–82.

Beauvais, A., Ritz, M., Parisot, J.-C., Dukhan, M., Bantsimba, C., 1999. Analysis of poorly stratified lateritic terrains overlying a granitic bedrock in West Africa, using 2-D electrical resistivity tomography. Earth Planet. Sci. Lett. 173, 413–424.

Beres, M., Haeni, F.P., 1991. Application of ground penetrating radar methods in hydrogeological studies. Ground Water 29, 375–386.

Bocquier, G., 1973. Genèse et évolution de deux toposéquences de sols tropicaux du Tchad. Interprétation géodynamique. Thèse Doct. Sc.,Univ. Strasbourg, Mém. ORSTOM, 62, Paris, France.

Boulet, R., 1978. Toposéquences de sols tropicaux en Haute-Volta. Equilibre et déséquilibre pédoclimatique. Thése Doct. Sc., Univ. Strasbourg, Mém. ORSTOM, 85, Paris, France.

Dahlin, T., Owen, R., 1998. Geophysical investigations of alluvial aquifers in Zimbabwe. Proceedings of the 4th EEGS Meeting. Barcelona, 14–17 September 1998, pp. 151–154.

Davis, J.L., Annan, A.P., 1989. Ground-penetrating radar for high-resolution mapping of soil and rock stratigraphy. Geophys. Prospect. 37, 531–551.

Doolittle, J.A., Collins, M.E., 1998. A comparison of EM induction and GPR methods in areas of karst. Geoderma 85, 83–102.

Edwards, L.S., 1977. A modified pseudo-section for resistivity and induced polarization. Geophysics 42, 1020–1036.

Freeland, R.S., Yoder, R.E., Ammons, J.T., 1998. Mapping shallow underground features that influence site-specific agricultural production. J. Appl. Geophys. 40, 19–27.

Gorin, S.R., 1989. Exploration of subsurface interfaces using high-frequency seismic reflection and ground-penetrating radar methods. MSc Thesis, Wesleyan Univ., Middletown.

Grandin, G., 1976. Applanissements cuirassés et enrichissement des gisements de manganèse dans quelques régions d'Afrique de l'Ouest. Thèse Doct. Sc., Univ. Strasbourg, Mém. ORSTOM, 82, Paris, France.

Griffiths, D.H., Barker, R.D., 1993. Two-dimensional resistivity imaging and modelling in areas of complex geology. J. Appl. Geophys. 29, 211–226.

Griffiths, D.H., Turnbull, J., Olayinka, A.I., 1990. Two-dimensional resistivity mapping with a computer-controlled array. First Break 8, 121–129.

Hazell, J.R.T., Cratchley, C.R., Jones, C.R.C., 1992. The hydrogeology of crystalline aquifers in northern Nigeria and geophysical techniques used in their exploration. In: Wright, E.P., Burger, W.G. (Eds.), Hydrogeology of Crystalline Basement Aquifers in Africa. Geol. Soc. Special Publication, vol. 66, pp. 155–182.

Jol, H.M., Smith, D.G., 1991. Ground penetrating radar of northern lacustrine deltas. Can. J. Earth Sci. 28, 1939–1947.

Loke, M.H., 1997. RES2-DINV Software User's Manual.

Michel, P., 1973. Les bassins des fleuves Sénégal et Gambie. Etudes géomorphologiques. Mém. ORSTOM, 63, Paris, France.

Nahon, D., 1976. Cuirasses ferrugineuses et encroutements calc-

aires au Sénégal Ocidental et en Mauritanie. Systèmes évolutifs: géochimie, structures, relais et coexistence. Thèse Doct. Sc., Univ. Strasbourg, Mém. Sci. Géol., 44, France.

Nahon, D.B., 1991. Introduction to the Petrology of Soils and Chemical Weathering. Wiley, New York.

Palacky, G.J., Kadekaru, K., 1979. Effect of tropical weathering on electrical and electromagnetic measurements. Geophysics 44, 69–88.

Ritz, M., Parisot, J.C., Diouf, S., Beauvais, A., Diome, F., Niang, M., 1999. Electrical imaging of lateritic weathering mantles over granitic and metamorphic basement of eastern Senegal, West Africa. J. Appl. Geophys. 41, 335–344.

Tardy, Y., 1993. Pétrologie des latérites et des solstropicaux. Masson, Paris, France.

Thomas, M.F., 1994. Geomorphology in the tropics. A study of weathering and denudation in low latitudes. Wiley, New York.

van Overmeeren, R.A., 1994. Georadar for hydrogeology. First Break 8, 401–408.

VOLET III

VOLET III – GEOCHRONOLOGIE DES ALTERATIONS LATERITIQUES

1. PETRO GEOCHIMIE ET GEOCHRONOLOGIE DES ALTERATIONS LATERITIQUES MANGANESIFERES

La datation des objets géologiques d'origine supergène est un problème fondamental en géosciences si l'on veut avancer dans la compréhension de l'évolution long terme des systèmes d'altération latéritique et de la morphogenèse des paysages de la zone intertropicale. Les critères géomorphologiques et pétrographiques conduisent généralement à attribuer des âges différenciés aux latérites et aux surfaces qui leur sont associées. Une expertise fine de ces critères est cependant nécessaire pour interpréter correctement les données géochronologiques obtenues.

La méthode $^{40}Ar/^{39}Ar$ calibrée il y a une douzaine d'années sur des minéraux latéritiques manganésifères riches en potassium de la famille des cryptomélanes (Vasconcelos, 1992, 1994) a permis des avancées significatives dans la connaissance des mécanismes, et de la géochronologie des processus, de l'altération latéritique, en relation avec les variations climatiques et paléoclimatiques. Cette méthode a été appliquée aux cryptomélanes caractérisés dans les gisements manganésifères d'origine surpergène du Brésil et du Burkina Faso.

Au Brésil, des âges $^{40}Ar/^{39}Ar$ ont été obtenus sur deux générations de cryptomélane entre 70-60 Ma et 47-48 Ma, montrant que l'altération manganésifère était favorable à la cristallisation de cryptomélane à la transition entre le Crétacé supérieur et le Paléocène ainsi qu'à l'éocène moyen (Ruffet et al., 1996).

Au Burkina Faso, trois groupes d'ages, 56-59, 44-47, et 24-27 Ma ont été obtenus sur des cryptomélanes développés respectivement au coeur, dans les cortex et dans les matrices emballant les pisolites (Colin et al., 2005). Les oxyhydroxydes, de fer et d'aluminium, ont également été caractérisés comme s'étant développés en alternance avec les différentes générations de cryptomélanes. Outre la caractérisation temporelle de différentes périodes d'altération manganésifères favorables à la cristallisation de cryptomélane, l'intervalle 56-47 Ma entre les deux générations de cryptomélane les plus anciennes contraint la période à effet de serre Tertiaire favorable au lessivage du potassium et du manganèse et à l'accumulation de l'aluminium, et dans une moindre mesure du fer au sein des profils bauxites globalement répandues à l'Eocène et aujourd'hui largement dénudées.

2. PRESENTATION DES ARTICLES SCIENTIFIQUES DU VOLET III

2 articles (Brésil et Burkina Faso) : géochronologie des oxyhydroxydes de manganèse potassique (cryptomélane), implications paléoclimatiques et paléogéomorphologiques.

Geochimica et Cosmochimica Acta (Ruffet et al., 1996) : géochronologie ^{40}Ar-^{39}Ar des cryptomélanes des cuirasses manganésifères du gisement d'Azul (Brésil).

Earth & Planetary Science Letters (Colin et al., 2005) : pétrologie-géochimie et datations ^{40}Ar-^{39}Ar des cryptomélanes des formations pisolitiques ferro-manganésifères du gisement de Tambao (Burkina Faso).

ARTICLE 8

Pergamon

Geochimica et Cosmochimica Acta, Vol. 60, No. 12, pp. 2219–2232, 1996

0016-7037/96 $15.00 + .00

PII S0016-7037(96)00080-4

A geochronological $^{40}Ar/^{39}Ar$ and $^{87}Rb/^{87}Sr$ study of K-Mn oxides from the weathering sequence of Azul, Brazil

G. RUFFET,[1] C. INNOCENT,[2] A. MICHARD,[2] G. FÉRAUD,[1] A. BEAUVAIS,[3] D. NAHON,[2] and B. HAMELIN[2]

[1]Institut de Géodynamique, URA CNRS 1279, Université de Nice-Sophia Antipolis, 06108 Nice Cedex 2, France
[2]Laboratoire de Géosciences de l'Environnement, URA CNRS 132, CEREGE, Europôle Méditerranéen de l'Arbois, BP80, 13545 Aix-en-Provence Cedex 4, France
[3]ORSTOM (UM GECO) Department of Geology, University of Washington, Seattle, WA 98195, USA

(*Received July* 12, 1995; *accepted in revised form February* 26, 1996)

Abstract—K-Mn oxides of hollandite group minerals such as cryptomelane ($K_{1-2}(Mn^{3+}, Mn^{4+})_8O_{16}nH_2O$) are often precipitated authigenically in weathering profiles. The presence of structural K allows these minerals to be dated by the K-Ar and $^{40}Ar/^{39}Ar$ methods, making it possible to study the progression of oxidation fronts during weathering processes. Within the context of a recent $^{40}Ar/^{39}Ar$ study of cryptomelane from the Azul Mn deposit in the Carajàs region (Amazônia, Brazil), Vasconcelos et al. (1994) defined three age clusters (65–69, 51–56, and 40–43 Ma) and proposed that they correspond to the episodic precipitation of the three generations of Mn oxide that have been identified in the deposit (Beauvais et al., 1987).

We performed a laser probe $^{40}Ar/^{39}Ar$ and $^{87}Rb/^{87}Sr$ study on new samples from the same Mn deposit. Our $^{40}Ar/^{39}Ar$ data confirm that cryptomelane is a suitable mineral for $^{40}Ar/^{39}Ar$ dating, although in some cases we clearly identify the existence of ^{39}Ar recoil effects. Although the corresponding age spectra are generally strongly disturbed, our results also confirm that the earliest cryptomelane generation is of Upper Cretaceous-Paleocene age. We obtained good plateau ages from veins and concretions of the second cryptomelane generation. Some of these results allow definition of a well-constrained age cluster at 46.7–48.1 Ma not observed by Vasconcelos et al. (1994). A petrographic study confirms that none of the samples analyzed in the present study contained material associated with the third generation of cryptomelane. We propose that these new results support the idea of a more or less continuous crystallization of K-Mn oxides, mainly constrained by local factors, rather than the model advanced by Vasconcelos et al. (1994), which suggests that each cryptomelane generation corresponds to distinct weathering events related to global climatic changes.

$^{87}Sr/^{86}Sr$ data show large variations, clearly inherited from the 2.1 Ga parent rock of the Mn protore. The Rb/Sr results demonstrate that minimum fractionation occurs during cryptomelane crystallization, except for the latest generation, which is depleted in Sr. This precludes use of the Rb/Sr radiochronometer for dating secondary Mn oxides in laterites.

1. INTRODUCTION

Weathering is one of the main processes in the geomorphologic and geochemical evolution of the Earth's surface. Lateritic terrains, which represent approximately one third of the continental surface and form the substrate of equatorial forests, are the end-products of long-term exposure of cratonic rocks under tropical climate. The precise determination of the rate of continental crust weathering is thus a critical parameter for soil sciences and paleoclimatology. However, direct dating of weathering phenomena remained a very difficult problem until recently. The open-system evolution of most weathering profiles precludes direct radiochronological dating using most standard radiometric techniques. Hence, current studies focus on the search for supergene minerals, which may behave as closed systems for at least one isotopic chronometer.

K-bearing supergene minerals such as alunite and jarosite, or K-Mn oxides of the hollandite group such as cryptomelane, are widely present in soils and weathering profiles. Cryptomelanes are important components of Mn-bearing laterites from West Africa (Nahon et al., 1984; Perseil and Grandin, 1985) and Brazil (Herz and Banerjee, 1973; Beauvais et al., 1987). Vasconcelos et al. (1994) showed that cryptomelane and hollandite are potentially suitable minerals for dating weathering processes by the K-Ar and $^{40}Ar/^{39}Ar$ methods. Their $^{40}Ar/^{39}Ar$ results yielded internally consistent results for a series of distinct cryptomelane generations formed during lateritization of Archean and Proterozoic bedrocks in the Carajás Region, Amazonia (Brazil), and led to the proposition that the three age clusters were associated with distinct crystallization events correlated with major environmental changes and climatic periods. These results gave thus the first absolute time constraints on the rate of development of laterite sequences.

The aims of the present work are (1) to discuss the analytical problems which can be encountered during $^{40}Ar/^{39}Ar$ laser-probe analyses of cryptomelanes, (2) to add new $^{40}Ar/^{39}Ar$ results to one of the profiles studied by Vasconcelos et al. (1994), in order to improve the statistical significance of the age distribution of the Mn oxides at this site, (3) to test whether the various cryptomelane generations are related to major environmental changes, or to continuous weathering with various stages related to differences in weathering rates of the minerals forming the source rock, and (4) to determine whether cryptomelanes also behave as a closed system for Rb-Sr. Coupled K-Ar and $^{87}Rb/^{87}Sr$ studies have been successfully applied previously to some phyllosilicates like

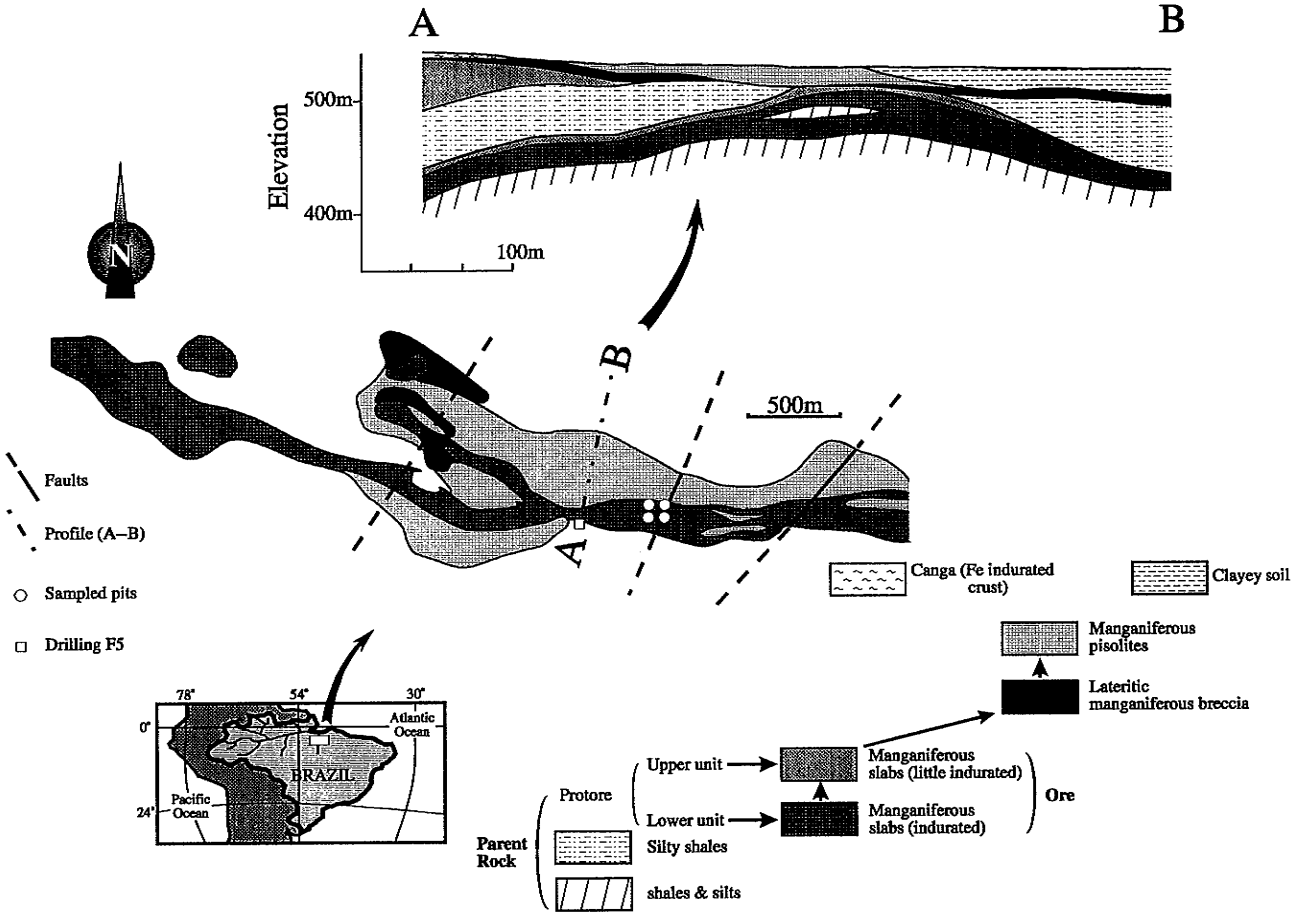

FIG. 1. Geological map and profile (labelled A–B on map) of the Azul ore deposit (after Bernardelli and Beisiegel, 1978) with the location of the four shafts (described by Beauvais (1984)) in which samples were handpicked for this study. Drilling F5 reaches the fresh (unweathered) parent rock.

glauconites (Morton and Long, 1980), smectites (Clauer et al., 1984), celadonites (Staudigel et al., 1986), and illites (Clauer et al., 1993). The crystallographic structure of cryptomelane may host Rb as well as K, and thus cause large fractionation of the Rb/Sr ratio. Fifteen new samples from the Azul Mn-ore (Carajàs mountains, Para state, Brazil), one of the sites previously studied by Vasconcelos et al. (1994), were analyzed with the Rb/Sr and $^{40}Ar/^{39}Ar$ methods.

2. SAMPLES

2.1. Geological Setting and Sampling

The Azul Mn-ore is located near the Fe deposit of Carajàs (Para State, Brazil) at about 500 km south of Belem. It developed on Lower Precambrian sedimentary shales (Rio Fresco Group). The weathering sequence consists of four main horizons (Fig. 1): the relics of the non-manganiferous parent rock horizon (shales and silts); the Mn-oxides "plaquettes" horizon (manganiferous indurated and little indurated slabs); the brecciated Mn-oxides horizon (lateritic manganiferous breccia), and the pisolitic horizon (manganiferous pisolites).

The parent rock was reached by drilling to a depth of 100 m (Drilling F5, Fig. 1). The oxidized horizons were sampled in several pits, about 40 m deep, which reached various horizons along the slope of the plateau.

Samples were collected from the four profiles (Fig. 1) described by Beauvais (1984), approximately 300 m away from the section studied by Vasconcelos et al. (1994). Locations and description of the samples are reported in the Appendix. Fifteen samples were analyzed, corresponding to eight whole-ore samples collected in the different units, five "separates" extracted from veins or concretions (labeled by "II" after the reference of the corresponding whole-ore), one sample of lithiophorite (#22-III), and one clay matrix (#15-III). The whole-ore samples range from dark bluish metallic blocks to dull-black, more friable pieces. Two of the "separates" come from millimetric veins visible in polished whole-ore sections (#22-II and #32-II), one (#28-II) from a light-grey metallic rim, one millimeter thick, on the faces of a fissure, and two (#7-II and #31-II) from brownish submillimetric botryoïdal rim covering the faces of fissures. All of the analyzed samples are essentially composed of cryptomelane, although X-ray diffraction reveals the presence of small amounts of nsutite and pyrolusite.

2.2. Mineralogical Evidence for Successive Generations of Mn Oxides

The Azul profile is composed of different generations of Mn oxides, among which, several generations of cryptomelane have been differentiated (Beauvais et al., 1987).

The parent rock is composed of 65% rhodochrosite, 15% phyllosilicates, 10% quartz, 5% feldspars, and 5% sulfides. The rhodochrosite consists of "egg-fish" shaped micronodules of tiny crystals (2–10 μm) or of sparitic crystals (50 μm), located in veins crossing the bedding of the shale. The chemical composition of the rhodochrosite,

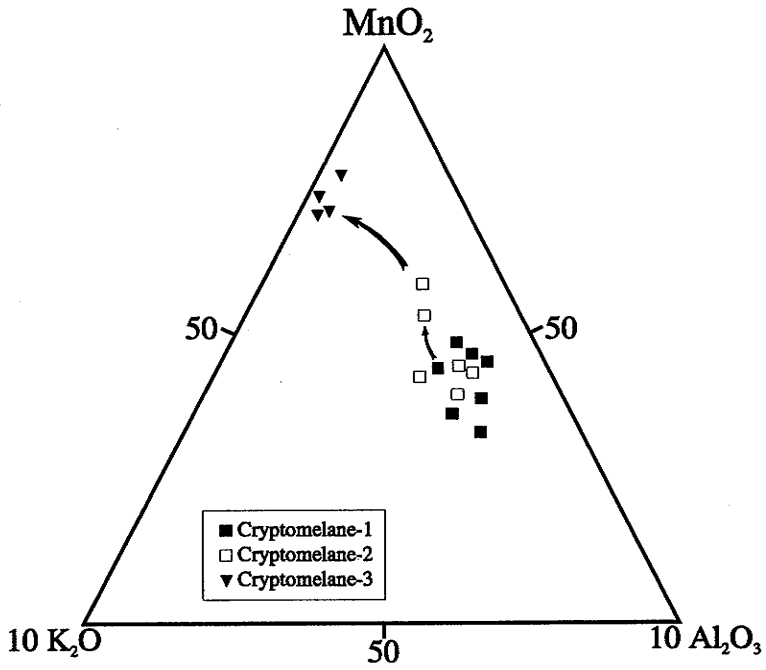

FIG. 2. Chemical compositions of different generations of cryptomelane plotted in a $MnO_2-10K_2O-10Al_2O_3$ triangular diagram.

obtained from microprobe analyses by Beauvais et al. (1987) (fifteen analyses) is:

$$(Mn^{2+}_{0.93}Fe^{2+}_{0.04}Mg_{0.01}Ca_{0.02})CO_3.$$

The X-ray diffraction pattern is: 3.660 Å; 2.840 Å; 2.386 Å; 2.169 Å; 1.998 Å; 1.825 Å; 1.760 Å; and 1.538 Å. Quartz grains are mostly detrital grains (20–50 μm), but can also occur as euhedral crystals (100–200 μm), in association with veins of rhodochrosite. Phyllosilicates are detrital grains of muscovite and chlorite, ranging in size from 10 to 30 μm. Feldspars (<50 μm) are K-feldspars. Sulfides consist of pyrite and covellite, as euhedral crystals, along with rhodochrosite.

The Mn-oxides "plaquette" horizon results from weathering of the two different units of rhodochrosite-bearing shales of the Rio Fresco Group. The original rhodochrosite weathers directly into a first generation of cryptomelane (thereafter labeled "cryptomelane-1"). The chemical composition of cryptomelane-1 is shown on a triangular diagram (Fig. 2) (Beauvais et al., 1987) (seven analyses; sample #1). The main X-ray patterns are 6.90 Å, 4.90 Å, 2.39 Å, and 2.14 Å. The cryptomelane structure consists of a framework of double chains of edge-sharing Mn-O octahedra containing large tunnels filled with K^+ ions. Most of the Mn is Mn^{4+} but some Mn^{3+} substitutes for Mn^{4+} to balance the positive charge of tunnel cations (Post et al., 1982; Hypólito et al., 1984). The composition is $K_xMn^{4+}_{8-x}Mn^{3+}_xO_{16}$ (Vicat et al., 1986), with x ranging from 0.2 to 1.0 in cryptomelanes from lateritic profiles.

Cryptomelane-1 consists of tiny aggregated crystals (up to a few tens micrometers) that pseudomorphically replace rhodochrosite grains. This is manifested by the preservation of the original sedimentary structure of the parent rock, and of the original fish-egg shape of the nodules (Fig. 3). The strong increase in density implies that pseudomorphic replacement of rhodochrosite by cryptomelane-1 requires a net import of Mn (Beauvais et al., 1987; Merino et al., 1993).

Direct pseudomorphs of rhodochrosite by cryptomelane have been already observed at Moanda (Gabon) (Nziengui-Mapangou, 1981), although direct replacement of rhodochrosite by manganite (MnOOH) is more commonly observed. Recent thermodynamic studies (Parc et al., 1989; Nahon and Parc, 1990) have shown that manganite is not stable for high CO_2 pressures ($\log f CO_2 > -2.0$) and that cryptomelane can form directly from weathering of Mn carbonates at sufficient K^+ concentrations ($\log [K^+]/[H^+] > 3$).

Cryptomelane-1 and nsutite (a more highly oxidized mineral containing less Mn3+), can be intermingled in samples and are generally difficult to separate (Fig. 3). The nsutite formula is $Mn^{4+}_{1-y}Mn^{3+}_yO_{2-y}(OH)_y$ with $y < 0.05$ (Giovanoli and Leuenberger, 1969).

FIG. 3. Reflected light (×4): C1 is the first generation of cryptomelane (cryptomelane-1) associated with few nsutite in pseudomorph after the parent rock. Notice that they preserved the original microlaminated and egg-fish texture. C2 is the second generation of cryptomelane (cryptomelane-2) along with few nsutite, crossing the C1. Sample #28.

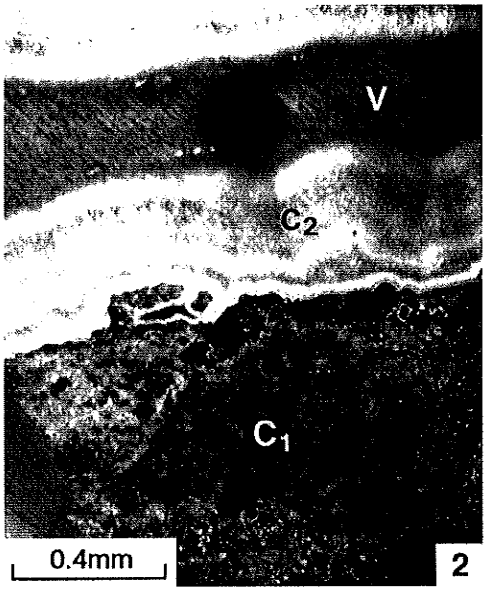

FIG. 4. Reflected light (×4): Fibroradiated crystals of cryptomelane-2. V is void and C1 is cryptomelane-1 with preserved original texture. Sample #31.

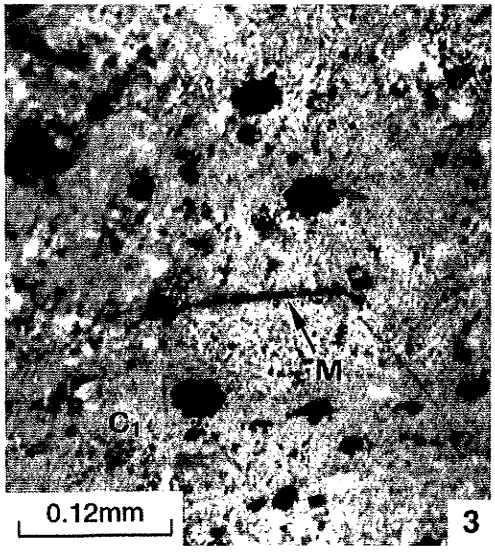

FIG. 5. Reflected light (×16): M is a detrital muscovite grain within the cryptomelane-1 (C1). Sample #32.

The walls of open fissures or microscopic tubules, crossing the fish-egg texture, often show recrystallization of nsutite and cryptomelane into a new generation of cryptomelane-2 and nsutite-2 (Figs. 3, 4). Recrystallization is indicated by the fact that (1) the fish-egg microtexture is now erased and (2) that cryptomelane-2 and nsutite-2 show fibroradiated crystals perpendicular to the walls of the fissures and tubules (Fig. 4). This second generation of cryptomelane-2 is slightly enriched in K. It is generally very difficult to separate completely cryptomelane-1 from cryptomelane-2, in which tiny remnants of cryptomelane-1 can persist.

Higher in the weathering profile, i.e., in more oxidized environments, pyrolusite (well-ordered MnO_2) replaces cryptomelane-2 and nsutite-2 in the same structural position. Pyrolusite is thus the final end-product of the weathering sequence (Bricker, 1965; Garrels and Christ, 1965). However, at the stage where pyrolusite precipitates, most detrital muscovite grains (15% of the parent rock) are not yet entirely weathered into kaolinite (Fig. 5). K-micas persist in the upper part of the weathering profile because K^+ cations are more solidly bound to the muscovite structure than they are in K-feldspars, which weather as soon as the weathering front develops. Thus, K^+ ions released during the early dissolution of detrital K-feldspars lead to the formation of cryptomelane-1 and cryptomelane-2, while leaching of interlayer K from detrital muscovite grains occurs after the precipitation of pyrolusite, and leads to the late destabilization of MnO_2 into a new generation of cryptomelane-3 (Beauvais et al., 1987; Vasconcelos et al., 1994). Well-developed crystals of pyrolusite (~100 μm), observed in the upper part of the weathering profile of Azul, show dissolution features on their faces. Cryptomelane-3 precipitates as tiny needles in these dissolution voids and progressively replaces the whole pyrolusite (Fig. 6). The shape of the original pyrolusite can be preserved through this pseudomorphic replacement by cryptomelane-3.

It is important to stress that, in contrast with the samples studied by Vasconcelos et al. (1994), none of the samples analyzed in the present study contained cryptomelane-3.

Finally, when muscovite is entirely weathered into kaolinite, Al released by kaolinite weathering can feed lithiophorite formation at the top of the profile.

3. ANALYTICAL TECHNIQUES

Massive samples were sawed. The veins were extracted from the whole ore either with a small handsaw or with metal tweezers. The lithiophorite was scraped out with a clean needle. The kaolinitic clay was separated away from the ore by vibrating the sample in an ultrasonic bath and pouring off the suspendant. All samples were rinsed several times in distilled water in an ultrasonic bath.

3.1. Rb-Sr Method

Samples of about 10 mg were dissolved in concentrated HCl (5 mL) and spiked with ^{84}Sr and ^{85}Rb. The clay was dissolved in a $HF-HNO_3-HClO_4$ mixture (5 mL). All samples were then dried and redissolved in aqua regia (1 mL), dried again, and finally dissolved in a few drops of dilute HCl. Rubidium was collected by precipitating Rb perchlorates and Sr was eluted on a AG50W X8 cation column (Alibert et al., 1983).

Rubidium and Sr were loaded on single W filaments with Ta oxide and run on a VG Sector 54-30 mass spectrometer. Strontium

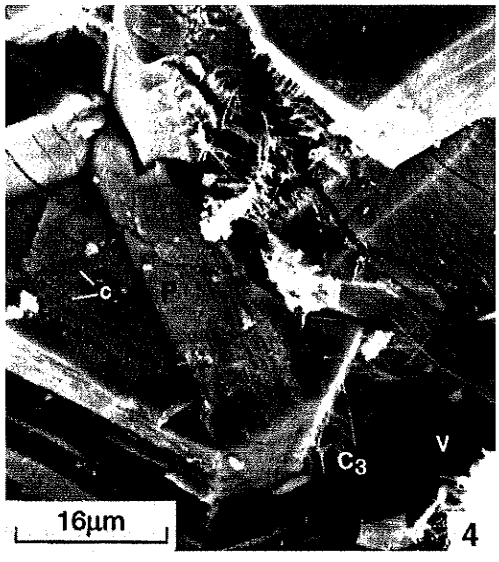

FIG. 6. SEM observation P is a crystal of pyrolusite. Along the cracks and fissures crossing pyrolusite, needles of cryptomelane develop. This is the third generation of cryptomelane (C3). V is void. In Beauvais et al. (1987)

Table 1. Rb/Sr data

Sample	Lithology	Rb (ppm)	Sr (ppm)	1/Sr (ppm)	$^{87}Rb/^{86}Sr$	$^{87}Sr/^{86}Sr$	2σ
#1	Whole-ore	24.34	142.05	0.0070	0.684	0.766860	0.000010
#7	Whole-ore	23.83	138.99	0.0072	0.684	0.752736	0.000009
#7-II	Concretion	25.80	159.33	0.0063	0.646	0.751376	0.000008
#15	Whole-ore	24.16	109.46	0.0091	0.880	0.762337	0.000007
#22	Whole-ore	62.83	105.53	0.0095	2.375	0.813724	0.000010
#22-II	Vein	68.79	153.96	0.0065	1.782	0.811822	0.000043
#22-III	Lithiophorite	41.39	179.99	0.0056	0.917	0.795445	0.000013
#28	Whole-ore	49.41	160.45	0.0062	1.228	0.789596	0.000006
#28-II	Vein	60.70	43.59	0.0229	5.554	0.811186	0.000009
#31	Whole-ore	37.99	296.36	0.0034	0.511	0.759074	0.000008
#31-II	Concretion	61.86	75.41	0.0133	3.272	0.795461	0.000012
#32	Whole-ore	18.81	442.19	0.0023	0.170	0.744916	0.000008
#32-II	Vein	26.81	502.91	0.0020	0.213	0.745237	0.000012
#34	Whole-ore	27.72	546.52	0.0018	0.202	0.747518	0.000014
#34 Dupl.	Whole-ore	24.87	659.36	0.0015	0.150	0.746628	0.000008

Rubidium and Sr concentrations and strontium isotopic compositions of the analysed samples.

isotopes were measured using a dynamic multicollection mode. Repeated analyses of NBS 987 standard gave an average value of: 0.710205 ± 16 ($2\sigma_m$ on twenty-four runs). Strontium total blanks were negligible, lower than 300 pg.

3.2. $^{40}Ar/^{39}Ar$ method

The grains analyzed with the laser probe were carefully hand-picked under a binocular microscope from coarse fractions (0.5–2 mm) of the crushed samples. The samples were irradiated at the McMaster reactor (Hamilton, Canada) with a total flux of 9×10^{18} $n.cm^{-2}$. All of the analyzed samples were gathered in a narrow zone at the same level within the irradiation can in order to minimize the effect of the flux gradient, which is estimated to be less than ±0.5%. The irradiation standard was the amphibole MMhb1 (Samson and Alexander, 1987; 520.4 Ma).

The step-heating experiments on single grains (described in detail by Scaillet et al., 1990; Ruffet et al., 1991) were performed with a laser-probe using a Coherent Innova 70-4 continuous Ar-ion laser model with a maximum output power of 6 Watts in multiline mode. The laser beam was focused through an optical system onto a sample located in a UHV sample chamber (a Cu sample-holder, beneath a Pyrex window, in a stainless steel chamber).

Each laser experiment lasts 5 min: (1) 3 min in the purification line (laser heating of the sample and cleanup of the released gas) and (2) 2 min of inlet time into the mass spectrometer. The laser beam size is at least 2.5 times greater (up to 6 mm) than the sample size, in order to obtain a homogeneous temperature over the whole grain. The temperature is not known but its homogeneity is controlled by observing the heated mineral with a binocular microscope, coupled with a color video camera and a high resolution video recorder. The laser heating time (1 min) is kept constant for each step-heating experiment. The fusion of the mineral is achieved by sharply focusing the laser spot.

The mass spectrometer consists of a 120° M.A.S.S.E.® tube, a Bäur Signer® source, and an SEV 217® electron-multiplier (total gain: 5×10^{12}). The purification line comprises an SAES GP50W getter with St101® Zr Al alloy operating at 400°C and

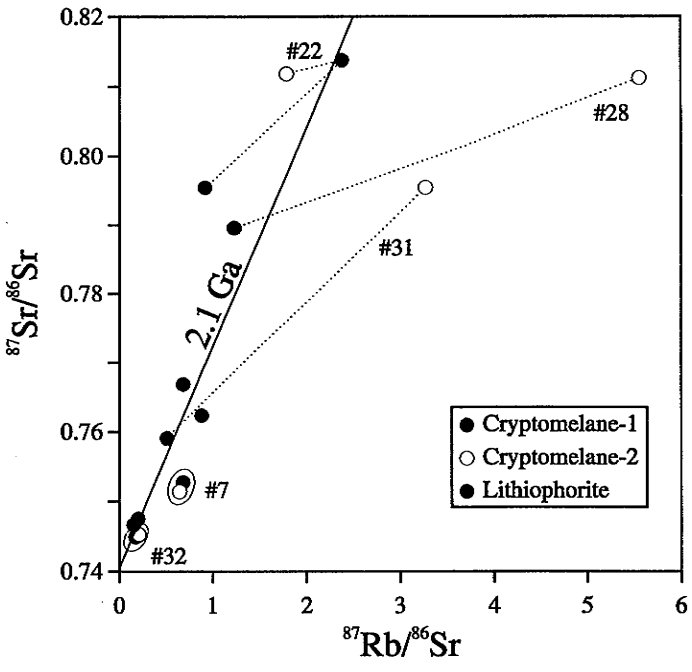

FIG. 7. Diagram $^{87}Sr/^{86}Sr$ vs. $^{87}Rb/^{86}Sr$ with 2.1 Ga reference isochrone.

TABLE 2. $^{40}Ar/^{39}Ar$ analytical data

Step n°	$^{40}Ar_{atm.}$ (%)	$^{39}Ar_K$ (%)	$^{37}Ar_{Ca}/^{39}Ar_K$ (x10^{-4})	$^{40}Ar^*/^{39}Ar_K$	Age (Ma)
#1 Cryptomelane (Single grain) (J=0.0164325)					
1	91.1	0.36	0.0280	1.65	48.3 ± 40.7
2	79.4	3.77	0.0688	1.71	49.9 ± 4.9
3	59.0	3.64	0.0918	1.55	45.3 ± 5.3
4	67.1	3.04	0.0845	1.01	29.8 ± 6.6
5	60.0	5.62	0.0961	1.14	33.3 ± 3.6
6	24.5	23.01	0.0515	2.09	60.8 ± 1.3
7	9.4	14.82	0.0311	2.29	66.7 ± 1.4
8	8.5	19.76	0.0388	2.17	63.1 ± 1.1
9	20.5	19.43	0.0923	1.29	37.9 ± 1.1
10	27.7	5.08	0.0987	1.20	35.1 ± 2.8
Fuse	41.0	1.48	0.1072	1.00	29.4 ± 12.7
				Total age:	52.4 ± 0.7
#7 Cryptomelane (Single grain) (J=0.0164325)					
1	75.0	61.86	0.0743	1.72	50.3 ± 2.4
2	42.0	11.35	0.0494	1.48	43.3 ± 2.2
3	64.0	9.76	0.1178	0.68	20.2 ± 2.7
4	53.4	13.36	0.1339	0.54	15.9 ± 2.1
5	66.1	2.04	0.0522	1.01	29.6 ± 8.9
6	72.6	0.61	0.0000	0.60	17.6 ± 34.9
Fuse	76.2	1.02	0.0451	0.54	15.8 ± 21.2
				Total age:	41.0 ± 1.6
#7 Cryptomelane (Single grain) (J=0.0164325)					
1	34.5	3.78	0.2075	1.28	37.7 ± 1.7
2	49.5	5.20	0.0836	1.28	37.5 ± 1.9
3	36.7	4.75	0.1785	1.20	35.2 ± 1.9
4	9.8	8.84	0.1339	1.28	37.6 ± 1.1
5	5.8	24.22	0.0920	1.47	43.0 ± 0.5
6	5.2	14.75	0.0865	1.68	49.2 ± 0.5
7	5.8	7.94	0.0598	1.67	49.0 ± 0.9
8	6.0	11.30	0.0707	1.45	42.5 ± 0.6
9	6.9	14.43	0.1124	0.90	26.4 ± 0.7
Fuse	17.8	4.78	0.1197	0.90	26.5 ± 2.5
				Total age:	39.8 ± 0.3
#7-II Cryptomelane (Single grain) (J=0.0164325)					
1	96.7	0.78	0.1461	0.58	17.2 ± 19.7
2	80.2	6.08	0.0383	1.08	31.8 ± 4.0
3	71.4	7.37	0.0348	1.36	39.9 ± 3.2
4	44.2	13.38	0.0196	1.63	47.6 ± 1.4
5	18.9	20.24	0.0159	1.63	47.8 ± 0.8
6	15.3	17.77	0.0106	1.62	47.5 ± 0.9
7	20.8	10.98	0.0260	1.56	45.8 ± 1.1
8	38.4	8.60	0.0565	1.33	38.9 ± 1.6
Fuse	16.4	14.79	0.0145	1.42	41.5 ± 0.9
				Total age:	44.0 ± 0.5
#15 Cryptomelane (Single grain) (J=0.0164325)					
1	96.9	0.04	0.0000	0.50	14.8 ± 71.8
2	93.4	3.48	0.0626	2.00	58.2 ± 5.5
3	49.8	2.87	0.0472	2.61	75.7 ± 2.0
4	42.4	4.22	0.0377	2.67	77.6 ± 1.5
5	17.5	6.94	0.0342	2.61	75.9 ± 1.0
6	8.8	9.57	0.0240	2.31	67.2 ± 0.7
7	5.6	19.39	0.0199	2.21	64.4 ± 0.4
8	4.8	28.27	0.0182	2.15	62.7 ± 0.2
9	7.9	13.65	0.0217	2.10	61.3 ± 0.4
10	35.8	4.01	0.0544	2.22	64.6 ± 1.1
11	14.6	2.62	0.0438	2.80	81.2 ± 1.3
Fuse	28.9	4.94	0.0331	2.14	62.3 ± 1.1
				Total age:	65.5 ± 0.3
#22 Cryptomelane (Single grain) (J=0.0164325)					
1	99.0	0.41	0.1192	1.18	34.6 ± 55.4
2	97.9	3.41	0.1033	1.14	33.4 ± 9.4
3	96.9	5.60	0.0968	1.27	37.3 ± 8.2
4	95.3	6.76	0.0930	1.22	35.9 ± 5.0
5	86.6	8.99	0.0499	1.83	53.3 ± 2.0
6	58.1	15.36	0.0447	2.30	67.0 ± 1.8
7	43.8	19.28	0.0390	2.32	67.5 ± 1.0
8	39.0	16.61	0.0258	2.37	68.8 ± 0.9
9	35.7	7.66	0.0202	2.71	78.5 ± 1.3
10	33.1	5.55	0.0112	5.04	143.5 ± 2.0
11	40.4	3.91	0.0273	11.71	317.5 ± 4.1
Fuse	65.7	6.46	0.0389	4.00	114.9 ± 1.7
				Total age:	79.1 ± 0.8
#22-II Cryptomelane (Single grain) (J=0.0164325)					
1	34.0	13.46	0.1232	1.35	39.5 ± 1.4
2	13.7	10.83	0.1313	1.56	45.6 ± 0.9
3	4.7	9.83	0.1760	1.94	56.5 ± 1.1
4	3.4	41.92	0.0409	2.24	65.1 ± 0.3
5	1.4	14.05	0.0314	3.30	95.2 ± 0.8
6	1.5	3.11	0.0837	20.45	522.6 ± 4.5
Fuse	1.4	6.79	0.0000	6.96	195.4 ± 1.9
				Total age:	86.1 ± 0.4

$^{40}Ar_{atm}$ = atmospheric ^{40}Ar. $^{40}Ar^*$ = radiogenic ^{40}Ar. Ca = produced by Ca-neutron interferences. K = produced by K-neutron interferences. Age(Ma) = the date is calculated using the decay constants recommended by Steiger and Jager (1977). The error is at the 1σ level and does not include the error in the value of the J parameter. Correction factors for interfering isotopes produced by neutron irradiation were $(^{39}Ar/^{37}Ar)_{Ca} = 7.0 \times 10^{-4}$, $(^{40}Ar/^{39}Ar)_{Ca} = 2.8 \times 10^{-4}$, $(^{40}Ar/^{39}Ar)_K = 2.58 \times 10^{-2}$.

a −95°C cold trap. Static measurements of argon isotopes correspond to eleven peak hopping scans. Backgrounds of the extraction and purification laser system were measured every first or third step and subtracted from each argon isotope from the subsequent gas fraction(s). Typical blank values were $2.7 \times 10^{-12} < M/e40 < 1.0 \times 10^{-11}$ and $1.0 \times 10^{-13} < M/e36 < 3.8 \times 10^{-13}$ cm^{-3} STP.

All isotopic measurements are corrected for potassium and calcium isotopic interferences, mass discrimination, and atmospheric argon contamination. All errors are quoted at the 1σ level and do not include the errors on the $^{40}Ar^*/^{39}Ar_K$ ratio and age of the monitor. The error on the $^{40}Ar^*/^{39}Ar_K$ ratio of the monitor is included in the calculation of the plateau age error bars. To define a plateau age, we need at least three consecutive steps, corresponding to a minimum of 70% of the total $^{39}Ar_K$ released, and the individual fraction ages must agree within 2σ error with the "integrated" age of the plateau segment.

4. RESULTS

4.1. Rb-Sr Results

Both the cryptomelane whole-ores and the separates, exhibit relatively low Rb concentrations (19–69 ppm) and higher Sr concentrations (44–659 ppm; Table 1). The two "separate" samples (#28-II and #31-II) that displayed $^{40}Ar/^{39}Ar$ plateau ages (see below) have the lowest Sr contents (less than 100 ppm), with Rb concentrations similar to other samples (around 60 ppm). These results contradict the expectation that the formation of cryptomelane would fractionate the Rb/Sr ratio, as this ratio remains lower than one in all samples.

The clayey matrix is also depleted in Sr (48 ppm), and even more in Rb (2 ppm). The lithiophorite contains respectively 41 and 180 ppm of Rb and Sr.

In spite of these low Rb/Sr ratios, all analyzed cryptomelane samples (whole-ores and separates) have radiogenic strontium isotopic compositions ranging from 0.7449 to 0.8137. $^{87}Sr/^{86}Sr$ ratios of the lithiophorite and the clayey matrix are also within this range. The discrepancy between two analyses of distinct aliquots of sample #34 (0.7466 and 0.7475) indicates the degree of isotopic heterogeneity existing within a sample.

The data do not define an isochron in the Rb-Sr isochron diagram (Fig. 7). However, the results for the whole-ore

TABLE 2. (Continued)

Step n°	$^{40}Ar_{atm.}$ (%)	$^{39}Ar_K$ (%)	$^{37}Ar_{Ca}/^{39}Ar_K$ ($x10^{-4}$)	$^{40}Ar^*/^{39}Ar_K$	Age (Ma)
#28 Cryptomelane (Single grain) (J=0.0164325)					
1	59.7	0.56	0.2064	0.83	24.5 ± 6.5
2	47.2	7.08	0.0769	1.18	34.6 ± 0.8
3	30.7	3.93	0.1414	1.45	42.5 ± 1.0
4	23.4	3.48	0.0674	1.55	45.4 ± 1.6
5	16.0	3.54	0.0226	1.66	48.6 ± 1.0
6	8.7	3.64	0.0016	2.17	63.3 ± 0.8
7	5.3	4.63	0.0082	2.56	74.2 ± 1.0
8	3.9	8.44	0.0419	2.78	80.6 ± 1.4
9	3.1	14.99	0.0814	2.49	72.3 ± 0.3
10	2.2	15.07	0.0190	2.46	71.5 ± 0.4
11	1.3	9.46	0.0427	2.65	76.9 ± 0.5
12	1.2	6.93	0.0506	3.10	89.5 ± 0.7
13	1.4	3.96	0.1433	5.19	147.7 ± 1.2
Fuse	1.3	14.29	0.0265	3.48	100.2 ± 0.5
				Total age:	75.4 ± 0.2
#28-II Cryptomelane (Single grain) (J=0.0164325)					
1	98.5	1.23	0.0554	1.15	33.8 ± 11.2
2	92.4	3.99	0.0253	1.50	43.9 ± 4.6
3	17.2	6.14	0.0109	1.54	45.2 ± 0.7
4	7.2	11.15	0.0080	1.60	46.9 ± 0.4
5	3.5	17.29	0.0080	1.63	47.8 ± 0.4
6	2.7	24.27	0.0080	1.64	47.9 ± 0.3
7	2.9	23.87	0.0074	1.65	48.3 ± 0.3
8	24.8	6.12	0.0071	1.66	48.5 ± 0.8
9	79.7	2.28	0.0223	1.68	49.0 ± 3.6
Fuse	75.4	3.67	0.0126	1.69	49.6 ± 1.9
				Total age:	47.5 ± 0.3
#31 Cryptomelane (Single grain) (J=0.0164325)					
1	49.8	0.00	0.0000	26.24	646.9 ± 2361.5
2	100.0	0.10	–	–	– ± –
3	94.7	1.04	0.0547	1.27	37.3 ± 16.2
4	85.9	1.14	0.0877	1.88	54.8 ± 8.5
5	79.6	1.10	0.0636	2.09	60.8 ± 8.8
6	75.7	1.82	0.0479	2.28	66.4 ± 5.5
7	69.7	2.03	0.0327	2.28	66.3 ± 5.8
8	60.7	2.58	0.0376	2.40	69.7 ± 4.7
9	60.9	2.90	0.0517	2.44	70.8 ± 3.3
10	64.8	2.36	0.0564	2.44	70.9 ± 4.8
11	60.0	4.20	0.0398	2.35	68.4 ± 2.6
12	47.4	5.15	0.0599	2.31	67.1 ± 2.3
13	26.2	7.18	0.0459	2.27	66.0 ± 1.0
14	12.4	11.15	0.0287	2.19	63.6 ± 0.8
15	7.8	17.33	0.0326	2.12	61.8 ± 0.5
16	8.0	13.37	0.0283	2.08	60.6 ± 0.8
17	7.4	13.08	0.0279	2.04	59.4 ± 0.6
18	21.0	4.92	0.0395	1.96	57.1 ± 1.8
Fuse	68.1	8.55	0.0400	1.79	52.2 ± 2.1
				Total age:	61.8 ± 0.5
#31-II Cryptomelane (Single grain) (J=0.0164325)					
1	22.6	0.00	2.8456	5.10	145.1 ± 489.9
2	85.1	0.62	0.0313	0.90	26.4 ± 6.6
3	91.1	1.88	0.0231	1.04	30.7 ± 3.5
4	82.6	1.34	0.0317	1.11	32.6 ± 4.3
5	64.4	1.41	0.0191	1.29	37.8 ± 4.1
6	48.1	1.40	0.0259	1.36	39.8 ± 2.9
7	23.8	2.75	0.0139	1.51	44.3 ± 1.1
8	16.7	6.44	0.0103	1.60	46.7 ± 0.5
9	22.6	9.59	0.0111	1.58	46.2 ± 0.3
10	20.1	12.75	0.0108	1.59	46.6 ± 0.4
11	15.6	9.59	0.0093	1.62	47.3 ± 0.3
12	14.7	10.11	0.0087	1.61	47.1 ± 0.4
13	14.9	11.28	0.0107	1.61	47.1 ± 0.4
14	17.2	10.95	0.0114	1.60	46.7 ± 0.3
15	19.1	8.05	0.0143	1.57	45.9 ± 0.5
16	16.7	3.17	0.0194	1.58	46.1 ± 0.8
Fuse	42.4	8.69	0.0139	1.58	46.2 ± 0.5
				Total age:	45.8 ± 0.2
#32 Cryptomelane (Single grain) (J=0.0164325)					
1	90.1	0.51	0.0932	0.75	22.1 ± 11.9
2	76.1	4.87	0.0105	0.90	26.4 ± 2.0
3	76.8	4.19	0.0185	1.05	30.8 ± 1.6
4	65.2	5.59	0.0179	1.40	41.0 ± 1.7
5	32.0	5.66	0.0259	1.63	47.6 ± 1.4
6	15.2	6.61	0.0283	2.23	65.0 ± 0.9
7	8.2	10.94	0.0080	2.41	70.1 ± 0.8
8	7.1	14.94	0.0084	2.18	63.5 ± 0.5
9	7.1	11.45	0.0097	2.24	65.3 ± 0.5
10	7.7	7.51	0.0090	2.47	71.9 ± 0.7
11	17.3	5.07	0.0196	2.83	82.0 ± 1.2
12	53.3	5.02	0.0175	3.41	98.5 ± 2.2
Fuse	66.2	17.64	0.0111	2.01	58.5 ± 0.9
				Total age:	61.4 ± 0.3
#32-II Cryptomelane (Single grain) (J=0.0164325)					
1	91.2	0.35	0.0141	0.79	23.3 ± 10.7
2	89.1	2.10	0.0257	0.68	20.1 ± 3.9

samples show a positive correlation, corresponding to an age of 2.1 Ga. Three of the separate samples of cryptomelane plot also within this correlation, and are close to their respective whole-ore (Fig. 7). The clayey matrix is also within the same trend. On the other hand, the two samples #28-II and #31-II, with well-defined $^{40}Ar/^{39}Ar$ plateau ages, plot far away to the right of the correlation line, due to their lower Sr contents, and thus, higher, Rb/Sr ratios. Finally, the absence of any mixing line in the $^{87}Sr/^{86}Sr$ vs. 1/Sr diagram (not shown) clearly rules out a simple mixing process.

4.2. $^{40}Ar/^{39}Ar$ Results (Table 2)

Eight whole-ore samples and five separates (veins or concretions labelled by "II"), collected in the different units, were analyzed with the $^{40}Ar/^{39}Ar$ method. The results are illustrated in Figs. 8–13.

4.2.1. Whole ores

All the whole-ore samples display disturbed age spectra. The integrated ages range from 39.8 ± 0.3 Ma to 79.1 ± 0.8 Ma. In spite of the strong disturbances of the age spectra, similar features are found in various samples. (1) All of these samples but one (#7) display some apparent age segments older than 60–65 Ma in their age spectra. (2) Four samples, including the three samples from the clastic ore (#15, #28, and #32) show anomalously high ages in the low to intermediate temperature steps (Fig. 8). (3) These three samples from the clastic horizon, as well as one sample (#22) from the platey level, also show high ages up to 317.5 ± 4.1 Ma in the high temperature steps (Fig. 9). (4) Samples #1 and #34 display age spectra, with younger ages in the range 35–45 Ma, in the high temperature steps (Fig. 10). Sample #7, which is the only sample with all apparent ages lower than 50 Ma (Fig. 10), also shows low ages in the range 16–26 Ma, in the high temperature steps.

A broad age convergence in the intermediate temperature steps is observed around 60–70 Ma, when all age spectra (except #7) are grouped together (Fig. 11). A poorly constrained age cluster between 20 and 40 Ma also appears in the low temperature steps. Furthermore, sample #22 displays a "pseudo" plateau age (less than 70% of the total $^{39}Ar_K$ released) at 67.8 ± 0.8 Ma (Fig. 12).

TABLE 2. (Continued)

Step n°	$^{40}Ar_{atm.}$ (%)	$^{39}Ar_K$ (%)	$^{37}Ar_{Ca}/^{39}Ar_K$ ($x10^{-4}$)	$^{40}Ar^*/^{39}Ar_K$	Age (Ma)
3	96.0	3.97	0.0435	0.88	26.0 ± 4.5
4	85.2	4.50	0.0115	1.13	33.3 ± 3.2
5	77.1	5.18	0.0235	1.10	32.3 ± 1.8
6	62.7	4.48	0.0151	1.36	39.9 ± 1.1
7	43.0	4.91	0.0200	1.63	47.6 ± 0.9
8	19.7	7.62	0.0194	1.80	52.7 ± 0.6
9	11.5	14.91	0.0180	1.90	55.5 ± 0.3
10	10.9	16.60	0.0196	1.96	57.1 ± 0.3
11	11.3	9.16	0.0208	1.95	57.0 ± 0.4
12	13.5	4.41	0.0261	1.85	54.1 ± 0.9
13	13.7	11.29	0.0125	1.86	54.2 ± 0.4
Fuse	25.7	10.53	0.0130	1.86	54.2 ± 0.4
				Total age:	50.0 ± 0.3
#34 Cryptomelane (Single grain) (J=0.0164325)					
1	99.6	0.01	1.7898	0.27	7.9 ± 770.4
2	91.2	1.25	0.0273	1.23	36.0 ± 7.3
3	82.7	2.07	0.0449	1.30	38.1 ± 5.3
4	72.5	2.50	0.0358	1.39	40.6 ± 3.4
5	67.9	5.15	0.0462	1.07	31.5 ± 1.6
6	65.7	5.65	0.0582	0.94	27.5 ± 1.8
7	55.3	6.42	0.0589	1.36	39.8 ± 2.5
8	35.7	7.77	0.0240	2.24	65.3 ± 1.6
9	20.4	10.23	0.0293	2.60	75.4 ± 1.1
10	11.9	12.13	0.0265	2.46	71.5 ± 0.8
11	16.8	10.19	0.0174	2.36	68.5 ± 1.0
12	23.0	9.36	0.0197	2.16	63.0 ± 1.2
13	50.0	8.08	0.0356	1.77	51.7 ± 1.5
Fuse	74.4	19.18	0.0379	1.54	45.2 ± 1.3
				Total age:	55.2 ± 0.5

4.2.2. *Separates*

The age spectra obtained on separates are generally less disturbed than those obtained for the whole-ore samples. Four of the five samples display age spectra with flat segments (Fig. 12). Two real plateau ages at 46.7 ± 0.2 Ma and 48.1 ± 0.2 Ma are obtained for samples #31-II and #28-II, respectively. Two "pseudo" plateau ages (less than 70% of the total $^{39}Ar_K$ released) are displayed by samples #7-II and #32-II, respectively, at 47.3 ± 0.5 Ma and 55.6 ± 0.2 Ma. All of these age spectra present a staircase shape in the low temperature steps, with initial ages in the range 20–40 Ma.

Sample #22-II has the most disturbed age spectrum, with a general staircase shape very similar to that displayed by the corresponding whole-ore (Fig. 12). This age spectrum presents (1) a poorly defined level (one step) at 65.1 ± 0.3 Ma and (2) anomalously high ages in the high temperature steps up to 522.6 ± 4.5 Ma.

4.2.3. *Isochron analysis*

All of the samples were also analysed using $^{36}Ar/^{40}Ar$ vs. $^{39}Ar/^{40}Ar$ correlation diagrams (Turner, 1971; Roddick et al., 1980; Hanes et al., 1985). This analysis confirms the age of the plateaus observed on the age spectra of the separates (Table 3). It also confirms the existence of two poorly constrained "plateau" segments around 36–37 Ma in the low temperature steps, for two whole-ore samples (#7 and #22) (Table 3). The low values of the MSWD (less than 1), are related to the large error bars of the corresponding steps, with high amounts of atmospheric contamination. The high value of the MSWD parameter and the low value of the $(^{40}Ar/^{36}Ar)_i$ ratio of sample #32-II reflect the poor quality of the corresponding plateau segment.

4.2.4. *$^{37}Ar_{Ca}/^{39}Ar_K$ spectra*

Figure 13 shows that no clear relationship can be found between the shape of the $^{37}Ar_{Ca}/^{39}Ar_K$ spectra and the sample type (whole-ore or separate), as previously observed for the age spectra. Nevertheless, the two samples which display the plateau ages around 47 Ma (#28-II and #31-II) also have less disturbed $^{37}Ar_{Ca}/^{39}Ar_K$ spectra, with the lowest (around 0.01) $^{37}Ar_{Ca}/^{39}Ar_K$ ratio values (bold lines in Fig. 13).

5. DISCUSSION

5.1. Rb-Sr data

Our Rb-Sr data clearly indicate that the crystallization of cryptomelane produces a much lower fractionation between Rb and Sr than between K and Ca. Potassium contents range approximately from 1 to 3% in cryptomelanes, while Ca contents are much lower, averaging 0.1–0.2% (Beauvais, 1984). Therefore, K/Rb and Ca/Sr ratios av-

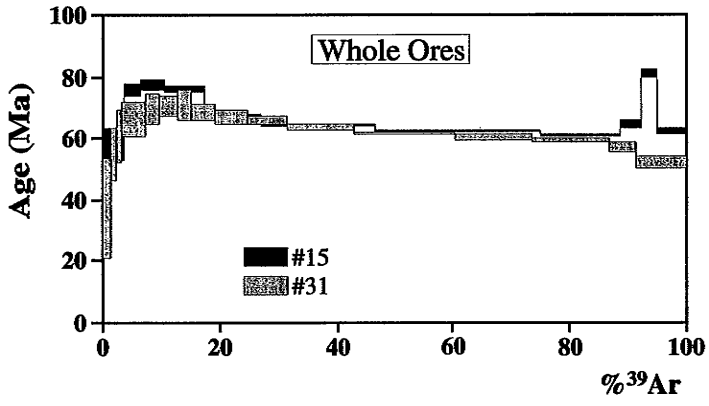

FIG. 8. Two of the four $^{40}Ar/^{39}Ar$ age spectra which display anomalously high ages in the low to intermediate temperature steps. The error bars for each temperature steps are at the 1σ level. The errors in the J-values are not included.

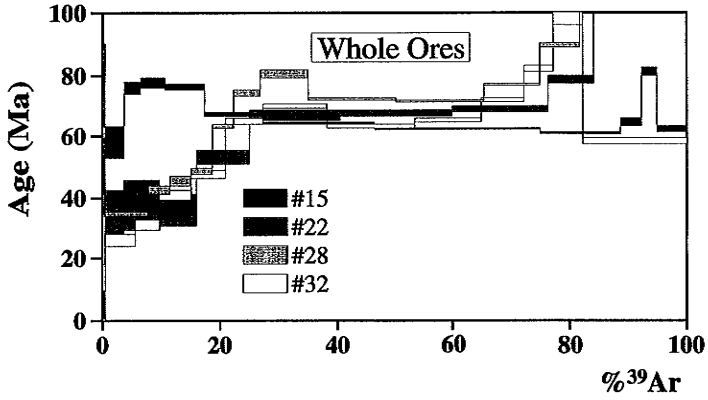

FIG. 9. $^{40}Ar/^{39}Ar$ age spectra with anomalously high ages in the high temperature steps. Same observations as for Fig. 8.

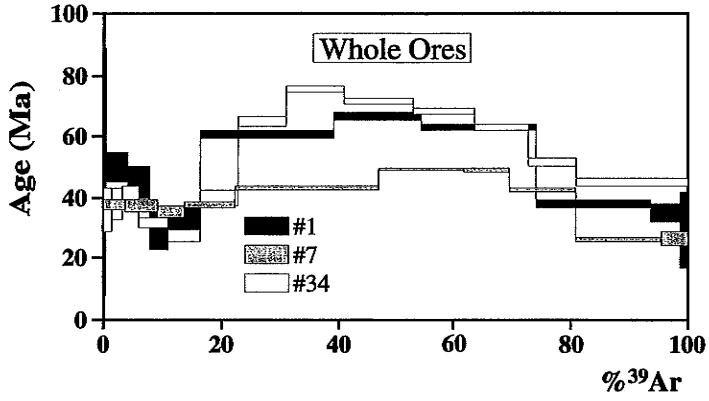

FIG. 10. $^{40}Ar/^{39}Ar$ age spectra with low ages in the low and high temperature steps. Same observations as for Fig. 8.

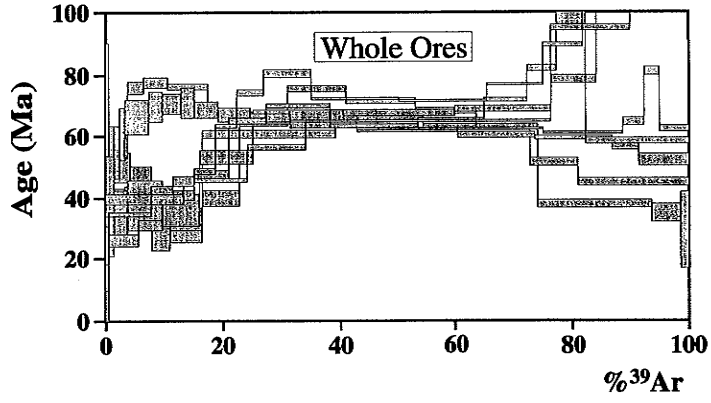

FIG. 11. $^{40}Ar/^{39}Ar$ age spectra of all the whole-ore samples (except sample #7). Same observations as for Fig. 8.

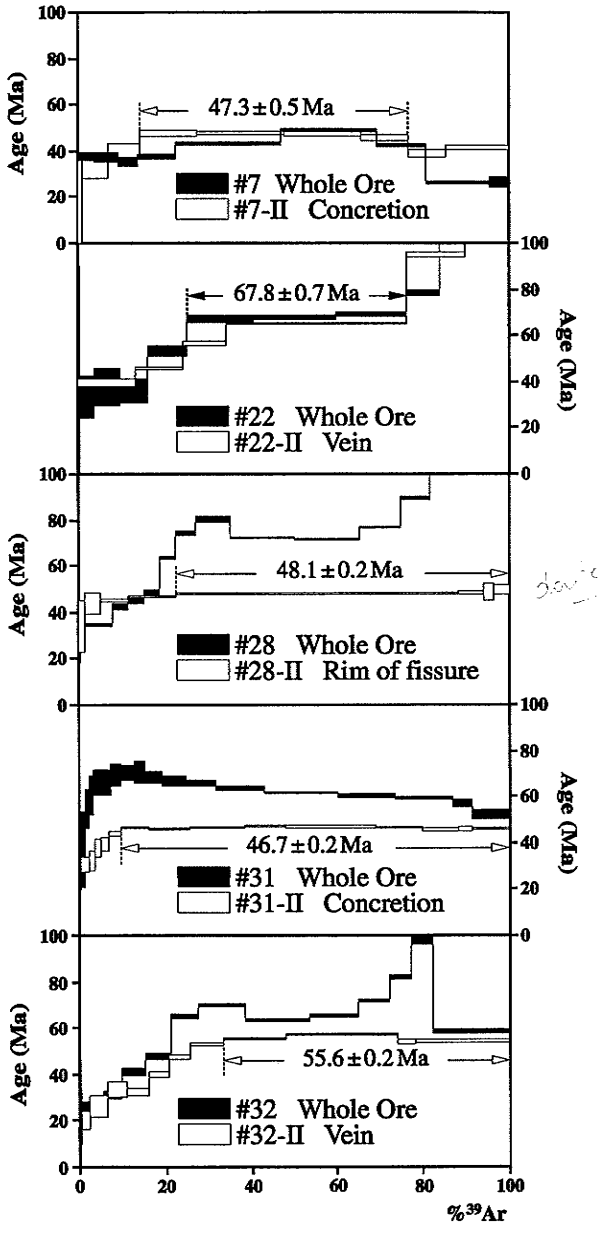

FIG. 12. $^{40}Ar/^{39}Ar$ age spectra of whole-ore and "separate" sample pairs. Same observations as for Fig. 8.

erage ≈500 and ≈10, compared, respectively, to mean crustal values of 200 and 40 (Taylor and McLennan, 1985). These low Ca/Sr ratios probably result from differing behaviour of the two alkaline-earth elements in the cryptomelane structure.

Similarly, Rb/Sr ratios exhibit a wide range of variation between 0.1 and 10 in continental sediments. Cryptomelanes from Azul fall within this range of variation, and consequently, do not show any evidence for a Rb enrichment relative to Sr.

The correlation line obtained in the isochron diagram can be interpreted as a 2.1 Ga reference isochron, in spite of the fact that the Rb-Sr chronometer clearly suffered some perturbation. This age, which corresponds to the formation of the Rio Fresco group containing the Mn protore (Beauvais et al., 1987; Machado et al., 1991; Macambira, 1992) suggests that the Rb-Sr chronometer has not been strongly affected by the first stage of weathering of the proterozoic sediments.

This could result from the presence of inherited phyllosilicates, such as muscovite, occasionally observed in thin sections (Fig. 5) and suggested by some of the $^{40}Ar/^{39}Ar$ results (see below). Nevertheless, traces of muscovite, when present in Mn oxides, cannot fully explain the radiogenic $^{87}Sr/^{86}Sr$.

Consequently, these data suggest that (1) the inherited Sr component is located within the crystal structure of cryptomelanes and (2) the pseudomorphic replacement of rhodochrosite by cryptomelane does not significantly disturb the Rb-Sr chronometer. Neither Rb nor Sr were significantly leached during the first stage of weathering, and both elements probably entered the cryptomelane crystal structure by K-replacement. Thus, this transformation took place in a closed system, at least at the scale of the entire sequence.

This conclusion is supported by the fact that Sr can be integrated within the hollandite crystal structure, (of which cryptomelane is the potassic endmember) (Burns and Burns, 1979), whereas Ca-hollandite has never been described so far. This could explain that Ca, but not Sr, was leached out of the Mn oxides.

Secondary concretions and veins of cryptomelane-2 (#7-II, #32-II, and #22-II) have similar Rb/Sr characteristics to those of whole-ores. This suggests that Sr was not removed during their crystallization. In contrast, the two samples with well-defined $^{40}Ar/^{39}Ar$ plateau ages (#28-II and #31-II) plot far away from the reference isochron (Fig. 7). This clearly indicates that the Rb-Sr system was disturbed during the crystallization of these Mn oxides, with a relative enrichment in Rb.

TABLE 3. Results of the analyses with the $^{36}Ar/^{40}Ar$ vs. $^{39}Ar/^{40}Ar$ correlation diagram method.

Sample	"Plateau" age	Isochron age	$(^{40}Ar/^{36}Ar)_i$	MSWD
#7-II	47.3 ± 0.5	47.1 ± 0.9	299.0 ± 15.9	1.12
#28-II	48.1 ± 0.2	47.8 ± 0.1	298.4 ± 3.0	3.55
#31-II	46.7 ± 0.2	47.1 ± 0.3	285.6 ± 5.5	1.29
#32-II	55.6 ± 0.2	57.0 ± 0.3	256.2 ± 10.1	16.4
#7	37.1 ± 0.8	37.3 ± 1.3	292.6 ± 19.0	0.63
#22	35.8 ± 4.3	37.4 ± 11.0	295.0 ± 3.1	0.04

The $(^{40}Ar/^{36}Ar)_i$ and ages are both calculated from the intercept of the best-fit line (York, 1969), with the respective axis of the correlation plot. MSWD = SUMS/(n − 2); SUMS: weighted sum of residuals; n: number of points fitted.

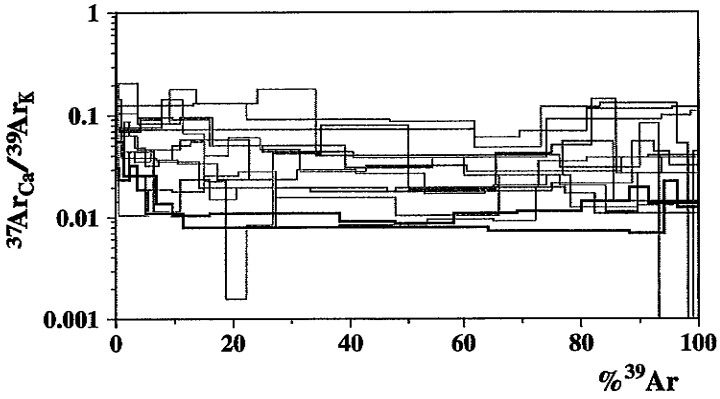

FIG. 13. $^{37}Ar_{Ca}/^{39}Ar_K$ spectra of all the studied samples. Black lines: $^{37}Ar_{Ca}/^{39}Ar_K$ spectra of samples #28-II and #31-II; Grey lines: all others $^{37}Ar_{Ca}/^{39}Ar_K$ spectra.

Unlike in the first generation, the initial textures were not preserved during the crystallization of these samples (Fig. 3), leading to much lower Sr contents in these minerals.

The two-point isochrons drawn between whole-ore samples and separates correspond to unrealistic ages of 351 and 93 Ma, much older than the $^{40}Ar/^{39}Ar$ ages. These results indicate that sample pairs formed by whole-ores and veins or concretions were not closed-systems for Rb and Sr after formation. This may result either from initial isotopic inhomogeneities between whole-ores and veins or concretions, or from continuous chemical exchange after formation.

5.2. $^{40}Ar/^{39}Ar$ Data

5.2.1. Age spectra shapes

One of the significant features of the age spectra, mainly for whole-ore samples, is that anomalously low or high ages are often observed within a spectrum, in the low or high temperature steps, respectively.

The low ages in the low temperature steps are observed for almost all the age spectra, often with a staircase shape in the first 10–20% of the total $^{39}Ar_K$ released.

Low ages in the high temperature steps are also observed in three age spectra: #1, #7, and #34 (Fig. 10). Furthermore, samples #7-II and #31 (Figs. 12, 8) also show, to a lesser extent, slightly younger ages in the final stages of degassing of $^{39}Ar_K$. When the low ages occur both in the low and high temperature steps, the resulting age spectrum has an upward-convex shape (#1, #7, #34) (Fig. 10).

These low ages are generally correlated to higher $^{37}Ar_{Ca}/^{39}Ar_K$ ratios. Low ages in the low temperature steps, combined with high $^{37}Ar_{Ca}/^{39}Ar_K$ ratios are frequently observed for other kinds of minerals and are generally explained by the presence of poorly crystallized alteration phases. However, this hypothesis cannot explain the low ages in the high temperature steps, as these alteration phases release their radiogenic Ar in a lower temperature domain than that of the "primary" minerals. On the other hand, convex-upward age spectra have been found in white micas (e.g., Wijbrans and McDougall, 1986) and were interpreted as indicating the presence of two mixed white mica generations with distinct isotopic closure ages. These authors explained the lowering of the apparent ages in the initial and final degassing steps by a larger temperature span of the degassing spectrum of the youngest mica generation. This hypothesis can also be invoked to explain the convex-upward age spectra displayed by some of our cryptomelane samples.

The distinct ages which are found in the low and high temperature steps (e.g., #34) (Fig. 10) can be explained either by distinct overlaps of the degassing spectra in the two temperature domains or by the presence of an alteration phase which preferencially degasses in the low temperature steps. Whatever the case, the highest ages of the age-spectra bumps give a minimum estimate of the true age of the oldest manganese oxide generation (see for instance samples #7 and #7-II, which display concordant ages in the intermediate temperature steps and discordant ages outside this temperature domain (Fig. 12)).

Four samples display age spectra with higher ages in the low (#15 and #31) (Fig. 8) or intermediate temperature steps (#28 and #32) (Fig. 9). The latter samples also show steep staircase shapes for the first 25% of the total $^{39}Ar_K$ released. A common problem of the $^{40}Ar/^{39}Ar$ dating method is the loss by recoil of neutron irradiation-generated $^{39}Ar_K$, especially when the material studied is very fine-grained (Turner and Cadogan, 1974; Harrison, 1983; Foland et al., 1992). Classically, the age spectrum displays old apparent ages, due to the $^{39}Ar_K$ loss, in the low temperature steps, followed by a slow decreasing staircase shape of the apparent ages towards higher temperature steps (Turner and Cadogan, 1974). Samples #15 and #31 (Fig. 8) display age spectra which correspond exactly to this model, except for the lowest temperature steps. In these two samples, the $^{39}Ar_K$ displaced during the n,p transmutation definitely left the irradiated system, since low ages are observed only in the very first steps, corresponding only to a few percents of the total $^{39}Ar_K$ released. By contrast, low ages in the low temperature steps are observed in a larger degassing domain of samples #28 and #32 (Fig. 9). This may result from the incorporation of the displaced $^{39}Ar_K$ from the K-rich Mn oxides into other K-poor Mn oxides or alteration phases. In these samples, disturbed by $^{39}Ar_K$ recoil, the decreasing staircase shape of the age spectra in the intermediate to high temperature steps displays apparent ages

which tend towards, and may eventually reach, the true age of the mineral. Vasconcelos et al. (1994) did not observed any direct evidence of recoil in their samples. This may result from the large atmospheric contamination in the low to intermediate temperature steps of their experiments, which may hide the recoil effects, and which did not occur in our samples for some unknown reason.

Five of our samples (#15, #22, #22-II, #28, #32) (Figs. 9, 12) give unrealistically old ages in the high temperature steps, which may reflect the presence of inherited hypogene minerals, such as muscovite or K-feldspar, as also revealed by the petrographic observation (Fig. 5). Indeed, muscovite releases its radiogenic argon in an higher temperature domain than cryptomelane (or other Mn oxides) (Vasconcelos et al., 1994).

5.2.2. *Chronological implications*

In addition to the methodological questions discussed above, five observations remain to be discussed which are relevant to the chronology of evolution of the Azul Mn ore:

1) All whole-ore age spectra (except that of sample #7) show an age convergence around 60–70 Ma in the intermediate temperature steps (Fig. 11).
2) The age spectra displayed by the "separate" samples are less disturbed and give different ages than those of the corresponding whole-ores (Fig. 12).
3) One of the "separate" sample (#32-II) displays a poorly constrained plateau age at 55.6 ± 0.2 Ma (Fig. 12).
4) Very good plateau ages are displayed by three separate samples (#28-II, #7-II, #31-II). These ages are concordant within error bars and allow calculation of a mean value of 47.4 ± 0.1 Ma (Fig. 12).
5) Three whole-ore samples display low ages around 37 Ma in the low (#7, #22) or in the high (#1) temperature steps (Figs. 9, 10).

Vasconcelos et al. (1994) defined three age clusters for the Azul Mn-ore, respectively, at 65.5–68 Ma, 51–56 Ma, and 40–43 Ma. They proposed that these age clusters characterize the episodic precipitation of the three successive Mn-oxide generations of the Azul Mn deposit as a result of superimposed weathering events.

Our data confirm that cryptomelane-1 probably formed between 60 and 70 Ma as proposed by Vasconcelos et al. (1994). We find evidence for some Early Paleocene-Upper Cretaceous ages in all the whole-ore samples (except #7) (Figs. 11, 14) and one separate sample (#22-II). Furthermore, one whole-ore age spectrum (#22) displays a plateau segment at 67.8 ± 0.8 Ma (51% of the total $^{39}Ar_K$ released) (Fig. 12). This age cluster is not very well constrained, probably because whole-ore samples are mixtures of cryptomelane and other constituents, unlike separates which are primarily composed of cryptomelane. The lower ages in the low or high temperature steps may be related to the presence of younger cryptomelane generations in the whole-ore samples, as discussed above.

The age at 55.6 ± 0.2 obtained for the separate sample #32-II is only constrained by one sample, and the plateau age is of poor quality. Nevertheless, this result is concordant with the age cluster at 51–56 Ma defined by Vasconcelos et al. (1994) for the Azul area (Figs. 12, 14).

The most reliable ages, according to the usual criteria of the $^{40}Ar/^{39}Ar$ method (see above), are displayed by the three "separate" samples. These early Eocene ages, with a mean value at 47.4 ± 0.1 Ma are clearly distinct from the two age clusters (51–56 Ma and 40–43 Ma) that were attributed respectively to the second and third cryptomelane genera-

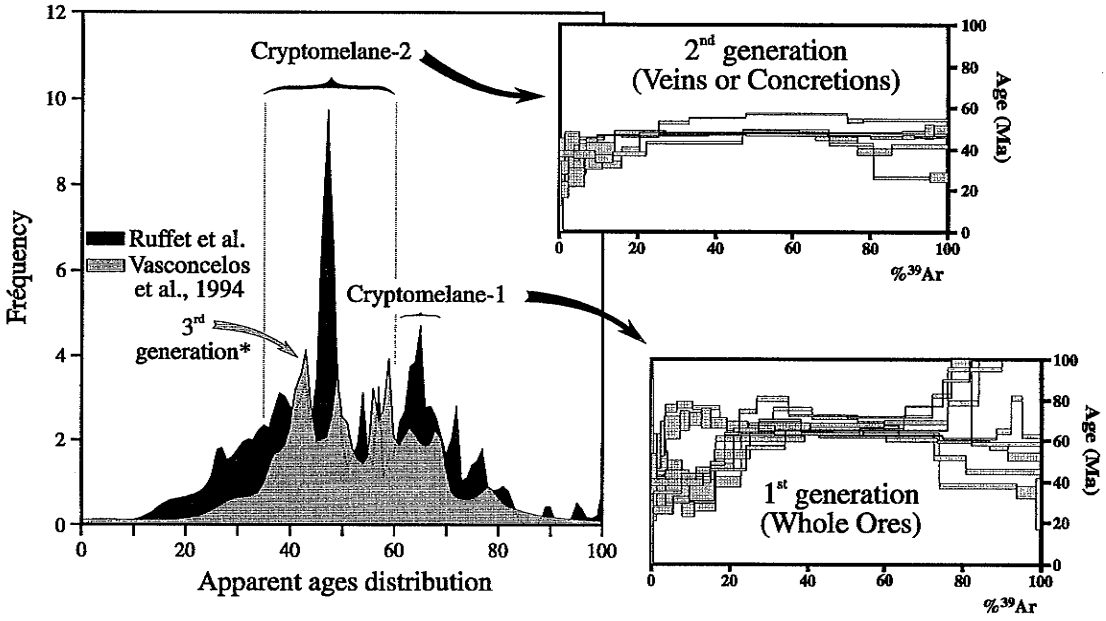

FIG. 14. Distribution of all the apparent ages (step-heating increments) of the age spectra from this study (black) and from the study (Azul area) of Vasconcelos et al. (1994) (light grey). The age spectra of the second cryptomelane generation do not include sample #22-II, whereas the age spectra of the first cryptomelane generation do not include sample #7. *: third cryptomelane generation (or cryptomelane-3) defined by Vasconcelos et al. (1994).

tions by Vasconcelos et al. (1994) (Figs. 12, 14). Moreover, these separate samples are essentially composed of the second generation of cryptomelane. As emphasized above, no occurence of the third cryptomelane generation described by Beauvais et al. (1987) or Vasconcelos et al. (1994) has been detected in the samples of this study. We nevertheless obtained low ages (around 37 Ma) from three whole-ore samples (Figs. 9, 11, 14).

Therefore, we believe that these results contradict the model proposed by Vasconcelos et al. (1994), which proposes that each cryptomelane generation corresponds to distinct weathering events corresponding to global climatic changes. Cryptomelane-2 and -3 may have formed simultaneously and more or less continuously over several million years (from 56 Ma to 40 and possibly 37 Ma). This interpretation seems more compatible with the petrographic evidence that each generation of Mn oxide replaces progressively the previous generation through dissolution and in situ recrystallization. Although the mineralogical "evolutionary sequence" suggests a gradation from bottom to top of the profiles and from upstream to downstream of the sequence, this does not imply a simple spacial nor temporal spacing of crystallization events. Because of the complex path of water circulation and residence time within the profiles, the crystallization of the different generations of cryptomelane may occur sequentially at a given location, but simultaneously at different locations in the profile. In fact, no simple correlation is observed between sample depth and the age or shape of the $^{40}Ar/^{39}Ar$ age spectra (see for instance, samples #1, #7, and #15 (Figs. 8, 10), collected at different depth in profile A1P 170).

A final noticeable feature of the Azul chronology is that the formation of cryptomelane seems to have stopped much earlier than at other locations in Brazil. The youngest age found by Vasconcelos et al. (1994) is 41 ± 2 Ma. More recent crystallization events may have occurred, as indicated by the few age segments at 37 Ma displayed by some of our whole-ore samples. Nevertheless, these lower Eocene ages are much older than those found in the Igarapé Bahia profile (Carajàs mountains) (Vasconcelos et al., 1994). This difference remains to be explained, and is most likely associated with local factors rather than continental-scale climate changes. One hypothesis involves a decrease of K available for recrystallization in the Mn-protore, due to exhaustion of the original K-bearing minerals in the parent rock. Systematic budget calculations, as well as comparisons with other locations in the same continental area will have to be carried out to solve this problem.

6. CONCLUSIONS

1) These results show that cryptomelane is a suitable mineral for dating with the $^{40}Ar/^{39}Ar$ method as previously proposed by Vasconcelos et al. (1994). However, problems related to ^{39}Ar recoil during neutron irradiation, contamination by hypogene phases, or the presence of multiple generations of Mn-oxides are encountered.

2) Fine-scale sampling allowed by the laser probe $^{40}Ar/^{39}Ar$ technique makes it possible to analyse separately distinct generations of Mn oxides extracted from a single sample. The most reliable ages were obtained on separates, either millimetric veins crosscutting the samples or millimeter-thick concretions covering the faces of fissures.

3) Little Rb/Sr fractionation occurs during cryptomelane crystallization. Large variations of the $^{87}Sr/^{86}Sr$ ratio are found among the samples, inherited from the 2.1 Ga old parent rock. This shows that little isotopic homogenization occurred during the crystallization of the Mn oxides, which, thus, cannot be dated by the Rb/Sr method.

4) Our data confirm that the oldest and first cryptomelane generation (cryptomelane-1), formed by pseudomorphic replacement of rhodocrosite, probably developed between 60 and 70 Ma.

5) Some of the samples of the second cryptomelane generation displayed ages around 47 Ma, distinct from the two age clusters at 51–56 and 40–43 Ma defined by Vasconcelos et al. (1994). Furthermore, hints of younger ages, around 37 Ma, without any evidence of a third cryptomelane generation, are observed in the age spectra of some of our samples.

6) These results suggest, in contradiction with the interpretation of Vasconcelos et al. (1994), that the evolution of Mn oxides and cryptomelane in the weathering profile essentially results from a continuous process and that successive petrographic generations may form simultaneously within one profile.

7) Although the previous conclusion may put some limitations to the use of the K-Mn oxides as paleoclimatic "tracers", the $^{40}Ar/^{39}Ar$ study of these minerals provides, nevertheless, the first absolute radiochronological constraints on the development of tropical weathering. This invaluable information will clearly be extremely useful in the near future, for paleoalteration studies and for more precisely understanding both the mechanisms and timing of laterite formation.

Acknowledgments—This work has been founded by the INSU–ORSTOM program PEGI (Programme d'étude de la géosphère intertropicale). J. J. Motte and R. Dassule are thanked for drawing some of the figures. W. Barthelemy is acknowledged for technical assistance in the solid source mass spectrometry. E. Brown is greatly thanked for correcting the manuscript.

Editorial handling: K. R. Ludwig

REFERENCES

Alibert C., Michard A., and Albarède F. (1983) The transition from alkali basalts to kimberlite: isotope and trace element evidence from melilitites. *Contrib. Mineral. Petrol.* **82,** 176–186.

Beauvais A. (1984) Concentrations manganésifères latéritiques. Etude pétrologique de deux gîtes sur roches sédimentaires précambriennes. Gisements de Moanda (Gabon) et d'Azul (Brésil). Thèse d'Université (Poitiers).

Beauvais A., Melfi A., Nahon D., and Trescases J. J. (1987) Pétrologie du gisement latéritique manganésifère d'Azul (Brésil). *Mineral. Deposita* **22,** 124–134.

Bernardelli A. and Beisiegel V. R. (1978) Geologia economica da jazida de manganes do Azul. *An. XXX Congr. Bras. Geol.* **4,** 1431–1444.

Bricken O. (1965) Some stability relations in the system $Mn–O_2–H_2O$ at 25 and one atmosphere total pressure. *Amer. Mineral.* **50,** 1296–1354.

Burns R. G. and Burns V. M. (1979) Manganese oxides. In *Marine Minerals* (ed. P. H. Ribbe); *Rev. Mineral.* 1–46.

Clauer N., Giblin P., and Lucas J. (1984) Strontium and Ar isotope studies of detrital smectites from the Atlantic Ocean (D.S.D.P., legs 43, 48 and 50). *Chem. Geol.* **2,** 141–151.

Clauer N., Chaudhuri S., Kralik M., and Bonnot-Courtois C. (1993) Effects of experimental leaching on Rb-Sr and K-Ar isotopics systems and REE contents of diagenitic illite. *Chem. Geol.* **103,** 1–16.

Foland K. A., Hubacher F. A., and Arehart G. B. (1992) $^{40}Ar/^{39}Ar$ dating of very fined grained samples: An encapsuled-vial procedure to overcome the problem of ^{39}Ar recoil loss. *Chem. Geol.* **102,** 269–276.

Garrels R. M. and Christ C. L. (1965) *Solutions, Minerals and Equilibria.* Freeman Cooper & Company.

Giovanoli R. and Leuenberger V. (1969) Uber die oxidation von manganoxihydroxide. *Helvetica Chim. Acta* **52,** 2333–2347.

Hanes J. A., York D., and Hall C. M. (1985) An $^{40}Ar/^{39}Ar$ geochronological and electron microprobe investigation of an Archean pyroxenite and its bearing on ancient atmospheric compositions. *Can. J. Earth. Sci.* **22,** 947–958.

Harrison T. M. (1983) Some observations on the interpretation of $^{40}Ar/^{39}Ar$ age spectra. Isotope *Geoscience* **1,** 319–338.

Herz N. and Banerjee S. (1973) Amphibolites of the lafaiete, Minas Gerais, and the Serra Do Navio Manganese Deposits, Brazil. *Econ. Geol.* **68,** 1289–1296.

Hypólito R., Valarelli J. V., Giovanoli R., and Netto S. M. (1984) Gibbs free energy of formation of synthetic cryptomelane. *Chimia* **38,** 427–429.

Macambira M. (1992) Chronologies U–Pb, Rb/Sr, K/Ar et croissance de la croûte continentale dans l'Amazonie du Sud-Est; exemple de la région de Rio Maria, province de Carajàs, Brésil. Thesis, Univ. Montpellier II.

Machado N., Lindenmayer Z., Krogh T. E., and Lindenmayer D. (1991) U–Pb geochronology of archen magmatism and basement reactivation in the Carajas area, Amazon shield, Brazil. *Precambrian Res.* **49,** 329–354.

Merino E., Nahon D., and Wang Y. (1993) Kinetics and mass transfer of pseudomorphic replacement: application to replacement of parent minerals and kaolinite by Al, Fe and Mn oxides during weathering. *Amer. J. Sci.* **293,** 135–155.

Morton J. P. and Long L. E. (1980) Rb-Sr dating of paleozoic glauconite from the Llano region, Central Texas. *Geochim. Cosmochim. Acta* **44,** 663–672.

Nahon D. and Parc S. (1990). Lateritic concentrations of manganese oxyhydroxides and oxides. *Geolg. Rundsch.* **79,** 2, 319–326.

Nahon D., Beauvais A., Nziengui-Mapangou P., and Ducloux J. (1984) Chemical weathering of Mn-garnets under lateritic conditions in Northwest Ivory coast (West Africa). *Chem. Geol.* **45,** 53–71.

Nziengui-Mapangou P. (1981) Pétrologie comparée de gisements manganésifères supergènes en Afrique (gisement de Ziémougoula en Côte d'Ivoire et gisement de Moanda au Gabon). Thesis Univ. of Poitiers unpubl.

Parc S., Nahon D., Tardy Y., and Vieillard P. (1989) Estimated solubility and fields of stability for cryptomelane, nsutite, birnessite and lithiophorite based on natural lateritic weathering sequences. *Amer. Mineral.* **74,** 466–475.

Perseil E. A. and Grandin G. (1985) Altération supergène des protores à grenats manganésifères dans quelques gisements d'Afrique de l'Ouest. *Mineral. Deposita* **20,** 211–219.

Post J. E., Von Dreele R. B., and Buseck P. R. (1982) Symmetry and cation displacements in Hollandites: structure refinements of Hollandite, Cryptomelane and Priderite. *Acta Cryst.* **B38,** 1056–1065.

Roddick J. C., Cliff R. A., and Rex D. C. (1980) The evolution of excess argon in alpine biotites-A ^{40}Ar-^{39}Ar analysis. *Earth Planet. Sci. Lett.* **48,** 185–208.

Ruffet G., Féraud G., and Amouric M. (1991) Comparison of ^{40}Ar-^{39}Ar conventional and laser dating of biotites from the North Trégor Batholith. *Geochim. Cosmochim. Acta* **55,** 1675–1688.

Samson S. D. and Alexander E. C., Jr. (1987) Calibration of the interlaboratory ^{40}Ar-^{39}Ar dating standard, MMhb-1. *Chem. Geol.* **66,** 27–34.

Scaillet S., Féraud G., Lagabrielle Y., Ballèvre M., and Ruffet G. (1990) ^{40}Ar-^{39}Ar laser-probe dating by step-heating and spot fusion of phengites from the Dora Maira nappe of the Western Alps, Italy. *Geology* **18,** 741–744.

Staudigel H., Gillis K., and Duncan R. (1986) K-Ar and Rb-Sr ages of celadonites from the Troodos ophiolite. *Geology* **14,** 72–75.

Steiger R. H. and Jäger E. (1977) Subcommission on geochronology: convention on the use of decay constants in geo- and cosmochronology. *Earth Planet. Sci. Lett.* **36,** 359–362.

Taylor S. R. and McLennan S. M. (1985) *The Continental Crust/its Composition and Evolution; Geoscience texts.* Blackwell.

Turner G. (1971) ^{40}-^{39}Ar ages from the lunar Maria. *Earth Planet. Sci. Lett.* **11,** 169–191.

Turner G. and Cadogan P. H. (1974) Possible effects of ^{39}Ar recoil in ^{40}Ar-^{39}Ar dating. *Proc. 5th Lunar Conf.* **2,** 1601–1615.

Vasconcelos P. M., Renne P. R., Brimhall G. H., and Becker T. A. (1994) Direct dating of weathering phenomena by ^{39}Ar-^{40}Ar and K-Ar analysis of supergene K-Mn oxides. *Geochim. Cosmochim. Acta* **58,** 1635–1665.

Vicat J., Fanchon E., Strobel P., and Qui D. T. (1986) The structure of $K_{133}Mn_8O_{16}$ and cation ordering in hollandite-type structures. *Acta Cryst.* **B42,** 162–167.

Wijbrans J. R. and McDougall I. (1986) $^{40}Ar/^{39}Ar$ dating of white micas from an Alpine high-pressure metamorphic belt on Naxos (Greece): the resetting of the argon isotope system. *Contrib. Mineral. Petrol.* **93,** 187–194.

York D. (1969) Least squares fitting of a straight line with correlated errors. *Earth Planet. Sci. Lett.* **5,** 320–324.

APPENDIX

1) A1P 170 profile

a) #1, collected in the indurated Mn-ore level, is composed of black cryptomelane with some nsutite and small layers of grey pyrolusite. The whole sample was analyzed, since it was not possible to separate the different phases.

b) #7 was also collected in the indurated Mn-ore level. The massive ore (#7) contains principally cryptomelane and nsutite. Cryptomelane-2 appears as disseminated brown concretions (#7-II), which were separated and analyzed separately.

c) #15 was sampled in the clastic ore. The ore itself (#15) is composed of small exfoliated plates and blocks, made of cryptomelane with very little nsutite, packed in a reddish, clayey matrix (#15-III) made of kaolinite and minor gibbsite.

2) A1P 175 profile

#22 was collected in the little indurated ore. The ore (#22) is bluish to black, and is very rich in cryptomelane. Veins of cryptomelane-2 (#22-II) crosscut the platey layering. Lithiophorite has (#22-III) crystallized in the ore cavities.

3) A1P 163 profile

#28 was collected in the clastic ore. It is composed of consolidated, cemented plates (#28), crosscut by a system of small fractures filled by secondary minerals, in which grey-coloured, cryptomelane-2 has been recognized (#28-II).

4) A1P 162 profile

#31 was collected in the poorly consolidated ore. The ore (#31) is blue to blackish, and plates are cemented. Cryptomelane constitutes the main mineral species, and is associated with nsutite. Brown concretions of cryptomelane-2 (#31-II) may also be observed.

5) Samples collected out of the weathering profiles

#32 was sampled at the surface level in the Mn mine and is issued from the clastic ore. The ore (#32) is very rich in cryptomelane. A crosscutting vein of cryptomelane-2 (#32-II), separated from the ore, was also analyzed.

#34 was sampled in a cross-section along a cutting. The sample is blue to grey and belongs to the poorly consolidated ore. Two phases can be distinguished. Both are enriched in cryptomelane, with also nsutite and kaolinite. We only analyzed the whole-ore.

ARTICLE 9

Available online at www.sciencedirect.com
SCIENCE DIRECT
ELSEVIER
Earth and Planetary Science Letters 238 (2005) 172–188
EPSL
www.elsevier.com/locate/epsl

First $^{40}Ar/^{39}Ar$ geochronology of lateritic manganiferous pisolites: Implications for the Palaeogene history of a West African landscape

F. Colin [a,b], A. Beauvais [a,b,*], G. Ruffet [c], O. Hénocque [b]

[a] *I.R.D., UR037, BP A5, 98848 Nouméa, Nouvelle-Calédonie, France*
[b] *CEREGE, UMR 161, BP 80, 13545 Aix-en-Provence Cedex 4, France*
[c] *Géosciences Rennes, CNRS-Université de Rennes 1, Campus de Beaulieu Av. du Général Leclerc, 35042 Rennes Cedex, France*

Received 3 December 2004; received in revised form 14 May 2005; accepted 27 June 2005
Available online 22 August 2005
Editor: E. Boyle

Abstract

A pisolitic superficial formation deriving from the geochemical degradation of a previous massive manganiferous crust has been investigated in West Africa using $^{40}Ar/^{39}Ar$ laser probe analysis on different generations of cryptomelane from Fe–Mn pisolites and their embedding lateritic matrices. Prior to the ^{40}Ar–^{39}Ar geochronological analysis, a detailed petrographical study has allowed the identification of successive assemblages from Mn-pisolites to (Fe,Mn)-pisolites embedded in Mn-rich and Fe-rich matrices, respectively. The age spectra obtained for pisolites, including cores, cortices and matrices enables the definition of three age clusters around 56–59, 44–47, and 24–27 Ma. The first two age clusters with the petrographical and geochemical results obtained on the different assemblages indicate that the development of the pisolitic crust first induced Mn-leaching and Fe-Al accumulations due to warmer and wetter climatic conditions in the age interval 56–47 Ma that characterizes the Tertiary greenhouse effect period propitious to bauxite formation in West Africa. The absence of $^{40}Ar/^{39}Ar$ ages between 44 and 27 Ma only means that geochemical conditions for cryptomelane crystallisation were not fulfilled, but could still be favourable to Fe- and/or Al-oxy-hydroxides formation, before drier climatic conditions became rather effective at the Oligocene period to sustain mechanical erosion rather than chemical weathering processes. The age cluster 24–27 Ma indicates however a reactivation of the manganiferous lateritic weathering late Oligocene. The $^{40}Ar/^{39}Ar$ dating results are discussed in terms of climatic condition changes during the Palaeogene that were favourable to the genesis of either Al- and Fe- or Mn-oxy-hydroxides in the course of development and evolution of the pisolitic formation. The $^{40}Ar/^{39}Ar$ dating also provides a new highlight to large-scale geomorphological patterns of West Africa.

Keywords: $^{40}Ar/^{39}Ar$-geochronology; Cryptomelane; Lateritic pisolites; Paleoclimate; Planation landsurface; Burkina Faso; West Africa

* Corresponding author. I.R.D., UR037, BP A5, 98848 Nouméa, Nouvelle-Calédonie, France. Tel.: +33 687 26 07 59; fax: +33 687 26 07 69.
E-mail address: Anicet.Beauvais@noumea.ird.nc (A. Beauvais).

0012-821X/$ - see front matter © 2005 Elsevier B.V. All rights reserved.
doi:10.1016/j.epsl.2005.06.052

1. Introduction

Since Cretaceous, rocks of tropical shields have been weathered under the effect of chemical and physical earth surface processes, into more or less dissected thick lateritic weathering mantles including at their top either aluminous, ferruginous, or manganiferous crusts [1,2]. These crusts often evolved under the influence of chemical and physical degradation processes into a pebbly layer essentially made up of nodules and/or pisolites embedded in a lateritic matrix [3–5]. In tropical areas, the lateritic weathering mantles capped with such crusts may constitute a long record of the past climatic conditions [6–9]. Age and dynamics of lateritic weathering systems and associated landforms are poorly known. Direct dating of weathering events remains thus a very tough issue for research devoted to the knowledge of long-term evolution of tropical landscapes. We propose to investigate a pisolitic superficial formation developed over a massive manganiferous crust, (*i*) by providing detailed petrographical observations and geochemical analyses of the different facies of that formation, and (*ii*) by performing $^{40}Ar/^{39}Ar$ laser probe and step heating analyses on different generations of cryptomelane identified in those facies. The main purpose of such investigations is first and foremost to constrain the age of weathering profiles and associated lateritic landsurfaces, in relation with specific paleoclimates. We will also discuss the spatial and temporal geomorphologic relations with the other lateritic formations capping stepped landsurfaces of the region, e.g., bauxites, and the Paleogene climatic changes suggested by our dating results.

Cryptomelane is a ubiquitous mineral of lateritic manganese weathering mantles and associated manganese crusts with concretionary or massive structures that can be sometimes pisolitic [10–13]. Absolute dating of cryptomelane of lateritic manganese ore deposits is an important scientific issue because it would allow constraining stages of past climatic changes from the knowledge of "weathering timescales" [8,14]. Pisolitic layers in tropical soil sequences are the product of the near-surface geochemical and structural degradation of massive lateritic crusts [3,4], which occurs under the effect of climatic condition changes. Detailed geochemical investigations on these superficial materials are as

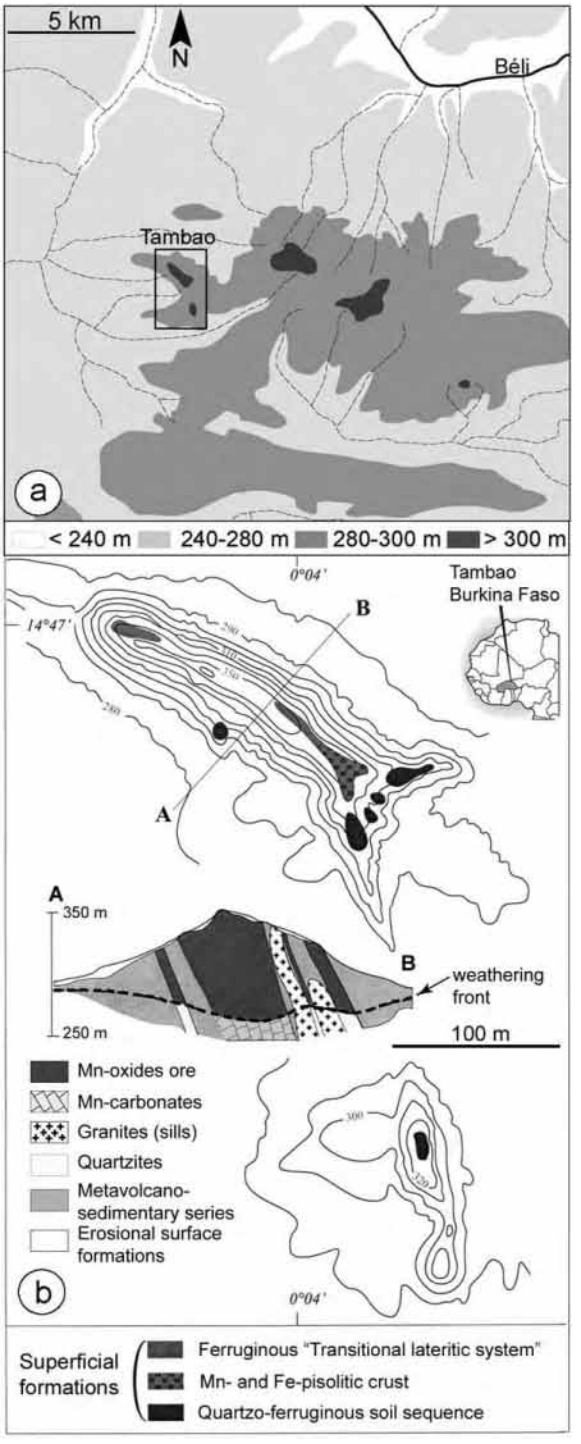

Fig. 1. *(a)* Location and geomorphologic patterns of the Mn-rich formations of the tambao Manganese ore deposit with *(b)* a section (A–B) across the main geological formations.

useful for the understanding of environmental changes as the study of the underlying massive lateritic crusts. $^{40}Ar/^{39}Ar$ laser probe analysis performed on cryptomelane-rich pisolites constitute an essential research issue for a best understanding of the geochemistry and the enrichment of manganese in lateritic weathering environments, and subsequently, the dynamics of Fe-laterites associated to the Mn-ore deposits throughout the tropical climatic belt.

Today, one of the most efficient dating techniques is $^{40}Ar/^{39}Ar$ laser-probe and step heating of K-bearing Mn^{4+}-oxyhydroxides found as cryptomelane [8]. This Mn-oxide is the K-rich end-member of the hollandite group ($X(Mn^{4+}Mn^{2+})_8O_{16}$-(X-Ba, K, Na, Pb)) minerals, the tunnel structure of which incorporating large cations as K^+, Ba^{2+}, Pb^{2+}, or Na^+ [15–18]. The first K-Ar and conventional $^{40}Ar/^{39}Ar$ dating experiments indicated that the cryptomelane structure is able to retain radiogenic argon [6,19–22]. Recent developments of the $^{40}Ar/^{39}Ar$ laser probe method stimulate new interest in geochronological studies of cryptomelane, this technique being very appropriate to study small volumes of sample that can be extracted from the host rock to ensure optimum conditions for analysis [8,23,24]. The very small amount of material required by the actual technique implies a very fine scale sampling in order to analyse distinct generations of cryptomelane with reduced mixing problems [25]. The improved technique is well adapted to analyse cryptomelane extracted from pisolite banded-structures. $^{40}Ar/^{39}Ar$ dating results have been thus obtained, for the first time in Africa, on different pisolitic crust facies collected at the Tambao manganese deposit, Burkina Faso (Fig. 1), which is one of the most cryptomelane-rich manganese ore deposits known in the world [11].

2. Geological setting

The manganese ore deposit of Tambao (14°47′N – 0°4′E, northern Burkina Faso) is located in the Subsahelian zone, hosting a high-grade manganese ore reserve of about 15 Mt, which is distributed in four sub-vertical massive supergene manganese oxide layers exposed on two hills (Fig. 1b). Mn-oxide layers alternate with deeply weathered Birimian metamorphic volcanic and sedimentary series composed of manganese carbonate rocks (mainly rich in rhodochrosite), tuffs and spessartine-bearing quartzite. About 75% of the manganese oxide ore is the product of in situ weathering of the rhodochrosite-rich metasedimentary beds, observed in drill cores [26]. The rest is derived from spessartine-rich quartzites, which were described by Perseil and Grandin [11,27]. The weathering profile is about 70 m thick and it is developed at the expense of the Birimian rocks and granitic sills. The lateritic soil sequence is overlain by a fragmented pisolitic crust, which can be observed between 320 and 340 m in altitude (Fig. 1b).

3. Geomorphologic issue

Various stages of large scale morphogenesis in inter tropical Africa have been characterized by successive episodes of lateritic weathering with differentiated types of more or less indurated crusts capping different stepped landsurfaces [2,28–31]. Bauxites are generally attributed to the Cretaceous–Eocene period and they occupy the highest elevations that correspond to the so-called “African landsurface”. In contrast, younger landsurfaces bearing quartz-rich ferricretes stand at lower elevations, and they were considered to having been formed during the Miocene and throughout the Pliocene and Quaternary [2,32,33]. A singular landsurface bearing quartz-poor ferricretes was also described as a distinct geomorphological level stepped in between the landsurfaces bearing bauxites and quartz-rich ferricretes in many African countries [3,28,29]; it was named “transitional lateritic system” by Grandin [29]. This author proposed that the successive stepped landsurfaces reflected successions of wet and dry climates on the basis of previous geomorphologic studies [28,34]. Boulangé [3] suggested however that a genetic relationship could exist between the bauxite of the “African landsurface” and the ferricrete of the “transitional lateritic system”. It is interesting to note that the highest Fe-Mn pisolitic crust of the larger hill at the Tambao Mn-ore deposit stands at the same elevation as some regional relics of the “transitional lateritic system”. Based on sole geomorphologic observations the Tambao landsurface bearing the pisolitic material can be correlated either to the “African landsurface”, if bauxite and quartz-poor ferricretes of the “transitional

lateritic system" are cogenetic [3], or to a younger landsurface in the hypothesis of a "transitional lateritic system" disconnected from the bauxitic "African landsurface" [29]. A detailed petrographical and $^{40}Ar/^{39}Ar$ geochronological study of the pisolitic lateritic material covering a relic of such a landsurface may provide very significant information about its origin and its genetic relation with the underlying Mn-crust, but also with the Al - and Fe-lateritic materials capping the other stepped lateritic landsurfaces.

4. Method and analytical techniques

4.1. Petrographic, mineralogical and geochemical analysis

Seven samples were collected from the upper surface pisolitic crust of the main hill at the Tambao deposit. Thin sections were made from the collected samples. The mineralogical study of pisolites and surrounding matrix was carried out using optical microscopy performed on a Leica DMRXP microscope, X-ray diffraction using a Philips PW 1710 diffractometer with a Co-tube anode ($k\alpha1 = 1.78896$; $k\alpha2 = 1.79285$), and scanning electron microscopy (Philips 515 coupled to Edax EDX semi quantitative analyzer). Electron microprobe analyses were obtained on minerals identified on thin sections, using a CAMEBAX microprobe set (15 kV, 20 mA, 1μm size diameter). ICP-OES analyses were also obtained on bulk rock samples, and also on matrix and pisolite separates.

4.2. $^{40}Ar/^{39}Ar$ laser probe analysis

Twenty-one sub-millimetric fragments were extracted from thin slabs, 0.5 mm thick, they were

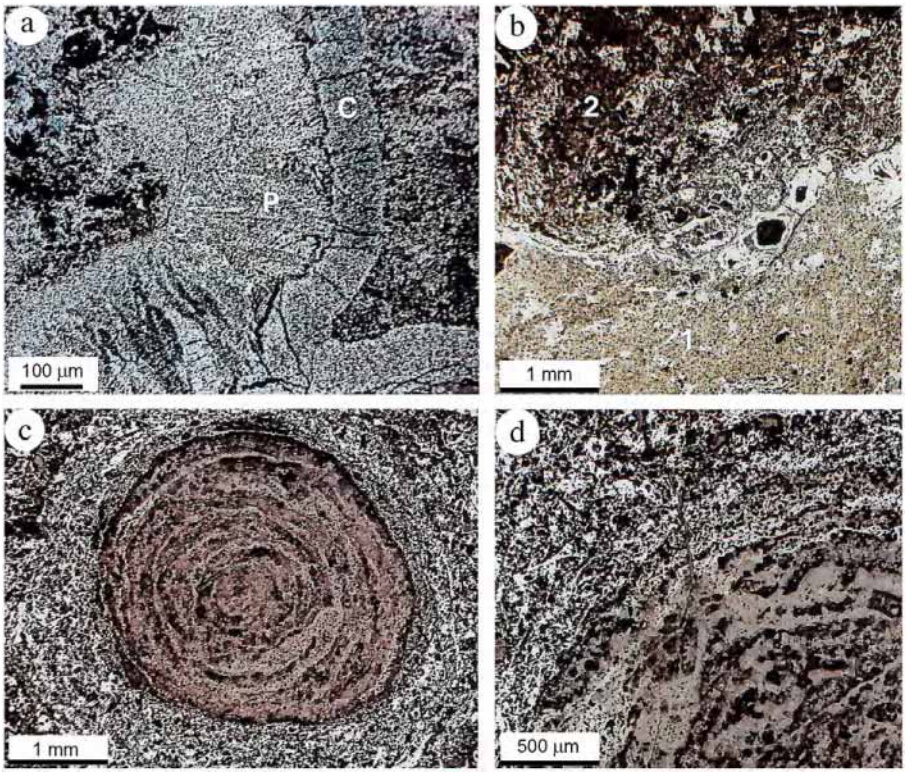

Fig. 2. Photomicrographs of *(a)* the cryptomelane (C)-pyrolusite (P) paragenesis in the massive ore, *(b)* the transition between massive ore (1) and Mn-matrix (2) of the pisolitic crust, *(c)* a detail of the transition between pisolite and Mn-matrix, and *(d)* cryptomelane concentration around pisolite.

Table 1
ICP analytical data obtained on (a) whole (b) massive and pisolitic ore samples and on (c) matrices and (d) pisolites separates

#	Weight %												ppm				
	n	SiO_2	Al_2O_3	Fe_2O_3	MnO	MgO	CaO	Na_2O	K_2O	TiO_2	P_2O_5	LOI	Total	Ba	Cr	Zn	Zr	Sr
a																		
190	2	0.955	2.51	2.15	81.43	0.39	0.2	0.1	0.71	0.13	0.21	10.54	99.305	1714	21	166	40	259
106	1	6.12	5.35	3.26	65.15	0.11	0.46	0.32	5.52	0.56	0.5	13.47	100.82	1280	18	283	112	632
107	1	3.81	3.31	1.87	66.52	0.71	0.72	0.38	2.34	0.19	0.13	14	93.98	2571	20	142	20	358
b																		
Col6	1	4.89	19.45	13.99	30.5	0.83	0.8	0.09	3.09	1.07	0.67	17.36	92.73	3670	–	–	340	940
Col8	1	13.77	25.28	2.26	34.75	0.44	0.22	0.08	3.2	0.58	0.25	17.46	98.25	5280	–	–	160	835
Col9	1	16.05	20	0.97	42.1	0.46	0.19	0.1	3.52	0.36	0.24	15.15	99.1	1830	–	–	80	865
168	2	15.35	16.07	1.375	47.01	0.29	0.34	0.14	1.96	0.39	0.07	14.01	96.99	1755	42	174	116	893
169	1	20.60	23.79	13.62	21.24	0.18	0.50	0.43	1.32	0.90	0.22	11.77	94.57	5703	211	140	280	640
170	1	13.17	30.67	10.56	23.72	0.42	0.66	0.10	1.27	1.11	0.18	17.66	99.52	3120	180	138	390	589
171	1	16.54	21.53	2.32	38.86	0.14	0.40	0.09	2.19	0.70	0.11	14.60	97.48	2774	40	192	198	705
172	2	13.96	26.14	13.81	23.74	0.64	0.52	0.06	0.87	0.85	0.2	16.99	97.76	2100	417	108	295	311
173	1	6.30	25.82	7.75	35.22	0.11	0.38	0.20	2.18	1.15	0.11	18.58	97.80	8085	72	54	371	395
189	2	11.03	14.2	1.545	52.61	0.32	0.39	0.11	2.21	0.68	0.12	14.69	97.895	3504	30	137	247	639
190	2	5.18	8.48	2.685	67.3	0.37	0.2	0.16	1.62	0.4	0.16	13.3	99.835	4977	27	130	113	340
700	1	19.05	23.86	6.67	31.25	0.20	0.56	0.12	1.42	0.89	0.18	14.77	98.97	5459	148	119	248	721
701	1	18.65	21.17	3.53	37.69	0.22	0.55	0.08	1.61	0.78	0.14	14.60	99.02	7061	73	147	203	934
702	1	14.22	26.95	10.05	30.08	0.18	0.41	0.06	1.55	1.07	0.12	14.88	99.57	5968	159	160	247	756
703	1	19.83	28.62	4.69	27.22	0.20	0.60	0.08	1.52	0.91	0.32	15.52	99.51	3660	63	132	287	694
704	1	24.25	22.32	1.96	33.53	0.16	0.43	0.07	1.60	0.65	0.14	14.24	99.35	29	46	152	175	837
705	1	19.30	19.00	1.97	41.17	0.10	0.21	0.14	1.79	0.62	0.12	14.79	99.21	3124	42	145	168	778
706	1	19.42	24.34	5.43	32.14	0.11	0.21	0.08	1.31	1.10	0.13	14.31	98.58	14 260	64	173	300	1175
c																		
189	2	9.545	12.8	1.38	55.96	0.37	0.4	0.16	2.66	0.76	0.09	14.45	98.54	3488	26	137	276	665
706-1	1	18.85	21.6	3.9	37.56	0.11	0.22	0.8	1.43	1	0.12	14.9	99.77	16 624	63	195	242	1049
705	1	21.32	24.31	1.92	34.18	0.09	0.18	0.14	1.91	0.77	0.1	14.52	99.44	1050	60	136	216	520
171	1	21.35	23.91	1.69	33.05	0.12	0.21	0.12	2.1	0.75	0.06	13.95	97.31	609	70	163	183	368
704	1	21.86	27.93	1.42	31.45	0.12	0.24	0.18	1.87	0.72	0.1	13.81	99.7	664	26	153	193	521
701	1	17.4	31.42	6.32	25.86	0.12	0.25	0.07	1.39	0.98	0.13	15.54	99.48	3785	158	106	247	470
700	1	21.63	30.7	3.57	24.38	0.14	0.33	0.08	1.48	1.03	0.13	15.15	98.62	2559	77	142	254	496
169-1	1	20	23.82	14.97	21.81	0.16	0.4	0.08	1.4	0.83	0.33	14.31	97.98	4336	274	138	246	539
172	2	15.2	31.24	12.01	21.23	0.36	0.38	0.35	1.01	0.66	0.52	15.79	98.72	3270	367	109	375	660
702	1	14.24	32.95	15.3	17.11	0.29	0.37	0.08	0.82	1.38	0.5	16.96	100	2277	222	98	398	448
173-2	1	9.07	40.32	14.35	12.02	0.13	0.14	0.1	0.6	1.52	0.17	21.82	100.24	1562	159	31	458	136
169-2	1	17.95	33.92	18.07	9.31	0.22	0.56	0.16	0.69	1.23	0.35	16.2	98.66	1648	308	88	475	314
706-2	1	27.46	39.38	11.42	3.62	0.11	0.15	0.07	0.18	1.78	0.16	15.8	100.13	1068	390	44	448	94
d																		
168	2	11.51	14.48	1.88	52.25	0.37	0.56	0.09	2.19	0.42	0.06	14.57	98.385	2552	33	193	123	979
169	2	22.98	24.91	5.835	27.29	0.25	0.64	0.49	1.01	0.75	0.37	14.97	99.47	6471	135	105	270	618
170	2	13.72	18.68	4.235	42.23	0.71	0.93	0.55	1.81	0.77	0.35	15.75	99.72	5551	65	201	293	1052
171	2	16.06	19.33	2.345	42.07	0.34	0.52	0.09	1.43	0.63	0.14	15.49	98.405	4624	30	167	198	737
172	2	15.17	23.64	4.405	35.78	0.4	0.5	0.1	1.66	0.83	0.12	16.56	99.145	4868	60	168	295	672
173	2	1.94	20.38	2.70	41.92	0.20	0.16	0.08	1.86	0.78	0.10	18.86	88.95	5793	28	48	280	310
700	1	16.59	20.63	2.69	40.16	0.21	0.70	0.12	1.58	0.68	0.15	15.05	98.56	7494	31	108	175	918
701	1	14.51	19.61	2.17	42.55	0.18	0.40	0.06	1.53	0.65	0.12	15.51	97.29	7017	36	161	158	973
702	1	11.09	22.35	5.03	40.63	0.24	0.50	0.07	1.73	0.81	0.38	16.29	99.12	7763	41	207	302	959
703	1	14.83	18.16	3.08	43.54	0.20	0.86	0.09	2.20	0.66	0.38	14.50	98.5	3776	36	138	207	1152
704	1	16.93	20.92	2.33	41.39	0.18	0.61	0.13	1.38	0.66	0.17	14.91	99.61	2878	26	149	160	844

Table 1 (*continued*)

#	Weight %												ppm				
	n	SiO_2	Al_2O_3	Fe_2O_3	MnO	MgO	CaO	Na_2O	K_2O	TiO_2	P_2O_5	LOI	Total	Ba	Cr	Zn	Zr	Sr
705	1	14.95	18.11	2.29	47.92	0.11	0.24	0.12	1.76	0.61	0.14	14.28	100.53	4412	37	160	186	893
706	1	18.25	20.42	5.00	37.16	0.11	0.23	0.14	1.45	1.06	0.12	14.89	98.83	15 190	61	186	263	1408

=Sample name; *n*=number of analyses. When duplicated analyses were performed (*n* = 2), mean values were reported.

cut facing the petrographical thin sections, using a 250μm thick saw that allows a carefull control of the exact positions of the extracted fragments within the matrices and the cortices of pisolites. The samples were wrapped in Al-foil. These Al-packets were stacked to form a column within which packets of monitor samples were inserted every 8 to 10 samples. This distribution allows precise determination of the vertical flux gradient during irradiation with errors as low as ±0.2%. All the samples were irradiated in the 5C position of the McMaster reactor (Hamilton, Canada) together with amphibole monitor Zartman Hb3gr [35–37] (1072 Ma), for various durations.

^{40}Ar–^{39}Ar analyses were performed by step heating experiments on single grains with a laser-probe using a Coherent Innova® 70-4 continuous argon-ion laser with a maximum output power of 6 W in multiline mode [38]. The laser beam was defocused through an optical system onto a sample located in a UHV sample chamber, i.e., a copper sample-holder, beneath a Pyrex window, in a stainless steel chamber. Each laser experiment lasted 3 min, including 1 min for the laser heating of the sample. The laser beam was at least 2.5 times greater than the sample size, in order to obtain a homogeneous temperature over the entire grain. The temperature is not known but observing the heated mineral with a binocular microscope coupled with a video color camera and a high-resolution video recorder warrants its homogeneity. Fusion of the mineral was achieved by sharply focusing the laser spot onto the grain. The isotopic composition of argon was analyzed using a mass spectrometer (VG® 3600) working with a Daly® detector. Static measurements of argon isotopes correspond to 11 peak hopping scans. Backgrounds of the extraction and purification line were measured every first or third step and subtracted from each argon isotope from the subsequent gas fractions. Typical blank values were in the ranges $3.2\times10^{12}<M/e40<4.8\times10^{-13}$, $7.4\times10^{-14}<M/e39<4.6\times10^{-15}$, $6.6\times10^{-14}<M/e38<3.5\times10^{-16}$, $1.3\times10^{13}<M/e37<1.7\times10^{-14}$ and $7.6\times10^{-14}<M/e36<2.1\times10^{-15}$ cm^3 STP. All isotopic measurements were corrected for K, Ca and Cl isotopic interferences, mass discrimination and atmospheric argon contamination. The date is calculated using the decay constants recommended by Steiger and Jäger [39]. All errors are quoted at the 1σ level and do not include the error on the $^{40}Ar^*/^{39}Ar_K$ ratio and age of the monitor. The error on the $^{40}Ar^*/^{39}Ar_K$ ratio of the monitor is included in the calculation of the plateau age error. To define a plateau age, at least three consecutive steps are needed, corresponding to a minimum of 60% of the total ^{39}Ar released, and the individual fraction ages must agree within 2σ error bars with the "integrated" age of the plateau segment. The term "pseudo-plateau" was applied, each time less than 60% of ^{39}Ar degassing or when one of the other criteria was not strictly fulfilled.

5. Results and discussion

5.1. Petrographical, mineralogical and geochemical patterns

Samples typically contain large quantities, >50% of the bulk volume, of well-developed concentric pisolites with diameters ranging between 2 and 7 mm. These pisolites are either still attached to the compact Mn-pisolitic crust or loose and embedded in matrices of variable colours, grey-black, pink and brown, both deriving from the superficial evolution of the underlying massive Mn-crust. The different colours of matrices correspond to different chemical and mineralogical compositions, manganiferous, kaolinitic and ferruginous, and even gibbsitic, according to an increasing degree of lateritic weathering.

The massive Mn-crust consists of cryptomelane and pyrolusite, which has also been petrographically detected in a sample at the interface between the Mn-pisolitic crust and the massive oxide ore (Fig. 2a). That is confirmed by a very low K_2O content of the pyrolusite-bearing sample with respect to the other massive ore samples (BF96-190; Table 1a). Pisolites consist of kaolinite and cryptomelane in concentric banded structure (Figs. 2c,d and 3). This chemical and mineralogical pattern also occurs in the matrix at the transition with the massive Mn-crust (Fig. 2b). Pisolites have Al and Mn contents ranging from 15% to 25% of Al_2O_3 and from 22% to 50% of MnO (Table 1d and Fig. 4a). These chemical variations reflect progressive manganese leaching, which is higher in matrices than in pisolites (Fig. 4). Potassium is partly leached, as shown by K_2O weight percent contents ranging from 5.5% in the massive ore to 0.87% in the most depleted pisolitic samples and even less in the matrix and pisolite separates (Table 1 and Fig. 4b).

The transformation of the massive ore into a pisolitic crust results thus in Mn- and K-leaching, formation of kaolinite, and an increase of porosity (Figs. 2b and 4b). The good correlation observed between K_2O and MnO contents, in the course of manganese leaching within pisolites and matrices (Fig. 4b), suggests however that cryptomelane is the most abundant Mn-oxide, as confirmed by SEM observations (Fig. 3). Unlike pisolites, the embedding matrices are highly affected by manganese leaching (Fig. 4a and b), which is associated with the formation of kaolinite (Fig. 3), hematite and goethite in successive stages (Figs. 4a and 5). Small manganiferous domains can also be preserved even in strongly Mn-leached matrices (Table 1c).

In a first weathering stage, the leaching of manganese and consecutive formations of kaolinite and iron oxides in matrices are the result of an increase in lateritic weathering, characterized by Fe_2O_3 contents ranging from 11.4 to 18 wt.% (Table 1c; samples 169-1 to 706-2). Such enrichment is not so important in pisolites (Table 1d and Fig. 4a).

The late weathering stage is characterized by an absolute enrichment of Al_2O_3 (Fig. 4a), which reaches 40.3% in the matrices and 24.9% in the pisolites (Table 1c and d). The relative geometry of secondary cryptomelane and gibbsite crystallisations with respect to the matrix porosity in Fig. 5a and b, suggests that the Al-hydroxide appears after Mn-leaching from the cryptomelane that effectively creates the large porosity into which secondary gibbsite can lately crystallize. Cryptomelane precipitations with partial dissolution features are effectively observed on the inner edges of pores of the kaolinitic and ferruginous matrices (Fig. 5b), in which Mn–Fe cutanes indicate short distance chemical transfers (Fig. 5d). The gibbsite and iron-gibbsite absolute accumulations mainly occur in Mn-leached domains of the kaolinite and goethite-rich matrices and of manganese pisolites (Fig. 5c). Gibbsite crystallizes from previous kaolinite rich matrices that indicate an autochthonous origin of Al (Fig. 5a), but such a mechanism is limited with respect to the Al-absolute enrichment reflected by the secondary gibbsite filling the matrix porosity (Fig. 5a, c and d).

The complexity of the internal structure of pisolites reflects the occurrence of contrasted geochemical dissolution and accumulation cycles of Mn-, Fe- and Al-oxy-hydroxides, respectively, as previously reported by Beauvais and Nahon [4] from samples collected at Moanda (Gabon) and Ziémougoula (Ivory Coast). The $^{40}Ar/^{39}Ar$ dating measure of cryptomelane crystallisations preceding and following the secondary development of gibbsite and Fe-oxihydroxides is thus of prime importance to understand the evolution of the pisolitic crust itself but also to define its temporal relation with the other lateritic formations, e.g., bauxites and 'transitional ferruginous system', which were developed in or nearby our study area. The petrographical observations suggest however a transition between humid and more contrasted climatic conditions during which pisolites and a Fe–Mn matrix are formed from the geochemical degradation of a previous massive Mn-crust. Humid and well-drained conditions are effectively required for manganese leaching and accumulation of Si, Al, Fe, to form kaolinite, Fe- and Al-oxy-hydroxides successively (Fig. 4a).

5.2. $^{40}Ar/^{39}Ar$-dating results

$^{40}Ar/^{39}Ar$ laser-probe dating was experimented on twenty-one fragments extracted from different pisolitic facies. Five experiments were performed on submillimetric fragments of matrices and twelve experi-

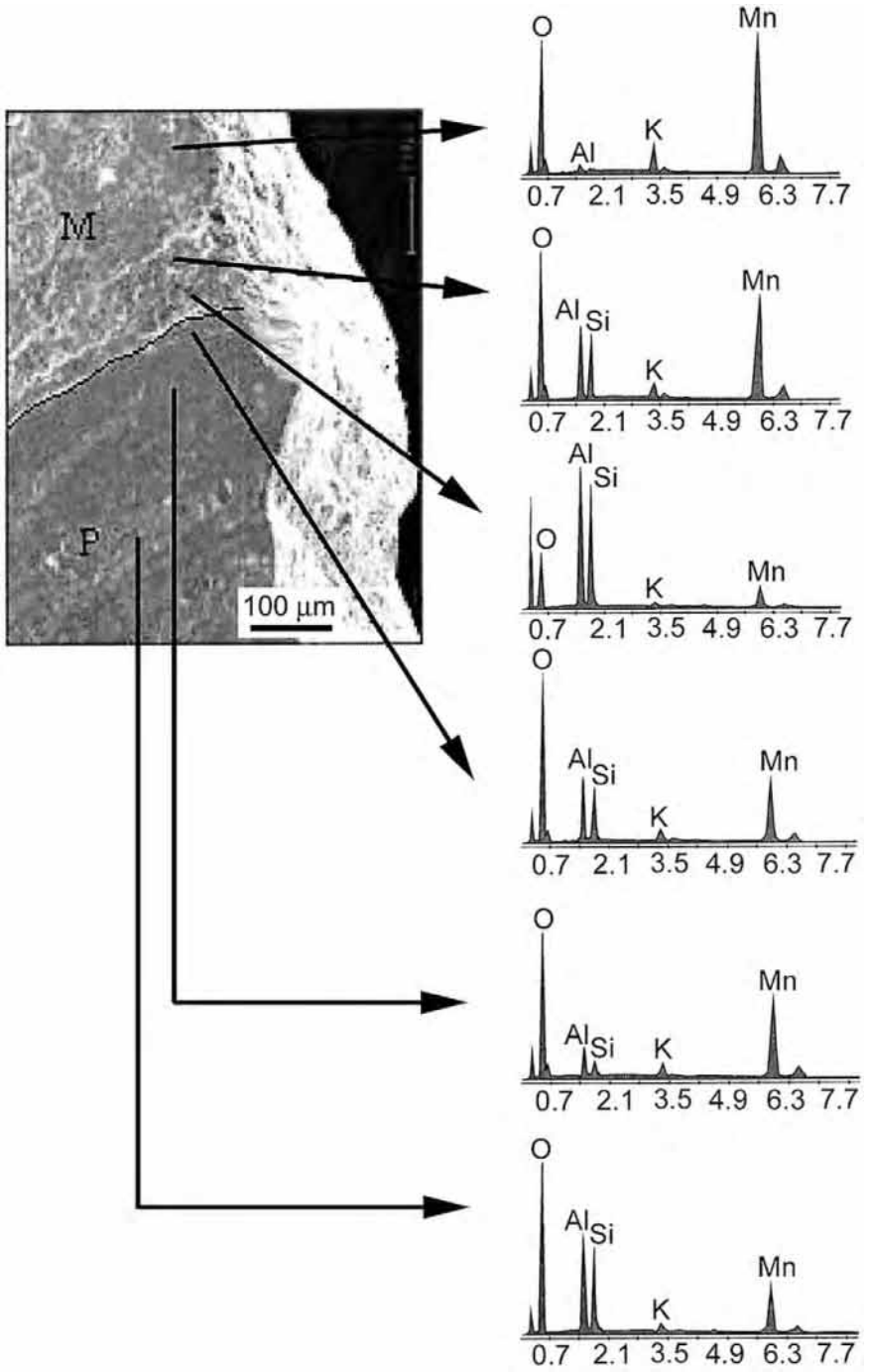

Fig. 3. SEM observation of the transition between pisolite and Mn-matrix with associated EDX analyses showing the geochemical spatial distribution of kaolinite (Si, Al) and cryptomelane (K, Mn).

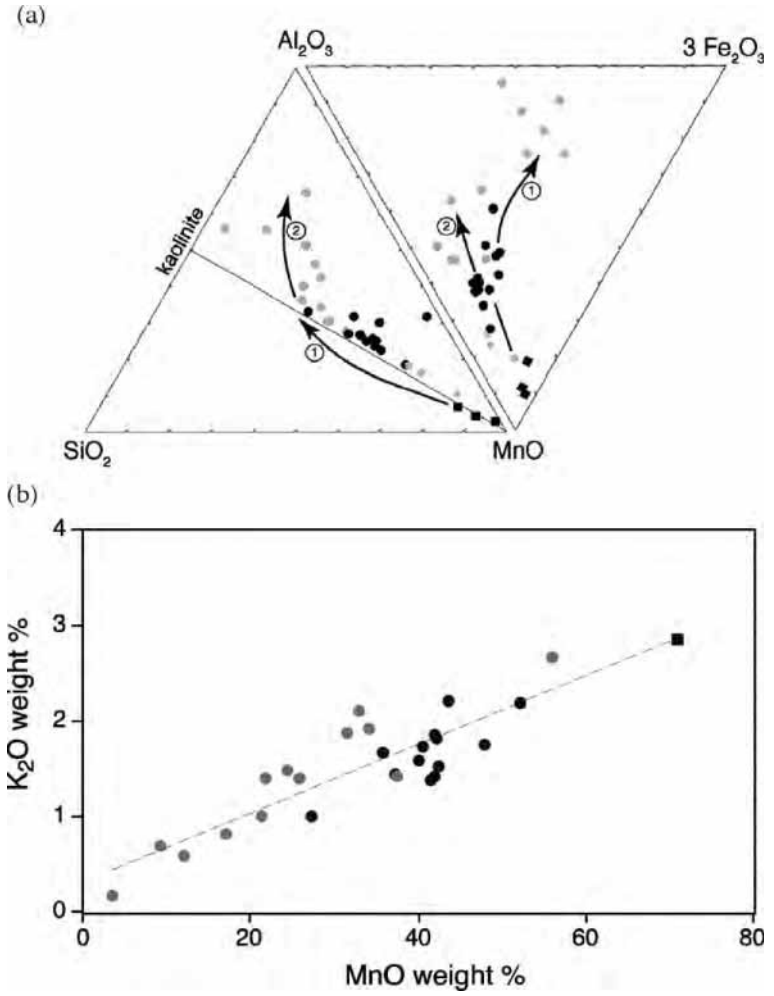

Fig. 4. Geochemical evolution from the massive ore to pisolitic facies. *(a)* Ternary diagrams of Al_2O_3 wt.%-SiO_2 wt.%-MnO wt.%, and Al_2O_3 wt.%-MnO wt.%-3 Fe_2O_3 w.t% (the arrows indicate (1) Mn-leaching with kaolinite and Fe_2O_3 enrichments, and (2) absolute Al_2O_3 accumulation). *(b)* Binary plot of K_2O wt.% vs. MnO wt.%. (Black squares=massive ore; grey stars=transition facies; black circles=pisolite facies; grey circles=matrix facies).

ments on fragments of pisolites. These analyses were complemented by four experiments on Mn-cutan fragments, one experiment on a manganese nodule of the Fe-pisolitic crust and another one on a massive ore sample collected just at the interface between the massive ore and the pisolitic crust. See Table 2 in the *EPSL Online Background Dataset*[1] for ^{40}Ar-^{39}Ar analytical data of each sample step heating.

[1] http://www.elsevier.nl/locate/epsl.

5.2.1. Pisolites core and pisolitic Mn-crust fragments

Age spectra have been obtained on pisolite fragments (BF96-168-4-a and BF96-168-1) from the Mn-pisolitic crust, and on a Mn-glaebular nodule (BF96-172-1) from the Fe-pisolitic crust (Fig. 6). Age spectra have a staircase-shape with (*i*) low ages in the low temperature steps, that define only a weak cluster in the range 21–26 Ma, and (*ii*) rather flat age segments, sometimes slightly hump-shaped, in the intermediate to high temperature steps with relatively concordant apparent ages in the range 56–59 Ma. The very slight

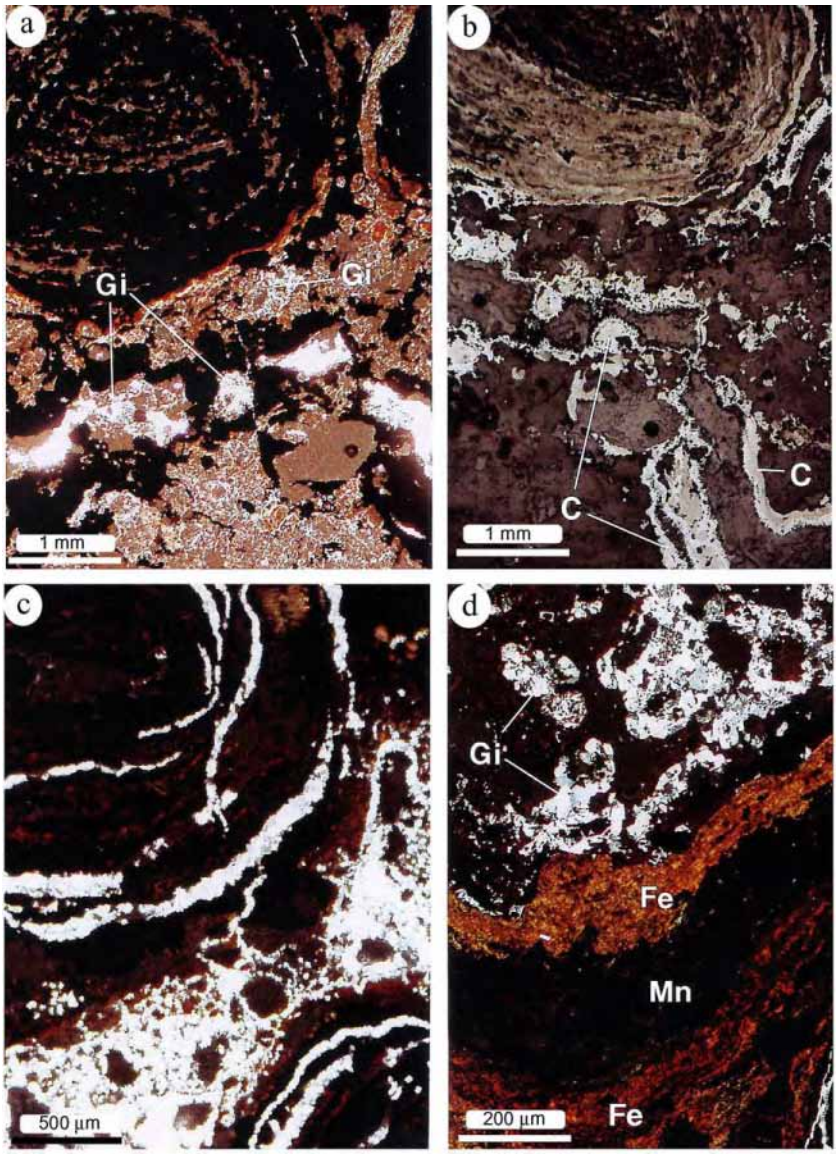

Fig. 5. Photomicrographs of *(a)* gibbsite crystallizations (Gi) in the porosity of the Al-pisolitic crust, *(b)* cryptomelane crystallizations (C) observed under reflected light of (a), *(c)* secondary gibbsite crystallisations in the Mn-leaching created-porosity of pisolite and matrix of the Fe-pisolitic crust, *(d)* secondary gibbsite crystallisations (Gi) and Fe–Mn cutanes (Fe and Mn) at the transition between matrix and pisolite of the Fe-pisolitic crust.

hump-shape of the age spectrum obtained for the glaebular nodule (BF96-172-1) allows definition of a plateau age at 58.6 ± 0.2 Ma, with 61.8% of the ^{39}Ar released (Fig. 6). This plateau age and the apparent age frequency peak at 56–59 Ma coincide with a pseudo-plateau age of 59.0 ± 0.1 Ma, with 45% of the total ^{39}Ar released, measured for a fragment of cryptomelane collected at the interface between the massive oxide ore and the Mn-pisolitic crust (Fig. 6; BF96-190).

Pisolite cores from the same pisolitic crust display rather well clustered apparent ages in the range 56–59 Ma. The slight humps observed on some samples (Fig. 6; BF96-168-4-a and BF96-168-1) could suggest some ^{39}Ar recoil, the age maxima around 61–62 Ma

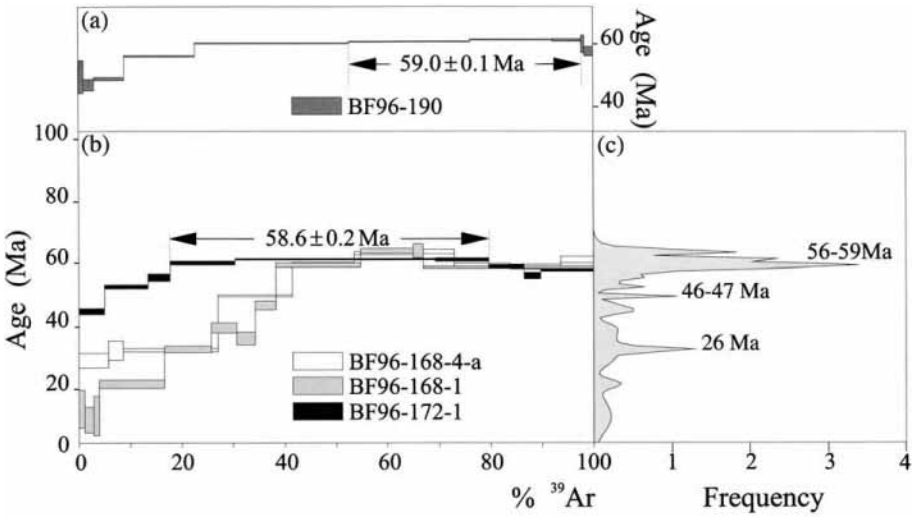

Fig. 6. $^{40}Ar/^{39}Ar$-spectra of cryptomelanes extracted from *(a)* the interface between massive ore and pisolitic crust and *(b)* sub-fragments of pisolites, with *(c)* the resulting age frequency diagram.

being analytical artefacts [40]. The 56–59 Ma ages are concordant with two-pseudo plateau ages obtained on the cryptomelane fragment at the interface between the massive oxide ore and the Mn-pisolitic crust (Fig. 6). The low-temperature steps from this last sample show clear evidence for a weathering event with an age around 46–47 Ma consistent with the formation process of such a pisolitic system, as supported by the petrographical study. The matrix is continuously transformed during the progressive development of pisolites. The disturbance can be associated with the growth of new and younger oxide generations. The oldest ages are thus coherently obtained for Mn-cores of pisolites and for massive ore samples, whereas the youngest ages characterise the Mn-matrices and the outermost rims of pisolites.

5.2.2. Matrices and external pisolite rims

Most of the age spectra obtained for Mn-matrix samples (3 of 4 samples; BF96-168-5-c, COL9-b-1,-b-2,-b-3) are characterized by a staircase-shape with low apparent ages in the low temperature steps for 10% to 15% of the ^{39}Ar released, which are concordant around 24–27 Ma as shown clearly by the frequency peak of apparent ages (Fig. 7). Rather flat age segments, in the intermediate to high temperature steps, converge unequivocally in the 44–47 Ma range. An external rim fragment, extracted from a pisolite of the Mn-pisolitic crust (BF96-168-6) provided a pseudo-plateau age at 46.6 ± 0.1 Ma, with 51% of the ^{39}Ar released (Fig. 7).

The systematic staircase shape of the age spectra displayed by matrix samples may result from partial losses of radiogenic argon as a consequence of either a thermal geological event or an increase in temperature during irradiation [41]. The first possibility is extremely unlikely in supergene geological context [42], and the second is not in agreement with the fact that all samples irradiated at distinct durations, 5, 25 and 70 h, show similar staircase age spectra (Fig. 7). The age spectra shapes are also quite reproducible for fragments of distinct samples from the Mn-pisolitic crust (Fig. 7). On the basis of $^{39}Ar_K$ recoil studies, some authors have obtained age spectra with staircase shapes for cryptocrystalline materials, e.g., glaucony [43–45]. The occurrence of recoil effect for well-crystallized cryptomelane samples is however unlikely considering the high density of this mineral ($d=4.3$) and its rather sizeable thickness [25]. During the pisolite formation and evolution, the cryptomelane K-Ar system could however be disturbed by secondary dissolution-reprecipitation processes with either a remobilization of the low energy sites, i.e., partial dissolution of the "inherited" crystal structure, and-or a crystallization of a new cryptomelane genera-

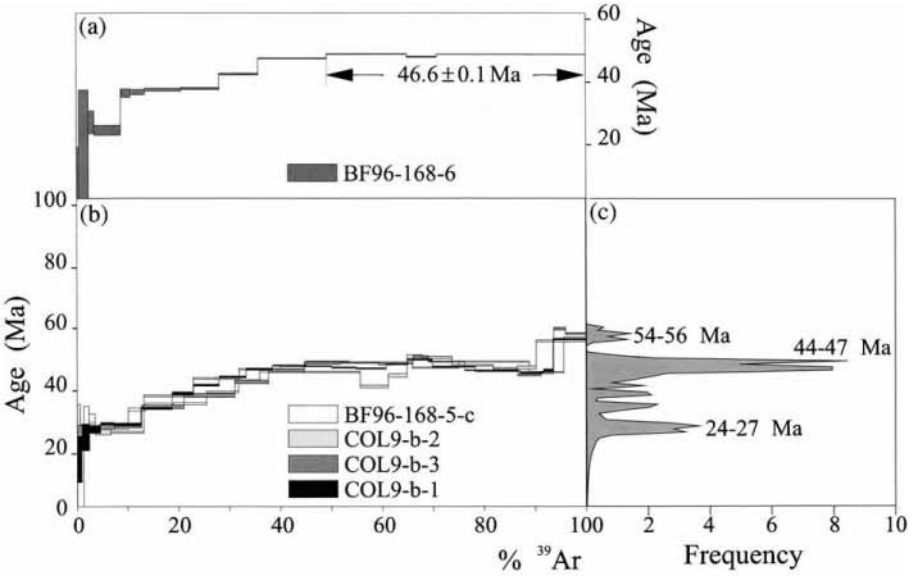

Fig. 7. $^{40}Ar/^{39}Ar$-spectra of cryptomelanes extracted from *(a)* pisolite outer rim and *(b)* sub-fragments of Mn-matrix, with *(c)* the resulting age frequency diagram.

tion. The concordant apparent ages around 24–27 Ma observed in the low temperature steps of Mn-matrix samples with a well defined frequency peak in the apparent age frequency diagram (Fig. 7), may characterise a quite significant weathering event. The frequency peak of apparent ages at 44–47 Ma for the Mn-matrix samples is also in good agreement with the pseudo-plateau age of the external rim of the pisolite at 46.6 ± 0.1 Ma (Fig. 7), thus constraining the age of the Mn-matrix formation.

5.2.3. Mn-cutans

The Mn-cutan age spectra are very different from the age spectra, obtained for matrices and pisolite fragments, as they are characterized by a rapid increase of apparent ages in the first 20% of ^{39}Ar released followed by a decrease of apparent ages defined by a saddle shape in the medium to high temperature steps (Fig. 8). The saddle minima range between 50 and 54 Ma with a pseudo plateau age for one sample (BF96-172-3-b2) with 24% of ^{39}Ar released at 50.2 ± 0.1 Ma (Fig. 8).

Apparent age decreases observed in intermediate to high temperature steps (Fig. 8), suggest $^{39}Ar_K$ recoil as first described by [46]. Such spectrum shape was previously observed during $^{40}Ar/^{39}Ar$ analyses of mixtures of different cryptomelane generations [24,25]. In the present case, $^{39}Ar_K$ recoil is probably due to poorly crystalline cryptomelane of Mn-cutanes, which are rather small, 1μm thick, and intergrowths with iron oxides and clay minerals. The apparent low ages in the low temperature steps balance the high ages in the intermediate temperature steps. It implies that the minimum age of the decreasing segment is the maximum estimate of the true age of the sample, at ca. 50 Ma as suggested by (*i*) the very flat segment observed in sample BF96-172-3-b-2, and (*ii*) the higher saddle minima displayed by samples with a further pronounced staircase shape, e.g., 52.9 Ma for sample BF96-172-3-a or 53.8 Ma for sample BF96-172-3-c (Fig. 8). These results support the idea developed by Hénocque et al. [25] that phase mixtures can induce $^{39}Ar_K$ recoil even though K is exclusively associated to cryptomelane, a phenomenon previously documented for weathered biotites, biotite/chlorite intergrowths and K-felspar overgrowths [38,44,47,48].

Before interpreting and discussing the $^{40}Ar/^{39}Ar$ results as a whole, it should be noted that the very low analytical errors obtained on plateau or pseudo plateau ages are no indication of the duration of involved long-lasting climatic intervals.

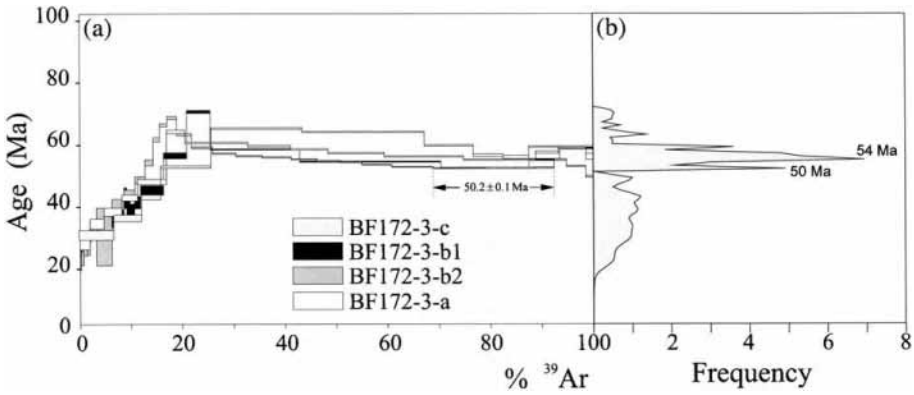

Fig. 8. ^{40}Ar/^{39}Ar-spectra of cryptomelanes extracted from *(a)* sub-fragments of Mn-cutans, with *(b)* the resulting age frequency diagram.

5.3. What do ^{40}Ar–^{39}Ar geochronological results tell us?

Petrographical and geochronological results obtained on pisolites highlight the geochemical relations between massive ore, peripheral pisolite rims and the matrices, and show that the pisolite growth and matrix re-organization are nearly synchronous. ^{40}Ar/^{39}Ar results allow the establishment of a chronology of the pisolitic crust formation at the Tambao Mn deposit.

The pisolites of Mn- and Fe-pisolitic crusts record the oldest cryptomelane formation event, which is clearly identified around 56–59 Ma with a reliable age at 58.6 ± 0.2 Ma for cryptomelane extracted from a nodule. This age interval is also concordant with the age 59 ± 0.1 Ma obtained for a cryptomelane sample collected at the interface between the massive ore and the Mn-pisolitic crust. Between 56 and 47 Ma, no significant ages are recorded by pisolites or matrices that is concordant with the effective dissolution of manganese oxides affecting the primary 56–59 Ma old manganese pisolitic crust. This dissolution induces manganese loss and relative/absolute iron and aluminium enrichment. These geochemical mechanisms could indicate a secondary 'bauxitic' evolution of the pisolitic lateritic formation, suggesting a climatic evolution towards wetter and warmer conditions at that time [49], propitious for an Early-Eocene bauxite development in West Africa [2,28,50]. This interpretation is in good agreement with the development of manganese-iron cutanes around 50 Ma, and also with the formation of thick cryptomelane-rich concretions in the massive oxide ore between ca 47 and 50 Ma [25]. The age interval between 56 and 47 Ma could thus represent a time span during which bauxitic profiles could have been developed in West Africa under warmer conditions, which are also documented by global marine δ^{18}O data [51] (Fig. 9).

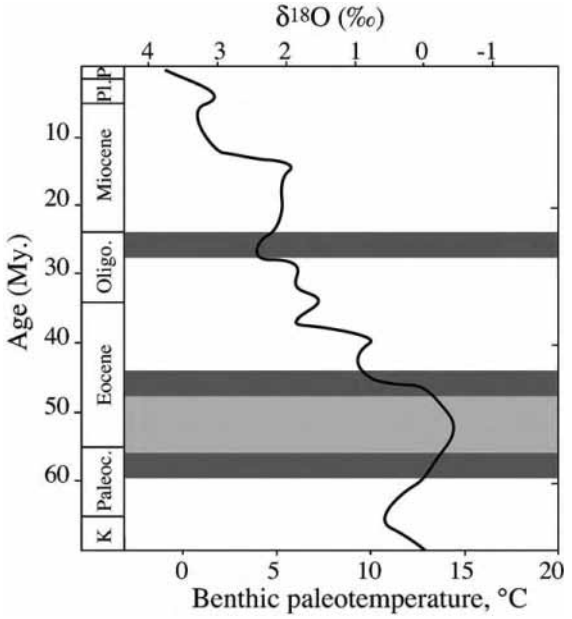

Fig. 9. Comparison between the three-cryptomelane ^{40}Ar–^{39}Ar-age-clusters (grey bands) obtained by this study and the global marine δ^{18}O-paleotemperature curve from benthic foraminifera defining the Tertiary greenhouse effect period (light grey) (Modified from Savin [51]) ; (K: Cretaceous; Pl.: Pleistocene; P: Pliocene).

Most cryptomelane extracted from the Mn-matrix of the Mn-pisolitic cortices are characterised by apparent ages in the range 44–47 Ma that indicates a significant second event of manganiferous lateritic weathering at Tambao. The absence of significant clusters of apparent ages between 44 and 27 Ma does not simply mean that drier conditions prevailed during all this period in the sub-Saharan area as our petrographic study reveals the formation of secondary gibbsite after dissolution of cryptomelane, which the crystallisation ages range between 44 and 47 Ma. Cooler conditions for mid-Eocene period are however reflected by an increase of ^{18}O in benthic foraminifera [51], and by a forest regression associated to an increase of erosion in the sub-Sahelian area as expected by palaeoceanographic and sedimentary studies [52–54]. The widely accepted cooling period ranging from middle Eocene to end of mid-Oligocene [54,55], should be also tempered by the occurrence of tropical climatic conditions in the Sahelian and sub-Sahelian zones from the Eocene to Miocene [57]. Relatively wet and hot global climatic conditions were also advocated for that period [49], which could have been propitious for the development of ferruginous weathering profiles in the tropical zone of the African continent. The third significant event documented by age spectra in the 24–27 Ma range for Mn-matrices, reflects a partial reactivation of manganiferous lateritic weathering processes in Tambao at that time. The three cryptomelane age-intervals, 59–56, 47–44 and 27–24 Ma could be signatures of transitory climatic conditions towards global warmer or cooler climatic periods (Fig. 9), the ages 56 and 47 Ma providing time boundaries for the optimum of the Tertiary greenhouse effect period during which a global bauxitic phase set up in between the mid-latitudes [50].

Geomorphological observations of West African Al- and Fe-crusts capping plateaus have suggested that the highest ones, the bauxitic hills and the adjacent ferruginous plateaus, might have developed from the Eocene to the Pliocene [29,58,59]. Boulangé [3] proposed that a genetic relationship might exist between the bauxites and the adjacent ferruginous laterites of the transitional lateritic system, by arguing that Fe was leached during the bauxite transformation, and then precipitated nearby to form lower and younger ferruginous systems. The pisolitic crust of Tambao could result from similar geochemical mechanisms of remobilization, lateral migration of leached manganese and secondary accumulations of iron and aluminium, as supported by our petrographical observations and $^{40}Ar/^{39}Ar$ dating results. Intensive in situ chemical weathering could have been effective during the Paleocene and the Eocene periods, under hot and humid climatic conditions [49,55,56], which could have been quite favourable to bauxite formation. The 47 Ma age could be thus the younger boundary age for bauxite formation in West Africa. The absence of ages between 44 and 27 Ma could simply indicate a change in environmental and geochemical conditions that could have been still

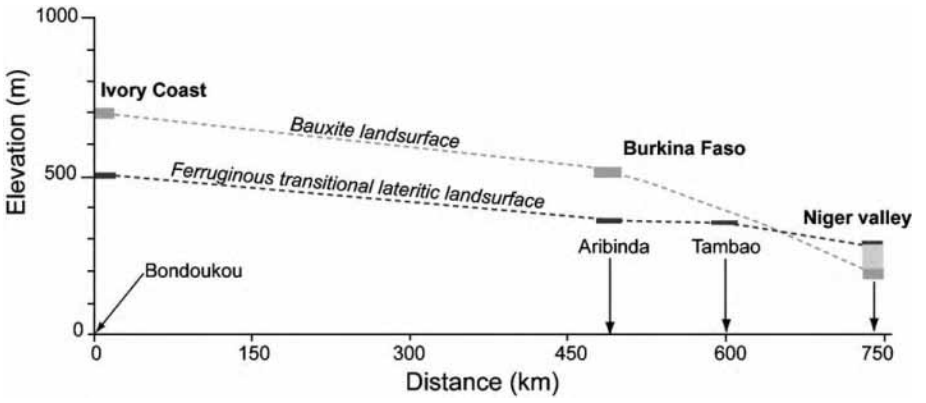

Fig. 10. Geomorphological relationships between bauxite and ferruginous transitional lateritic landsurfaces in West Africa (Modified from Hénocque, 1999, [61]; Black=relics of ferruginous transitional lateritic system; grey=relics of bauxite landsurface; light grey="continental terminal" sedimentary formation, [60]).

propitious for ferruginous rather than for manganiferous lateritic weathering. That does not prevent the upper Oligocene being globally drier and cooler under the tropics [49], contributing thus to the shaping of landsurfaces capped with the previously formed aluminous, ferruginous or manganiferous crusts.

On the basis of relic lateritic plateaus correlation, the large-scale extension of the bauxite and ferruginous transitional lateritic landsurfaces shows an elevation difference of about 40 m between the two at Tambao, while the sedimentary formation of the "continental terminal" is embedded in between the two landsurfaces [60,61] (Fig. 10). Although bauxites have been eroded and ferricretes of the transitional lateritic system are strongly dismantled at Tambao, this geomorphological sketch suggests that the absolute Al-enrichment in the pisolitic surface deposits of Tambao is a result of the geochemical dissolution of previous bauxitic profiles, which could have been developed nearby the manganese ore deposit [29], or even upon the metavolcano-sedimentary series adjacent to the Mn-carbonates (Fig. 1b). The intersection of the two correlated landsurfaces between Tambao and the Niger Valley (Fig. 10) also supports the genetic relationship between bauxite and the ferricrete of transitional lateritic system.

6. Conclusion

The pisolitic crusts of the Tambao manganese ore deposit are characterized by distinct episodes of cryptomelane crystallisations during pisolite formation that results also in Mn-leaching associated with Si-Al enrichments and goethite precipitations, followed by gibbsite neoformation in the embedding matrices. The Al-enrichment suggests a genetic relationship between bauxites of the old "African Surface" and the adjacent Mn- and Fe-pisolitic crusts. Although few $^{40}Ar/^{39}Ar$ age spectra exhibit plateau or pseudo-plateau ages, this relation is still supported by the rather good reproducibility of $^{40}Ar/^{39}Ar$ dating results that allow the definition of three age clusters, 56–59 Ma, 44–47 Ma and 24–27 Ma. These results confirm that chemical weathering processes required for cryptomelane development were active at Tambao during the Paleogene. The $^{40}Ar/^{39}Ar$ dating results suggest however that the pisolite formation has been developed under humid tropical contrasted conditions after a time span of intense lateritic weathering favourable to bauxitic rather than to manganiferous lateritic weathering, starting late Paleocene and ending mid-Eocene. The age interval 56–47 Ma may allow definition of the time constraints for the Tertiary greenhouse effect period. The lack of significant apparent ages between 44 and 27 Ma indicates a change of geochemical weathering processes, which could have been favourable to the development of ferruginous profiles during the period ranging from middle Lutetian to mid-Oligocene, the upper Oligocene being generally characterised as dry, cool and propitious for mechanical erosion rather than for chemical weathering.

Acknowledgements

This is a contribution of IRD UR-037 and CEREGE UMR-161 (France), with financial support from DBT-PROSE and IRD scientific programs. Facilities for performing $^{40}Ar/^{39}Ar$ analyses have been provided by the geochronological laboratory of Geosciences Azur (UMR CNRS 6526) of Nice University (France). Georges Grandin is thanked for fruitful discussions, and Bruno Boulangé for sharing his knowledge on West Africa bauxites. Nicolas Perrier is also thanked for having verified the English. Greg Retallack is also thanked for his stimulating review of the manuscript.

Appendix A. Supplementary data

Supplementary data associated with this article can be found, in the online version, at doi:10.1016/j.epsl.2005.06.052.

References

[1] D. Nahon, Introduction to the Petrology of Soils and Chemical Weathering, John Wiley & Sons, New York, 1991, 313 pp.
[2] Y. Tardy, Pétrologie des Latérites et des Sols Tropicaux, Masson, Paris, 1993, 459 pp.

[3] B. Boulangé, Les formation bauxitiques latéritiques de Côte-d'Ivoire, Les Faciès, Leur Distribution et L'évolution Du Modelé, Mémoire, vol. 175, ORSTOM, Paris, 1984, 363 pp.
[4] A. Beauvais, D. Nahon, Nodules et pisolites de dégradation des profils d'altération manganésifères sous conditions latéritiques. Exemples de Côte d'Ivoire et du Gabon, Sci. Geol., Bull. 38 (1985) 359–381.
[5] D. Nahon, Evolution of iron crust in tropical landscapes, in: S.H. Colemans, D.P. Dethier (Eds.), Rates of Chemical Weathering of Rocks and Minerals, Academic Press, 1986, pp. 169–191.
[6] P.M. Vasconcelos, T.A. Becker, P.R. Renne, G.H. Brimhall, Age and duration of weathering by ^{40}K-^{40}Ar and ^{40}Ar/^{39}Ar analysis of Potassium–Manganese Oxides, Science 58 (1992) 451–455.
[7] A. Beauvais, Geochemical balance of lateritization processes and climatic signatures in weathering profiles overlain by ferricretes in Central Africa, Geochim. Cosmochim. Acta 63 (1999) 3939–3957.
[8] P.M. Vasconcelos, K-Ar and ^{40}Ar/^{39}Ar geochronology of weathering processes, Annu. Rev. Earth Planet. Sci. 27 (1999) 183–229.
[9] J.W. Li, P. Vasconcelos, Cenozoic continentall weathering and its implications for the palaeoclimate: evidence from ^{40}Ar/^{39}Ar geochronology of supergene K-Mn oxides in Mt Tabor, central Queensland, Australia, Earth Planet. Sci. Lett. 200 (2002) 223–239.
[10] J.F. Holtrop, The manganese deposits of the Guyana shield, Econ. Geol. 60 (1965) 1185–1212.
[11] E.A. Perseil, G. Grandin, Evolution minéralogique du manganèse dans trois gisements d'Afrique de l'Ouest: Mokta, Tambao, Nsuta, Miner. Depos. 13 (1978) 295–311.
[12] D. Nahon, A. Beauvais, J.J. Trescases, Manganese concentration through chemical weathering of metamorphic rocks under lateritic conditions, in: J.I. Drever (Ed.), The Chemistry of Weathering, Reidel Pub. Comp., 1985, pp. 277–291.
[13] A. Beauvais, A. Melfi, D. Nahon, J.J. Trescases, Pétrologie du gisement latéritique manganésifère d'Azul (Brésil), Miner. Depos. 22 (1987) 124–134.
[14] Y. Feng, P. Vasconcelos, Quaternary continental weathering geochronology by laser-heating ^{40}Ar/^{39}Ar analysis of supergene cryptomelane, Geology 29 (2001) 635–638.
[15] A. Byström, A.M. Byström, The crystal structure of Hollandite, the related manganese oxide minerals, and α-MnO_2, Acta Crystallogr. 3 (1950) 146–154.
[16] A.D. Wadsley, The crystal structure of Psilomelane, $(Ba,H_2O)_2Mn_5O_{10}$, Acta Crystallogr. 6 (1953) 433–438.
[17] S. Turner, P.R. Buseck, Manganese oxide tunnel structures and their intergrowths, Science 203 (1979) 456–458.
[18] R.M. McKenzie, Manganese oxides and hydroxides, in: J.B. Dixon, S.B. Weed (Eds.), Minerals in Soil Environments, Soil Science Society of America, 1989, pp. 439–465.
[19] F.V. Chukhrov, L.L. Shanin, L.P. Yermilov, Feasibility of absolute-age determination for potassium-carrying manganese minerals, Int. Geol. Rev. 8 (1966) 278–280.
[20] L.P. Yashvili, R.K. Gukasyan, Use of cryptomelane for potassium-argon dating of manganese ore of the Sevkar-Sargyukh deposit, Armenia, Dokl., Earth Sci. Sect. 212 (1974) 49–51.
[21] I.M. Varentsov, D.I. Golovin, Groote Eylandt manganese deposit, North Australia: K-Ar age of cryptomelane ore and aspects of genesis, Rep. Acad. Sci. USSR 294 (1987) 203–207.
[22] A. Segev, L. Halicz, B. Lang, G. Steinitz, K-Ar dating of manganese minerals from the Eisenbach region, Black Forest, Southwest Germany, Schweiz. Mineral. Petrogr. Mitt. 71 (1991) 101–114.
[23] P.M. Vasconcelos, P.R. Renne, G.H. Brimhall, T.A. Becker, Direct dating of weathering phenomena by ^{40}Ar/^{39}Ar and K-Ar analysis of supergene K-Mn oxides, Geochim. Cosmochim. Acta 58 (1994) 1635–1665.
[24] G. Ruffet, C. Innocent, A. Michard, G. Féraud, A. Beauvais, D. Nahon, B. Hamelin, A geochronological ^{40}Ar/^{39}Ar and ^{87}Rb/^{87}Sr study of K-Mn oxides from the weathering sequence of Azul (Brazil), Geochim. Cosmochim. Acta 60 (1996) 2219–2232.
[25] O. Hénocque, G. Ruffet, C. Colin, G. Féraud, ^{40}Ar/^{39}Ar dating of West African lateritic cryptomelanes, Geochim. Cosmochim. Acta 62 (1998) 2739–2756.
[26] P. Picot, R. Trinquard, La manganosite (MnO) du gîte de manganèse de Tambao (Haute-Volta), Bull. Soc. Fr. Minéral. Cristallogr. 92 (1969) 500–502.
[27] E.A. Perseil, G. Grandin, Altération supergène des protores à grenats manganésifères dans quelques gisements d'Afrique de l'Ouest, Miner. Depos. 20 (1985) 211–219.
[28] P. Michel, Les bassins des fleuves Sénégal et Gambie. Etudes géomorphologiques, Mém., vol. 63, ORSTOM, Paris, 1973, 1170 pp.
[29] G. Grandin, Aplanissements cuirassés et enrichissement des gisements de manganèse dans quelques régions d'Afrique de l'Ouest, Mém., vol. 82, ORSTOM, Paris, 1976, 275 pp.
[30] G. Millot, Weathering sequences, climatic planations, leveled surfaces and palaeosurfaces, Development in Sedimentology, vol. 35, VIIth Internat. Clay Conf., Bologne, 1981, pp. 585–593.
[31] B. Boulangé, G. Millot, La distribution des bauxites sur le craton ouest-africain, Sci. Géol., Bull. 41 (1988) 113–123.
[32] E.T. Brown, D.L. Bourlès, F. Colin, Z. Sanfo, G.M. Raisbeck, F. Yiou, The development of iron crust lateritic systems in Burkina Faso, West Africa, examined with in situ produced cosmogenic nuclides, Earth Planet. Sci. Lett. 124 (1994) 19–33.
[33] F. Colin, Z. Sanfo, E.T. Brown, D. Bourlès, A. Edou Minko, Gold: a tracer of the dynamics of laterites, Geology 25 (1997) 81–84.
[34] J. Vogt, Aspects de l'évolution morphologique récente de l'Ouest Africain, Ann. Géogr. Fr. 68 (1959) 193–206.
[35] R.E. Zartman, A geochronological study of the Love Grove Pluton from the Llano uplift, Texas, J. Petrol. 5 (1964) 359–408.
[36] G. Turner, ^{40}Ar–^{39}Ar ages from the lunar maria, Earth Planet. Sci. Lett. 11 (1971) 169–191.
[37] J.C. Roddick, High precision intercalibration of ^{40}Ar/^{39}Ar standards, Geochim. Cosmochim. Acta 47 (1983) 887–898.

[38] G. Ruffet, G. Féraud, M. Amouric, Comparison of ^{40}Ar–^{39}Ar conventional and laser dating of biotites from the North Trégor Batholith, Geochim. Cosmochim. Acta 55 (1991) 1675–1688.

[39] R.H. Steiger, E. Jäger, Subcommission on geochronology: convention on the use of decay constants in geo- and cosmochronology, Earth Planet. Sci. Lett. 36 (1977) 359–362.

[40] T.M. Harrison, Some observations on the interpretation of $^{40}Ar/^{39}Ar$ age spectra, Isot. Geosci. 1 (1983) 319–338.

[41] I. McDougall, T.M. Harrison, Geochronology and Thermochronology by the $^{40}Ar/^{39}Ar$ Method, Oxford Univ. Press, London/New York, 1988, 212 pp.

[42] S. Hautmann, H.J. Lippolt, $^{40}Ar/^{39}Ar$ dating of central European K-Mn oxides — a chronological framework of supergene alteration processes during the Neogene, Chem. Geol. 170 (2000) 37–80.

[43] K.A. Foland, J.S. Linder, T.E. Laskowski, N.K. Grant, $^{40}Ar/^{39}Ar$ dating of glauconites: measured^{39}Ar recoil loss from well-crystallized specimens, Isot. Geosci. 2 (1984) 241–264.

[44] J.C. Hess, H.J. Lippolt, Kinetics of Ar isotopes during neutron irradiation: ^{39}Ar loss from minerals as a source of error in $^{40}Ar/^{39}Ar$ dating, Chem. Geol. 59 (1986) 223–236.

[45] P.E. Smith, N.M. Evensen, D. York, First succesful $^{40}Ar/^{39}Ar$ dating of glauconies: argon recoil in single grains of cryptocrystalline material, Geology 21 (1993) 41–44.

[46] G. Turner, P.H. Cadogan, Possible effects of ^{39}Ar recoil in ^{40}Ar–^{39}Ar dating, Proc. 5th lunar Conf., vol. 2, 1974, pp. 1601–1615.

[47] C.H. Lo, T.C. Onstott, ^{39}Ar recoil artifacts in chloritized biotite, Geochim. Cosmochim. Acta 53 (1989) 2697–2711.

[48] J.-P. Girard, T.C. Onstott, Application of $^{40}Ar/^{39}Ar$ laser-probe and step-heating techniques to the dating of diagenetic K-feldspar overgrowths, Geochim. Cosmochim. Acta 55 (1991) 3777–3793.

[49] Y. Tardy, C. Roquin, Dérive des Continents, Paléoclimats et Alteration Tropicales, Editions BRGM, Orléans, 1998, 473 pp.

[50] G. Grandin, M. Thiry, Les grandes surfaces continentales tertiaires des régions chaudes. Succession des types d'altération, Cah. ORSTOM, Sér. Géol. 13 (1983) 3–18.

[51] S.M. Savin, The history of the Earth's surface temperature during the past 100 millions years, Annu. Rev. Earth Planet. Sci. 5 (1977) 319–355.

[52] B.U. Haq, J. Hardenbol, P.R. Vail, Chronology of fluctuating sea levels since the Triassic, Science 235 (1987) 1156–1167.

[53] A. Ly, R. Anglada, Le Bassin Sénégalo-mauritanien dans l'évolution des marges périatlantiques au Tertiaire, Cah. Micropaléontol. 6 (1991) 23–40.

[54] H. Chamley, P. Debrabant, R. Flicoteaux, Comparative evolution of the Senegal and eastern central Atlantic basins, from mineralogical and geochemical investigations, Sedimentology 35 (1988) 85–103.

[55] D.R. Prothero, The Eocene–Oligocene transition: paradise lost, in: D.J. Bottjer, R.K. Bambach (Eds.), Critical Moments in Paleobiology and Earth History Series, Columbia University press, New York, 1994, 291 pp.

[56] K.A. Salamy, J.C. Zachos, Latest Eocene–Oligocene climate change and southern ocean fertility: inferences from sediment accumulation and stable isotope data, Pal. Pal. Pal., vol. 145, 1999, pp. 61–77.

[57] C.A. Kogbe, M.A. Sowumi, The age of the Gwandu formation (Continental Terminal) in Northwestern Nigeria as suggested by sporo-polinitic analysis, Savana 4 (1975) 47–55.

[58] R. Boulet, La géomorphologie et les principaux types de sol en Haute-Volta septentrionale, Cah. ORSTOM Sér. Pédol., vol. 8, 1970, pp. 245–271.

[59] P. Michel, Cuirasses bauxitiques et ferrugineuses d'Afrique Occidentale- Aperçu chronologique, Trav. Doc. Géogr. Trop. 33 (1978) 11–32.

[60] P. Gavaud, Les grands traits de la pédogenèse au Niger méridional, Trav. Doc., vol. 76, ORSTOM, Paris, 1977, 104 pp.

[61] O. Hénocque, Dynamique de l'altération supergène du craton Ouest-Africain. Pétrologie et datation des latérites manganésifères de Tambao (Burkina Faso), Ph. D thesis, Aix-Marseille III Univ., 1999, 208 pp.

PERSPECTIVES

PERSPECTIVES

Les objectifs scientifiques futurs s'inscrivent dans une perspective résolument globale de définition des facteurs de **formation et d'évolution des latérites** et des relations entre **dénudation et morphogenèse tropicale,** de **datation des matériaux latéritiques,** de **quantification des taux de dénudation** et **de modélisation de la morphogenèse continentale** pour le paléogène et le néogène en domaine cratonique (*Afrique*, Inde, Australie) et Insulaire (*Nouvelle-Calédonie*).

Depuis environ une décennie, la possibilité d'utiliser des données numériques d'altitude (MNT) permet d'étudier les relations entre les grandes altérations latéritiques (bauxite et cuirasses) et les processus morphogénétiques à l'échelle continentale, afin d'établir des bilans de transfert de masse (dénudation, sédimentation) aux mêmes échelles (Pazzaglia et al., 1995 ; Leturmy et al., 2003 ; Lucazeau et al., 2003). Les relations entre tectonique, climat, érosion et façonnement des reliefs peuvent également être analysées sous un angle plus large et plus global qu'auparavant (Pinet et Souriau, 1988 ; Summerfield et Hulton, 1994 ; Summerfield, 1996).

Les capacités actuelles de traitement des données numériques de terrain à l'échelle continentale (Peulvast et de Claudino Sales, 2004), et de datations des matériaux latéritiques sous-tendant les reliques de surfaces latéritiques d'aplanissement permettent de revisiter les modèles d'évolution géomorphologique long terme (Colin et al., 2005).

Le continent africain constitue un cadre de référence pour mener de telles études intégrées puisqu'il présente les plus grandes surfaces couvertes de latérites résiduelles diversifiées. On y trouve en effet des bauxites largement répandues en Afrique de l'Ouest (notamment en Guinée), des cuirasses et carapaces dites ferrugineuses plus ou moins indurées et évoluées largement développées en Afrique Centrale (RCA) et des latosols à gravillons et/ou nodules ferrugineux s'imbriquant au cœur et autour des domaines à cuirasses latéritiques d'Afrique Centrale et de l'Ouest (Fig. 5).

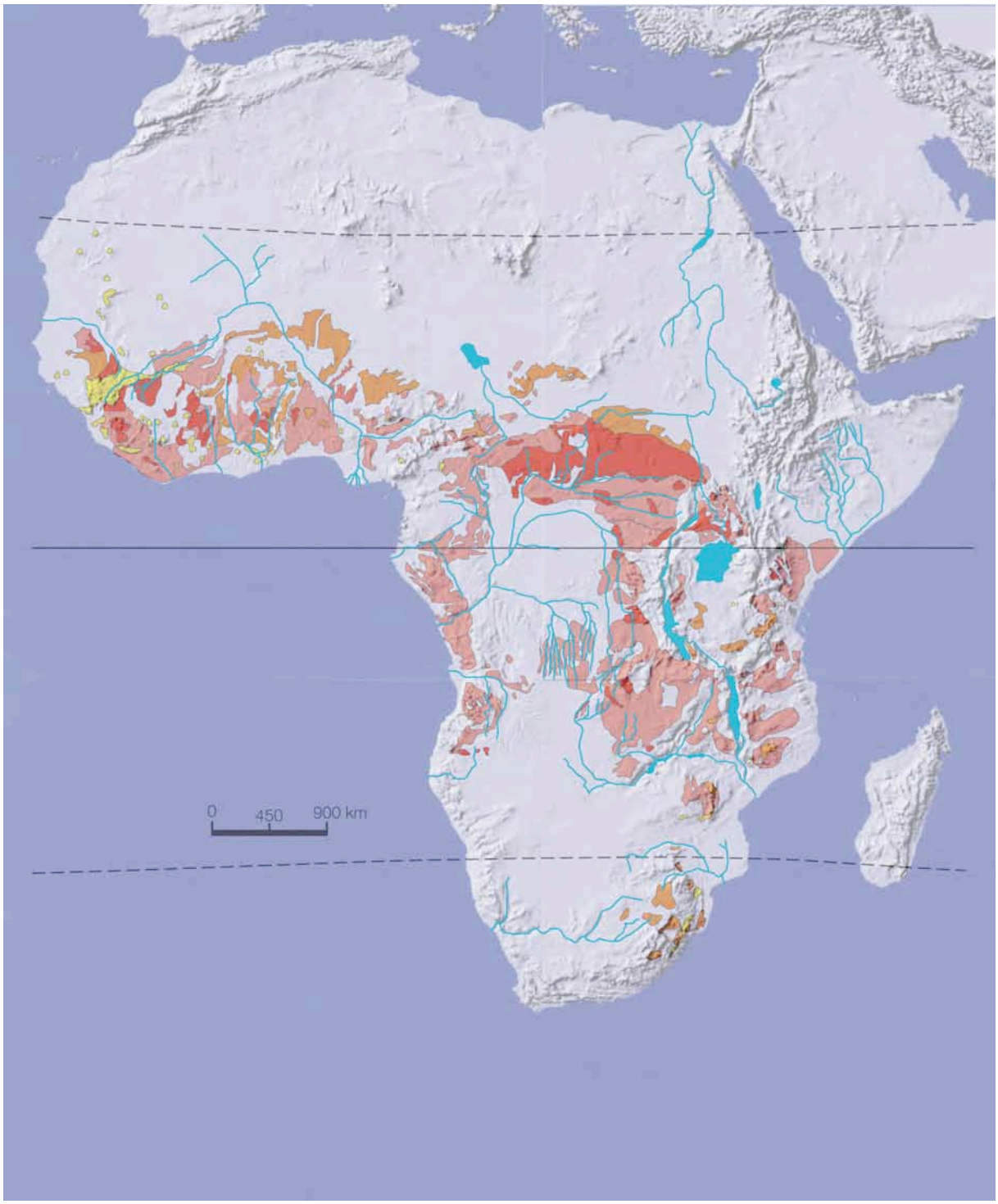

Figure 5. Distribution des formations latéritiques en Afrique, superposées au MNT GTopo 30 (Modifié d'après Beauvais, 1991 ; Jaune = bauxites ; orangé = sols ferrugineux tropicaux à carapace ferrugineuse ; rouge = cuirasses ferrugineuses ; rose = sols ferrallitiques rouges à nodules ferrugineux ; bleu = rivières, fleuves et lacs).

1. FACTEURS DE FORMATION ET DE L'EVOLUTION DES LATERITES

À l'échelle continentale, la distribution latitudinale et altitudinale des latérites (Fig. 5) impliquent de considérer à la fois le climat et les mouvements verticaux de la lithosphère comme facteurs de leur formation et de leur évolution.

Sur les cratons stables tropicaux, les alternances climatiques sur le long terme (100 Ma) ont engendré de grandes périodes d'altération et d'érosion, qui ont contribué respectivement à la formation et au démantèlement des manteaux d'altération bauxitique et ferrugineuse dans toute la ceinture intertropicale, dont les limites ont migré au cours de la dérive tectonique des plaques continentales (Tardy et Roquin, 1998).

Les mouvements tectoniques de la lithosphère peuvent aussi jouer un rôle dans les processus d'altération et d'érosion à la surface des masses continentales (Taylor et Howard, 1998). Le soulèvement de portions de lithosphère peut ainsi accentuer les processus d'altération sous les surfaces soulevées, mais aussi les processus d'incision et d'érosion au cœur et à la périphérie de ces surfaces (Gregory et Chase, 1994 ; Summerfield, 1996).

L'influence des variations des facteurs climatiques et des mouvements tectoniques (épeirogéniques) sur la dynamique des processus d'altération et d'érosion sera examinée à l'échelle de grands espaces continentaux et sur des échelles de temps compatibles avec la genèse des altérations latéritiques (bauxites et cuirasses d'Afrique), y compris les accumulations supergènes de métaux dont certaines sont d'intérêt économique (gisements de manganèse, et nickel en Nouvelle-Calédonie).

Si les latérites sont les produits résiduels de la dénudation des roches de la croûte terrestre, elles sont aussi, pour la plupart, à l'état de reliques sur les lambeaux étagés des surfaces d'aplanissement qui apparaissent ainsi comme autant d'étapes dans la morphogenèse tropicale sur le long terme, dont il convient de préciser la chronologie en datant chaque fois que possible les matériaux latéritiques associés (cuirasses manganésifères et ferrugineuses).

2. DENUDATION ET MORPHOGENESE TROPICALE

La dénudation intègre l'altération chimique des roches de la croûte continentale et l'érosion mécanique des matériaux latéritiques résiduels de cette altération, les deux processus transformant les géomorphologies par l'exportation de grandes quantités de matières vers les

bassins (onshore et offshore). Intégrée sur le long terme (100 Ma) la dénudation est responsable de la morphogenèse actuelle des continents de la ceinture intertropicale, caractérisée par des reliques étagées de surfaces d'aplanissement pouvant porter des matériaux latéritiques, chaque niveau de surface marquant une étape de l'enfoncement des résaux hydrographiques dans les paysages. Les matériaux latéritiques transportés actuellement par les rivières et fleuves majeurs des domaines intertropicaux sont essentiellement composés d'argile (kaolinite dominante) et d'oxyhydroxydes de fer (goethite dominante) provenant des manteaux d'alteration sous cuirasses latéritiques (refs.). Sur le long terme, l'exportation vers les bassins de grandes quantités de matériaux fins (kaolinite + goethite) issus des horizons d'altération sous-jacents aux cuirasses bauxitiques et ferrugineuses a pu participer au démantèlement de ces cuirasses, dont les éléments latéritiques grossiers ont été dispersés plus bas, puis ont été recyclés dans les pédiments et-ou glacis cuirassés (ferrugineux et manganésifères), dont certains sont encore fonctionnels aujourd'hui. De nombreuses observations montrent une certaine allochtonie des matériaux latéritiques sur les pédiments et-ou glacis, les latérites strictement autochtones étant le plus souvent conservées sur les reliefs reliques dominants (Beauvais et al., 1999). À l'échelle continentale (Afrique, Inde, Australie, Amérique du sud), le couplage dénudation-morphogenèse a généré une mosaïque de matériaux latéritiques très diversifiés (Fig. 5), dont la cartographie en 3D est à la base de la reconstitution des paléoenvironnements et de l'établissement des modèles de morphogenèse d'échelle continentale.

Une telle cartographie peut conduire à une chronologie relative des reliques des différentes surfaces d'aplanissement étagées, proposée comme hypothèse, avant l'acquisition de données géochronologiques sur les matériaux latéritiques résiduels associés (oxyhydroxydes de manganèse et fer + kaolinite).

3. GEOCHRONOLOGIE DES PROCESSUS D'ALTERATION ET D'EROSION

L'un des objectifs fondamentaux du projet est la datation des latérites afin de caler les grandes phases d'altération et d'érosion paléogène et néogène. Des âges $^{40}Ar/^{39}Ar$ bien contraints sur les cuirasses manganésifères (Vasconcelos, 1999 ; Ruffet et al., 1996 ; Hénocque et al., 1998) peuvent permettre d'estimer des vitesses d'altération mais aussi d'érosion (Mouélé, 2004) si les objets datés sont replacés dans une séquence géomorphologique étagée dont la chronologie relative est bien comprise. Les groupes d'âges

$^{40}Ar/^{39}Ar$ contribuent aussi à préciser les grandes périodes climatiques et paléoclimatiques favorables à l'altération latéritique (Colin et al., 2005 ; Fig. 6).

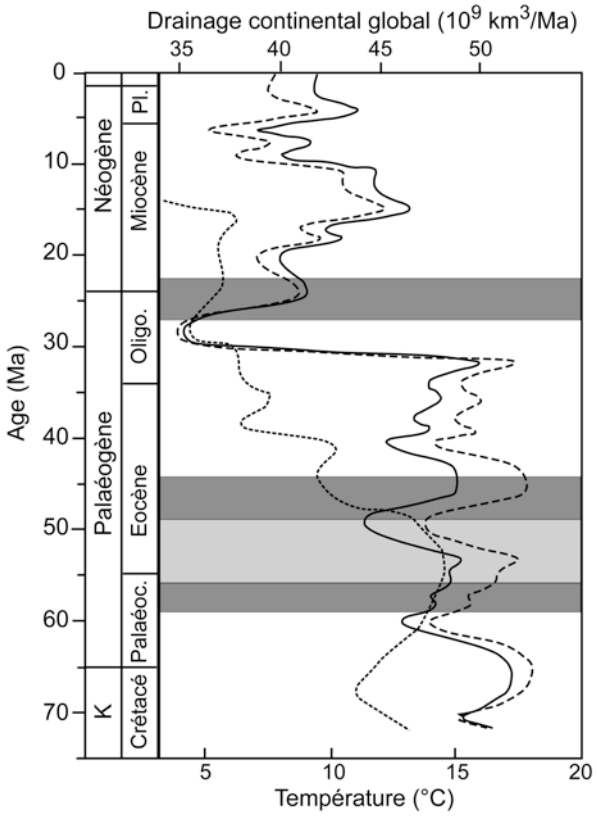

Figure 6. Superposition des groupes d'âges ^{40}Ar-^{39}Ar (gris) obtenus sur les cryptomélanes des pisolites ferro-manganésifères du gisement de Tambao au Burkina Faso et des courbes de paléotempératures océaniques estimées à partir des mesures de $\delta^{18}O$ dans les foraminifères benthiques (Savin, 1977) (pointillés fins et serrés), paléotempératures (courbe pleine) et drainage (pointillés) continentaux globaux (Tardy et Roquin, 1998), définissant la période à effet de serre Tertiaire (gris clair). (K : Crétacé ; Palaéoc. : Palaeocène ; Oligo. : Oligocène ; Pl. : Pliocène

On envisage également d'appliquer la méthode (U-Th)/He pour dater la formation des goethites (Shuster et al., 2005). La méthode des isotopes stables de l'oxygène pourrait aussi être appliqué aux oxyhydroxydes de fer comme la goethite pour caractériser les conditions hydroclimatiques de leur formation (Yapp, 2000 ; Girard et al., 2000, 2003).

Récemment, les kaolinites des profils d'altération du bassin amazonien ont été aussi datées par Résonance Paramagnétique Electronique (RPE) et mesure des défauts structuraux intracristallins induits par les radiations naturelles (Balan et al., 2005). La datation des matériaux kaolinitiques des manteaux d'altération sous-jacents aux cuirasses bauxitiques,

ferrugineuses, et-ou managnésifères ainsi que celle des kaolinites préservées au sein de ces cuirasses seraient d'un apport considérable en complément des âges obtenus sur les oxyhydroxydes de Fer et Mn par radio isotopie U-Th/He et ^{40}Ar-^{39}Ar.

Toutes ces méthodes seront testées, puis appliquées aux cuirasses ferrugineuses de Nouvelle-Calédonie essentiellement constituées de goethite avant de l'être à celles d'Afrique et d'Inde, qui présentent un attrait supplémentaire pour les possibilités de datations des kaolinites et des oxyhydroxydes de manganèse.

Les matériaux latéritiques replacés dans un ensemble lithologique et géomorphologique bien défini peuvent alors apparaître comme de bons marqueurs des climats et paléoclimats qui régnaient à l'époque de leur formation (Thiry, 2000). Des données géochronologiques couplées à des mesures de taux de dénudation et de sédimentation devraient également permettent à terme de proposer un modèle intégré de morphogenèse à l'échelle continentale en relation avec les grands évènements climatiques et tectoniques.

4. BILAN DE LA DENUDATION ET MODELISATION DE LA MORPHOGENESE CONTINENTALE

Les taux de dénudation seront quantifiés dans différents contextes lithologiques et morphoclimatiques (continent africain, Nouvelle-Calédonie) en couplant trois approches, pour lesquelles l'acquisition de données géochimiques et minéralogiques sur les roches et les différents matériaux latéritiques sera centrale.

La production *in situ* du ^{10}Be sera mesurée dans les silicates (quartz) présents dans la partie supérieure des sols et des manteaux d'altération pour déterminer les taux d'érosion intégrés sur des échelles de temps de quelques millénaires et 1 million d'années (Braucher et al., 1998a et 1998b).

La distribution spatiale des latérites résiduelles et des reliques de surfaces géomorphologiques porteuses ainsi que celle des bassins d'accumulation sédimentaire intracratonique établie à l'échelle continentale à partir de modèle numérique de terrain (SRTM90), permettra d'estimer les taux de dénudation en intégrant les volumes de matériaux d'altération manquants entre les différentes familles de surfaces latéritiques, traduits en volumes équivalents de crôute continentale altérée. Les compositions chimiques moyennes des matériaux latéritiques érodés et de la crôute continentale seront utilisées dans le calcul des

taux de dénudation intégrés à l'échelle continentale. Le bilan entre les taux de dénudation et de sédimentation dans les bassins sédimentaires offshore et intra-continentaux (exemple de l'Afrique de l'Ouest) sera défini.

Les données géochronologiques obtenues sur des matériaux latéritiques repositionnés sur leur surface respective permettront aussi d'estimer des taux de dénudation qui pourront être comparés à ceux qui seront obtenus par l'analyse quantitative des MNT. Un modèle global de morphogenèse à l'échelle continentale sera proposé in fine; ce modèle rendra compte des grandes phases climatiques d'altération et d'érosion ainsi que du couplage avec les grands évènements tectoniques pour expliquer la succession spatio-temporelle des grandes surfaces géomorphologiques d'aplanissements latéritiques sur le long terme (Roessner et Strecker, 1997).

REFERENCES BIBLIOGRAPHIQUES

REFERENCES CITEES

Alexander L.T., Cady J.G. (1962) - Genesis and hardening of laterite in soils. Tech. Bull., Department of Agric., Washington, 1282.

Ambrosi J-P., Nahon D. (1986a) - Petrological et geochemical differentiation of lateritic iron crust profiles. *Chem. Geol*., **57**, 371-393.

Ambrosi J-P., Nahon D., Herbillon A. J. (1986b) - The epigene replacement of kaolinite by hematite in laterite- Petrographic evidence and the mechanisms involved. *Geoderma*, **37**, 283-294

Balan E., Allard T., Fritsch E., Sélo M., Falguères C., Chabaux F., Pierret M-C., Calas G. (2005) - formation and evolution of layeritic profiles in the middle Amazon basin : Insights from radiation-induced defects in kaolinite. *Geochim. Cosmochim. Acta*, **69**, 9, 2193-2204.

Beauvais A. (1991) - Paléoclimats et dynamique d'un paysage cuirassé du Centrafrique. Morphologie, Pétrologie et Géochimie. Doctorat Université de Poitiers, 315 p.

Beauvais A. (1999) - Geochemical balance of lateritization processes and climatic signatures in weathering profiles overlain by ferricretes in central Africa. *Geochim. Cosmochim. Acta*, **63**, 23/24, 3939-3957.

Beauvais A., Bertaux J. (2002) - *In situ* characterization and differentiation of kaolinites in lateritic weathering profiles using infrared microspectrometry. *Clays and Clay Minerals*, **50**, 3, 314-330.

Beauvais A., Colin F. (1993) - Formation and transformation processes of iron duricrust systems in tropical humid environement. *Chem . Geol*., **106**, 77-101.

Beauvais A., Ritz M., Parisot J-C., Bantsimba, C. (2003) - Testing etching hypothesis in shaping granite dome structures beneath lateritic weathering landsurfaces using ERT method. *Earth Surface Processes and Landforms*, **28** (10), 1071-1080.

Beauvais A., Ritz M., Parisot J-C., Bantsimba, C., Dukhan, M. (2004) - Combined ERT and GPR methods for investigating two stepped lateritic weathering systems. *Geoderma*, **119**, 121-132.

Beauvais A., Ritz M., Parisot J-C., Dukhan, M., Bantsimba, C. (1999) - Analysis of poorly stratified lateritic terrains overlying a granitic bedrock in West Africa, using 2D electrical resistivity tomography. *Earth and Planetary Science Letters*, **173**, 413–424.

Beauvais A., Roquin C. (1996) - Petrological differentiation patterns and geomorphic distribution of ferricretes in Central Africa. *Geoderma*, **73**, 63-82.

Beauvais A., Tardy Y. (1991) - Formation et dégradation des cuirasses ferrugineuses sous climat tropical humide à la lisière de la forêt équatoriale. *Comptes Rendus de l'Académie des Sciences*, **313**, sér. II, 1539-1545.

Berner R. A. (1994) - Geocarb II : a revised model of atmospheric CO_2 over Phanerozoïc time. *Amer. J. Sci*., 294, 56-91.

Berner R. A., Lasaga A, Garrels R. M. (1983) - The carbonate-silicate geochemical cycle an dits effect on atmospheric carbon dioxide over the past 100 millions years. *Amer. J. Sci*., **283**, 641-683.

Boeglin J.L. and Mazaltarim D. (1989) - Géochimie, degrés d'évolution et lithodépendance des cuirasses ferrugineuses de la région de Gaoua au Burkina-Faso. *Sci. Géol., Bull.*, **42** (1), 27-44.

Boeglin J-L., Probst J-L. (1998) - Physical and chemical weathering rates and CO_2 consumption in atropical lateritic environment : the upper Niger basin. *Chem. Geol*., **148**, 137-156.

Boulet R. (1974) - Toposéquences de sols tropicaux en Haute-Volta : équilibre dynamique et bioclimats. Thèse Sci., Université de Strasbourg, Mém. ORSTOM, Paris, **85**, 272 p.

Braucher R., Bourlès D. L., Colin F., Brown E. T., Boulangé B. (1998a) - Brazilian laterite dynamics using in situ-produces ^{10}Be. *Earth Planet. Sci. Lett*., **163**, 197-205.

Braucher R., Brown E. T., Bourlès D. L., Colin F. (2003) - In situ-produced ^{10}Be measurements at great depths : implications for production rates by fast muons. *Earth Planet. Sci. Lett*., **211**, 251-258.

Braucher R., Colin F., Brown E. T., Bourlès D. L., Bamba A., Raisbeck G. M., Yiou F. (1998b) - African laterite dynamics using in situ-produced 10Be. Geochim. Cosmochim. Acta, **62**, 9, 1501-1507.

Braun J-J., Pagel M., Herbillon A., Rosin C. (1993) - Mobilisation and redistribution of REEs and thorium in syenictic lateritic profile : a mass balnce study. *Geochim. Cosmochim. Acta*., **57**, 4419-4434.

Brimhall G. H., Dietrich W. E. (1987) - Consecutive mass balance relations between chemical composition, volume, density, porosity, and strain in metasomatic hydrochemical systems : results on weathering and pedogenesis. *Geochim. Cosmochim. Acta*., **51**, 567-587.

Brown E. T., Bourlès D. L., Colin F., Sanfo Z., Raisbeck G. M., Yiou F. (1994) - The development of iron crust lateritic systems in Burkina Faso, West Africa examined with in itu –produced cosmogenic nuclides. *Earth Planet. Sci. Lett*., **124**, 19-33.

Brown E. T., Colin F., Bourlès D. L. (2003) - Quantitative evaluation of soil processes using in situ-produced cosmogenic nuclides. *C. R. Géoscience*, **335**, 1161-1171.

Buchanan F. (1807) – A journey from Malabar through the countries of Mysor, Canara and Malabar. London, East India Company, **2**, 436-460.

Büdel J. (1982) - Climatic geomorphology. Princeton University Press, Princeton, New Jersey.

Chevillotte V. (2005) - Morphogenèse tropicale en contexte epirogénique modéré. Exemple de la Nouvelle-Calédonie (Pacifique Sud-Ouest). Doctorat d'Univ., Université de Nouvelle-Calédonie, Nouméa, 164 p.

Chauvel A. (1977) - Recherches sur la transformation des sols ferrallitiques dans la zone tropicale à saisons contrastées. Thèse Sci., Université de Strasbourg, Trav. & Doc. ORSTOM, Paris, **62**, 532 p.

Colin F., Beauvais A., Ruffet G., O. Hénocque (2005) - First $^{40}Ar/^{39}Ar$ geochronology of lateritic manganiferous pisolites: implications for the Paleogene history of a West African landscape. *Earth and Planetary Science Letters*, 238, 172-188.

Colin F., Alarcon C., Viellard Ph. (1993) - Zircon : an immobile index in soils ? *Chem. Geol*., **107**, 273-276.

Colin F., Vieillard Ph. (1991) - Behavior of gold in the lateritic environement : weathering and surface dispersion of residual gold particles at Dondo-Mobi, Gabon. *Appl. Geochem*., **6**, 279-290.

Didier Ph., Fritz B., Nahon D., Tardy Y. (1985) - Equilibres entre kaolinites ferrifères, goethites alumineuses et hématites alumineuses dans les sytèmes cuirassés. Rôle de l'activité de l'eau et de la taille des pores. *Sci. Géol. Bull*., **38**, 4, 383-397.

Dupré B., Dessert C., Oliva P., Goddéris Y., Vuers J., françois L., Millot R., Gaillardet J. (2003) - Rivers chemical weathering and Earth's climate. *C. R. Geoscccience*, **335**, 1141-1160.

Edmond J. M., Palmer M. R., Measurezs C. I., Grant B., Stallard R. F. (1995) - The fluvial geochemistry and denudation rates of the Guyana shileds in Venezuela, Colombia, and Brazil. *Geochim. Cosmochim. Acta*, **59**, 3301-3325.

Fitzpatrick R. W. (1983) - Iron compounds as indicators of pedogenetic processes: examples from the southern hemisphere. In *Iron in soils and clay minerals*, J. W. Stucki et al. (eds), 351-396.

Fitzpatrick R. W. and Schwertmann U. (1982) - Al-substituted goethite - An indicator of pedogenic and other weathering environments in South Africa. *Geoderma*, **27**, 335-347.

Fritz B. (1975) - Etude thermodynamique des réactions entre minéraux et solutions. Application à la géochimie des altérations et des eaux continentales. Sci. Géol. Mém., Strasbourg, 41, 152 p.

Fritz B., Tardy Y. (1973) - Etude thermodynamique du système gibbsite, quartz, kaolinite, gaz carbonique. Application à la genèse des podzols et des bauxites. *Sci. Géol. Bull*., **26**, 4, 339-367.

Fritz B., Tardy Y. (1976) - Séquences des minéraux secondaires dans l'altération des granites et roches basiques, modèles thermodynamiques. *Bull. Soc. Géol. France*, **18**, 1, 7-12.

Gaillardet J., Dupré B., Allègre C. J., Négrel P. (1997) - Chemical and physical denudation in the Amazon river basin. *Chem. Geol*., **142**, 141-173.

Garrels R. M., Christ C. L. (1965) - Solutions, minerals and equilibria. Harper and Row, 450 p.

Gibbs M. T., Bluth G. J. S., Fawcett P. J., Kump L. R. (1999) - Global chemical erosion over the past 250 Ma : variations due to changes in paleogeography, paleoclimate and paleogeology. *Am. J. Sci*., **299**, 611-651.

Girard J-P., Freyssinet Ph., Chazot G. (2000) - Unravelling climatic changes from intraprofile variations in oxygen and hydrogen istopic composition of goethite and kaolinite in laterites : an integrated study from Yaou, french Guiana. *Geochim. Cosmochim. Acta*, **64**, 3, 409-426.

Girard J-P., Freyssinet Ph., Morillon A-C. (2003) - Oxygen isotope study of Cayenne duricrust paleosurfaces : implications for past climate and lateritization processes over French Guyanna. *Chem. Geol*., **191**, 329-343.

Grandin G. (1976) - Aplanissements cuirassés et enrichissement des gisements de manganèse dans quelques régions d'Afrique de l'Ouest. Mém. ORSTOM, Paris, **82**, 275 p.

Gregory K. M., Chase C.G. (1994) - Tectonic and climatic significance of a late Eocene low-relief, high-level geomorphic surface, Colorado. *J. Geoph. Res*., **99**, B10, 20141-20160.

Hénocque O., Ruffet G., Colin C., Féraud G. (1998) - $^{40}Ar/^{39}Ar$ dating of West African lateritic cryptomelanes. *Geochim. Cosmochim. Acta*, **62**, 2739-2756.

King L. C. (1962) - *The morphology of the Earth. A study and synthesis of World scenery*. Oliver & Boyd Eds., Edimburgh, London, 725 p.

Leprun J-C. (1979) - Les cuirasses ferrugineuses des pays cristallins de l'Afrique Occidentale sèche. Genèse, transformation, dégradation. Thèse Sci., Université de Strasbourg, Mém. Sci. Géol., Strasbourg, **58**, 224 p.

Leturmy P., Lacazeau F., Brigaud F. (2003) - Dynamic interactions between the Gulf of Guinea passive margin and the Congo river drainage basin. 1. Morphology and mass balance. *J. Geoph. Res*., **108**, B8, 2383.

Lucazeau F., Brigaud F., Leturmy P. (2003) - Dynamic interactions between the Gulf of Guinea passive margin and the Congo river drainage basin. 2. Isostasy and uplift. *J. Geoph. Res*., **108**, B8, 2384.

Mestraud J. L. (1982) - Géologie et ressources minérales de la République Centrafricaine (Etat des connaissances à la fin 1963). *Mém. BRGM* **60**, Orléans, France, 186 p.

Meybeck M. (1987) - Global chemical weathering of surficial rock estimated from river dissolved loads. *Amer. J. Sci*., **287**, 401-428.

Michel P. (1973) - Les bassins des fleuves Sénégal et Gambie. Étude géomorpholopgique. Mém. ORSTOM, Paris, **63**, 752 p.

Millot G. (1970) - Geology of clays. Springer Verlag, Heidelberg, 429 pp.

Millot G. (1977) - Géochimie de la surface et formes du relief. Présentation. *Sci. Géol. Bull.*, **30**, 292-233.

Millot G., Bonifas M. (1955) - Transformationsisovolumétriques dans les phénomènes de latéritisation et de bauxitisation. *Bull. Serv. Carte Géol. Als. Lor*., **8**, 3-10.

Mouele F. (2004) - Evolution des latérites manganésifères de Serra de Navio (Brésil). Pétrlogie et datation $^{40}Ar/^{39}Ar$ des cryptomélanes. Doctorat, Université Paulk Cézanne d'Aix-Marseille, 283 p.

Muller J-P., Manceau A., Calas G., Allard T., Ildefonse P., and Hazemann J-L. (1995) - Crystal chemistry of kaolinite and Fe-Mn oxides: relation with formation conditions of low temperature systems. *Am. J. Sci*., **295**, 1115-1155.

Nahon D. (1976) - Cuirasses ferugineuses et encroûtements clacires au Sénégal Occidental et en Mauritanie. Systèmes évolutifs : géochimie, strcutures, relais et co-existence. Thèse Sci., Université S^{t} Jérôme, Marseille, Mém. Sci. Géol., Strasbourg, **44**, 232 p.

Nahon D. (1986) - Evolution of iron crusts in tropical landscapes. In : Rates of chemical weathering of rocks and minerals, Colman S. M., Dethier D. P. eds., Academic Press, 169-191.

Nahon D. (1991) - Introduction to the petrology and chemical weathering. John Wiley & Sons, 313 p.

Nahon D., Melfi A., Conte C. N. (1989) - Présence d'un vieux système de cuirasses ferrugineuses latéritiques en Amazonie du Sud. Sa transformation in situ en latosols sous la forêt équatoriale actuelle. C. R. Acad. Sci., Paris, 308, sér. II, 755-760.

Partridge T. C., Maud R. R. (1987) - Geomorphic evolution of southern Africa since the Mesozoic. *S. Afr. J. Geol*., **90**, 2, 179-208.

Pazzaglia F. J., Brandon M. T. (1996) - Macrogeomorphic evolution of the post-Triassic Appalachian mountains determined by deconvolution of the offshore basin sedimentary record. *Basin Res*., **8**, 255-278.

Pedro G. (1968) - Distribution des principaux types d'altération chimique à la surface du globe. *Rev. Géogr. Phys. Géol. Dyn*., **10**, 5, 457-470.

Petit M. (1982) - Essai de cartographie mondiale du cuirassement. Travaux et documents du CEGET, **1**, 1-15.

Peulvast J-P., de Claudino Sales V. (2004) - Stepped surfaces and paleolandsurfaces in the northern Brazilian " Nordeste " : constraints on models of morphotectonic evolution. *Geomorphology*, **62**, 89-112.

Pinet P., Souriau M. (1988) - Continental erosion and large scale relief. *Tectonics*, **7**, 563-582.

Probst J-L. (1992) - Géochimie et hydrologie de l'érosion continentale. Mécanismes, bilan global actuel et fluctuations au cours des 500 derniers millions d'années. Sci. Géol. Mém., Strasbourg, **94**, 161 p.

Probst J-L., Mortatti J., Tardy Y. (1994) - Carbon river fluxes and global weathering CO2 consumption in the Congo and Amazon river basins. *Applied Geochem.*, **9**, 1, 1-13.

Ritz M., Parisot J-C., Diouf S., Beauvais A., Diome F., Niang M. (1999) - Electrical imaging of lateritic weathering mantles over granitic and metamorphic basement of eastern Senegal, West Africa. *Journal of Applied Geophysics*, **41**, 335-344.

Roessner S., Strecker M. R. (1997) - Late cenozoic tectonics and denudation in the central Kenya Rift : quantification of long-term denudation rates. *Tectonophysics*, **278**, 83-94.

Ruffet G., Innocent C., Michard A., Féraud G., Beauvais A., Nahon D., Hamelin B. (1996) - A geochronological $^{40}Ar/^{39}Ar$ and $^{87}Rb/^{87}Sr$ study of K-Mn oxides from the weathering sequence of Azul (Brazil). *Geochim. Cosmochim. Acta*, **60,** 2219-2232.

Schwertmann U. and Carlson L. (1994) - Aluminum influence on iron oxides: XVII. Unit-cell parameters and aluminum substitution of natural goethites. *Soil Sci. Soc. Am. J.*, **58**, 256-261.

Schwertmann U. and Kämpf N. (1985) - Properties of goethite and hematite in kaolinitic soils of southern and central Brazil. *Soil Sci.*, **139**, 344-350.

Shuster, D. L., Vasconcelos P. M., Heim J. A., Farley K. A. (2005) - Weathering geochronology by (U-Th)/He dating of goethite. *Geochim. Cosmochim. Acta*, **69**, 659-673.

Soler J. M., Lasaga A. C. (1996) - A mass transfer model of bauxite formation. *Geochim. Cosmochim. Acta*, 60, 4913-4931.

Summerfield M. A. (1996) - Tectonics, geology, and long-term landscape development. In : *The physical geography of Africa*, W. M. Adams, A. S. Goudie, A. R. Orne (eds.), Oxford regional environments, **1**, 1-17.

Summerfield M. A., Hulton N. J. (1994) - Natural controls of fluvial denudation rates in major world drainage basins. *J. Geoph. Res.*, **99**, B7, 13871-13883.

Stallard R. F. (1995) - River chemistry, geology, geomorphology and soils in the Amazon and Orinoco basins. In : *The chemistry of weathering*, J. I. Drever (Ed.), D. Reidel publishing company, pp. 293-316.

Tardy Y. (1969) - Géochimie des altérations. Étude des arènes et des eaux de quelques massifs cristallins d'Europe et d'Afrique. Thèse Sci., Univ. Strasbourg, *Mém. Serv. Carte Géol. Alsace Lorraine*, **31**, 199 p.

Tardy Y. (1986) - Le cycle de l'eau. Climats, paléoclimats et géochimie globale. Masson, Paris, 338 p.

Tardy Y. (1993) - Pétrologie des latérites et des sols tropicaux. Masspn, Paris, 535 p.

Tardy Y., Kobilsek B ; Paquet H. (1991) - Mineralogical composution and geographical distribution of African and Brazilian periatlantic laterites. The influence of continental drift and tropical paleoclimates during the past 150 million years and implications for India and Australia. *J. Afr. Earth Sci.*, **12**, 1/2, 283-295.

Tardy Y., Mazaltarim D., Boeglin J.L., Roquin C., Pion J.C., Paquet H. and Millot G. (1988a) - Lithodépendance et homogénéisation de la composition minéralogique et chimique des cuirasses ferrugineuses latéritiques. C. R. Acad. Sci, Paris, 307, sér. II, 1765-1722

Tardy Y., Melfi A. J., Valeton I. (1988b) - climats et paléoclimats tropicaux périatlantiques. Rôle des facteurs climatiques et thermodynamiques, température et activité de l'eau sur la répartition et la composition minéralogique des bauxites et des cuirasses ferrugineuses au Brésil et en Afrique. *C. R. Acad. Sci.*, Paris, **306**, sér. II, 289-295.

Tardy Y., Nahon D. (1985) - Geochemistry of laterites, stability of Al-goethite, Al-hematire and Fe3+-kaolinite in bauxites and ferricretes : an approach to the mechanism of concretion formation. *Am. J. Sci.*, **285**, 865-903.

Tardy Y., N'Kounkou R., Probst J-L. (1989) - The global water cycle and continental erosion during phanerozoïc times. *Amer. J. Sci.*, The Garrels issue, 289, 455-485.

Tardy Y., Novikoff A. (1988c) - Activité de l'eau et déplacement des équilibres gibbsite-kaolinite dans les profils latéritiques. *C. R. Acad. Sci., Paris*, **306**, 2, 39-44.

Tardy Y., Roquin C. (1998) - Dérive des continents, paléoclimats et altérations tropicales. Editions BRGM, Orléans, 473 p.

Taylor R. G., Howard K. W. F. (1998) - Post Plaleozoic evolution of weathered landsurfaces in Uganda by tectonically controlled deep weathering and stripping. *Geomorphology*, **25**, 173-192.

Théveniaut H., Freyssinet Ph. (2002) - Timing of lateritization on the Guiana Shield : synthesis of palaeomagnetic results from French Guiana and Suriname. *Palaeogeogr., Palaeoclimatol., Palaeoecol*., **178**, 1-2, 91-117.

Thiry M. (2000) - Palaeoclimatic interpretation of clay minerals in marine deposits : an outlook from the continental origin. *Earth-Science Rev*iews, **49**, 201-221.

Thomas M. F. (1994) - Tropical geomorphology in the tropics. A study of weathering and denudation in low latitudes. John Wiley & Sons, 460 p.

Trescases J-J. (1975) - L'évolution géochimique supergène des roches ultrabasiques en zone tropicale. Formation des gisements nickélifères de Nouvelle-Calédonie. *Mém. ORSTOM*, Paris, **78**, 259 p.

Trolard F., Tardy Y. (1987) - The stabilities of gibbsite, boehmite, aluminous hematites in bauxites, ferricretes and laterites as a function of water activity, temperature and particle size. *Geochim. Cosmochim. Acta*, **51**, 945-957.

Vasconcelos P. M., Becker T. A., Renne P. R. (1992). Age and duration of weathering by $^{40}K/^{40}Ar$ and $^{40}Ar/^{39}Ar$ analysis of K-Mn oxides. *Science*, **258**, 451-455.

Vasconcelos P.M. (1999) - K-Ar and $^{40}Ar/^{39}Ar$ geochronology of weathering processes. *An. Rev. Earth Planet. Sci*., **27**, 183-229.

Vasconcelos P. M., Renne P. R., Brimhall G.H., Becker T.A. (1994) - Direct dating of weathering phenomena by $^{40}Ar/^{39}Ar$ and K-Ar analysis of supergene K-Mn oxides. *Geochim. Cosmochim. Acta*, **58**, 1635-1665.

Yapp C. J. (2000) - Climatic implications of surface hydroxyl minerals : goethite as an example. *Geochim. Cosmochim. Acta*, **64**, 2009-2025.